

N° d'ordre :

École Doctorale Mathématiques, Sciences de l'Information et
de l'Ingénieur

UdS – INSA – ENGEES

THÈSE

Présentée pour obtenir le grade de

Docteur de l'Université de Strasbourg

Discipline : Génie Civil

Spécialité : Photogrammétrie

par

Mostafa MOHAMED

**Evaluation de la qualité des modèles 3D
de bâtiments en photogrammétrie numérique aérienne**

**Quality assessment of 3D building models
in airborne digital photogrammetry**

Soutenue publiquement le 30 septembre 2013

Membres du jury

Directeur de thèse : M. Pierre Grussenmeyer, Professeur des Universités, INSA Strasbourg

Rapporteur externe : M. Laurent Polidori, Professeur des Universités, ESGT, Le Mans

Rapporteur externe : M. Michel Kasser, Professeur des Universités, HEIG-VD, Yverdon

Examineur : M. Pierre Charbonnier, Directeur de recherches, MEDDE, LRPC Strasbourg

Examineur : Mme Tania Landes, Maître de conférences, INSA Strasbourg

Abstract

Keywords: Aerial imagery, LiDAR, 3D building modeling, Quality assessment, RMSE, Surface indices, Volume indices

Digital photogrammetry and LiDAR can be considered as two of the most important technologies that were developed recently in geomatics. Methods and tools for automatic or semi-automatic generation of 3D city models are developing rapidly, but the quality assessment of these models and spatial data are rarely addressed. Study on the evaluation of data/products from photogrammetric or LiDAR are often confined by visual evaluation of the results or even a simple difference calculations. A comprehensive evaluation in 3D is not trivial. Our goal is to provide a standard multidimensional approach for assessing the quality of 3D models of buildings in 1D, 2D and 3D.

The approach that is proposed focuses on the quality indices frequently encountered in the literature. These indices are similar to those encountered in the evaluation of classifications (errors of omission, commission) and pass through the space discretization in pixels (2D) or voxels (3D) for measuring the degree of superposition of 2D or 3D objects. The originality of this approach is built on the fact that the models used as input are not only limited to raster format, but also extended to vector format. It seems obvious that models defined in vector format are more faithful to reality than raster format. However, the confrontation of two vector models is more difficult, especially when determining the volume corresponding to the intersection of two models. Experiments in this study were focused on the evaluation of the quality of 3D models buildings in the city of Strasbourg, created from photogrammetric data, LiDAR data, or simultaneous combination of these two data sources.

For 1D assessment, homologous points of two buildings to be compared are analyzed. Two methods are applied. The first one is done by computing Root Mean Square Errors (RMSE) based on the deviations between both models (reference and test), in X, Y and Z directions. Second method is performed by applying the French legal text (arrêté sur les classes de précision) that is based on the instructions published in the Official Journal from October 30, 2003. This text concerns the accuracy classes applicable to categories of survey work.

The 2D evaluation of the geometry of the 3D model is based on the comparison of surfaces in two building models (reference and test) and through the calculation of a set of quality indices. These indices involve Boolean operations such as union and intersection of plane surfaces.

For 3D assessment, building models are considered as one object. Quality of the buildings is assessed by calculation of volumetric quality indices. The quality indices in 3D are deduced from the 2D quality indices and depend on the degree of superposition of the test volume and the reference volume. These indices take into account the volume of the intersection as well as the union volume of two vector

buildings. The state of the art confirms difficulties in determining the volume of intersection of two 3D models in vector format. The algorithm that is proposed for volume of intersection is based on the extraction of vertices of the 3D intersection shape.

Digital aerial images are available from UltraCam-X, Rollei and Zeiss LMK sensors. LiDAR datasets of the same site are also available. However, a reference model considered a priori more accurate is needed for each building model to be evaluated. The reference building models are the models reconstructed from UltraCam-X. 14 Ground Control Points (GCPs) were measured by GNSS systems in the test site.

In this thesis, three semi-automatic methods for 3D building reconstruction have been mentioned and carried out on the same test site. These methods are used to reconstruct 75 samples of 3D models from aerial images, 26 samples of 3D models from LiDAR and aerial images, and 8 samples of 3D models from LiDAR datasets. We assess the 3D vector building models reconstructed previously, by applying the proposed assessment methods in raster and vector format. The models reconstructed from aerial images give better results than the models constructed from other datasets. The models reconstructed from combination of LiDAR and aerial images give high RMSE in Z-direction. Worse results are obtained for models reconstructed with LiDAR datasets only.

The statistics of the (2D and 3D) quality indices calculated for assessing the building models are calculated. These results show that the 3D building models extracted from stereo-pairs are close from each other. Also, the models reconstructed from LiDAR or combination of LiDAR and aerial images are less accurate than the models reconstructed from aerial images alone. However, the mean values of quality indices cannot be considered alone. In order to evaluate the building reconstruction quality in detail and to analyze the values of the quality indices, one should check the quality indices for each building separately. Moreover, the quality indices are affected by the building size. Small buildings generally lead to bad results.

In conclusion, three semi-automatic methods for 3D building reconstruction have been mentioned and carried out. The quality evaluation of 3D building models has been achieved by applying the proposed quality assessment approach in raster and vector format. These approaches consider the accuracy of the 3D building models based on the comparison of points in 1D, of surfaces in 2D, and of volumes in 3D. 1D assessment gives an overall idea about the reliability of the reconstructed models. 2D assessment checks the superimposition of faces, despite its dependency on the size of the polygons to be compared. 3D assessment compares the buildings in 3D through the comparison of their volumes of intersection. 3D assessment is taking into account the direction of errors (shifts in X, Y, and Z or rotations). This approach is suitable for 3D building vector models created from aerial images and/or LiDAR datasets. Future researches will focus on the extension of this approach to complex building models.

Résumé

Mots-clés: Imagerie aérienne, LiDAR, modèles 3D de bâtiments, évaluation de la qualité, Erreur Moyenne Quadratique, indices de qualité

Les systèmes de photogrammétrie numérique et de balayage laser aéroportés, étroitement liés aux évolutions technologiques, sont essentiels pour l'acquisition et l'extraction de l'information géographique en 3D. Les méthodes et les outils de génération automatique ou semi-automatique de modèles 3D urbains se développent rapidement, mais l'évaluation de la qualité de ces modèles et des données spatiales sur lesquelles ils s'appuient n'est que rarement abordée. Les travaux relatifs à l'évaluation des données/produits photogrammétriques ou laser-grammétriques se cantonnent souvent à une évaluation visuelle des résultats voire à un simple calcul d'écarts, une évaluation complète en 3D n'étant pas triviale.

Notre objectif est de proposer une approche multidimensionnelle standard pour évaluer la qualité des modèles 3D de bâtiments en 1D, 2D et 3D. Elle suppose toutefois de disposer, pour chaque modèle de bâtiment à évaluer, de son modèle de référence, considéré comme étant a priori plus précis. Deux méthodes sont présentées pour l'évaluation 1D. La première se base sur l'analyse de l'erreur moyenne quadratique en X, Y et Z calculée à partir des écarts entre les deux modèles (référence et test). La deuxième solution s'appuie sur les instructions parues au Journal Officiel du 30 octobre 2003 et exigent le respect de classes de précisions. L'approche que nous proposons se penche sur le calcul d'indices de qualité fréquemment rencontrés dans la littérature. Ces indices rejoignent ceux rencontrés dans l'évaluation des classifications (erreurs d'omission, de commission) et passent par la discrétisation de l'espace en pixels (2D) ou en voxels (3D) pour mesurer le degré de superposition d'objets 2D ou 3D. L'originalité de notre approche réside dans le fait que les modèles employés en entrée ne se limitent pas au mode raster, mais s'étendent au mode vecteur. Il semble évident que les modèles définis en mode vecteur s'avèrent plus fidèles à la réalité qu'en mode raster. En revanche, la confrontation de deux modèles vectoriels est plus délicate, notamment lorsqu'il s'agit de calculer le volume correspondant à l'intersection des deux.

L'évaluation 2D de la géométrie du modèle 3D est basée sur la comparaison des plans des deux modèles de bâtiments (référence et test) et passe par le calcul d'un ensemble d'indices de qualité. Ces indices font intervenir des opérations booléennes telles que l'union et l'intersection de surfaces de plans homologues.

Pour l'évaluation 3D, chaque modèle 3D de bâtiment est considéré comme un objet à part entière. Les indices de qualité, déduits de ceux définis en 2D, se rapportent dans ce cas au degré de superposition du volume testé et du volume de référence. Ils prennent en compte le volume de l'intersection ainsi que le volume de l'union des deux bâtiments.

La zone d'étude qui a permis d'expérimenter notre approche est située sur le territoire de la ville de Strasbourg. Nous disposons sur cette zone d'images

aériennes numériques à haute résolution spatiale acquises avec des caméras de type UltraCam-X (Vexcel), Rollei (moyen format) et par une chambre de prise de vue métrique Zeiss LMK. Des données LiDAR à un seul écho couvrent le même secteur géographique. Ces données n'ont pas été acquises la même année, mais permettent toutefois d'être combinées, étant donné que nos objets d'étude sont des bâtiments 3D présents dans tous les jeux de données. Les modèles 3D des bâtiments de référence ont été reconstruits par voie photogrammétrique à partir des images UltraCam-X géoréférencées préalablement à l'aide de 14 points d'appui mesurés avec un système GNSS.

Les modèles évalués ont été reconstruits en considérant trois approches semi-automatiques de reconstruction de bâtiments en 3D : l'une s'appuyant exclusivement sur des images aériennes, l'autre exclusivement sur des données LiDAR et la troisième sur la combinaison des deux. Nous disposons actuellement de 75 échantillons de modèles 3D obtenus à partir des images aériennes, 26 échantillons de modèles 3D issus à la fois des données LiDAR et des images aériennes, et 8 échantillons de modèles 3D issus des données LiDAR seules. L'approche d'évaluation multidimensionnelle décrite précédemment, aussi bien pour des modèles vectoriels que rasters, a été appliquée à cet important échantillon de modèles 3D de bâtiments.

Les statistiques sur les indices de qualité 2D et 3D calculés montrent que les modèles 3D de bâtiments extraits à partir des couples d'images stéréoscopiques sont cohérents. Les modèles reconstruits à partir des données LiDAR ou de la combinaison des données LiDAR et des images aériennes sont moins exacts. Cette imprécision est à rapporter essentiellement à la qualité des données brutes transmises. Cependant, afin d'évaluer la qualité de la reconstruction du bâtiment en détail et d'analyser les défauts liés à sa géométrie, il faut interpréter les indices de qualité pour chaque bâtiment séparément. Par ailleurs, les valeurs des indices sont également affectées par la taille du bâtiment. Ainsi, les indices de qualité calculés pour des petits bâtiments conduisent généralement à de moins bons résultats.

En conclusion, cette thèse a abouti à l'élaboration d'une approche d'évaluation multidimensionnelle de bâtiments en 3D, reconstruits à partir de trois méthodes semi-automatiques. L'approche a été validée pour des modèles vectoriels et rasters. Notre approche considère l'exactitude des modèles 3D de bâtiments calculée sur la base de comparaisons de points en 1D, de surfaces en 2D, et de volumes en 3D. L'évaluation 1D donne une idée globale de la fiabilité des modèles reconstruits en fournissant une mesure métrique de proximité des points homologues. L'évaluation 2D qualifie le degré de superposition des faces, en dépit de sa sensibilité à la taille des polygones. Une évaluation 2D satisfaisante ne valide toutefois pas encore le modèle reconstruit, puisque deux plans parfaitement superposés dans le système d'axes parallèles au plan sont susceptibles d'être décalés en profondeur. Ce défaut est révélé dans l'étape de l'évaluation 3D. L'évaluation 3D analyse les bâtiments en tant qu'objets à part entière en estimant le degré de superposition des volumes à tester et des volumes de référence. Les futures recherches porteront sur l'extension de cette approche à la construction de modèles 3D plus complexes de bâtiments.

Acknowledgements

This thesis is the reward of four years of research at INSA-Strasbourg. The completion of this thesis would not have been possible without the help and support of many people.

First and foremost, I am very grateful to my supervisors, Prof. Pierre GRUSSENMEYER, for giving me the privilege of working under his supervision, for his scientific support, continuous encouragement and valuable advice throughout my research and for always being approachable and taking time to discuss problems, despite other responsibilities. Also, his willingness to motivate me contributed tremendously to my project.

Special thanks also to all Photogrammetry and Geomatics Group members at INSA-Strasbourg, especially Prof. Tania LANDES who provided me useful advice and for providing an excellent source of ideas during the countless discussions on the research. I also, sincerely thank to Dr. Hakim BOULAASSAL and Samuel GUILLEMIN.

I thank Dr. Wuming ZHANG and his team work at State Key Laboratory of Remote Sensing Science, Beijing Key Laboratory of Environmental Remote Sensing and Digital City, School of Geography, Beijing Normal University China for working together since 2010.

For this dissertation I would like to thank my reading committee members: Prof. Laurent POLIDORI, Prof. Michel KASSER and Prof. Pierre CHARBONNIER for their time, interest, and helpful comments.

Finally, I thank my family for their moral support and encouragement. Special thanks go to my parents as without their love and support I would have never got this far.

Notations

<i>Ar</i>	Reference area
<i>At</i>	Tested area
ADS	Airborne digital sensor
AIC	Aerial Industrial Camera
ALS	Airborne laser scanner
AT	Aerial triangulation
<i>C</i>	Security coefficient
CCD	Charge-coupled device
CMOS	Complementary metal oxide semiconductor
DEM	Digital elevation model
DHM	Digital height model
DMC	Digital mapping camera
DN	Digital number
DTM	Digital terrain model
EO	Exterior orientation
FOV	Field of view
GCP	Ground control points
GNSS	Global Navigation Satellite System
GSD	Ground sample distance
IMU	Inertial measurement units
INS	Inertial navigation systems
JAS	Jena airborne scanner
LiDAR	Light Detection And Ranging
LPS	Leica photogrammetric suite
MD	Mean Distance
<i>MP</i>	Megapixels
NIR	Near Infrared
<i>RMSE</i>	Root mean square error
<i>SD</i>	Standard deviation
<i>SR</i>	Surface of reference
<i>ST</i>	Surface of test
RGB	Red Green Blue
ρ_d	Detection rate
ρ_q	Quality rate
ρ_b	Branch factor
ρ_m	Miss factor
ρ_f	False alarm rate
ρ_{qw}	Weighted quality rate
TIN	Triangulated irregular network

UAVs	Unmanned Aerial Vehicles
V_{pd}	Volumetric detection rate
V_{pq}	Volumetric quality rate
V_{pb}	Volumetric branch factor
V_{pm}	Volumetric miss factor
V_{pf}	Volumetric false alarm rate
V_{pqw}	Volumetric weighted quality rate
VR	Reference volume
VT	tested volume
X_c, Y_c, Z_c	Coordinates of centroid
$X_{ref}, Y_{ref}, Z_{ref}$	Coordinates of reference point
$X_{test}, Y_{test}, Z_{test}$	Coordinates of test point
$[xx]$	Precision class

Contents

Abstract	i
Résumé	iii
Acknowledgements	v
Notations	vii
List of Figures	xiv
List of Tables	xx
1 Introduction	1
1.1 Motivation	1
1.2 Research problems	5
1.3 Research objective	7
1.4 Outline of the thesis	8
2 Short review about data acquisition	11
2.1 Sensors technology	12

2.2	Digital colour imaging	13
2.3	Airborne digital cameras	14
2.3.1	Airborne digital frame cameras	15
2.3.2	Airborne digital linear cameras	20
2.4	Principles of image processing in photogrammetry	22
2.4.1	Image Orientation	23
2.4.2	Image matching	25
2.5	3D building modeling	30
2.6	Summary	33
3	State of the art of accuracy assessment	35
3.1	Accuracy, precision and error	35
3.2	Types of errors	37
3.3	Accuracy assessment	38
3.3.1	Qualitative assessment	39
3.3.2	Quantitative assessment	40
3.3.2.1	Quantitative assessment using RMSE computation	41
3.3.2.2	Quantitative assessment using computation of qual- ity indices	43
3.4	Summary	49
4	Developed approach for accuracy assessment	51
4.1	Proposed multi-dimensional accuracy assessment approach	51
4.1.1	1D accuracy assessment	52
4.1.2	2D accuracy assessment	57
4.1.3	3D accuracy assessment	59

4.2	Geometric computations	63
4.2.1	Intersection of two lines in the same plane	63
4.2.2	Intersection of a line with a plane	65
4.2.3	Area computation	66
4.2.3.1	Raster format (pixel)	66
4.2.3.2	Vector format	68
4.2.4	Volume computation	70
4.2.4.1	Raster format (voxel)	70
4.2.4.2	Vector format	71
4.3	Summary	75
5	Application of the approach on multiple datasets	77
5.1	Test site and data used	77
5.2	Data collection and image processing results	82
5.3	Preparation of the reference and test models	83
5.3.1	Preparation of the reference models	83
5.3.2	3D building models reconstructed from digital images	84
5.3.3	3D buiding models reconstructed from combination of Li- DAR and airborne imagery datasets	88
5.3.4	3D building models reconstructed from LiDAR dataset	90
5.4	Assessment of building models	91
5.4.1	1D accuracy assessment	92
5.4.1.1	Using RMSE computations	92
5.4.1.2	Using the French legal text published in 2003 (arrêté sur les classes de précision)	93
5.4.2	2D accuracy assessment	95

5.4.2.1	Models reconstructed from airborne imagery dataset	95
5.4.2.2	Models reconstructed from combination of LiDAR and imagery datasets	98
5.4.2.3	Models reconstructed from LiDAR dataset	100
5.4.2.4	Models created from image matching	102
5.4.3	3D accuracy assessment	106
5.4.3.1	Models reconstructed from airborne imagery dataset	106
5.4.3.2	Models reconstructed from combination of LiDAR and airborne imagery datasets	109
5.4.3.3	Models reconstructed from LiDAR dataset	112
5.4.4	Comparison between 2D and 3D assessments	116
5.5	Discussion about raster and vectors models	117
6	Conclusion and perspectives	121
Appendices		
A	Volumes and RMSE of building models	125
B	Surface quality indices	135
C	Volume quality indices	143
D	Publications	151
E	Definition of Points, lines, and planes in space	181
E.1	Points in space	181
E.2	Lines in space	181
E.3	Planes in space	183
E.4	Plane fitting	183

<i>Contents</i>	xiii
F Arrêté du 30 octobre 2003	185
Bibliography	189
Résumé des travaux en français	201

List of Figures

1.1	Part of a 3D building as point clouds (above) and in raster format (below) [Hinks et al., 2013]	6
1.2	Reference (red colour) and tested (blue colour) objects.	8
2.1	CCD and CMOS technology [Petrie and Walker, 2007].	13
2.2	Airborne frame images [Sandau, 2009].	15
2.3	Rollei AIC digital aerial camera [Lemmens, 2008].	16
2.4	The Leica RCD30 system operator (left), camera head (middle), and camera controller (right) [Wagner, 2011b].	17
2.5	UltraCam-X digital aerial camera system [Gruber et al., 2008].	18
2.6	UltraCam Eagle aerial camera [Gruber et al., 2011].	19
2.7	Airborne linear imaging system [Kheiri, 2006].	20
2.8	Three-line imaging system (TLS)[Sandau, 2009].	20
2.9	Airborne linear cameras: ADS80 [Wagner, 2011a].	22
2.10	Image and ground coordinate systems [Konecny, 2003].	23
2.11	Elements of exterior orientation [Kraus, 1993].	25
2.12	Process of DTM generation using LPS software	27
2.13	Correlation and search windows	28

3.1	Simple representation for avoiding confusion between accuracy and precision (celebrating200years.noaa.gov).	36
3.2	Procedure for quality assessment of a DTM [Podobnikar, 2009]. . .	39
3.3	Elements of the BOS method suggested by [Tveite and Langaas, 1999].	44
3.4	Relationship between reference area A_r and tested area A_t	45
3.5	Distance weighted transformation for each 2D surface (x is the pixel element and d_{min} is the minimum distance between the pixel element and the tested surface).	47
3.6	Quality rates represented in gray values (dark means high values); a) in 2D; b) in 3D [Meidow and Schuster, 2005].	49
4.1	Multi-dimensional approach developed for the assessment of buildings reconstructed in 3D.	52
4.2	Correspondences between homologous nodes in the reference (in black) and the test (in red) models.	53
4.3	False corresponding points between the reference and the test models.	54
4.4	Corresponding centers of gravity points of reference (in blue) and test models (in red).	55
4.5	Comparison of 3D building models: volume of reference (VR, in pink), volume of the model to test (VT, in blue), volume of the intersection shape (VI, in green).	60
4.6	Distance transformation between 3D reference and test model (y is the voxel element and d_{min} is the minimum distance between the voxel element and the tested model).	62
4.7	Intersection of a line with a plane.	65
4.8	Representation of the rasterization process of 2D polygon.	68
4.9	Intersection area calculation for vector polygons in 2D.	70

4.10	Representation of the voxelization process of 3D building.	71
4.11	Calculation of convex hull (a) and the intersection shape (b).	73
4.12	Main steps of the process leading to the calculation of the intersection volume of two vector building models.	74
5.1	Distribution of UltraCam-X (large format in vertical strip), RolleiDB44 (medium format in horizontal strip), and Zeiss LMK images (large format in horizontal strip).	78
5.2	Reduced format of one image of UltraCam-X camera (Strasbourg City).	79
5.3	Reduced format of one image of RolleiDB44 camera (Strasbourg City).	80
5.4	Reduced format of one image of Zeiss LMK camera (Strasbourg City).	81
5.5	Reference 3D building models reconstructed from UltraCam-X images.	84
5.6	Flowchart of 3D building modeling from aerial images.	85
5.7	Example of a 3D building model reconstructed from aerial images.	86
5.8	A part of an aerial UltraCam-X image (above) over Strasbourg city and 3D building reconstruction results from UltraCam-X stereopairs (below).	87
5.9	Flowchart of the reconstruction process using LiDAR data and aerial images [Zhang et al., 2011].	88
5.10	3D building reconstruction combination of LiDAR and airborne images.	90
5.11	3D building reconstruction from LiDAR data; a) Roof reconstruction; b) 3D building reconstruction	91

5.12	Quality indices used for 2D assessment and calculated for models obtained from airborne imagery dataset; a) for raster models; b) for vector models.	97
5.13	Quality indices used for 2D assessment and calculated for models obtained from combination of LiDAR and imagery datasets; a) for raster models; b) for vector models.	99
5.14	Quality indices used for 2D assessment and calculated for models obtained from LiDAR dataset; a) for raster models; b) for vector models.	101
5.15	3D point clouds produced from UltraCam-X image (1,976,578 points).	103
5.16	3D point clouds produced from Rollei image (746,475 points). . . .	103
5.17	Fitting plane from 3d dataset [Mohamed and Grussenmeyer, 2011].	104
5.18	Reference and test model obtained from aerial images (8 of 75 buildings).	107
5.19	Quality indices used for 3D assessment and calculated for models obtained from airborne images; a) for raster models; b) for vector models.	108
5.20	Models obtained from combination of aerial images and LiDAR datasets (8 of 26 buildings).	109
5.21	Quality indices used for 3D assessment and calculated for models obtained from combination of LiDAR and images; a) for raster models; b) for vector models.	111
5.22	Models obtained from LiDAR datasets.	113
5.23	Quality indices used for 3D assessment and calculated for models obtained from LiDAR datasets; a) for raster models; b) for vector models.	115
E.1	Point P in space.	182

E.2	Line in space from point B to point P.	182
E.3	Plane in 3D.	183
E.4	Projection of points on the fitted plane.	184

List of Tables

2.1	Technical specifications of Rollei AIC sensor [Lemmens, 2008]. . . .	16
2.2	Technical specifications of Leica RCD30 system [Wagner, 2011b]. . .	17
2.3	Technical specifications of UltraCam-X sensor [Lemmens, 2008]. . .	18
2.4	Specifications of UltraCam Eagle sensor [Gruber et al., 2011]. . . .	19
2.5	Technical specifications of ADS40 sensor [Lemmens, 2008].	21
4.1	Maximum number of points allowed to exceed first threshold.	56
4.2	Quality indices used to evaluate surface areas of polygons.	58
5.1	Brief characteristics of photogrammetric datasets.	78
5.2	Brief characteristics of the LiDAR datasets.	81
5.3	Accuracy of exterior orientation parameters for UltraCam-X images.	82
5.4	Accuracy of exterior orientation parameters for RolleiDB44 images.	83
5.5	Accuracy of exterior orientation parameters for Zeiss-LMK images.	83
5.6	RMSE results based on homologous nodes.	92
5.7	RMSE results based on gravity centers of homologous planes.	92
5.8	Statistics of 2D quality indices obtained for buildings reconstructed from airborne imagery dataset.	96
5.9	Statistics of 2D quality indices obtained for buildings reconstructed from combination of imagery and LiDAR datasets.	98

5.10	Statistics of 2D quality indices obtained for buildings reconstructed from LiDAR dataset.	100
5.11	Mean Distances calculated for (MD) in computing medium plane .	104
5.12	2D quality indices calculated for planes extracted from point clouds.	105
5.13	Mean distance calculation between two planes.	106
5.14	Statistics of 3D quality indices obtained for buildings reconstructed from airborne images.	107
5.15	Statistics of 3D quality indices obtained for buildings reconstructed from combination of images and LiDAR datasets.	110
5.16	Statistics of 3D quality indices obtained for buildings reconstructed from LiDAR dataset.	113
5.17	Results of statistical F-test applied between quality indices calculated for the 2D and 3D assessments.	116
5.18	Comparison between raster and vector based on modeling of buildings.	118
5.19	Results of statistical F-test applied between raster and vector data structure.	119
A.1	Volumes of buildings reconstructed from UltraCam-X and Zeiss-LMK.	127
A.2	Volumes of buildings reconstructed from UltraCam-X and combination of of UltraCam-X with LiDAR.	128
A.3	Volumes of buildings reconstructed from UltraCam-X and LiDAR. .	128
A.4	RMSE computed from corresponding vertices for aerial images. . . .	130
A.5	RMSE computed from corresponding vertices for combination of aerial images and LiDAR datasets.	131
A.6	RMSE computed from corresponding vertices for LiDAR dataset. .	131
A.7	RMSE computed from gravity centers of homologous planes for aerial images.	133

A.8	RMSE computed from gravity centers of homologous planes for combination of airborne imagery and LiDAR datasets.	134
A.9	RMSE computed from gravity centers of homologous planes for LiDAR dataset.	134
B.1	2D quality indices based on vector models reconstructed from airborne imagery.	137
B.2	2D quality indices based on vector building models reconstructed from integration of airborne imagery and LiDAR datasets.	138
B.3	2D quality indices based on vector building models reconstructed from LiDAR dataset.	138
B.4	2D quality indices based on raster building models reconstructed from airborne imagery.	140
B.5	2D quality indices based on raster building models reconstructed from combination of airborne imagery and LiDAR datasets.	141
B.6	2D quality indices based on raster building models reconstructed from LiDAR dataset.	141
C.1	3D quality indices based on vector building models reconstructed from airborne imagery.	145
C.2	3D quality indices based on vector building models reconstructed from combination of airborne imagery and LiDAR datasets.	146
C.3	3D quality indices based on vector building models reconstructed from LiDAR datasets.	146
C.4	3D quality indices based on raster building models reconstructed from airborne imagery datasets.	148
C.5	3D quality indices based on raster building models reconstructed from combination of airborne imagery and LiDAR datasets.	149

C.6 3D quality indices based on raster building models reconstructed from LiDAR dataset.	149
---	-----

Chapter 1

Introduction

1.1 Motivation

Digital photogrammetry and LiDAR can be considered as two of the most important technologies that were developed during the last years in the field of geomatics. They are essential for quantitative information extraction such as lengths, areas and volumes. The two technologies, LIDAR and photogrammetry, were treated by researchers as complementary to each other [Baltsavias, 1999]. Photogrammetry and LiDAR datasets are used since many years for the 3D reconstruction of objects such as buildings. Digital airborne cameras are now penetrating the fields of photogrammetry and remote sensing. It is possible to obtain with this new generation of airborne cameras different sets of geometric and spectral data with high geometric and radiometric resolutions.

The 3D city modeling is a real challenge that depends on the data acquisition and its succeeding processing. This application is not especially new but need accurate datasets and methods in order to provide good results. The digital photogrammetry development and the use of high resolution digital camera allows to get accurate models. Airborne Laser Scanners (ALS) have the great potential to enable with high speed acquisition of 3D data especially in urban areas. Even the data acquisition seems easy, the subsequent processing steps (filtering, segmentation, reconstruction) are more or less complex. Development of fully automatic

algorithms providing reliable 3D building models remains an essential challenge, due to the complexity of urban scenes [Akca et al., 2010]. The complementarity of photogrammetry and LiDAR datasets are utilized to perform a primitive-based 3D building reconstruction [Zhang et al., 2011]. But, what about the quality of these reconstructed models? The assessment of the results is a very important step in the work flow.

In recent years, many authors have given special attention to accuracy assessments of the 3D building models. Quality assessment is critical and important for 3D building models production for several reasons. Firstly, it may give important information about deficiencies of an approach and may take place to help in focusing a further research activity. Secondly, quality evaluation is needed in order to compare the results of different approaches and to convince the user. Moreover, the approach can be used in an operational workflow [Schuster and Weidner, 2003]. Furthermore, quality values enable the contractor to check his measurements and the customer to check the quality of the delivered data with respect to specifications of contracts. While the general emphasis is to develop methods and tools for automatic, or semi-automatic generation of city models, the concept of quality evaluation has also become very important. No standard solutions are available, although city models are being produced worldwide at a fast rate [Akca et al., 2010].

All accuracy assessments include three fundamental steps [Congalton and Kass, 2009]:

- Firstly, designing the accuracy assessment sample. Sampling design plays a critical role in accuracy assessment;
- Secondly, collecting data for each sample;
- Finally, analyzing the results.

The computation of quality assessment is based on the comparison of these measurements to more accurate datasets which are considered as reference datasets. Because high quality reference data are difficult to obtain, reference data can be considered as follows [Meidow and Schuster, 2005]:

- 1- If the reference data is error-free, absolute quality assessments can be stated.
- 2- If the reference data is accurate, the quality measures for the test datasets are an approximation for the qualities.

3- If both datasets have the same accuracy, the inner accuracy (precision) can be deduced leading to quality measures from repeated measurements.

Digital mapping camera evolution is one of the important topics that was introduced at the 53rd Photogrammetric Week, held in Stuttgart from 5th to 9th September 2011. Some of the reported works in this topic are introduced next. [Cramer, 2011] presented an important question "Geometry Perfect – Radiometry Unknown?". The importance of standards and calibrations of cameras sensors were introduced. Also, the development of Unmanned Aerial Vehicles (UAV) was shown. [Wagner, 2011a] described the Leica ADS80 sensor and the high resolution mode using RMSE. Also, commercial Leica XPro software has been introduced. It uses an innovative approach to aerial triangulation and time of processing is much reduced. [Wagner, 2011b] has introduced the Leica RCD30 medium format camera. The camera provides 60 Megapixels (MP) image format and it was designed to acquire multispectral RGB and NIR imagery. [Neumann, 2011] presented details of the new Z/I's DMC II. It has 250 MP image format at $5.6 \mu m$ pixel size. The camera is manufactured by DALSA company which is specialized in the design and manufacture of electronic imaging components. [Gruber et al., 2011] presented the new version of the UltraCam Eagle with 260 MP at $5.2 \mu m$. It has 4 lens cones for panchromatic images and 4 lens for multispectral images. Bing-Maps contributions to urban modelling, comprising 3D modelling from aerial and terrestrial photos were represented. The potential of unmanned aerial vehicles for mapping has been presented by [Eisenbeiss, 2011], especially helicopter systems. The advantages as well as the limitations of UAV have been described.

Empirical tests to evaluate different kinds of airborne datasets have been achieved by a recent project of DGPF (German Society for Photogrammetry, Remote Sensing and Geoinformation). This project was carried out in Vaihingen/Enz test field nearby Stuttgart, Germany. This project aimed at an independent and comprehensive evaluation on the performance of digital airborne cameras, as well as providing a standard empirical dataset for the next years [Jacobsen et al., 2010] and [Cramer, 2010]. The main object of DGPF tests was not to compare the performances of sensors but to evaluate the sensors specific strengths. The test frame was based on cameras systems DMC, UltraCam-x, quarto digital CAM, line scanning systems ADS40 and JAS-150 in a comparison with analogue cameras (RMK-Top15). The absolute accuracy RMSE in horizontal component was about 0.25 pixel related to GSD and about 0.5 pixel for the vertical component.

In this case the accuracy of reference point based on static GPS observations was about 1cm for horizontal and 2cm for vertical coordinates.

The previous tests for airborne datasets are achieved using RMSE calculations. 2D and 3D models reconstructed from these kinds of airborne datasets should be assessed.

Several methods will be presented to evaluate photogrammetry and LiDAR datasets. Assessment is generally considered at the end of a work and frequently limited to a visual check. Visual evaluation is used in [Lesparre and Gorte, 2012] for 3D city models produced with LiDAR data. A multi-dimensional assessment approach has been developed in this work to evaluate 3D building models.

In 1D assessment, calculation of Root Mean Square Errors (RMSE) for analyzing the precision of the 3D building is an interesting process. It shows the shifts between reference and tested models in X, Y and Z directions [Jamet et al., 1995] and [Cramer, 2010]. [Grussenmeyer et al., 1994] proposed statistical techniques in order to calculate horizontal and vertical RMSE of restitution for different kind of objects (point and surface). Usually the corner points of buildings are used for RMSE computation. Furthermore, in [Zhan et al., 2005], Euclidean distance between the centres of the mass of an extracted object and the corresponding object is used to measure positional accuracy. The computation of RMSE based on homologous nodes, the correspondences from reference to test points are identified by finding the nearest neighbours of each pair of points. This method is intuitive and simple, but it assumes that every closest homologous point should correspond to each other. This assumption can easily fail when the two point sets are not close. The computation of RMSE between centres of gravity of homologous surfaces that compose the tested and respectively the reference building is suggested in [Zeng et al., 2013].

In 2D assessment, because many users are working with 2D features such as roofs and facades, 2D assessment approaches must be considered. Several methods are investigated by computing 2D quality indices. Numerous approaches were introduced in the literature. These approaches are applied to models in raster and vector format. The studies address to evaluate 2D surfaces and 3D building models which have been produced with aerial imagery data [McGlone and Shufelt, 1994]; [Ragia, 2000]. The evaluation has been achieved by computing specific quality parameters. These parameters are determined by a topological and geometrical

analysis. Quality evaluation of 3D building models reconstructed from photogrammetric data are discussed in [Schuster and Weidner, 2003].

In 3D assessment, considering a building as one object, 3D comparisons seem to be more appropriate than 2D comparisons. An approach for quantitative quality evaluation of 3D building models is presented. This approach consists of an evaluation of the building detection such as completeness. This approach is an extend of the work of [Ragia, 2000]. Evaluation of 3D building models from LiDAR datasets is presented in [Rutzinger et al., 2009] and [Akca et al., 2010].

A multi-criteria evaluation system for 2D building extraction from remotely sensed data has been proposed by [Zeng et al., 2013]. Three components have been considered in the evaluation system. Firstly, the traditional classifications accuracy such as completeness and correctness have been included. The resemblance between reference and extracted buildings has been described. Finally, the positional accuracy is measured by distances computation at feature points such as building's centroid.

Related works have been done by the Photogrammetry and Geomatics Group at INSA-Strasbourg. In the context of assessing the quality of planes detection in a 3D building reconstruction process based on LIDAR data, several solutions have been suggested [Tarsha-Kurdi et al., 2008]. For evaluating the quality of geometric facade models reconstructed from TLS data, [Landes et al., 2012a] suggested the use of quality indices and RMSE calculations.

1.2 Research problems

The entities "shape" and "position" can be represented more accurately in vector than in raster format. The conversion between both data structures is sometimes necessary. The 1D, 2D or 3D assessment approach allows highlighting the source of deviations in the tested buildings. Based on literature review, problems are highlighted regarding to the assessment approaches of 3D building models. This research is designed to find solutions for the following limitations.

- 1- In 1D assessment, quality measures such as RMSE cause problems applied to complex buildings structures especially in point matching.

2- In 2D assessment, the problem is not fully solved by researchers. In principle, the quality indices in 2D do not take into account the threshold in third dimension.

3- In 3D assessment, the 3D quality indices are computed only from raster data structure. Based on the comparison of the test and reference datasets, intersection or union sets have to be determined. However in the case of volume determinations these calculations and the corresponding data structures are rather complex and therefore extensive in terms of implementation [Meidow and Schuster, 2005]. But, it seems obvious that models defined in vector mode are more faithful to reality than raster mode as shown in figure 1.1. The confrontation of two vector models is more difficult, especially when determining the volume corresponding to the intersection of the two. So, our challenge is to introduce the first experiment of an algorithm to compute the intersection of area and volume in vector format.

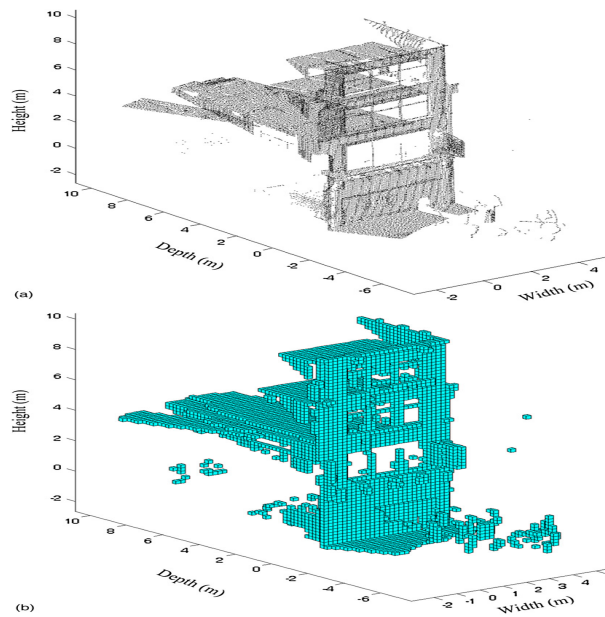


FIGURE 1.1: Part of a 3D building as point clouds (above) and in raster format (below) [Hinks et al., 2013]

1.3 Research objective

With photogrammetric and LiDAR datasets, 3D models of objects can be obtained using automatic or semi-automatic methods. Methods and tools for automatic or semi-automatic generation of 3D city models are developing rapidly, but the quality assessment of these models and of spatial data are rarely addressed. Based on the limitations mentioned previously, the objectives of this research are to find solutions in order to assess the accuracy of models reconstructed from digital airborne sensors and/or LiDAR datasets. This work will describe and analyze the assessment approach developed for evaluating these models. The evaluation of 3D building models reconstructed from photogrammetric or LiDAR data is often confined by visual evaluation or by simple calculation such as difference measurements. Evaluation of 3D building models as one object is not trivial. Our goal is to provide a multi-dimensional approach for assessing the quality of 3D models of buildings in 1D, 2D and 3D. The challenge of this work is built on the fact that the models used as input are not only limited to raster data structure, but are also extended to the vector data structure. The geometric computations in vector data structure are more complex, especially when determining the volume corresponding to the intersection of two models. The idea behind the multi-dimensional approach is to consider:

- 1D (point) accuracy assessment (figure 1.2-a).
- 2D (surface) accuracy assessment (figure 1.2-b).
- 3D (volume) accuracy assessment (figure 1.2-c).

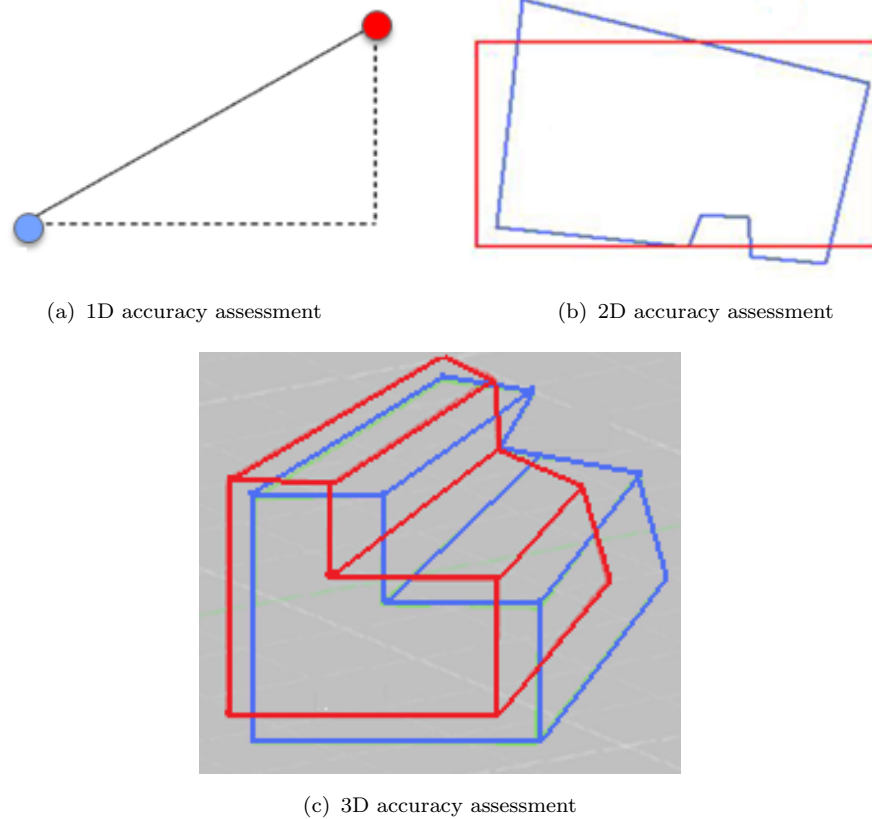


FIGURE 1.2: Reference (red colour) and tested (blue colour) objects.

1.4 Outline of the thesis

The material of the thesis is presented in six chapters, the main outline of each can be given as follows:

Chapter 2: Short review about data acquisition

The 3D city modeling is a real challenge that depends on the data acquisition and its succeeding processing. The quality of the reconstructed building models mainly depend on the quality of the acquired datasets. The digital airborne sensors development and the use of high resolution digital cameras allow to get accurate models. Developments of these digital sensors allow to improve 3D building modeling. In this thesis, we use the data from airborne sensors. That's why this chapter will give an overview of digital airborne sensor systems, including different types of camera systems (in particular those used in our study). This chapter introduces the sensors technology (CCD and CMOS), the concept of digital color imaging,

and the data acquisition from different types of digital cameras (frame and line). It also provides a review of image processing steps in photogrammetry. Dense point clouds of reliable points extracted from digital images is presented. Also, a review of some reported works for reconstruction of building models is introduced.

Chapter 3: State of the art of accuracy assessment

This chapter contains a literature study over different methods used to assess the 3D data reconstructed from airborne digital sensors. Qualitative and quantitative assessments are introduced. General information about error and uncertainty definitions and error sources in photogrammetry is given.

Chapter 4: Developed approach for accuracy assessment

The multi-dimensional approach for accuracy assessment is introduced. The methods to calculate areas and volumes in raster and vector format are presented. The implemented method and the achievement of the study are described based on the comparison of some objects to accurate reference measurements.

Chapter 5: Application of the approach on multiple datasets

In this chapter the study area and datasets used in the study are presented. After describing the study area, the datasets, reference and test data are introduced. Three methods for building model reconstruction are applied on real data. This chapter, mainly focuses on the results of accuracy evaluation. It is divided in three sections, (i) the results of the 3D data reconstructed from airborne imagery data, (ii) the results of the 3D data reconstructed from LiDAR data, and (iii) the results of the 3D data reconstructed from the combination of airborne imagery and LiDAR data. Finally, an accuracy evaluation of point clouds reconstructed from airborne images is carried out.

Chapter 6: Conclusion and perspectives

Finally, the conclusion of the study is completed by some ideas about future studies.

Chapter 2

Short review about data acquisition

This chapter will give an overview of digital airborne sensor systems, including different types of camera systems. Currently, datasets from airborne digital imaging sensors are available on the market. Advantages of digital cameras are widely understood. In digital technology, there is no photo lab, no scanning, and no noise from film grain and no cost of duplication [Leberl et al., 2002]. There have been fundamental changes recently in sensors, platforms and applications. Digital airborne cameras are now penetrating the fields of photogrammetry and remote sensing. Due to the last results in research and development in this field as for instance in detector technology, computing power, memory capacity position and orientation measurement, it is now possible to generate with this new generation of airborne cameras different sets of geometric and spectral data with high geometric and radiometric resolutions.

The benefits of digital cameras over film cameras include better radiometric performance and elimination of film processing and scanning costs. Availability of image content in digital format enables a highly automated workflow, creating the possibility of generating photogrammetric products such as orthophotos and mosaics with little delay between capture and end product. This might allow, for example, rapid response after a disaster [Lemmens, 2004].

The accuracy of the final 3D model is in close relation with the orientation process of the images used to reconstruct this model. It is demonstrated that image

orientation is achievable with satisfactory results in terms of accuracy of the resulting 3D models. This chapter highlights a state-of-the-art review on the data acquisition and image processing aspects of digital photogrammetric images. An important contribution to this part is a characterization of the photogrammetric image acquisition and image product generation systems. Data acquisition in photogrammetry is concerned with obtaining reliable information about the properties of surfaces and objects. This is accomplished without physical contact with the objects [Schenk, 2005].

Airborne sensors are the most important photogrammetric instruments. Aerial cameras can produce sharp images in rapid succession under the adverse conditions of a moving aircraft. Any error, distortion, or compromise in the clarity of the image will result in mapping and positioning errors.

In digital photogrammetry, the illumination in the image plane of the camera is not recorded photographically, but by electronic methods. Digital photogrammetry has become a mature technology. The use of analytical plotters has been reduced since digital photogrammetric workstations are more frequently used in modern photogrammetric production workflow. Such workstations are user-friendly and their handling is no longer restricted to specialists only. Digital photogrammetry benefits from a high degree of automation.

A digital image consists of two dimensional matrix elements. Each element is called a pixel [Kraus, 1993]. The area of each element is related to the spatial resolution of camera and the ability to identify the objects. Every pixel has a Digital Number (DN) usually coded from 0 for black to 255 for white in a gray scale (2^8 combinations). Also, 2^{16} or 2^{32} combinations exists. Colour images have three matrices with the same range (image block with 3 layers). The CCD or CMOS sensor in a digital camera are used for converting lights into electrons.

2.1 Sensors technology

There are several important advances in the two main semi-conductor technologies, Charge-Coupled Device (CCD) (see figure 2.1-a) and Complementary Metal Oxide Semiconductor (CMOS) (see figure 2.1-b) that are used in airborne imaging [Petrie and Walker, 2007]. Both solid state devices can convert light into

electrons that can be easily measured, resulting in a radiometric intensity value [McGlone, 2004].

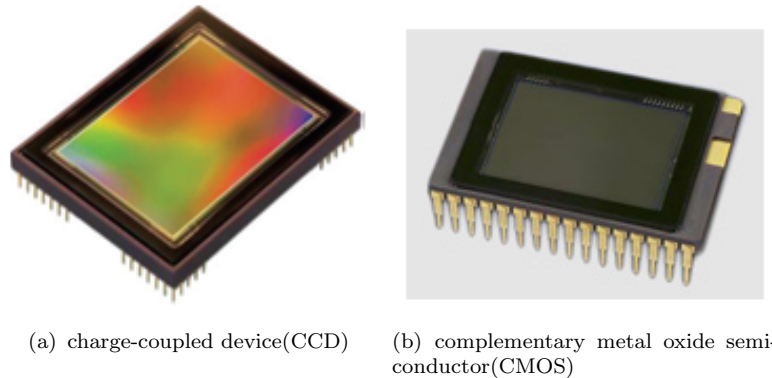


FIGURE 2.1: CCD and CMOS technology [Petrie and Walker, 2007].

CCD is used in medium-format airborne imaging; a similar transformation has also taken place in terms of the number of pixels that are now available within the resulting image. In the case of large-format digital cameras, the majority of these types use the CCD technology such as in the case of the Microsoft (Vexcel) UltraCam and Intergraph DMC camera systems.

CMOS is produced in large quantities by the manufacturers and is a relatively cheap technology. Early, CMOS chips are used for imaging purposes, but the image quality was poor due to their inferior light sensitivity. Modern CMOS sensors use a more specialized technology and light sensitivity of the sensors have rapidly increased in recent years. CMOS devices are now found in airborne digital cameras.

In case of colour imaging, (blue, red, or green) filters have been placed placed above the image sensor.

2.2 Digital colour imaging

The quality of an image captured by colour imaging systems depends on sensor spectral sensitivity. The sensitivity characteristic of sensors is critical to the success of imaging applications. The ultimate image quality is judged subjectively by human visual system.

Digital technology now enables unparalleled functionality and flexibility in the capture, processing, exchange, and output of colour images. In order to record and process colour images, it is essential to understand the mechanisms of colour vision and the capabilities and limitations of colour imaging devices.

One method of colour imaging sampling is based on applying a red, green, or blue colour filter directly onto each pixel colour filter placed above the image sensor. Electronic sensors generally are based on CCD or CMOS technology. Colour filters allow only specific spectral radiance to pass through.

Other method of colour imaging is to use multiple cameras, each one with different filters in order to collect the images in different spectral bands. After that, fusion of the individual spectrally separated images to form the final composite colour image will take place.

A Third method is the use of beamsplitters to separate the different spectral bands within a single camera which are combined later to form the final color image. This device is an optical device placed between the lens and the three separate image planes.

Sensors technologies are used in airborne digital cameras. With every airborne camera, the aim is to achieve the best signal to work with data that are possible to extract the information they contain. In The next section, we consider the digital airborne cameras and its various technical specifications. The principle of that is the quality of obtained data is based on these technical specifications.

2.3 Airborne digital cameras

There are many kinds of cameras used in photogrammetry. These types are changed in properties such as focal length, principal point, fiducial mark positions, and lens distortion. The first digital aerial cameras were presented to the photogrammetric community at the 19th Congress of the ISPRS in Amsterdam from 16 to 23 July 2000. Z/I imaging (today Intergraph) and LH (today Leica Geosystems) were the two companies responsible for this innovation. Many companies now manufacture digital aerial cameras. The data from digital cameras are recorded in digital format. Two main formats are available

[Petrie and Walker, 2007]. (i) area arrays from frame cameras; and (ii) linear arrays from pushbroom scanners.

2.3.1 Airborne digital frame cameras

Frame format sensors are sequentially exposure of the entire image plane, figure 2.2. Airborne digital frame cameras can be further subdivided into three specific categories. These categories may be classified as small format, medium format, and large format imaging systems. The format is based on the size of the image sensor.

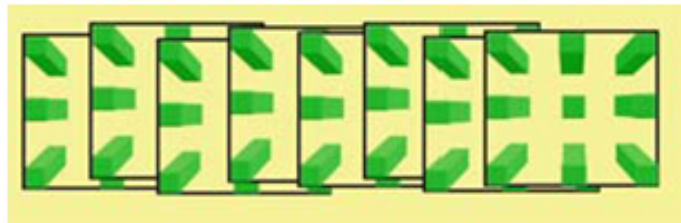


FIGURE 2.2: Airborne frame images [Sandau, 2009].

- Small format cameras are equipped with sensors up to 16 Megapixels [Li et al., 2008].

Small format camera systems are becoming popular due to their low cost, reasonable accuracy, and simple implementation [Abd-Elrahman et al., 2001]. In general, these cameras are relatively compact, lightweight, and capable of operating in largely automated modes. Small format of digital airborne sensors are currently used in the market now. However, it can also be seen that the main emphasis has been on the production of true color and false colour images for environmental monitoring and agricultural applications over relatively small areas. In this kind of sensors, very large numbers of images are needed at any project in comparing with medium or large format. The small-format cameras produce colour images using mosaic filters and Bayer interpolation.

- Medium format cameras are equipped with sensors between 16 and 50 Megapixels.

Medium format digital systems are used for a wide range. medium format cameras can joint to with laser scanners systems. The largest providers of airborne medium

format cameras are the Applanix DSS and the Rollei AIC camera [Grenzdörffer, 2008]. Trimble announced that it has entered into an agreement to acquire the assets of RolleiMetric in 2008. The Aerial Industrial Camera (AIC) series from RolleiMetric is designed for aerial and industrial purposes. The Rollei AIC camera is shown in figure 2.3. Table 2.1 shows the technical specifications of AIC series from RolleiMetric.



FIGURE 2.3: Rollei AIC digital aerial camera [Lemmens, 2008].

Items	Specifications
Image format	22 and 39 MP
Pixel size	9 μm for 22 MP and 6.8 μm for 39 MP
Date of Introduction	2004
Focal distance	35 mm to 150 mm
Shutter speed	1/1000 second
Image size pixels	5440x4080 pixels for 22 MP 7228x5428 for 39 MP
Dimensions of the camera unit	11 x 14 x 15 cm
Weight	0.55 kg without lens

TABLE 2.1: Technical specifications of Rollei AIC sensor [Lemmens, 2008].

The lately announced medium-format cameras are the Leica RCD30. This type of camera is presented in [Wagner, 2011b]. This camera is a medium camera that acquires multispectral RGB and NIR airborne imagery by one camera head. The Leica RCD30 Series consists of the camera system operator, camera head, and camera controller as shown in figure 2.4. Table 2.2 shows the technical specifications of the Leica RCD30.



FIGURE 2.4: The Leica RCD30 system operator (left), camera head (middle), and camera controller (right) [Wagner, 2011b].

Items	Specifications
Image format	8956 x 6708 pixels
Pixel size	6 μm
Date of Introduction	2011
Focal distance	50 mm and 80 mm
Dimensions of the camera head	Height 147 mm Diameter 128 mm
Weight of camera head	3.5 kg

TABLE 2.2: Technical specifications of Leica RCD30 system [Wagner, 2011b].

- Large format cameras are equipped with large sensors with more than 50 Megapixels.

UltraCam is the Microsoft/Vexcel Imaging camera family that was introduced in May 2003 by the first digital aerial camera product UltraCam-D [Gruber et al., 2011]. Vexcel Imaging launched UltraCam-X in 2006, UltraCam-Xp in 2008, and UltraCam-XpWA in 2009. The UltraCam cameras are an example of large-format airborne digital frame camera. As shown in figure 2.5, the UltraCam-X system consists of the sensor unit, the storage unit and data capture system, the operators interface panel and two removable data storage units [Gruber et al., 2008]. Table 2.3 shows the technical specifications of UltraCam-X system.

By May, 2011 the 4th generation of UltraCam Eagle has been introduced, increasing the original swath width from 11,500 pixels to beyond 20,000 [Gruber et al., 2011] and [Leberl et al., 2012]. The overall weight of the on board equipment has been

reduced to 75 kg for the UltraCam Eagle. Figure 2.6 shows the UltraCam Eagle camera and table 2.4 presents the specifications of the camera.



FIGURE 2.5: UltraCam-X digital aerial camera system [Gruber et al., 2008].

Items	Specifications
Date of Introduction	2006
Panchromatic image size	14,430 x 9,420 pixels
Panchromatic physical pixel size	7.2 μm
Physical format of the focal plane	104 mm x 68.4 mm
Panchromatic lens focal distance	100 mm
Lens aperture	$f = 1/5.6$
Angle-of-view cross track	55 degree
Angle-of-view along track	37 degree
Colour image size	4810 x 3140 pixels
Colour lens system focal distance	33 mm
Colour lens aperture	$f = 1/4.0$
Dimensions of the camera unit	45 x 45 x 60 cm
Weight	~ 55 kg

TABLE 2.3: Technical specifications of UltraCam-X sensor [Lemmens, 2008].



FIGURE 2.6: UltraCam Eagle aerial camera [Gruber et al., 2011].

Items	Specifications
Date of Introduction	2011
Panchromatic image size	20,010 x 13,080 pixels
Panchromatic pixel size	5.2 μm
Physical format of the focal plane	104 mm x 68.4 mm
Panchromatic lens focal distance	80 mm
Lens aperture	$f= 1/5.6$
Angle-of-view cross track	55 degree
Angle-of-view along track	37 degree
Colour image size	6,670 x 4,360 pixels
colour pixel size	5.2 μm
Colour lens system focal distance	27 mm
Colour lens aperture	$f = 1/4.0$
Dimensions of the camera unit	43 x 43 x 67 cm
Weight	~ 75 kg

TABLE 2.4: Specifications of UltraCam Eagle sensor [Gruber et al., 2011].

2.3.2 Airborne digital linear cameras

The first commercial line scanner Airborne Digital Sensor ADS40 was developed by LH Systems jointly with DLR [Reulke et al., 2000]. Since their first introduction, linear array CCD cameras have played an important role in the airborne optical digital sensors market. This kind of camera is introducing a continuous strip image of the terrain. The angular extent of the image across track is referred to as the field of view (FOV) of the imagery (figure 2.7).

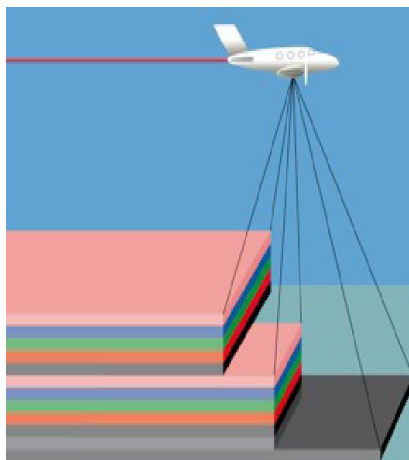


FIGURE 2.7: Airborne linear imaging system [Kheiri, 2006].

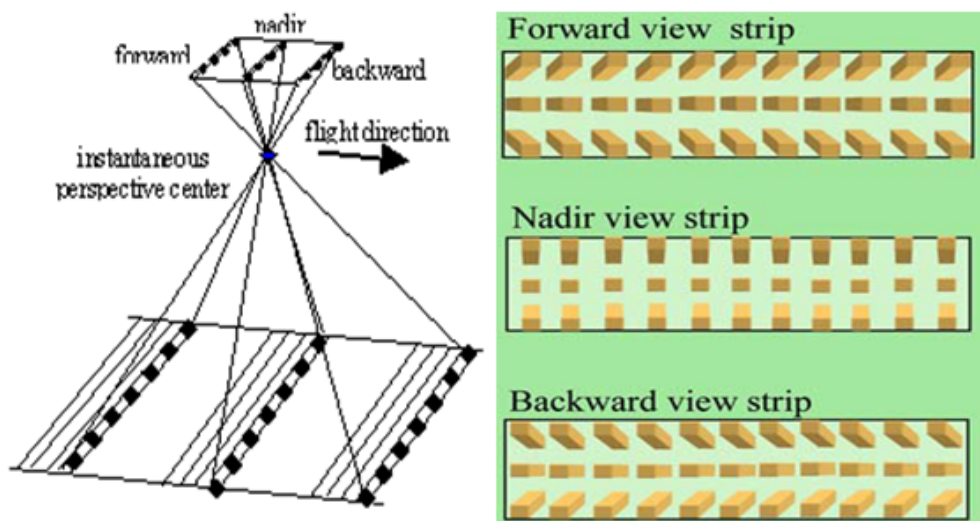


FIGURE 2.8: Three-line imaging system (TLS)[Sandau, 2009].

The three-line scanners (figure 2.8) produce three overlapping strip images that are acquired simultaneously using forward, nadir and backward pointing linear arrays, from which 3D stereo models can be formed. Seamless high resolution images can be obtained with three different viewing directions (forward, nadir, backward) as shown in figure. As in photographs taken with a matrix camera at 60% forward overlap, 60% of the objects appear in three photographs, creation of ortho-images from three-line imaging system is possible because these images are line-projection and less distorted than conventional aerial images. Multi-spectrum images can be acquired by replacing the filters and sensors as shown before.

The ADS camera has eight parallel sensor lines [Roeser et al., 2000], three panchromatic lines (forward, nadir, backward), three lines used as Red, Green and Blue channels and two different NIR channels. Their technical specifications are described in table 2.5. Several upgrades have been proposed by Leica since 2000, as ADS 80 in 2011. The ADS80 pushbroom camera is shown in figure 2.9. These investment allow to acquire data at higher speeds. The new sensor is smaller and light weight [Wagner, 2011a]. 145 kg is the total system weight in aircraft, 39 cm in diameter, and 70 cm in height. In addition, the spectral and radiometric characteristics have been improved than before.

Items	Specifications
Image size	12000 pixels/line
Pixel size	6.5 μm
Panchromatic lens focal distance	62.5 mm
Imaging rate (line/second)	830
Angle-of-view	64 degrees
Forward stereo angle	28 degrees
Backward stereo angle	14 degrees
FB stereo angle	42 degrees
F-number	4.0
Dimensions of the camera unit (<i>cm</i>)	Diameter 39, Height 79
Weight	224 kg

TABLE 2.5: Technical specifications of ADS40 sensor [Lemmens, 2008].



FIGURE 2.9: Airborne linear cameras: ADS80 [Wagner, 2011a].

2.4 Principles of image processing in photogrammetry

The next step, after the images recording is the post processing. The aim of this process is to establish the position and orientation of the camera at the instant of exposure. Sensor modeling is the most important process in order to acquire three-dimensional object space coordinates information from photogrammetric images. In order to carry out sensor modeling, a number of GCPs (Ground Control Points) or Global Navigation Satellite System (GNSS) and INS data are needed. Images can be oriented using two different methods. Firstly, orientation of images using ground control points that were surveyed on the ground using ordinary surveying techniques. Secondly, orientation of images using GNSS and INS techniques in which the position and the attitude of the camera are computed without ground control.

As mentioned before, the coordinates of a digital image are defined in a pixel coordinate system. A pixel coordinate system is usually a coordinate system with

its origin in the upper-left corner of the image, the x-axis pointing to the right, the y-axis pointing downward, and the units in pixels. The image coordinate system is defined as 2D system on image plane. The origin of the system is the image centre. The ground coordinate system is defined as the 3D coordinate system (X, Y, Z). The image and Ground system are as shown in figure 2.10.

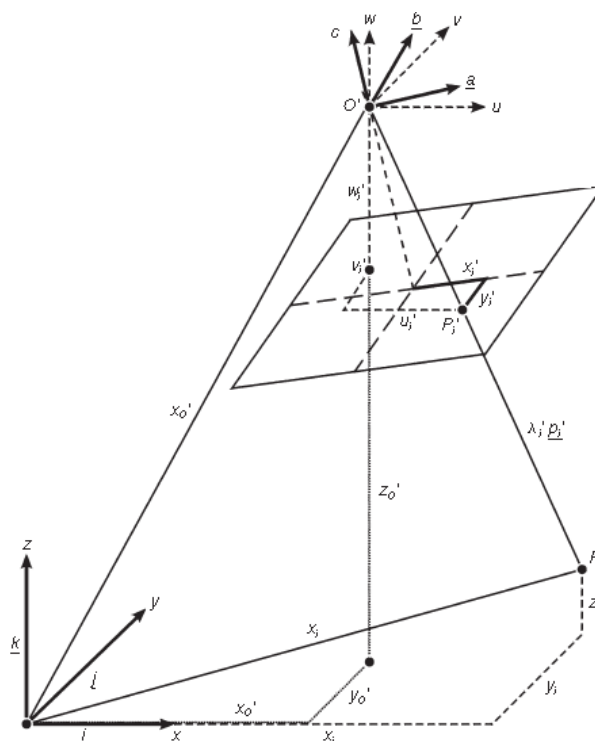


FIGURE 2.10: Image and ground coordinate systems [Konecny, 2003].

2.4.1 Image Orientation

Image orientation is needed for any task such as the generation of a digital terrain model, the computation of orthophotos, and the acquisition of data for geographic information systems. Image orientation relates to the determination of parameters defining particular photogrammetric models for geometric primitives such as points, lines, and areas from one coordinate system to another one. Image orientation has always been a focus in photogrammetry, in view of its importance [Heipke, 1996]. There is a geometric relationship between object on the ground and on images at the time of capture for each photograph. The orientation is the

procedure where the transformation parameters from one coordinate system to a second coordinate system are determined. A 2D orientation includes the shift and rotation of an object along a plane, and a 3D orientation includes the determination of the position and attitude of an object in coordinate systems. In photogrammetry, the orientations are described as interior and exterior orientations (relative and absolute orientations). The division to interior and exterior orientation relates to the camera body, whereas the relative and absolute orientations were introduced aside exterior orientations. Exterior Orientation (EO) parameters are (X, Y, Z) and (ω, ϕ, κ) of image during exposure. In photogrammetry, EO parameters are derived from Aerial Triangulation (AT). the computation of EO parameters also may need Ground Control Points (GCP) which are distributed evenly. The method that EO parameters recorded directly from GNSS/IMU is called Direct Georeferencing [Rizaldy and Firdaus, 2012].

In the case of digital photogrammetry, interior orientation is primarily used to transform the image pixel coordinate system or other image coordinate measurement system to the image space coordinate system [Karabork et al., 2004]. The variables associated with the internal geometry of an digital the aerial camera are Focal Length, Principal point, and Lens Distortion. The calibration certificates of the camera manufacturers are including the location of the principal point, the focal length and the radial symmetric lens distortion.

By exterior orientation, the collinearity condition is fulfilled all along to the object space. After exterior orientation of at least two images, the coordinated in 3D of object points and features can be computed. The exterior orientation describes the location and orientation of the bundle of rays in the object coordinate system with the 6 parameters: projection center coordinates (X_0, Y_0, Z_0) and the rotations around the 3 axis $(\omega, \Phi$ and $\kappa)$, see figure (2.11). These parameters can be obtained by direct method or indirect method.

For each GCP measured, there are two corresponding image coordinates (x and y). Thus, two collinearity equations can be formulated to represent the relationship between the ground point and the corresponding image measurements.

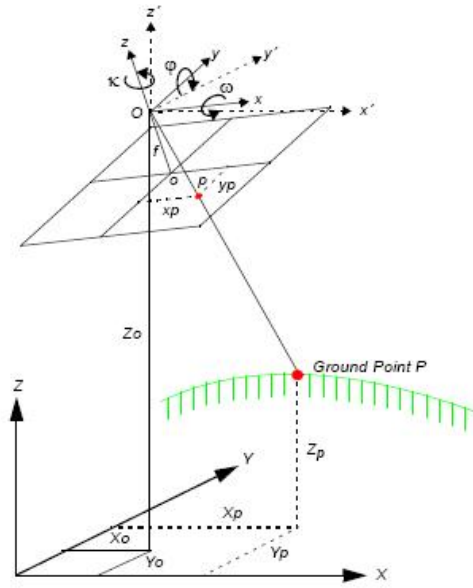


FIGURE 2.11: Elements of exterior orientation [Kraus, 1993].

$$x_a - x_0 = -f \cdot \frac{m_{11}(X_A - X_0) + m_{12}(Y_A - Y_0) + m_{13}(Z_A - Z_0)}{m_{31}(X_A - X_0) + m_{32}(Y_A - Y_0) + m_{33}(Z_A - Z_0)} \quad (2.1)$$

$$y_a - y_0 = -f \cdot \frac{m_{21}(X_A - X_0) + m_{22}(Y_A - Y_0) + m_{23}(Z_A - Z_0)}{m_{31}(X_A - X_0) + m_{32}(Y_A - Y_0) + m_{33}(Z_A - Z_0)} \quad (2.2)$$

2.4.2 Image matching

One of the practical applications of 3D reconstruction techniques is the automated generation of Digital Terrain Models (DTMs) from airborne images. DTM generation by airborne radar images is presented in [Polidori, 1997]. Stereo matching is used for finding corresponding pixels in a pair of images, which allows 3D reconstruction by triangulation, using the known orientation of the cameras [Hirschmüller, 2011]. This process can be achieved by establishing correspondences between sequences of 2D images of a scene taken at different times or displacements or from different perspectives. An effective way to increase the performance of image matching is to increase the number of stereoscopic measurements, which relies on a large amount of data in order to achieve a high redundancy [Nonin, 2003].

Many techniques have been proposed in photogrammetry and, later on, in computer vision. Image matching techniques for DEM computations are well known and available in commercial software packages. The process of stereo vision comprises six steps [Chong et al., 2000]: image acquisition, camera modeling, feature extraction, image matching, distance determination, and interpolation. Stereo image matching techniques can be classified into three categories: area-based, feature-based, and combination of them techniques. Area-based techniques match intensity levels in the local neighbourhood of a pixel in one image with intensity levels in a corresponding neighbourhood of a pixel in the other image. Feature-based techniques use higher-level features extracted from the two images as matching primitives rather than the low-intensity levels of area-based techniques.

In this study, dense point clouds were extracted from UltraCam-X and Rollei-db44 digital stereo images over Strasbourg City using ERDAS Leica Photogrammetric Suite (LPS version 2011) and eATE tools. In this work we followed the classical photogrammetric workflow available in ERDAS LPS environment [ERDAS Inc., 2011] for the processing of the stereo images and DTM generation (Figure 2.12). The process of generation of DSM using LPS can be divided into the following steps: digital image matching, ground point coordinate determination and DTM construction.

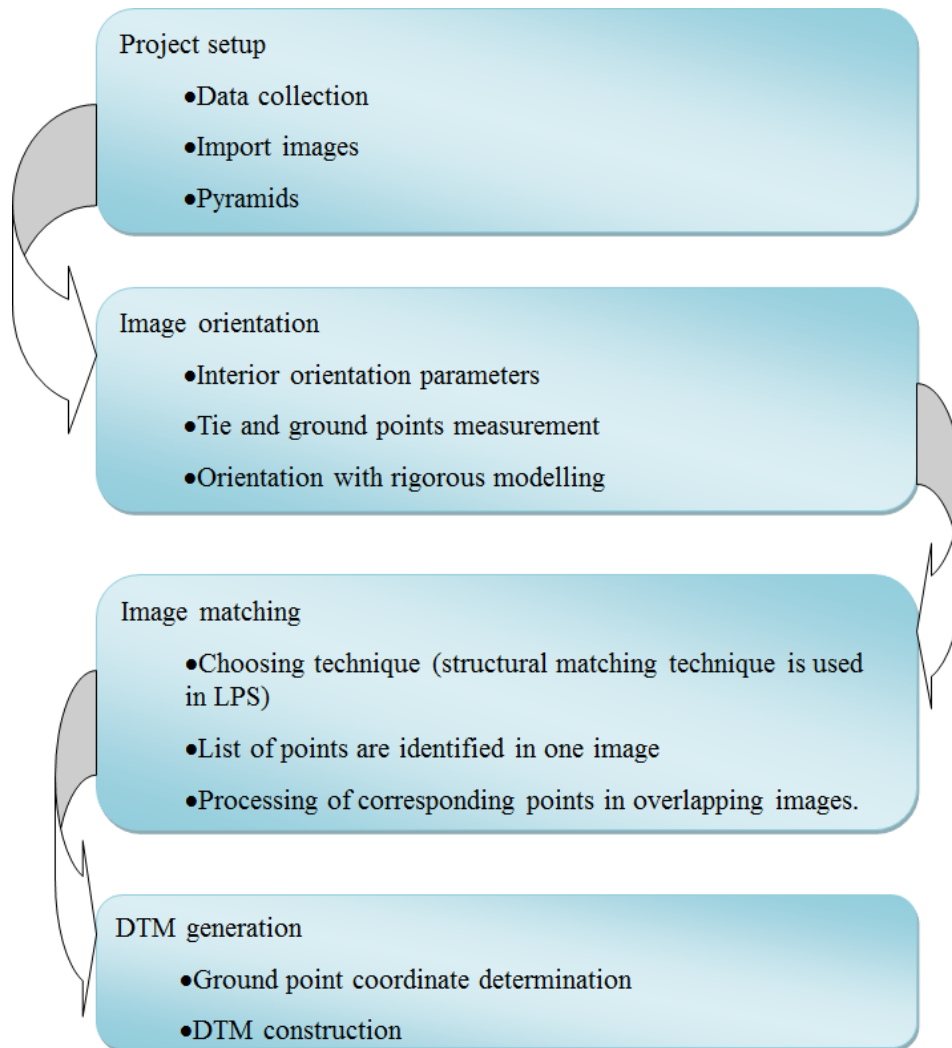


FIGURE 2.12: Process of DTM generation using LPS software

First step: Digital image matching

Three techniques are used for automatic image matching as shown before. These categories are area based matching, feature based matching, and structural matching techniques. Using area based method, digital numbers (DN) in small sub-arrays from each image are numerically compared to perform the image match. Cross correlation and least squares correlation techniques are well-known methods for area-based matching. Features extraction is involved in the feature based and it is therefore more complicated than the area based method. Feature points are also commonly referred to as interest points. Poor contrast areas can be avoided with feature-based matching. Structural matching technique is a combination of

area based matching and feature based techniques. Typically, the corresponding images are processed to highlight features. These identified features are then matched by the area based method [Wolf and Dewitt, 2000].

A list of interest or feature points is identified in the image, using an interest operator. These interest or feature points are described by the centre of a template window, that having sufficient variation of grey level and good contrast. When feature points have been successfully identified in the first image, LPS estimates the approximate position on the neighbouring overlapping image in the block and searches for the corresponding feature point in an rectangular window around that approximate position. An interest point on the reference image may have more than one possible match points on the conjugate images. In such case, the cross-correlation coefficients are calculated for each correlation window among the search window. Search window size, correlation window size, and correlation coefficient limit are three parameters that influence the success and accuracy of the matching results.

The first parameter that influences the point matching process is the search window size. The search window size is normally rectangular. X and Y refer to length and width of rectangle respectively, figure 2.13. The search window size X reflects the variation of ground elevations for that given window appearing on the surface of the Earth. The larger the range of ground elevation, the larger the search window size X . The width of search window Y depends on the geometric accuracy of the images to be matched. In case of aerial frame camera with accurate triangulation, the width of 3 pixels is sufficient. For images with accurate triangulation results, the epipolar line can be computed accurately enough. This is important for image matching since the search space for corresponding feature points.

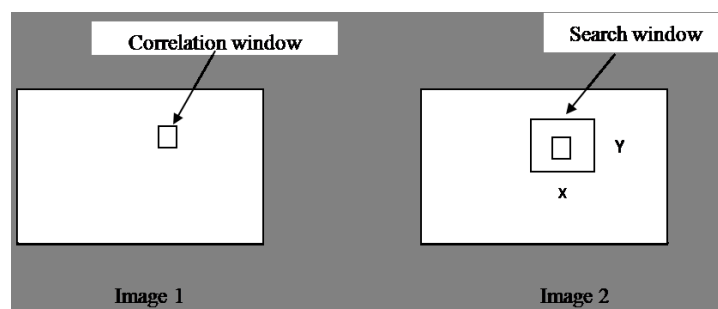


FIGURE 2.13: Correlation and search windows

Correlation window size is normally square shape, but it may be rectangular. Since variations caused by ground relief are larger in the epipolar line direction than across the epipolar line direction, size Y (across epipolar line) can be larger than size X (along epipolar line) [ERDAS Inc., 2011]. Correlation window defines the size of window that is used to compute the correlation coefficient between the points on corresponding overlapping images. If the ground has large variation in gray level, and colour intensity, a smaller window size can be used.

An important parameter which influences the point matching process is the correlation coefficient limit. This correlation coefficient threshold is used to determine whether two identified feature points are considered to be a possible match or not. The correlation limit is compared to the correlation coefficient that has been computed for two feature points appearing on two frames. These two points are to be considered as a match, if the correlation coefficient value is larger than the value of the correlation coefficient limit. A match point that having correlation coefficient equal to one are considered as correct match whereas zero correlation coefficient is considered as no match point.

Second step: Ground point coordinate determination

The second step of the DTM extraction process is the computation of the 3D ground coordinates. After finding the possible match and computing the cross correlation coefficient, different statistical measures are applied to determine the final matching points. Row and column pixel coordinates of these final image points are recorded. From these image points, the 3D coordinates of the ground feature are computed using collinearity Equations. These 3D coordinates associated with a mass point are generated by using space forward intersection. These computed points with known 3D coordinates are used as reference points for surface generation.

Third step: DTM construction

Various types of DTM formats as output are possible in LPS such as raster DTM, TIN, 3D shape file, ASCII etc. DTM mass points are used to generate DTM in any format. ASCII file and 3D shape file are simple vector description of the DTM mass points. A triangulated irregular network (TIN) is a digital representation of the earth surface. TIN is created from DTM mass points by using the Delaunay triangulation approach.

2.5 3D building modeling

3D building models have become one of the most important and attractive products of photogrammetry and LiDAR datasets. The digital photogrammetry developments and the use of high resolution digital cameras allow to get accurate models with the image matching technique. Digital images can be used for both aerial and terrestrial images. Aerial images are used to extract the forms of buildings. An advantage of aerial images is that they are widely used in reconstruction of 3D city models. In addition the textures of roofs are extracted from the same image. We concentrate our work on aerial images. Airborne LiDAR has become rather important for generating 3D building models. LiDAR systems collect X, Y, Z data at predefined intervals. This three-dimensional process allows to use appropriate filters, to separate the point clouds in each building [Prandi et al., 2008]. There are two approaches in acquiring LiDAR data. One is to acquire the LiDAR datasets from an airborne vehicle. This is commonly used by creating digital surface model (DSM), digital terrain model (DTM), and 3D models such as buildings and trees. Another approach is to get the LiDAR datasets from the terrestrial vehicle and extract the complicated geometries like the architectural components. The complementarity of photogrammetry and LiDAR datasets are utilized to perform a primitive-based 3D building reconstruction [Zhang et al., 2011].

Three methods are mainly used for creating 3D building models, and researchers are trying to develop more efficient and effective methods. These modeling methods are categorized into: automatic, semi-automatic, and manual. The manual method is to create all geometries of building models one by one using software packages such as CAD software that are commercially available. Manual recording is slow, expensive and requires well trained operators. The objective of automated data capture and interpretation is the rapid, reliable and accurate provision of data for data analysis and subsequent decision making. As long as such a fully, or at least close to fully, automatic process is not available, semi-automatic methods have to be developed [Ruther et al., 2002].

Fully automatic feature extraction systems until now are limited to specific applications. Research on automatic city modelling is still a very active area. Automatic city modelling aimed at polyhedral building objects, which mainly reflects the respective roof shapes and building footprints. Numerous approaches of 3D

building models from airborne and terrestrial images or laser scans were reviewed in [Haala and Kada, 2010]. Terrestrial data is essential for building facades. The visual appearance of building facades is improved using terrestrial images by suitable texturing methods. The developments of past and present trends in building roof reconstruction from elevation data are presented in this research. Footprints representation have been derived from DEM based on marked point processes [Ortner et al., 2007]. Combining LiDAR data and aerial images is proposed in [LI and WU, 2008] for building edge detection.

For the last decade, the automatic 3D reconstruction of building models has become a topic of interest. Satellite images [Lafarge et al., 2006], aerial images [Wang et al., 2008], LiDAR datasets [Tarsha-Kurdi et al., 2007]; [Verma et al., 2008]; [Rutzinger et al., 2009], and combination of aerial images with LiDAR datasets [Zhang et al., 2011]; [Zhang et al., 2012] were used to efficiently obtain 3D information on large scales. [Fruh and Zakhor, 2003] combined aerial images, airborne and terrestrial laser scanner to build 3D city models. [Boulaassal et al., 2011] combined airborne laser scanner, and terrestrial laser scanner to reconstruct 3D vector models of buildings.

Research in detection and reconstruction of building model from aerial images has been made by [Haala and Hahn, 1995]. With the aerial imagery, building roofs can be reconstructed in 3D. Vertical walls may be added by projecting the roof points down to an existing Digital Terrain Model (DTM), thereby generating a complete building model. Other techniques for extracting the vertical walls are using the 2D ground plane surface [Henricsson, 1997]. The role of color attributes for automated 3D building reconstruction from multiple color aerial images is addressed in [Henricsson, 1997].

The method used in our research is introduced in [Amat et al., 2010] and developed by [Mohamed et al., 2013]. Since the images are oriented, 3D information for the elements of the building, roof elements, walls, and footprints are necessary. The aerial images give an advantage to cover wide area such as cities. In addition, roof models are visible from aerial images. The aerial images processing are including stereo model processing, digitizing roofs points and 3D points at the ground. Then, the projection of these points onto the ground plane surface is done in order to obtain footprints and thus to create the walls (no facade details). Therefore it is not necessary to digitize the footprints of the buildings. Finally, planes of roofs,

faces and footprints are reconstructed. The presented reconstruction is based on the assumption that every solid object can be described by a decomposition of its boundary and the walls are vertical.

Several approaches have been presented for building extraction from LiDAR datasets. 3D building reconstruction can be represented from original LiDAR point clouds [Maas and Vosselman, 1999] or from a DSM interpolated from LiDAR point clouds. Parameters of standard gable roof type building in [Maas and Vosselman, 1999] were determined by invariant moment analysis. Using a technique based on intersection of planes fitted into triangulated point clouds, models of more complex building could be determined. Laplacian of Gaussian edge detector was used by [Wang, 1998] to extract edges from DSM image derived from LiDAR data. [Tarsha-Kurdi et al., 2007] presents the pertinence and advantages of combining simultaneously the point clouds and the normalized DSM (nDSM) in the main steps of a building reconstruction approach. Three main steps were followed at the proposed approach. First step is to extract the off-terrain mask based on DSM. Secondly, it combines the point clouds and the DSM for extracting a building mask from the off-terrain. Finally, based on the previously extracted building mask, the reconstruction of 3D flat roof models are carried out and analyzed.

Model-driven automatic method for reconstruction of roofs from LiDAR point clouds is presented in [Henn et al., 2013]. Firstly, based on the segmentation of footprints into rectangles, Then, roof models from a catalogue of standard roof types provided by the international standard City-GML are derived. The RANSAC procedure method is used plane detection.

The method used in our research for 3D building models reconstruction from airborne images was introduced in [Verma et al., 2008] and has been developed by [Mohamed et al., 2013]. This semi-automatic reconstruction process comprises 3 steps. Firstly, building point clouds are segmented to separate building roofs. Then, topological graph is constructed and the roof-topology graph is utilized to recognize shapes of buildings. Finally, building models are reconstructed with predefined models.

The two technologies, LiDAR and photogrammetry, are treated by researchers

as complementary to each other. The combination of both LiDAR and photogrammetry datasets is believed to lead to more accurate and complete products [Baltsavias, 1999]. [Haala and Brenner, 1999] combined multi-spectral imagery and laser altimeter data for classification to extraction of buildings, trees and grass-covered areas. Generating accurate surface models from both datasets is presented in [Mcintosh and Krupnik, 2002]. [LI and WU, 2008] proposed an adaptive method of building edge detection by combining LIDAR data and aerial images. Three steps were followed. Firstly, the objects and ground are separated by a filter based on morphological gradient. Secondly, the aerial image is smoothed by Gaussian convolution, and the gradients of the image are calculated. Finally, the edge buffer areas are created in image space by the edge points of the individual roof patch. An automatic method of boundary extraction using LiDAR-imagery fusion is suited to handle diverse building shapes in [Li et al., 2013]. Filtering, building detection, wall point removal and roof patch detection were four steps to detect the point clouds in each roof. Then, from airborne imagery, initial building edges were extracted. Finally, the roof patch and initial edges are integrated by mathematical morphology to form the final complete building boundaries.

The method used in our research for reconstruction 3D models from both datasets is introduced in [Zhang et al., 2011], [Zhang et al., 2012], [Zhou et al., 2012] and [Mohamed et al., 2013]. The researchers have developed a building modelling methods using these two kinds of data. The proposed method comprises following steps: (1) recognize primitives from LiDAR point clouds and roughly measured parameters of primitives as initial values, and (2) select primitives features on the imagery, and (3) optimize parameters of primitives by the constraints of LiDAR point clouds and imagery, and (4) represent 3D building model by these optimized primitives. It only uses the most straightforward features, i.e. planes of LiDAR point clouds and points of airborne imagery.

2.6 Summary

Literature revealed that recent developments in digital photogrammetry have greatly increased the applications in the field of photogrammetry. An overview of the airborne digital imaging sensors and systems has been given to show the

current state of the technology. In this chapter, the main mathematical principles used in photogrammetry which allows three-dimensional coordinates to be extracted from stereo photographs have been reminded. Camera parameters and ground control points are required for obtaining a photogrammetric solution. In a bundle adjustment the collinearity conditions for all photographs in a block are solved simultaneously using least-squares estimation. The quality of data, as well as the development level of the technology impact the quality of the 3D building models reconstructed from this data.

3D city models have been utilized in various fields such as 3D maps, urban planning, and 3D building modeling. As mentioned in this chapter, there are many different methods of reconstructing 3D building models from photogrammetry and LIDAR datasets. Researchers are trying to develop more efficient and effective methods. The modeling approaches are categorized into: automatic, semi-automatic, and manual ones. However, the various methods may deliver 3D models of different levels of quality. At this stage, it is the time to investigate the solutions provided in the literature for assessing the quality of the 3D building models produced from the photogrammetric data presented in this chapter.

Chapter 3

State of the art of accuracy assessment

In this part, a review of some reported works in the field of accuracy assessment applied to the data of digital airborne photogrammetric and LiDAR sensors and steps of processing will be given.

Because high quality reference datasets are difficult and expensive to obtain, the sampling design issues encountered in accuracy assessments are similar to those traditionally addressed by survey sampling methodology: how to choose samples in a cost-effective and at the same time statistically rigorous manner? Once the reference datasets are in hand, the next step in accuracy assessments is the analysis of tested data. The traditional analysis of accuracy assessment begins with detection of errors in the raw data.

3.1 Accuracy, precision and error

This section covers description terms and basic concepts related with measurement error, uncertainty, accuracy, and error sources studied in the literature. The terms of error, uncertainty and accuracy are related concepts and sometimes they are used interchangeably. However, these three terms have different meanings. Before data can be used for surveying and mapping projects, for engineering design, or for use in a geographic information system, they must be processed. One of the

most important aspects is to take into account that exact measurements do not contain errors.

Error is the difference between a measured value for any quantity and its true value. Accuracy is the measure of the absolute nearness of a measured quantity to its true value. Since the true value of a quantity can never be determined, accuracy is always an unknown [Ghilani and Wolf, 2006]. Accuracy is an issue pertaining to the quality of data and errors contained in a dataset. Precision refers to the closeness with which repeated measurements made under similar conditions are grouped together. High precision neither indicates high accuracy nor high accuracy implies high precision. But high accuracy and high precision are both expensive to obtain. Precision is affected only by the random errors in the measuring process while accuracy is affected by the precision as well as the existence of unknown or systematic errors. The difference between precision and accuracy is illustrated in figure 3.1.

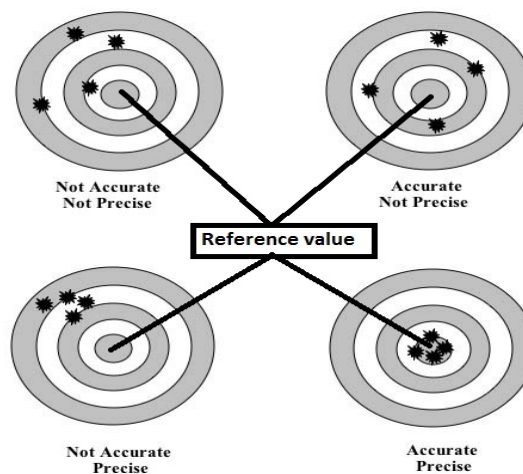


FIGURE 3.1: Simple representation for avoiding confusion between accuracy and precision (celebrating200years.noaa.gov).

According to theory of errors, all measurements contain errors and the true values of measurements are unknown. One can discover the existence of measurement errors in different ways. If the same measurement is repeated several times, one will normally get different results due to measurement errors. Another way to discover errors is to check whether the obtained measurement results satisfy some geometrical or physical relations which probably exist [Huaan, 2010].

Absolute accuracy has the same meaning as accuracy; absolute accuracy is the degree to which the position of a tested object conforms to its correct location according to an accepted coordinate system. In many standards, it is expressed as a circular error at the 90 or 95 percent probability level for horizontal accuracy such as in terms of the United States National Map Accuracy Standards (NMAAS) [Congalton and Kass, 2009]. Relative accuracy is the statistical evaluation of all random errors encountered in comparing one data set with respect to another data set.

The error in a quantitative attribute can be described as the difference between reality and our representation of reality, as explained in [Heuvelink, 1998] and [Heuvelink, 2007]. It includes not only mistakes, or faults but also the statistical concept of error i.e. variation. Precision and accuracy are ways of describing the error that can exist in tested data. Once these notions explained, it is the time to distinguish the the different types of errors.

3.2 Types of errors

In surveying, geodesy and photogrammetry, three types of errors are considered: systematic errors, gross errors and random errors [Ghilani and Wolf, 2006].

Systematic errors are the errors which follow certain physical or mathematical models. This kind of error might be constant or variable. If it is constant, it might be corrected by finding out the numerical value of the correction. If it is variable, the mathematical model describing it must be determined. In the first case, it may be called constant error or bias. This kind of errors might occur in photogrammetry during the interior orientation process. Interior orientation is carried out with the aim of finding three elements: the calibrated focal length, the location of the principal point and the parameters of lens distortion.

Gross errors are errors which do not follow certain physical or mathematical models. The source of these errors is the bad manipulation of the operator or the malfunctioning of instruments. These errors are usually recognized by their high residuals and can easily be detected. To avoid or reduce gross errors, one should take care of all steps of photogrammetric processing. Gross errors may be called blunders or outliers. Blunders can not be considered as a part of the sample from

a statistical point of view. For this reason, great care should be taken to avoid blunders while making observations. Often data or observations are checked on the basis of a three sigma test (3σ). In this test, the repeated observations of the same variable are averaged, and any additional observation which is higher than three standard deviations from the mean are rejected. A good example of this kind of error in photogrammetry is the wrong identification of ground control points and incorrect input of coordinates of points.

Random errors are the errors that remain once the systematic errors and blunders have been eliminated. They remain despite the control of the user and are present in all observations. Random errors result from unknown causes. Due to their unpredictability, random errors cannot be eliminated from observations. They are assumed to follow the normal or Gaussian distribution. The following statistical characteristics of a Gaussian distribution are:

- Errors of smaller magnitude occur more often than errors of larger magnitude.
- Positive errors and negative errors with same magnitude occur roughly at equal frequency.
- Very large errors are extremely unlikely.
- The probability for an error to occur in an interval of confidence can be estimated.

The quality of derived spatial data can be defined as a function of precision, accuracy and reliability with respect to random, systematic and gross errors, respectively [Cooper and Cross, 1988]. The accuracy of data is significant for most users and is closely related to the eradication of systematic effects. But these effects are more difficult to detect and eradicate than random and gross errors. Calibrating instruments, for example, consumer-grade digital cameras can assist in minimizing systematic effects. Accounting explicitly for all such effects can be difficult because of high correlation between calibration parameters. These difficulties justify seeking an alternative approach to minimize such systematic effects.

3.3 Accuracy assessment

Accuracy assessment of photogrammetry outputs is one of the most important steps in evaluating imaging sensor data. Without an accuracy assessment, the

output or results are of little value. Since the performance of data acquisition methods has improved, the quality evaluation of building data in 3D city modeling has become an important issue. Digital sensor camera systems produce 3D data and some methods were presented in order to evaluate the output. The accuracy of the derived data product mainly depends on the accuracy of a model which is the result of image processing such as the camera calibration, determination of the camera focal length, principal point shift and the distortion characteristics of the camera. Furthermore, the method of obtaining the exterior orientation parameters is essential. The accuracy assessment is usually performed in a qualitative and a quantitative way. Processing with both statistical and visual methods is the primary focus in [Podobnikar, 2009]. The methods addressed differ according to whether they use one or multiple datasets and by their expected outputs. These techniques may be used one after another. The study classified them into two complexes (complex 1 and complex 2): techniques using numerical processing and those using visualization (figure 3.2). As a final result, the datasets (DTM) are evaluated by statistical or visual methods within the reports.

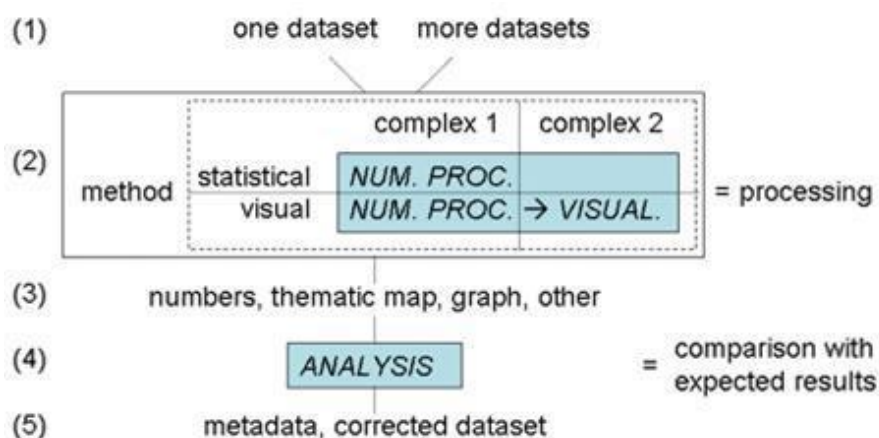


FIGURE 3.2: Procedure for quality assessment of a DTM [Podobnikar, 2009].

3.3.1 Qualitative assessment

Qualitative assessment of data relies on visual methods. Quality assessment can be performed before and/or after processing of data. Before generating the 3D data, one can estimate the expected quality that might result from the process and what quality is required with regard to the respected standards. These two

factors enable regular production and usability of the resulting models. A priori assessments are based mostly on analyses of the datasets and methods for the 3D production (such as DTM production), while a posteriori methods are based on the final output as described in [Podobnikar, 2009].

A special test was conducted to assess the quality and the reliability of the generated DTM via an airborne laser scanning system by [Al-Bayari et al., 2002]. To perform this test, an airborne laser scanner aligned with an airborne digital camera was mounted on a Helicopter (TopEye AB system). The test was performed in Italy and the flying height was about 200 meters. An overlap percentage of 50 % was maintained between two successive images. The digital camera is a Hasselblad camera with 2Kx3K resolution. An INS/GNSS system is integrated and used for position and orientation determination. A series of tests were done to check the DTM quality. The main approach used is based on comparing it to the DTM generated from the digital aerial photogrammetry with automatic and semi-automatic matching approaches. Additional comparison is conducted between the orthophoto created by stereoscopic model and the one created by the laser data and digital images.

Ideally, an assessment of digital spatial data quality is a comparison of our digital representation to the known feature on the ground. It includes qualitative as well as quantitative measures. The achievable qualitative assessment as well as quantitative assessment are important and should be completed by quantitative assessment. Quantitative assessment of photogrammetric and LiDAR datasets will be presented next section.

3.3.2 Quantitative assessment

Quantitative assessment of data is more important for 3D data production and it relies on statistical methods. Estimation and reporting of positional accuracy for new digital photogrammetric datasets has become an important issue. Any international standard requires a positional accuracy assessment. Quantitative assessment involves more than checking the coordinate location of a feature (positional accuracy). It includes other characteristics such as shape, direction (or angular measure), distance, area, and topology assessment.

3.3.2.1 Quantitative assessment using RMSE computation

An analysis of some standard methodologies for positional accuracy assessment of geographic databases is presented in [Loopez and Spain, 2007]. In this study, some aspects are taken into account like RMSE or SD (Standard Deviation) statistical formulation, the size of the control sample, the distribution and typology of the control elements.

Positional accuracy is the accuracy of the location of a tested point with regard to the reference one, i.e. its physical location on the ground. Positional accuracy based on National Map Accuracy Standards is measured in terms of RMSE [Congalton and Kass, 2009]. The RMSE is computed as the sum of the square of the differences (as will be shown in next chapter) between the position of the point on one data layer and the position of the same point on another data layer (often the ground or more accurate measurements) [Congalton, 2005].

In the case of point features, the distance between the tested and the reference source provides a convenient basis for measures of accuracy. Suitable measures include the root mean square distance, and percentiles of the distance distribution. The 90th and 95th percentiles are often used as the basis of map accuracy standards and as measures of accuracy for measurement instruments such as the GNSS. They are readily interpreted without substantial understanding of statistics. If the distribution of observed positions around the true position is normal or Gaussian, simple mathematical relationships exist between the percentiles of the distance distribution and other parameters such as the root mean square distance and the standard error [Goodchild and Hunter, 1997].

An approach to estimate the positional accuracy of a cadastral dataset derived from uncontrolled and unrectified aerial photography is presented in [Siriba, 2009]. The positional error according to [Shi and Liu, 2000] is considered as one of the most important issues in digital spatial datasets. In this study, Positional errors are brought about by field measurements, digitization and other processing and can be either systematic or random.

The accuracy of a map prepared by photogrammetric techniques depends on the accuracy of the ground control points, the ability to identify them on the imagery, and the scale of aerial photography. In digital photogrammetry context, mathematical models exist for estimating the expected standard error in horizontal

accuracy assessment (X, Y) and vertical accuracy assessment (Z) of the points [Konecny, 2008].

Some studies were also made to compare the results using the ground measurements. Recently, empirical tests have been applied by the German Society of Photogrammetry, Remote Sensing and Geoinformation (DGPF) by [Cramer, 2009] and [Cramer, 2010] on digital airborne cameras evaluation. The main object of (DGPF) tests is not to compare the performances of sensors first but to evaluate the sensors specific strengths. The DGPF project presents some findings, mainly focusing on geometrical topics. The test frame was based on cameras system DMC, UltraCam-x, quarto digital CAM, line scanning systems ADS40 and JAS-150 in a comparison with analogue cameras (RMK-Top15). The ground control points (GCP) are distributed in 7.4 x 4.7 km² area. The imaging data was acquired during 10 weeks in 6 different flight days. The flight campaign started at the beginning of July until the middle of September 2008. Additional flights were done in order to provide a reference for photogrammetrically derived surface models and multispectral land cover classifications (Leica ALS50 LiDAR, AISA+ and ROSIS hyper-spectral scanner). The results accuracy in this investigation was very similar for all sensor systems. RMSE computation is used for to evaluate these airborne digital cameras. The absolute accuracy RMSE in horizontal component was in the range of 0.25 pixel related to GSD and in vertical one in the range of 0.5 pixel.

The geometric assessment of ADS40 camera has been tested using RMSE computations by [Casella et al., 2008] and [Kocaman et al., 2007]. The ADS40 camera is a commercial example of the airborne three line scanner. Its particular sensor geometry requires new approaches and a specialization of methods and algorithms to solve the triangulation problem. The main goals of [Casella et al., 2008] study have been to investigate the geometric accuracy potential of the ADS40 camera under different network configurations, with different camera and trajectory models and different sets of additional parameters for self-calibration. Investigations have been performed by two independent research groups, that is the Institute of Geodesy and Photogrammetry (IGP), ETH Zurich, and the Geomatics Laboratory of the University of Pavia. The project contained three blocks of images with 2000 m, 4000 m and 6000 m flying heights with ADS40 camera. The test site was in Italy over the Pavia city. The average ground resolutions were approximately 20 cm, 40 cm, and 60 cm for the three blocks. 50 GCPs have been installed in the study area. The experimentations were performed with different numbers and

distributions of GCPs and with and without self-calibration procedures. In addition, two different trajectory models have been tested at the IGP, ETH Zurich. Also, direct georeferencing without the use of GCPs has been performed. The RMSE values, given in pixels, for planimetric and height, obtained with triangulation and self-calibration for the best cases of each block were (0.20 and 0.25 for 2000 m block), (0.20 and 0.30 for 4000 m block), and (0.13 and 0.24 for 6000 m block). The accuracy results of both groups are consistent and show significant improvements when self-calibration is performed.

Positional accuracy of airborne systems are not only dependent on the accuracy of individual components, for example, GNSS and INS. But also, it is dependent on variables such as the synchronization between different sensors, mounting platform stability, lens distortion, and weather conditions [Abd-Elrahman et al., 2001]. The evaluation of geometrical accuracy of 3D buildings produced by using LiDAR data and airborne imagery at the same time has been performed in [Zhang et al., 2012]. The geometrical construction is evaluated by determining the RMSE computation of tested points. This error is computed by finding corresponding centres of gravity of extracted building roofs. The solution of RMSE calculation based on centers of gravity is suggested by the German Association of Photogrammetry and Remote Sensing (DGPF) [Cramer, 2010]. Furthermore, in [Zhan et al., 2005], Euclidean distance between the centres of the mass of an extracted object and the corresponding object is used to measure positional accuracy. The computation of RMSE between centres of gravity of homologous surfaces that compose the tested and respectively the reference building is also suggested in [Zeng et al., 2013].

3.3.2.2 Quantitative assessment using computation of quality indices

A method for quantitative assessments of spatial accuracy and completeness for linear features is suggested and explored in [Tveite and Langaas, 1999]. The elements of the Buffer Overlay Statistics (BOS) method is shown in figure 3.3.

The geometric accuracy of a linear feature can be decomposed into two components:

- Firstly, positional accuracy can easily be given for well defined points on the feature (e.g. the end-points). For the rest of the linear feature, it is difficult to say anything about positional accuracy and to quantify it.

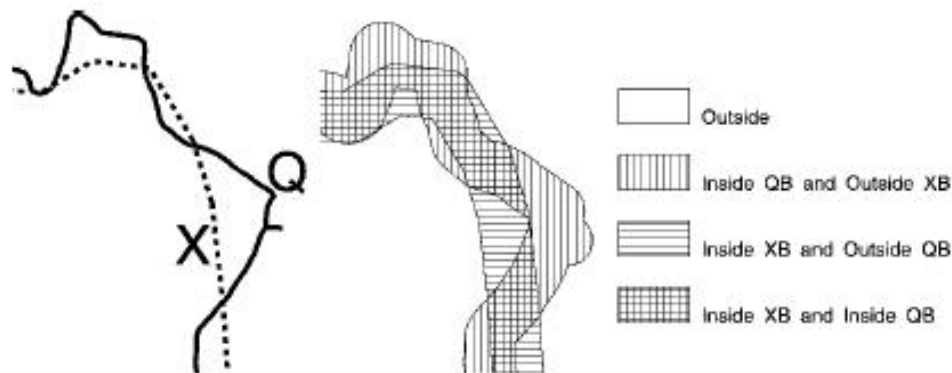


FIGURE 3.3: Elements of the BOS method suggested by [Tveite and Langaas, 1999].

- Secondly, to be able to say something about the accuracy of features, it is useful to talk about its shape fidelity as compared to a reference line. The shape similarity should be calculated by finding the superimposing of two line features.

The positional errors of line end-points can not be used to estimate the geometric accuracy of a line, even though they might give an indication of spatial bias. But for a large network of lines, the positional errors of these end points can be used as samples of the positional errors of the lines in the dataset. As such they can provide an indication of the positional accuracy of the line. A method was proposed in [Tveite and Langaas, 1999] in order to assess overall measures of accuracy and completeness of a line dataset relative to another line dataset of better quality using buffering. The method works by establishing a number of buffers of various sizes around the lines in both datasets and by comparing them (using overlay and statistics). The process was iterative. Figure 3.3 has been produced to visualize the above mentioned aspects of line data quality. The Buffer Overlay Statistics (BOS) method assumed homogeneous quality for the whole area of both the reference dataset and the dataset of unknown quality.

A method for quantitative assessments of completeness for 2D surfaces is suggested in [McKeown et al., 2000] and [McGlone and Shufelt, 1994]. This approach used well known quality indices, namely the detection rate ρd , the branch factor ρb and the quality rate ρq . [McKeown et al., 2000] and [Ragia, 2000] introduced mainly two approaches for quality evaluation of building models. Based on their

principle ideas, an approach has been developed in [Schuster and Weidner, 2003], taking the good aspects into account and combining them. This approach avoids, in their opinion, the single deficiencies, by using a combination of strategies and introducing supplementary quality measures. The 2D evaluation of the geometry of the surfaces is based on the comparison of surface areas in two building models (reference and test) and through the calculation of a set of quality indices. Figure 3.4 shows the relation between the reference surface area Ar and the tested surface area At .

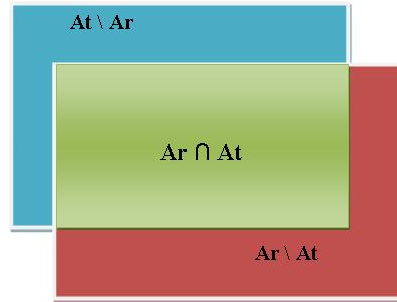


FIGURE 3.4: Relationship between reference area Ar and tested area At .

The first approach has been initiated by [McGlone and Shufelt, 1994] and developed by [McKeown et al., 2000]. This approach dealt with the evaluation of building extraction, in addition to other topographic objects like roads. The principle idea of their approach is to transform the evaluation of building models into the evaluation of a classification by discretizing the space in pixels (2D). The authors suggest to use specific quantities, namely the detection rate ρd , the branch factor ρb and the quality rate ρq . They are based on surface area comparison of Ar (area of reference polygon) and At (area of test polygon).

The detection rate ρd (equation 3.1) is the ratio between the intersection area between two planes and the reference plane. If the rate is close to 1, then the data will be of good quality.

$$\rho d = \frac{Ar \cap At}{Ar} \quad \rho d \in [0 : 1] \quad (3.1)$$

The quality rate ρq (equation 3.2) is the ratio between the intersection area between two planes (reference plane and test plane) and the union of two planes. If the rate close to 1 is then the data will be of good quality.

$$\rho q = \frac{Ar \cap At}{Ar \cup At} \quad \rho q \in [0 : 1] \quad (3.2)$$

The branch factor ρb (equation 3.3) is the the ratio of the part of the reference polygon which is not included in the polygon under study and the intersection of the two polygons. The factor is always positive and if the factor is close to zero, then the data will be of good quality.

$$\rho b = \frac{At \setminus Ar}{Ar \cap At} \quad \rho b \geq 0 \quad (3.3)$$

[McGlone and Shufelt, 1994] added the miss factor ρm (equation 3.4). The miss factor ρm is the ratio between the area of the tested plane that is not included in the plane intersection area and the intersection area between two planes. The factor is always positive and if it is close to zero then the tested model will be of good quality.

$$\rho m = \frac{Ar \setminus At}{Ar \cap At} \quad \rho m \geq 0 \quad (3.4)$$

The approach suggested by [Ragia, 2000] evaluates the building detection, the topology and the metric of building models using the quality rate ρq (equation 3.2) and the false alarm rate. The false alarm rate ρf (equation 3.5) is the ratio between the area of the reference plane not included in the plane intersection area and the reference plane. The factor is always positive and if it is close to zero then the tested model will be of good quality.

$$\rho f = \frac{At \setminus Ar}{Ar} \quad \rho f \geq 0 \quad (3.5)$$

[Schuster and Weidner, 2003] presented an approach for quantitative and qualitative evaluation of 2D surface models. The evaluation consists of an evaluation of the building detection, and an evaluation of the building reconstruction.

Any shift or rotation between the reference and the tested surface models will affect the intersection area between the surface models. But the same shift for a small or for a big building will not provide the same factors. The sensitivity of the previous indices regarding the effect of the building size, building shape, building shifts, rotations should be analyzed. In order to increase the influence of larger deviations between the reference and test sets on the quality measure, the weighted quality rate ρqw has been introduced in [Schuster and Weidner, 2003] and [Weidner, 2008]. Weighted quality evaluation was followed by distance transformation for each dataset and determination of connected components of the difference regions. Conversion from vector to raster format is necessary for computing the weighted quality rate ρqw . The calculation of this factor is based on the distance weighted transformation for each dataset (reference and test), as illustrated in figure 3.5 and expressed in equation 3.6.

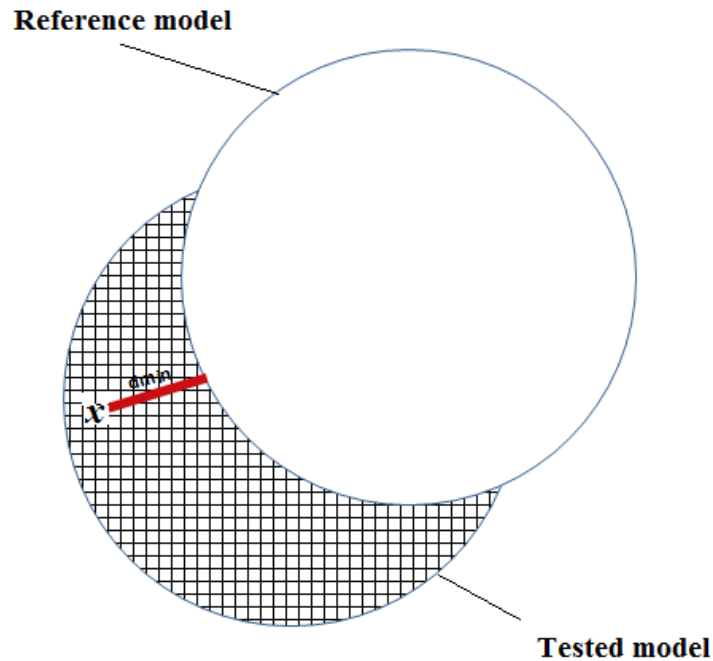


FIGURE 3.5: Distance weighted transformation for each 2D surface (x is the pixel element and d_{min} is the minimum distance between the pixel element and the tested surface).

$$\rho qw = 1 - \frac{A}{|SR \cap ST| + A} \quad \rho qw \in [0 : 1] \quad (3.6)$$

In equation 3.6, SR and ST are the surface of reference and surface to test respectively. A is defined as shown in equation 3.7.

$$A = \sum_{(x \in ST \setminus SR)} w(d(x, SR)) + \sum_{(x \in SR \setminus ST)} w(d(x, ST)) \quad (3.7)$$

In equation 3.7 $d(x, SR)$ and $d(x, ST)$ are the distance between the pixel x element and the surface SR and ST . It is given by the function 3.8.

$$d(x, S) = \inf\{\rho(x, s) : s \in S\} \quad (3.8)$$

Finally, the function 3.9 is the weighted function based on distances calculations.

$$w(d(x, S)) = \frac{1}{\Delta d} d(x, S) \quad (3.9)$$

Δd represents the pixel size of reference and test datasets.

Result assessments for 3D building models are mostly approached in a qualitative way. In [Meidow and Schuster, 2005] a grid of voxels in 3D has been presented to compute the volume and overlap voxels of volume. In the case of volume determinations these calculations and the corresponding data structures are rather complex and therefore extensive in terms of implementation and debugging. The suggested voxel-based approach circumvents these problems. The precision of the quality measures basically depends on the spatial resolution defined by the sizes of the volume cells. The voxel-based quality measures used have been introduced in the literature; [Ragia, 2000]. The resulting values of quality rate indices are decoded in gray level as shown in figure 3.6. A dark gray level means high quality rates whereas light grey values mean low quality rate indices. A test to compare the 2D and 3D shows that the quality rates of the 3D evaluation tend to be worse than those of the 2D evaluation.

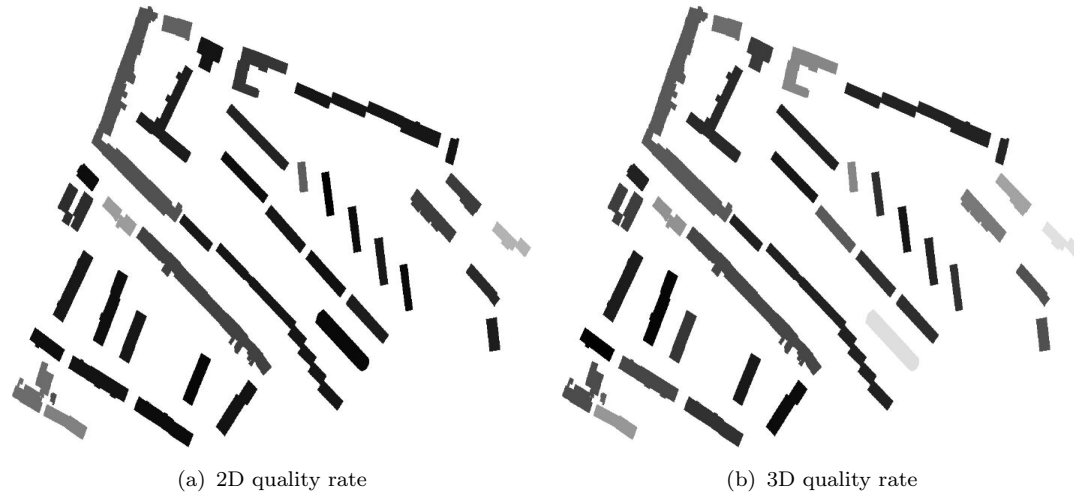


FIGURE 3.6: Quality rates represented in gray values (dark means high values); a) in 2D; b) in 3D [Meidow and Schuster, 2005].

3.4 Summary

Accuracy assessment calculations suppose that a reference model should be gained through an independent and more precise technique. Thus for gaining a reference model for precision calculations, it is appropriate to work on the same data, but to use a more precise method for the model creation. Also, the reference model can be extracted using the same technique but more accurate datasets. The multi-dimensional assessment approach has been applied to evaluate the building models produced in 1D, 2D, and 3D. point assessment gives an overall idea about the reliability of the reconstructed models. Surface assessment checks the superimposition of faces. 3D assessment compares the buildings in 3D through the comparison of their volumes intersection. The quality indices in 2D and 3D are useful for roughing out the detection quality but it should be completed by statistical computation such as RMSE.

Chapter 4

Developed approach for accuracy assessment

This chapter explains the strategies that have been followed to fulfil the aims and objectives of this research. The way to calculate intersections between lines and line with plane is presented. First, the proposed accuracy assessment is introduced. The 1D, 2D or 3D assessment approach allows highlighting the source of deviations in the tested buildings. The chapter is structured according to the aims and objectives outlined. This chapter mainly describes the multi-dimensional accuracy assessment approach developed for assessments in 1D, 2D and 3D.

4.1 Proposed multi-dimensional accuracy assessment approach

Studies on the evaluation of building models from photogrammetry or LiDAR are often confined by visual evaluation of the results or even a simple difference calculations like RMSE. A comprehensive evaluation in 3D is not trivial. We proposed a standard multi-dimensional approach for assessing the quality of 3D models of buildings in 1D, 2D and 3D. This part describes the 1D, 2D and 3D model accuracy assessment that will be applied to 3D building models. The inputs of our approach are reference and test models. The outputs in 1D assessment are the RMSE in X, Y, Z directions and test the 3D building model by applying

French legal text (arrêté sur les classes de précision). 2D and 3D quality indices are similar to those encountered in the evaluation of classifications (errors of omission, commission) and pass through the space discretization in pixels (2D) or voxels (3D) for measuring the degree of superposition of 2D or 3D objects. The originality of this approach was built on the fact that the models used as input are not only limited to raster format, but also extend to the vector format. It seems obvious that models defined in vector format are more faithful to reality than raster format. The flow of the proposed multi-dimensional assessment approach is shown in figure 4.1

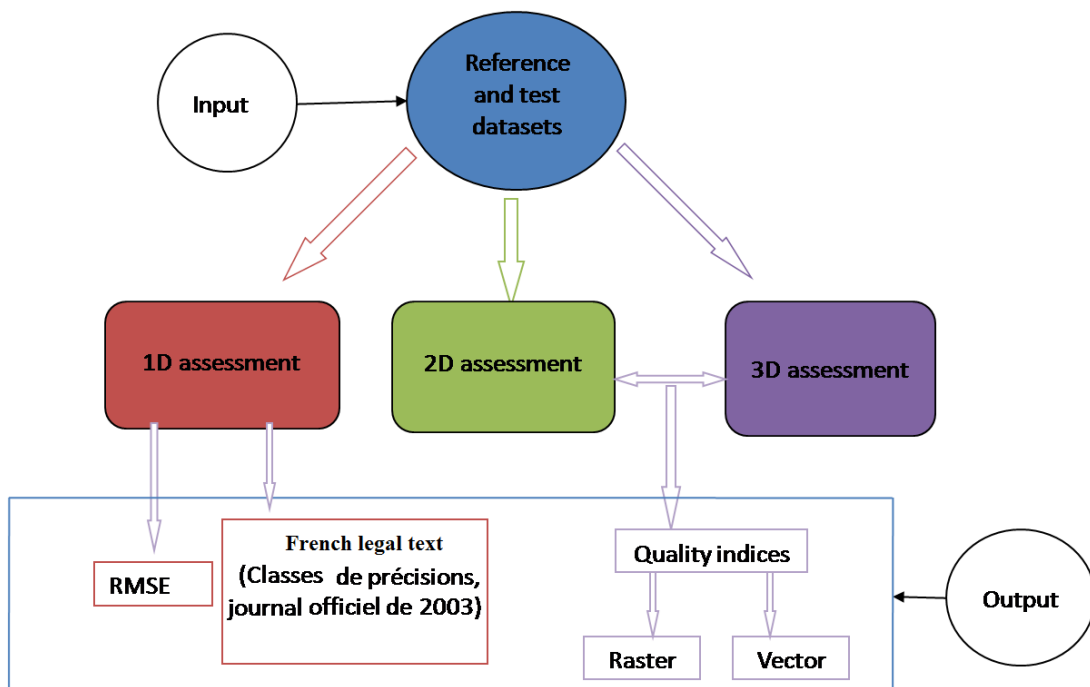


FIGURE 4.1: Multi-dimensional approach developed for the assessment of buildings reconstructed in 3D.

4.1.1 1D accuracy assessment

1D accuracy assessment can evaluate the output/product by comparing them points. Two methods are applied to compare two different 3D building models. The first one is done by computing RMSE errors based on the deviations between both models, in X , Y and Z directions. Deviations are not only calculated between homologous nodes, but also between centres of gravity of homologous planes that

compose the tested and respectively the reference building. Second method consists in applying the French legal text (arrêté sur les classes de précision) that is based on the instructions published in the Official Journal from October 30, 2003. This legal text suggests to define the accuracy classes for assessing the quality of different categories of survey works. It helps to determine if a survey work is acceptable regarding its quality and the precision requirements.

The RMSE calculation based on homologous nodes requires finding corresponding points. The correspondences are identified by finding the nearest neighbours of each pair of points from the reference model among those in the test model. Figure 4.2 shows these correspondences between the reference model (in black) and the test model (in red).

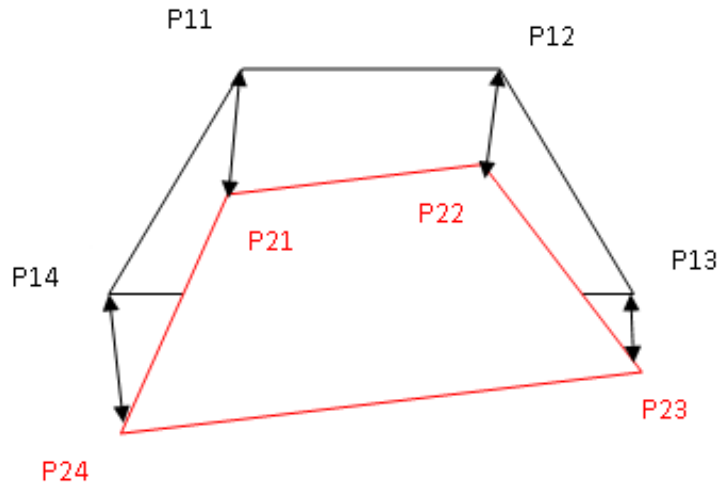


FIGURE 4.2: Correspondences between homologous nodes in the reference (in black) and the test (in red) models.

After the identification of matches, the RMSEs are computed in X, Y, and Z directions according to equations 4.1, 4.2, and 4.3.

$$RMSE_X = \sqrt{\frac{1}{N} \sum (X_{ref} - X_{test})^2} \quad (4.1)$$

$$RMSE_Y = \sqrt{\frac{1}{N} \sum (Y_{ref} - Y_{test})^2} \quad (4.2)$$

$$RMSE_Z = \sqrt{\frac{1}{N} \sum (Z_{ref} - Z_{test})^2} \quad (4.3)$$

Where $(X_{ref}, Y_{ref}, Z_{ref})$ are the coordinates of the nodes in the reference model and $(X_{test}, Y_{test}, Z_{test})$ are the coordinates of the nodes in the test model. N is the number of points.

This method is intuitive and simple but has practical limitations due to its assumption that every closest point in the reference model has as corresponding point in the test model. This assumption can easily fail when the two point sets are not coarse as shown in figure 4.3. In practice, the center of gravity point is more appropriate because with any distribution of vertices points, there is only one center of gravity as shown in figure 4.4. So, the RMSEs are computed between centres of gravity of homologous planes that compose the tested and respectively the reference building.

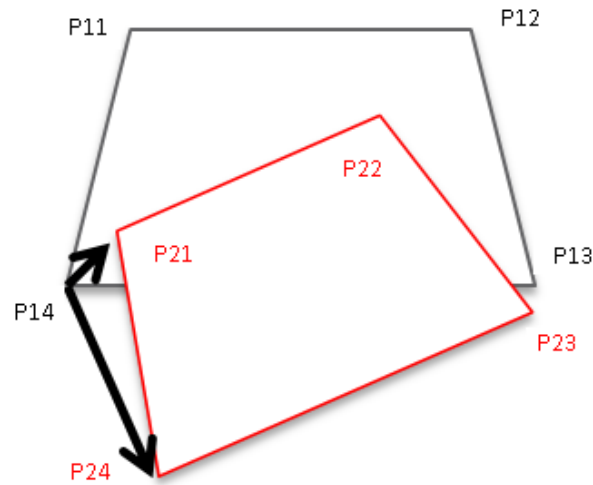


FIGURE 4.3: False corresponding points between the reference and the test models.

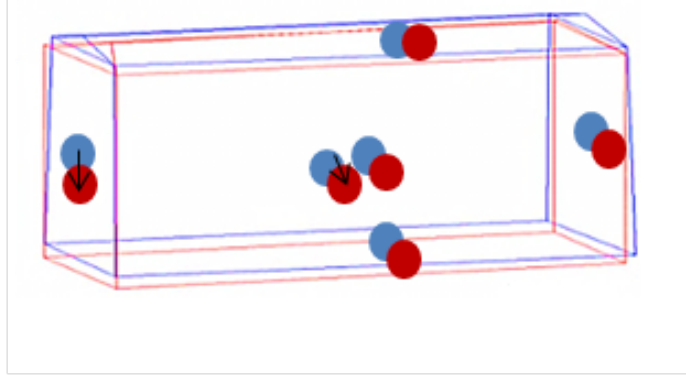


FIGURE 4.4: Corresponding centers of gravity points of reference (in blue) and test models (in red).

The coordinates of the center of gravity of any shape are found by averaging the X, Y, and Z coordinates of the vertices (see equations 4.4, 4.5, and 4.6). This formula also delivers the center of gravity of any set of points on the plane. Then, the RMSE can be calculated using equations 4.1, 4.2, and 4.3.

$$X_c = \left(\frac{x_1 + x_2 + x_3 + \cdots + x_N}{N} \right) \quad (4.4)$$

$$Y_c = \left(\frac{y_1 + y_2 + y_3 + \cdots + y_N}{N} \right) \quad (4.5)$$

$$Z_c = \left(\frac{z_1 + z_2 + z_3 + \cdots + z_N}{N} \right) \quad (4.6)$$

Where (X_c, Y_c, Z_c) are the coordinates of the centroid and (x_i, y_i, z_i) the coordinates of the vertices. N is the number of points.

Quality measures like the RMSE cause problems applied to complex buildings structures especially in the step of point matching.

The second method consists in applying a French legal text published in October 2003 (arrêté sur les classes de précision). The precision classification lies on three criteria (article 2.3.) to be simultaneously respected: a mean difference in position, the number of objects passing the first tolerance level, and the systematic nonconformity of objects beyond the second tolerance level. The bases of the legal text and the way to use it in different practical situations are presented in [Kasser, 2003]. A brief description of this legal text is given in the next paragraphs.

a- For a sample with N spatial objects, one computes the average difference between the observed values and the reference values. The mean difference in position is first subjected to a first tolerance defined in equation 4.7.

$$[xx] \left(1 + \frac{1}{2C^2} \right) \quad (4.7)$$

Where C is the security coefficient (coefficient de sécurité). $[xx]$ is the accuracy class (classe de précision).

b- The second condition at which the sample is subjected corresponds to an upper limit that only a certain number of points can exceed. This condition is given by equation 4.8

$$T = k[xx] \left(1 + \frac{1}{2C^2} \right) \quad (4.8)$$

Where k is a coefficient depending on the dimension in which the points are checked (one, two or three dimensions). k is equal to 3.23 (in 1D), 2.42 (in 2D), and 2.11 (in 3D).

The maximum number of points allowed to exceed this threshold is given by:

$$0.01N + 0.232\sqrt{N} \quad (4.9)$$

Where N is the total number of points forming the sample. When N is less than 5 points, no deviation greater than T is allowed (see table 4.1).

N	1 to 4	5 to 13	14 to 44	45 to 85	86 to 132	133 to 184	185 to 240	241 to 298	299 to 359	360 to 422
N'	0	1	2	3	4	5	6	7	8	9

TABLE 4.1: Maximum number of points allowed to exceed first threshold.

N' is the number of deviations allowed to exceed the threshold T for a sample of N elements.

c- No deviation is allowed to exceed the second threshold given in equation 4.10.

$$T = 1.5k[xx] \left(1 + \frac{1}{2C^2} \right) \quad (4.10)$$

The explanation of applying these thresholds to multiple datasets is shown in the next chapter.

4.1.2 2D accuracy assessment

Because many users are working with 2D forms such as roofs and facades, assessment solutions for 2D data must be considered. A method to evaluate 2D surface models is based on the comparison of 2D surfaces to accurate reference models. The 3D building models used in this work are decomposed in 2D planes composing the building. Our approach consists in comparing 2D surface areas from test models with 2D surfaces of reference models, by applying quality indices. The summary of these indices is shown in table 4.2. As mentioned in the state of the art, the quality indices are the detection rate (ρd), quality rate (ρq), miss factor (ρm), false alarm rate (ρf), branch factor (ρb), and weighted quality indices ($\rho q w$). Because we use them in a 2D assessment context, we will add the prefix "surface" and call them "surface detection rate", "surface quality rate", "surface miss factor", "surface false alarm rate", "surface branch factor", and "surface weighted quality indices". These indices are depending on the relations between the intersection or union areas of the reference and tested model. Satisfying results are reached when the values of ρd , ρq , and $\rho q w$ are close to 1, and the three others are close to 0. Surface areas as well as intersection and union computations will be presented in details in section 4.2.3. These quality indices are applied to roofs, faces, and footprint surfaces extracted from 3D building models.

We will consider the 2D surface models in raster as well as in vector format, because both formats have been encountered in the literature. It seems obvious that models defined in vector format are more faithful to reality than model in raster format. However, the confrontation of two vector models especially the calculation of intersection in 3D is more difficult.

The 2D assement based on the calculation of the quality indices of table 4.2 has been applied to the evaluation of photogrammetric data. This experiment has been published in [Mohamed and Grussenmeyer, 2011]. More information can be found in Appendix D. This method is applied for the comparison of 2D objects to accurate reference measurements. The comparison of data from Rollei medium format and UltraCam-X cameras has been done.

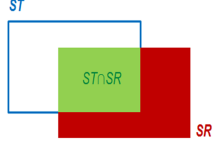


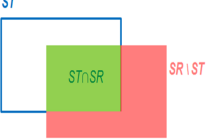

Index and equation	Explanation	
Surface detection rate: $\rho d = \frac{Ar \cap At}{Ar}$ $\rho d \in [0 : 1]$	$\rho d = 1$ means that the calculated polygon is perfectly superposed to the reference polygon.	
Surface quality rate: $\rho q = \frac{Ar \cap At}{Ar \cup At}$ $\rho q \in [0 : 1]$	$\rho q = 1$ means that parts which are common to both polygons are equal to the union of the two polygons.	
Surface branch factor: $\rho b = \frac{At \setminus Ar}{Ar \cap At}$ $\rho b \geq 0$	Ratio of the part of the reference polygon which is not included in the polygon under study and the intersection of the two polygons.	
Surface miss factor: $\rho m = \frac{Ar \setminus At}{Ar \cap At}$ $\rho m \geq 0$	Ratio of the part of the polygon being evaluated which is not included in a reference polygon and the intersection of the two polygons.	
Surface false alarm: $\rho f = \frac{At \setminus Ar}{Ar}$ $\rho f \geq 0$	Same numerator as previously, but compared to the area of the reference polygon.	
Surface weighted quality rate: $\rho q w = 1 - \frac{A}{ SR \cap ST + A}$ $\rho q w \in [0 : 1]$ $A = \sum_{(x \in ST \setminus SR)} w(d(x, SR)) + \sum_{(x \in SR \setminus ST)} w(d(x, ST))$ $d(x, S) = \inf\{\rho(x, s) : s \in S\}$ $w(d(x, S)) = \frac{1}{\Delta d} d(x, S)$	The preprocessing consists of a conversion from vector to raster followed by distance transformation for each data set and determination of connected components of the difference regions.	

TABLE 4.2: Quality indices used to evaluate surface areas of polygons.

The 2D assessment allows to assess the shape of the planes composing a building by superimposing them to the corresponding plane in the reference. However, it does not allow to check if the compared planes belong to the same frame. This can be done in the 3D assessment step.

4.1.3 3D accuracy assessment

Calculating uncertainties in a 3D model is not a trivial task. Considering a building as one object, volume comparisons seem to be more appropriate than surface areas comparisons. For assessing buildings in 3D, we developed an algorithm which allows to compare, in 3D, a test sample with its reference sample. We decided to work with quality indices inspired from the 2D assessment, but adapted to 3D. These modified quality indices are applied to 3D models in raster and vector data structure. These volumetric indices are the Volumetric detection rate ($V\rho d$), Volumetric quality rate ($V\rho q$), Volumetric miss factor ($V\rho m$), Volumetric false alarm rate ($V\rho f$), Volumetric branch factor ($V\rho b$), and Volumetric weighted quality indices ($V\rho qw$). These indices take into account the volume of the intersection as well as the union volume of two buildings. The computation of volumes in this work is done as well in raster as in vector format. It seems that models defined in vector format are more faithful to reality than raster format. However, raster format has also been taken into account, because it is often suggested in the literature.

The state of the art confirms difficulties in determining the volume of intersection of two 3D models in vector format [Meidow and Schuster, 2005]. The algorithm that is proposed for computing the volume of intersection is based on the extraction of vertices of the 3D intersection volume.

This work is a continuation of previous researches from our group (Photogrammetry and Geomatics Group) PAGE at INSA Strasbourg. The Group has already started a research field dealing with the assessment of planes detection of building roofs extracted from LIDAR data [Tarsha-Kurdi et al., 2008] and geometric facade models reconstructed from TLS data [Landes et al., 2012a]. Also, the evaluation of characteristic planes extracted from digital airborne images of two sensors (UltraCam-X and RolleiDB44) can be found in [Mohamed and Grussenmeyer, 2011].

This approach suggests a volume based comparison between a 3D building model and an accurate 3D reference model (figure 4.5). This principle is applicable as well to vector as to raster models. However, the calculation of the intersection shape requires to distinguish the models reconstructed in raster from those reconstructed in vector (section 4.2.4).

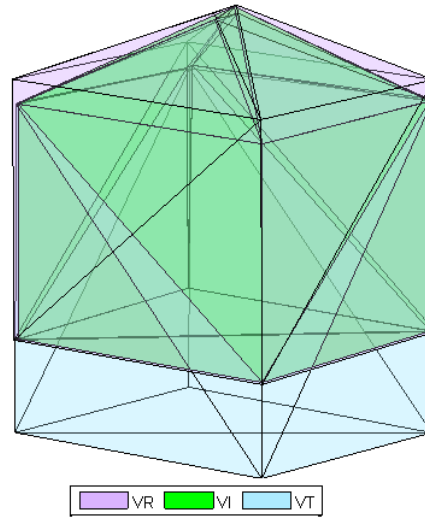


FIGURE 4.5: Comparison of 3D building models: volume of reference (VR, in pink), volume of the model to test (VT, in blue), volume of the intersection shape (VI, in green).

The volumetric indices developed in this work are explained here.

The modified detection rate $V\rho d$ is the ratio between the intersection volume (VI) between two models and the reference volume (VR). If the rate is close to 1, then the building model will be of good quality (see equation 4.11).

$$V\rho d = \frac{VR \cap VT}{VR} \quad V\rho d \in [0 : 1] \quad (4.11)$$

The modified quality rate $V\rho q$ is the ratio between the intersection volume between both models and the union of two volumes ($VR \cup VT$) (see equation 4.12). If the rate is close to 1 then the building model will be of good quality.

$$V\rho q = \frac{VR \cap VT}{VR \cup VT} \quad V\rho q \in [0 : 1] \quad (4.12)$$

The modified branch factor $V_{\rho b}$ is the ratio between the volume of the reference model not included in the volume of intersection ($VT \setminus VR$) and the intersection volume between two models (see equation 4.13). The factor is always positive and if the factor is close to zero, then the building model will be of good quality.

$$V_{\rho b} = \frac{VT \setminus VR}{VR \cap VT} \quad V_{\rho b} \geq 0 \quad (4.13)$$

The modified miss factor $V_{\rho m}$ is the ratio between the volume of the tested model that is not included in volume of intersection ($VR \setminus VT$) and intersection volume between two models (see equation 4.14). The factor is always positive and if the factor is close to zero then the building model will be of good quality.

$$V_{\rho m} = \frac{VR \setminus VT}{VR \cap VT} \quad V_{\rho m} \geq 0 \quad (4.14)$$

The modified false alarm rate $V_{\rho f}$ is the ratio between the volume of the reference model not included in the intersection volume and the volume of reference (see equation 4.15). The factor is always positive and if the factor is close to zero then the building model will be of good quality.

$$V_{\rho f} = \frac{VT \setminus VR}{VR} \quad V_{\rho f} \geq 0 \quad (4.15)$$

Like it has been done in section 4.1.2 for the 2D assessment steps, for increasing the influence of larger deviations between the reference and the test models on the quality evaluation the modified weighted quality rate $V_{\rho qw}$ is introduced. This index requires raster data structure. So, conversion of vector to raster format is necessary in the preprocessing of the modified weighted quality rate. Voxel (y) is the form for each assigned building model or building block. Followed by the distance transformation (dmin) for each dataset and determination of connected components of the different region, see figure 4.6.

$$V_{\rho qw} = 1 - \frac{V}{|VR \cap VT| + V} \quad V_{\rho qw} \in [0 : 1]. \quad (4.16)$$

VR and VT are the volume of the reference building and the volume of the test model respectively. V is defined by:

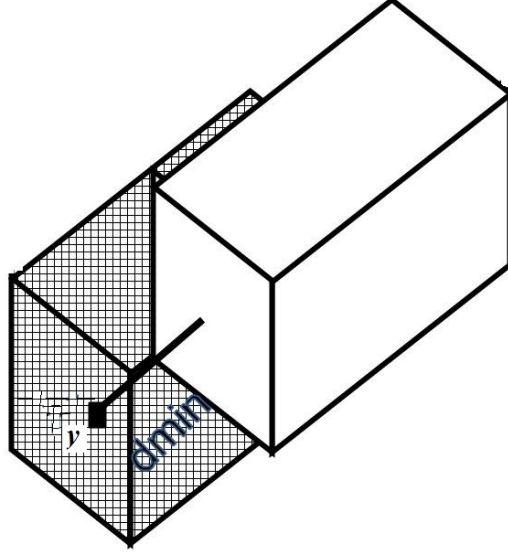


FIGURE 4.6: Distance transformation between 3D reference and test model (y is the voxel element and $dmin$ is the minimum distance between the voxel element and the tested model).

$$V = \sum_{(y \in VT \setminus VR)} w(d(y, VR)) + \sum_{(y \in VR \setminus VT)} w(d(y, VT))$$

The distances between the voxel element y and the tested model VT are given by the function:

$$d(y, VT) = \inf\{\rho(y, vt) : vt \in VT\} \quad (4.17)$$

and the weighted function based on distances calculation is given by:

$$w(d(y, VT)) = \frac{1}{\Delta d} d(y, VT) \quad (4.18)$$

Δd represents the voxel size chosen for the reference and the test model.

First experiments based on volumetric quality indices applied to 3D vector building models are presented in [Landes et al., 2012b]. Also, this approach has been used for assessing the 3D building models reconstructed from photogrammetry, LiDAR, and combination of them in [Mohamed et al., 2013].

The application of previously presented quality indices in 2D and 3D needs to remind several geometric computation.

4.2 Geometric computations

The operation of determining the union and intersection of areas (or volumes) when two models must be compared is a topic of geometric computation. This section describes the algorithms leading to calculate union and intersection of areas/volumes which occur when a model to be assessed is compared to a reference model. First of all, it is necessary to recall some basic concepts, such as the definition of points, lines and planes in the 3D space. Appendix E summarizes some of these definitions. Intersection between line and plane entities are presented her.

4.2.1 Intersection of two lines in the same plane

A 3D line can be represented by the intersection of two planes or by the connection of two points. To find the intersection point of two lines, get a view of lines to ensure that they intersect in a point. A line can be described by two points ($P1, P2$) or by a point and a vector (P, V). In which P is point of the line and V is the vector of the line.

The expression of 2 lines $L1$ and $L2$ in vector algebra is presented in equations 4.19 and 4.20.

$$L1 = P1 + aV1 \quad (4.19)$$

$$L2 = P2 + bV2 \quad (4.20)$$

where $P1$ is a point which belongs to $L1$ and $P2$ to $L2$. $V1$ and $V2$ are the direction vectors for each line.

If we assume that the lines intersect, we can look for the point on $L1$ that satisfies the equation for $L2$. This gives us this equation to solve.

$$P1 + aV1 = P2 + bV2 \quad (4.21)$$

Now rewrite it like this.

$$aV1 = (P2 - P1) + bV2 \quad (4.22)$$

Now take the cross product of each term with $V2$. This will make the term with b dropped out because the cross product of the vector $V2$ and it self ($V2 \times V2$) is equal to zero.

$$a(V1 \times V2) = (P2 - P1) \times V2 \quad (4.23)$$

let's denote

$$V = \text{cross}(V1, V2), \quad W = \text{cross}((P2 - P1), V2) \quad (4.24)$$

If the lines intersect at a single point, then the resultant vectors on each side of this equation must be parallel, and the left side must not be the zero vector. Check should be applied in order to make sure that it is true. Once one has checked this, it is possible to solve for a by taking the magnitude of each side and dividing. If the resultant vectors are parallel, but in opposite directions, then a is the negative of the ratio of magnitudes. Once a is found (equation 4.29), the intersection point $M1$ can be calculated by going back to $L1$ equation.

$$a = W/V, \quad M1 = P1 + aV1 \quad (4.25)$$

Lets take it with another side,

$$bV2 = (P1 - P2) + aV1 \quad (4.26)$$

Now take the cross product of each side with $V1$. This will make the term with a drop out because the cross product of the vector $V1$ and it self ($V1 \times V1$) is equal to zero.

$$b(V_2XV_1) = (P_1 - P_2)XV_1 \quad (4.27)$$

let's denote,

$$W_1 = \text{cross}(P_1 - P_2, V_1), \quad W_2 = \text{cross}(V_2, V_1) \quad (4.28)$$

Then,

$$b = W_1/W_2, \quad M_2 = P_2 + bV_2 \quad (4.29)$$

For checking the results, we must check that M_1 is equal to M_2 .

4.2.2 Intersection of a line with a plane

In this section, the problem of intersecting lines and planes is presented. As shown in Appendix E, the equation of the plane is defined as $AX + BY + CZ + D = 0$ and the normal vector n of the plane is $= [A \ B \ C]$. The intersection of the line L with the plane ρ (if it exists) is at point. So, the problem is to search about this point. Also, the line is defined by two points or a point and a direction as $p = P_1 + aV$. As shown in figure 4.7, the intersection point is a point on the line and it should also satisfy the plane equation.

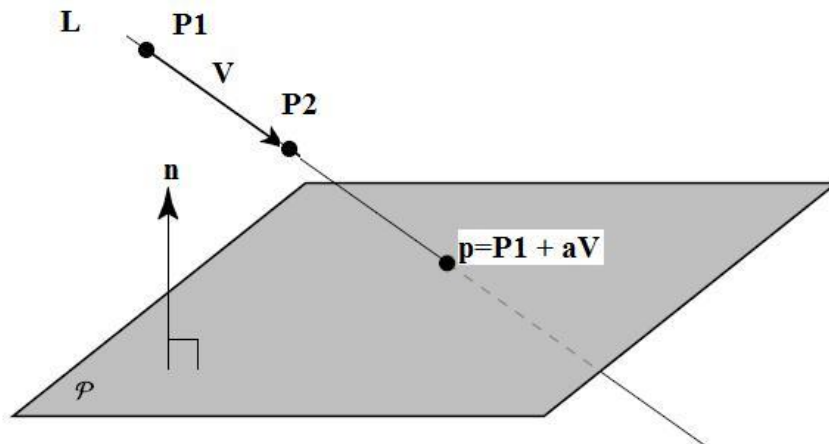


FIGURE 4.7: Intersection of a line with a plane.

Then, we replace by substitute the equation of line at the point of intersection p in plane equation 4.30.

$$A(P1x + aVx) + B(P1y + aVy) + C(P1z + aVz) + D = 0 \quad (4.30)$$

And solve for the parameter a :

$$a = \frac{-(AP1x + BP1y + CP1z + D)}{AVx + BVy + CVz} \quad (4.31)$$

By putting the equation in vector format

$$a = \frac{-(n.P1 + D)}{n.V} \quad (4.32)$$

Where $n.V$ is the scalar product of the plane normal and the line direction; if this value is equal to 0, then the line and the plane are parallel. If the line is in the plane, then there are an infinite number of intersections, and if the ray is not in the plane, there is no intersections. So, a check should be done first in order to know if the line and the plane intersect. After computing (a) value, computing the intersection coordinates point requires simply substituting the computed value back into the line equation $p = P1 + aV$.

The multi-dimensional assessment approach developed in 2D and 3D requires to calculate intersection shapes. For this reason, the concepts used for calculating surface areas and volumes must be presented. Also the way we calculate the intersection of polygons in 2D and polyhedron in 3D is detailed. Since buildings may be reconstructed in raster and in vector format, both cases are considered in the next sections.

4.2.3 Area computation

4.2.3.1 Raster format (pixel)

Recap of area computation

The most common method used to calculate areas in raster format is to sum the number of pixels which compose the polygon of interest. This can be done for a polygon stored as a simple raster or for a vector polygon which is converted into a grid of pixels.

To calculate the area using the raster concept the following steps must be considered:

Step 1: the three steps of plane fitting are applied to the 3D vertices points as explained in Appendix E; a) input 3D points that are needed to be fitted by a plane; b) calculate plane parameters containing this data (basis and normal vector for the plane); c) project this 3D data to the plane. Also, one of the aims of this step is to transform the coordinates of vertices points from global to local coordinates system. The aim of this process is to obtain a polygon in 2D space.

Step 2: a pixel-based 2D surface is generated using 2D vertices points of the polygon. A two dimensional grid is built with a pixel size. The distributions of pixels in X and Y directions are reconstructed by the following equations:

$$pixel_in_X - direction = (Xmax - Xmin)/pixel_size \quad (4.33)$$

$$pixel_in_Y - direction = (Ymax - Ymin)/pixel_size \quad (4.34)$$

Where $(Xmin, Ymin)$ and $(Xmax, Ymax)$ are the minimum and maximum values of the coordinates of vertices points. This method of rasterization generates pixels with the same size in X and Y direction. The choice of the size of the pixel in X and Y direction is based on the resolution of the input data for building extraction, the result accuracy of computation and time needed to process this data. In this experiment, the size of a pixel element has been set to 0.3 m in two directions. At this stage, the 2D polygon is described by a regular grid as shown in figure 4.8.

Step 3: This step consists in recording the pixels which are inside the 2D polygon using Matlab built in function (*in-polygon*). Finally, the surface area of the polygon is calculated by taking the sum of all pixels located inside the polygon (equation 4.35).

$$Area_raster_polygon = total_number_of_pixels * area_of_single_pixel \quad (4.35)$$

The rasterization process for a 2D polygon is illustrated in figure 4.8.

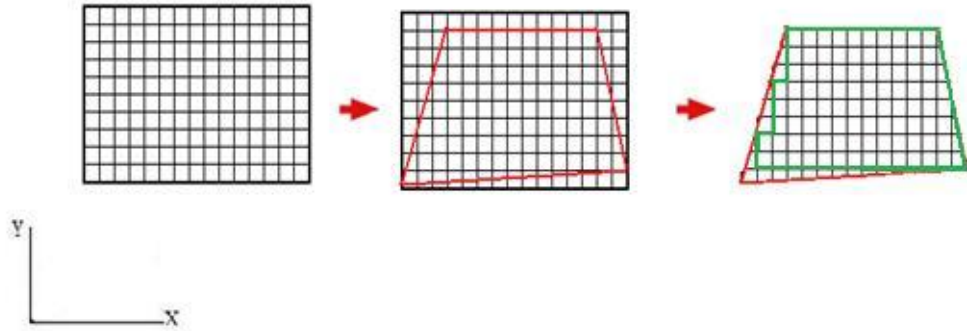


FIGURE 4.8: Representation of the rasterization process of 2D polygon.

Intersection area calculation

The area of intersection between two polygons (one of them describing the reference and the other one the test model) is computed after defining the pixels which belong to the overlapping area. In the same way, the intersection area is obtained by multiplying the number of pixels located in it, by the area of a pixel. Using rasterization might lead to a loss or a surplus in the pixels located on the boundary of the polygon. This affects the computation of the real area. Figure 4.8 shows the real surface with red colour and the computed surface with green colour.

4.2.3.2 Vector format

Recap of area computation

For the area computation of a polygon described in vector form, the formula based on Green's theorem [O'Rourke, J, 1998] is used and given in equation (4.36).

$$A = \frac{1}{2} |\sum_{k=1}^n X_k Y_{k+1} - X_{k+1} Y_k| \quad (4.36)$$

Where n is the number of nodes, $X_{n+1} = X_1$ and $Y_{n+1} = Y_1$. X and Y are the coordinates of vertices points of the polygon numbered in ascending order.

Intersection area computation

An algorithm has been developed for calculating the intersection area of 2 vector polygons in 2D, which covers all potential cases of intersections. It operates in two steps: the detection of the points located inside the polygons and the detection of

line intersections.

Step1: classification of the points located inside the polygons

Let's consider two vector polygons, drawn in red and black, as shown in figure 4.9-a. Points 3 and 5 are called "inside points". In figure 4.9-b, all points of the red polygon are classified as inside points, when it is compared to the black polygon. Matlab built-in function (*point-in-polygon*) provides a simple and commonly used technique for inside points detection, and works as follows. Assuming the polygon is defined by n points in an array P , the algorithm computes the summation of angles between the query point and every pair of points defining each edge of the polygon (i.e. the angle is formed by the $P[n]$ point, query point, and $P[n + 1]$). If this summation computes to 2π (or near 2π within some tolerance), then the point is inside the polygon. If the summation computes to zero (or near zero) then the point is outside the polygon.

Step2: detection of points at the intersection of lines

For example, in figure 4.9a, the point of intersection between line (2, 3) and line (5, 6) is an "intersection point" to consider, as well as the intersection point of lines (4, 3) and (5, 8). However, the intersection between lines (4, 3) and (6, 7) is not an intersection point to consider. That's why it must be checked if the intersection point lies on the edges of both polygons. This check is done by computing the distance between the intersection point and the two end points of the line. If the maximum of the two distances is shorter than the edge length, the point of intersection belongs to the edge. Then the resulting intersection area can be calculated based on the coordinates of its vertices (see equation (4.36)). The resulting intersection shape can therefore be created by joining the vertices by segments. Figure 4.9-c gives another example of the detection of intersection points.

After computing the surface areas, the 2D quality indices can be calculated. In 3D, we have to calculate volumes. This is the topic of the next section.

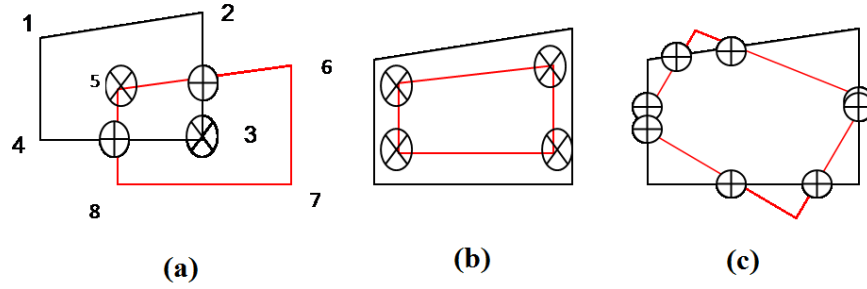


FIGURE 4.9: Intersection area calculation for vector polygons in 2D.

4.2.4 Volume computation

4.2.4.1 Raster format (voxel)

Recap of volume computation

The volume calculation of buildings defined in raster format is easier than in vector format. A voxel is defined as a pixel in 3D. A voxel-based 3D building model can be generated based on the 3D vertices points describing the building model. A three dimensional grid is built with a cell size. The number of voxels in X, Y, and Z dimension is calculated by the equations 4.37, 4.38, and 4.39.

$$\text{Voxels_in_X_direction} = (X_{max} - X_{min}) / \text{voxel_size} \quad (4.37)$$

$$\text{Voxels_in_Y_direction} = (Y_{max} - Y_{min}) / \text{voxel_size} \quad (4.38)$$

$$\text{Voxels_in_Z_direction} = (Z_{max} - Z_{min}) / \text{voxel_size} \quad (4.39)$$

Where $(X_{min}, Y_{min}, Z_{min})$ and $(X_{max}, Y_{max}, Z_{max})$ are the minimum and maximum values of the coordinates of the vertices points. *voxel_size* represents the voxel size. Choice of size of voxel in X, Y and Z directions as in 2D is based on the input data for building extraction, the result accuracy of computation and the time needed to process this data. In this experiment, the voxel element size as been set to $0.3 * 0.3 * 0.3$ m. Thus, the 3D building is decomposed in voxels, like a 3D array (figure 4.10). Finally, the volume of each voxel located inside the building is summed to calculate the total volume (equation 4.40).

$$Volume = total_number_of_voxels * volume_of_single_voxel \quad (4.40)$$

The voxelization process for a 3D building model is illustrated in figure 4.10.

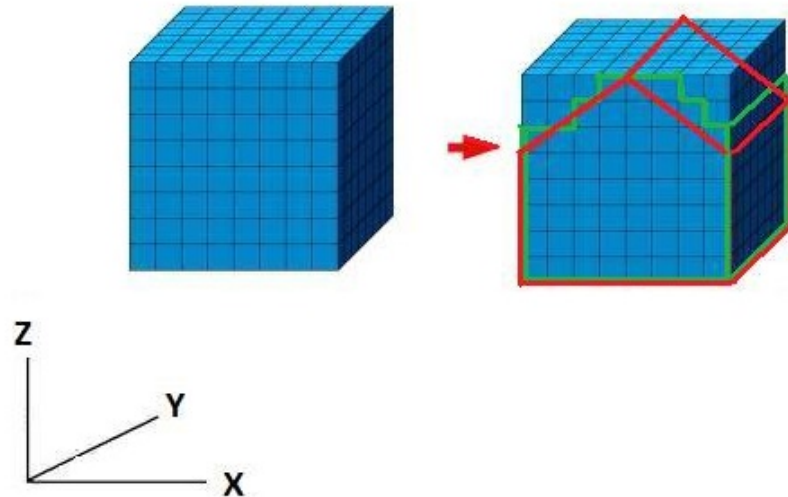


FIGURE 4.10: Representation of the voxelization process of 3D building.

Intersection volume calculation

The volume of intersection between two 3D models (one of them describing the reference and the other one the test model) is computed after defining the voxels which belong to the overlapping volume. In the same way, the intersection volume is obtained by multiplying the number of voxels located in it, by the volume of a voxel. Using voxelization might lead to a loss or a surplus in the voxels located on the boundary of the 3D intersection shape. This affects the computation of the real volume (figure 4.10).

4.2.4.2 Vector format

Recap of volume computation

In order to compute the volume of 3D objects defined as vector models, one has to solve two tasks. Firstly, we must determine the convex hull of the given boundary. Then, we must calculate the volume of the resulting 3D polyhedron.

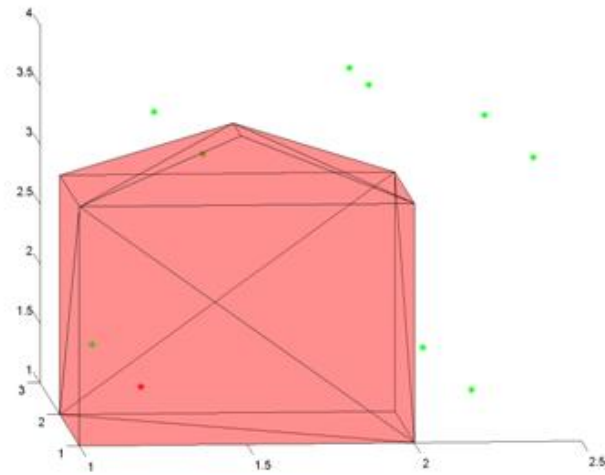
A convex hull is the boundary of a closed convex surface (mesh) generated by applying Delaunay triangulation on the vertices points. In three dimensions, the convex hull corresponds to a closed polyhedron. Convex hull calculation is a hard process in computational geometry [Barber et al., 1996]. A large class of algorithms that compute the exact volume of a convex object is based on triangulation methods [Büeler et al., 2000].

For instance, the result of convex hull calculation for a gable roof building is shown in figure 4.11-a. The convex hull of a set of points in two or three dimensions is given by application of a Matlab built-in function (*convhulln* in 3D) as presented in equation 4.41. These functions use meshed objects for storing and displaying polyhedra. The faces of such polyhedra are triangles.

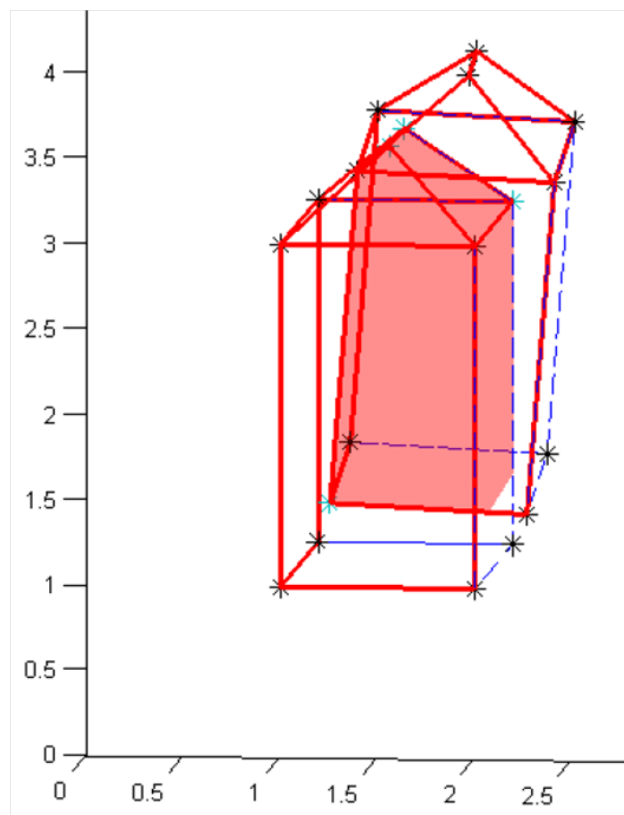
$$[K \quad V] = \text{convhulln}(x, y, z); \quad (4.41)$$

K is represented by a boundary triangulated 3D object. Each row of the matrix K represents a triangle. The volume, V , bounded by the 3D convex hull can optionally be returned by *convhulln*.

In a first step, the meshed model is computed. It is defined by the input points. The sum of the volumes composing the meshed model equals to the volume of the convex object (figure 4.11-a).



(a)



(b)

FIGURE 4.11: Calculation of convex hull (a) and the intersection shape (b).

Intersection volume calculation

The calculation of the volume of intersection between two 3D models reconstructed

in vector format provides more accurate results than in raster format, but it is also much more complicated. We propose an algorithm allowing to simplify this process. It is applicable on basic building shapes, which are assumed to have faces composed of planes. Our method consists of extracting the vertices of the shape describing the 3D intersection volume. The flowchart in figure 4.12 shows the main steps of the developed process.

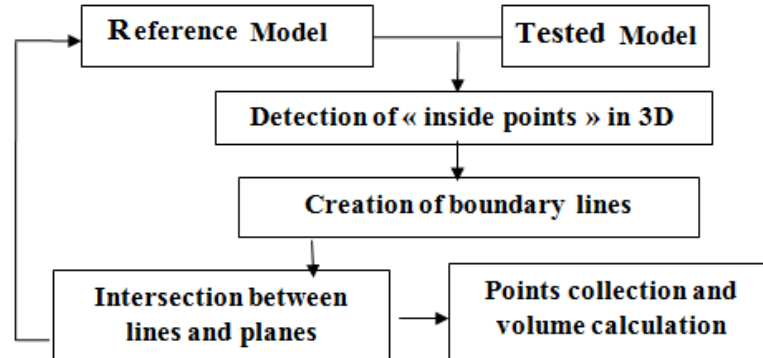


FIGURE 4.12: Main steps of the process leading to the calculation of the intersection volume of two vector building models.

The process consists of three main steps and is inspired from the process developed in 2D (section 4.2.3.2).

Step 1: detection of inside points

This step aims at searching about vertices of the reference points located inside the model to assess. The points that are inside the reference model are located on the positive side of the plane normals of all of its faces. The result of this process is shown in Figure 4.11(a) where inside points are in red and outside points in green color. These inside points represent only a part of the points describing the 3D intersection shape.

Step 2: creation of boundary lines and their intersection with planes

The second group of points describing the intersection shape can be determined by calculating the intersection of the lines composing the reference model with all planes that are composing the model to assess. This process can be achieved firstly by separating the edge lines of each plane of the reference model. Then, the duplicated lines (for instance a line describing the connection between a roof and a facade is decomposed into 2 same lines) are cancelled in order to avoid the creation of duplicates intersection points. After that, the intersections of all lines with all

planes of the model to assess are calculated. In order to check if the resulting point is located on the edge line (and not on the extension of the edge line) and simultaneously belongs to the face of model to assess, two tests must be made. Firstly, we test if the point is placed on the edge line by distance computation as shown in section 4.2.3.2. A second test is achieved by looking for the "points inside a polygon" in 2D (in the frame of the intersected plane), as explained in section 4.2.3.2.

Step 3: repetition of steps 1 and 2

Steps 1 and 2 are repeated by replacing the reference model by the model to assess for the process leading to the edge line creation. Then the intersection between lines of the model to assess with all the planes of reference model is performed. Finally, as a result of these steps, the coordinates of vertices of the intersection shape are determined and the volume of this shape can be calculated. Figure 4.11(b) shows the intersection shape (filled with red color) obtained by the intersection of a reference model and a test model.

4.3 Summary

The multi-dimensional approach developed for assessing the accuracy of 3D building models has been introduced in this chapter. Some principles that help in geometric computations have been presented. This chapter described also the algorithms leading to calculate union and intersection of areas/volumes.

In 1D assessment, the solution proposed for assessing of 3D building models assessment are the RMSE calculation in X, Y, Z directions and the application of a French legal text (arrêté sur les classes de précision).

In 2D, specific surface quality indices have been chosen, which require that 2D polygons composing the building are compared to their reference polygon. This requires the calculation of the intersection area of 2D polygons. It has been presented in this chapter, as well for raster as for vector building models.

The process performed in 2D has inspired the process developed for assessing buildings in 3D. Therefore, volumetric quality indices have been developed. They

require to compare two models in 3D. Although some assumptions are made regarding the shape of the buildings, the complex calculation of the 3D intersection shape has been detailed (for vector and raster models). It seems obvious that models defined in vector format are more faithful to reality than in raster format. However, the confrontation of two vector models is more difficult, especially when determining the volume corresponding to the intersection of two models.

The multi-dimensional approach is planned to be applied to 3D building models in both raster and vector data structure. The application of our multi-dimensional approach on real datasets will take place in the next chapter.

Chapter 5

Application of the approach on multiple datasets

In this chapter the study area and datasets used in the study are presented. Also the results of the processing chain applied on these datasets are detailed. Finally, the results of the accuracy assessment of the generated 3D models are exposed. The results of the accuracy evaluation are presented in three sections entitled, 1D assessment, 2D assessment, and 3D assessment. Analysis of the results of the experiments is achieved and followed by a discussion about the benefits and drawbacks of the developed approach.

5.1 Test site and data used

This test area is situated in the center of the city of Strasbourg, France. It is characterized by different kind of building shapes. These buildings can be used for testing the models extracted from photogrammetry, LiDAR, and combination of both.

For this test site, multiple datasets are distributed. Digital aerial images from UltraCam-X (4 images), Rollei (5 images) and frame Zeiss LMK (6 images) have been acquired on this area. The test area is therefore visible in multiple images. Table 5.1 shows brief characteristics of the photogrammetric data.

Sensor	Ultracam-X	RolleiDB44	Zeiss LMK
Acquisition date	2007	2004	1998
Focal length (mm)	100.500	80.553	211.03
Ground resolution (cm)	16	16	24
Pixel size (μm)	7.2	9	30
Flying height (m)	2300	1450	1700
Overlap %	65	60	70
Base (m)	527	265	556

TABLE 5.1: Brief characteristics of photogrammetric datasets.

Figure 5.1 shows the distribution of large format UltraCam-X images in vertical strip, frame Zeiss LMK images in horizontal strip, and medium format RolleiDB44 images in horizontal strip. In order to appreciate the high resolution of the airborne imagery data, examples of reduced format of UltraCam-X, RolleiDB44, and Zeiss LMK images have already been shown in figures 5.2, 5.3, and 5.4.

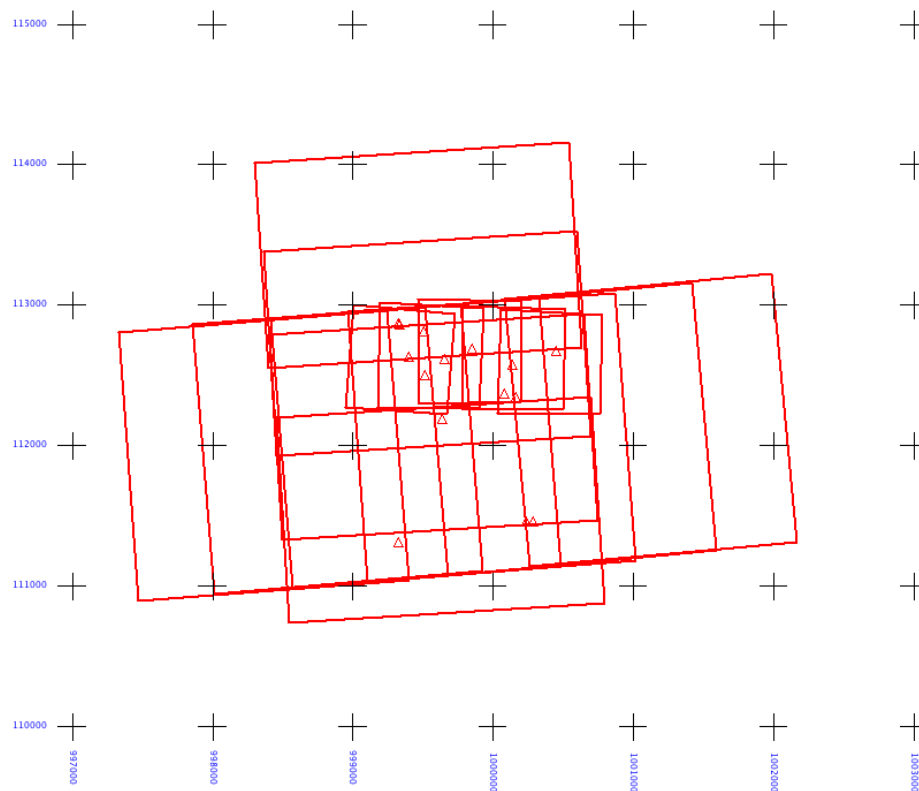


FIGURE 5.1: Distribution of UltraCam-X (large format in vertical strip), RolleiDB44 (medium format in horizontal strip), and Zeiss LMK images (large format in horizontal strip).



FIGURE 5.2: Reduced format of one image of UltraCam-X camera (Strasbourg City).



FIGURE 5.3: Reduced format of one image of RolleiDB44 camera (Strasbourg City).

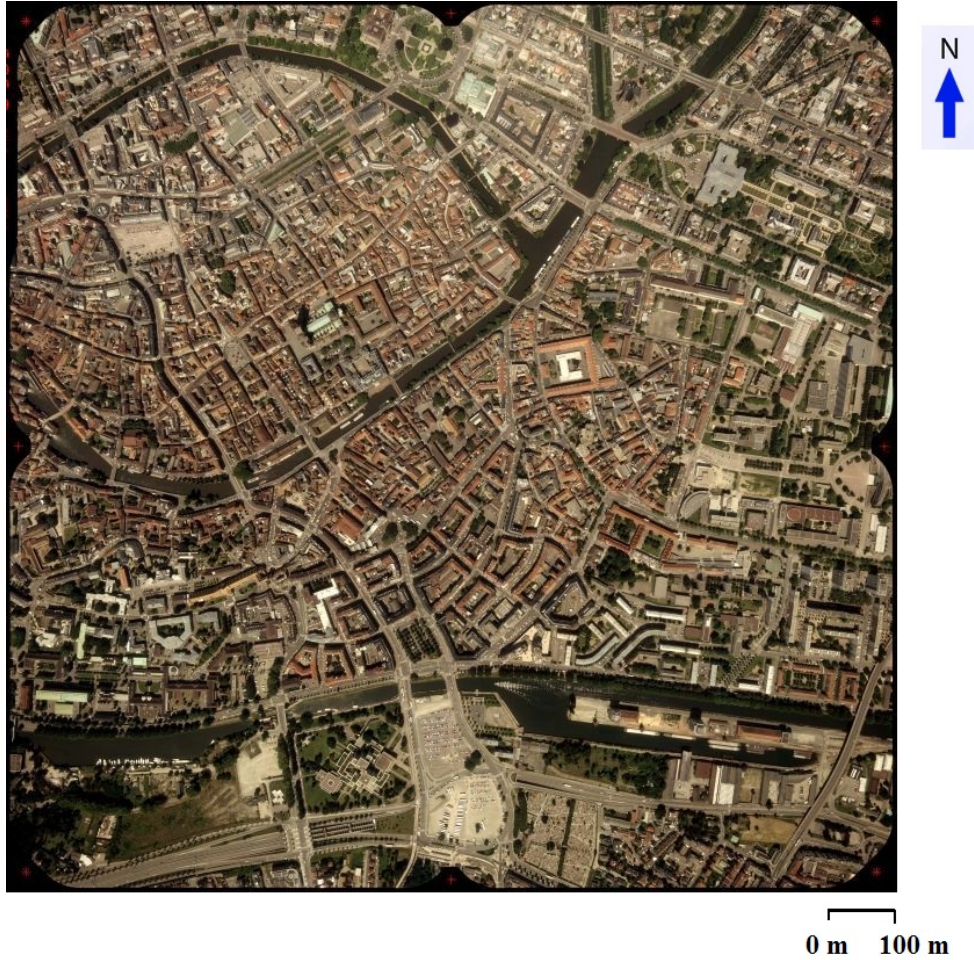


FIGURE 5.4: Reduced format of one image of Zeiss LMK camera (Strasbourg City).

On other hand, Airborne Laserscanner (ALS) dataset of the same zone are provided. LiDAR data is captured in 2004 with a TopScan / Optech ALTM 1225 system. It covers an area of 4 *km* long and 1920 *m* wide with a swath of 640 *m*. Table 5.2 shows brief characteristics of the LiDAR data.

Acquisition date	2004
Flying height (<i>m</i>)	1440
Density of points	1.3 points/ m^2
Pulse frequency	25 <i>kHz</i>
LiDAR system	TopScan / Optech ALTM 1225

TABLE 5.2: Brief characteristics of the LiDAR datasets.

5.2 Data collection and image processing results

Three blocks of 15 images from UltraCam-X, RolleiDB44 and Zeiss LMK cameras are available for the same zone in Strasbourg - France, figure 5.1. A set of 4 images in one vertical strip, the UltraCam digital camera provides an image format of 9420 pixels (long track) by 14430 pixels (cross track). The pixel size of the images is $7.2 \mu\text{m}$ while it is 16 cm in object space. A set of 5 images in one strip has been acquired with the RolleiDB44 medium format digital camera provides an image format of 4080 pixels (long track) by 4075 pixels (cross track). The pixel size of the images is $9 \mu\text{m}$ while it is 16 cm in object space. The Zeiss LMK camera provides a image format of 7680 pixels (long track) by 7680 pixels (cross track). The pixel size of the images is $30 \mu\text{m}$ while it is 24 cm in object space. 14 ground control points have been measured in 2011 with GNSS systems.

The all images to be used are digital aerial photographs with unknown imaging orientation parameters. The orientation of the images has been performed using the KLT software package in order to compute exterior orientation parameters. The camera information has been taken from the calibration sheet given by the camera owner. The exterior orientation approximations were achieved by bundle block adjustment. The RMSE of 14 GCPs in X, Y, Z directions are less than 9 cm.

The standard deviations of exterior orientation parameters from UltraCam-X, RolleiDB44, and Zeiss-LMK images are presented in tables 5.3, 5.4, and 5.5.

Image No	1	2	3	4
σ_{X_0} (m)	0.572	0.556	0.552	0.567
σ_{Y_0} (m)	0.818	0.768	0.771	0.820
σ_{Z_0} (m)	0.409	0.225	0.169	0.319
σ_{Ω} (deg)	0.022	0.020	0.020	0.022
σ_{Φ} (deg)	0.015	0.014	0.015	0.015
σ_{κ} (deg)	0.004	0.003	0.003	0.004

TABLE 5.3: Accuracy of exterior orientation parameters for UltraCam-X images.

Image No	1	2	3	4	5
σ_{X0} (m)	2.184	1.362	0.810	0.973	1.988
σ_{Y0} (m)	1.351	1.385	0.956	0.964	1.474
σ_{Z0} (m)	0.229	0.268	0.166	0.188	0.209
σ_{Omega} (deg)	0.052	0.054	0.037	0.038	0.057
σ_{Phi} (deg)	0.087	0.054	0.031	0.038	0.078
σ_{Kappa} (deg)	0.012	0.007	0.004	0.005	0.008

TABLE 5.4: Accuracy of exterior orientation parameters for RolleiDB44 images.

Image No	1	2	3	4	5	6
σ_{X0} (m)	0.256	0.227	0.214	0.214	0.255	0.252
σ_{Y0} (m)	0.176	0.161	0.155	0.155	0.160	0.177
σ_{Z0} (m)	0.189	0.124	0.078	0.080	0.128	0.194
σ_{Omega} (deg)	0.005	0.005	0.005	0.005	0.005	0.005
σ_{Phi} (deg)	0.008	0.007	0.007	0.007	0.007	0.008
σ_{Kappa} (deg)	0.002	0.002	0.002	0.002	0.002	0.002

TABLE 5.5: Accuracy of exterior orientation parameters for Zeiss-LMK images.

The tables 5.3, 5.4, and 5.5 show that the results SD of exterior orientation parameters for RolleiDB44 are worse than those of the UltraCam-X block and Zeiss-LMK. The higher accuracy corresponds to blocks with high overlaps where the lower accuracy is formed for blocks with lower overlaps. So, a large image overlap provides a strong block geometry. This positively influences the accuracy of exterior orientation parameters as proved in [Cramer, 2001].

5.3 Preparation of the reference and test models

5.3.1 Preparation of the reference models

The 3D reference buildings model have been reconstructed based on the photogrammetric processing of images acquired with UltraCam-X stereopairs because of their high quality compared to the other datasets. The pixel size is $7.2 \mu m$. After relative and absolute orientation of the images, the RMSE of 14 GCPs is less than 9 cm. The method of building models extraction will be explained in section 5.3.2. Figure 5.5 shows the 3D building models reconstructed from UltraCam-X images. Once the reference buildings models are reconstructed, they are used to test buildings reconstructed with other datasets and with several reconstruction

algorithms. The data used for creating the test models are :

- Airborne images from Zeiss LMK,
- LiDAR data only,
- Combination of airborne images from UltraCam and LiDAR data.

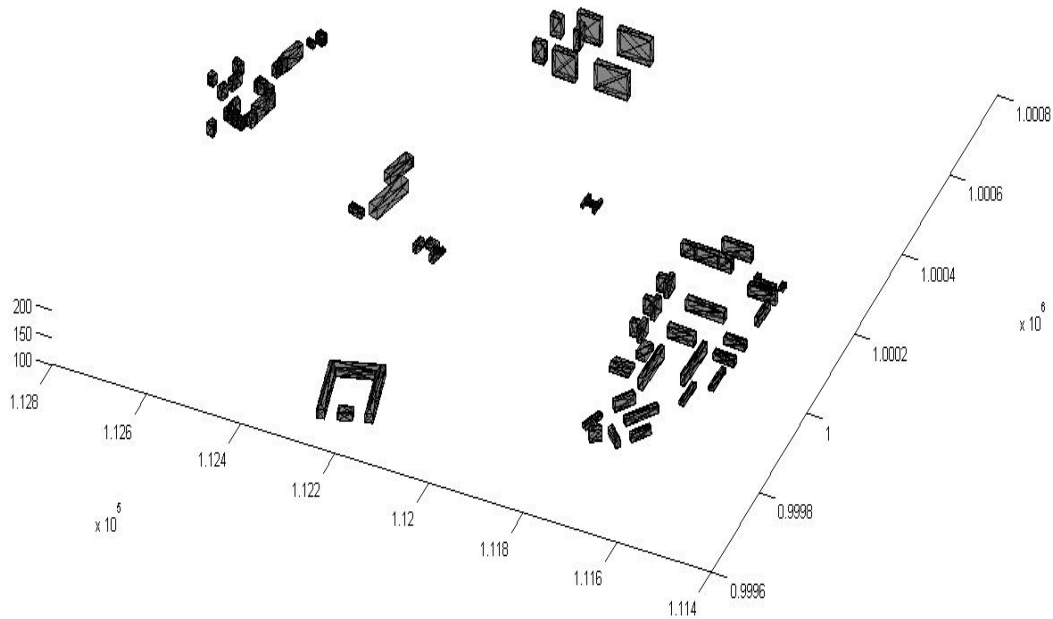


FIGURE 5.5: Reference 3D building models reconstructed from UltraCam-X images.

5.3.2 3D building models reconstructed from digital images

3D building modeling in the city using the technology of photogrammetry is one of the most important topics in photogrammetry. There are many different methods of 3D building modeling and many different applications for 3D city models. Some active works in the photogrammetric, remote sensing and computer vision communities are focused on the 3D building modeling approaches [Hammoudi and Dornaika, 2011]. There are two main approaches for constructing buildings in 3D: raster based and vector based approaches. In raster approaches,

the buildings are represented by uniform grids with (location and height) associated attributes. In vector approaches, the buildings are represented by linear features such as lines and surfaces.

The vector format for describing 3D geometry is considered to be more appropriate for urban areas modeling than the raster representation. 3D information for the elements of the building, roof elements, walls, and footprints are necessary for the modeling of a building. The aerial images give the advantage to cover wide areas at the scale of a city. In addition, roof models are visible from aerial images. However, architectural details such as windows, door or balconies may not be visible in aerial images [Amat et al., 2010]. The geometry of objects (roofs, walls, and footprints) can be extracted from multiple images. The flowchart of the semi-automatic approach developed for reconstructing a building based on stereo-images and used in this work is depicted in figure 5.6.

The first step of building reconstruction is roof digitizing. Then, the projection of these points onto the ground is done in order to obtain footprints. Finally, planes of faces are reconstructed. The manual work in this method is the points digitizing. Then the projection of roof points onto the ground for defining the wall is done automatically. The reconstruction approach is based on the assumption that:

- (a) every solid object can be described by a decomposition of its boundaries;
- (b) the walls are vertical and reach either the ground or another surface of the constructed model.

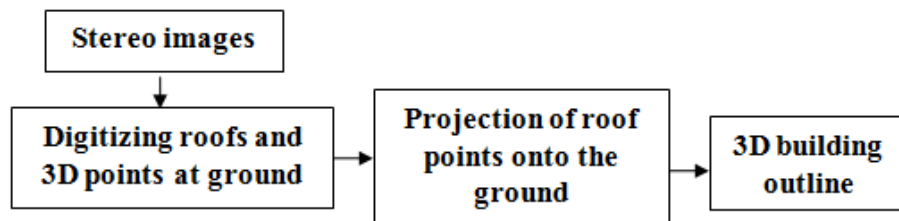


FIGURE 5.6: Flowchart of 3D building modeling from aerial images.

In this work, we restrict our building models to simple polyhedral models, as illustrated in figure 5.7.

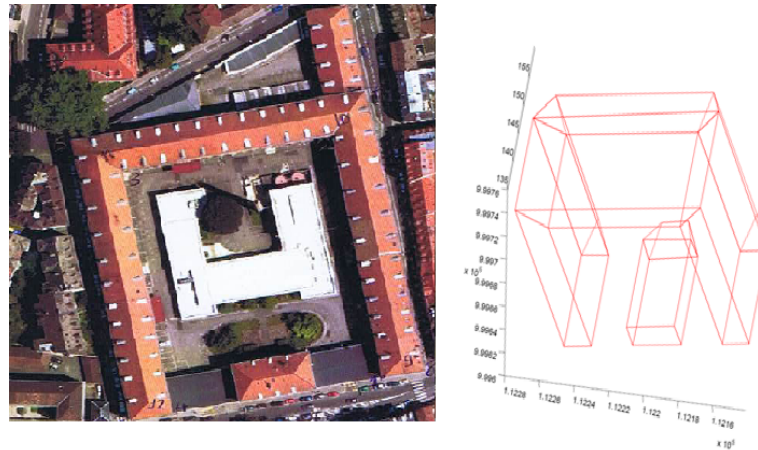


FIGURE 5.7: Example of a 3D building model reconstructed from aerial images.

Figure 5.8 shows the results of 75 samples of building models reconstructed in the test site, by using this semi-automatic solution. The reconstructed buildings in the test site have three types of roofs (flat, hip and gable roof).

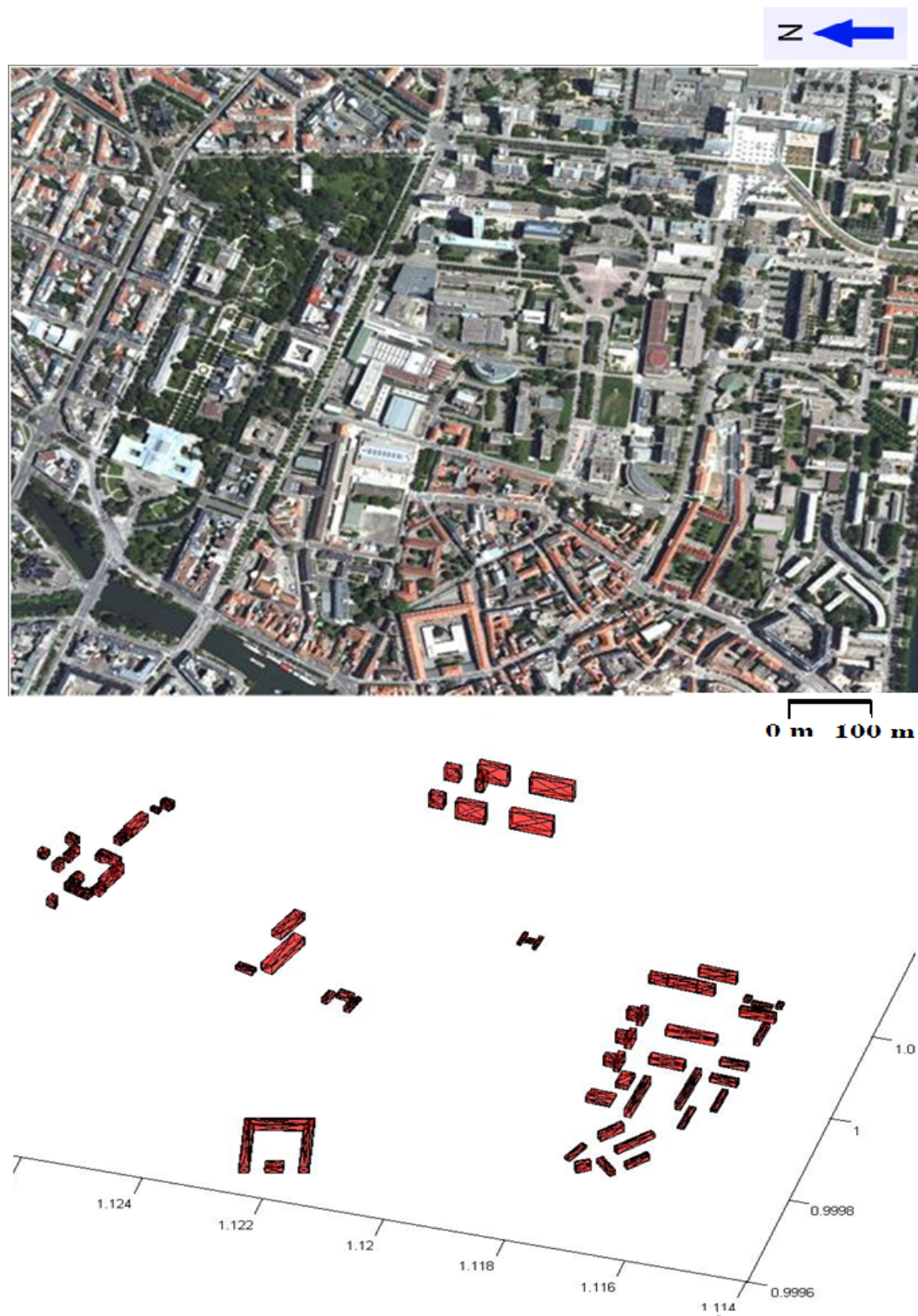


FIGURE 5.8: A part of an aerial UltraCam-X image (above) over Strasbourg city and 3D building reconstruction results from UltraCam-X stereopairs (below).

5.3.3 3D buiding models reconstructed from combination of LiDAR and airborne imagery datasets

Another way to create 3D buildings in photogrammetry consists in combining the airborne UltraCam-X images and LiDAR datasets. The semi-automatic method has been developed by [Zhang et al., 2011] is based on the complementarities of airborne LiDAR and airborne imagery (UltraCam-X). This work results from the cooperation of our group with Wuming Zhang, Key Laboratory of Remote Sensing Science, School of Geography, Beijing Normal University, in Beijing, China. The approach consists in 4 steps as shown in figure 5.9.

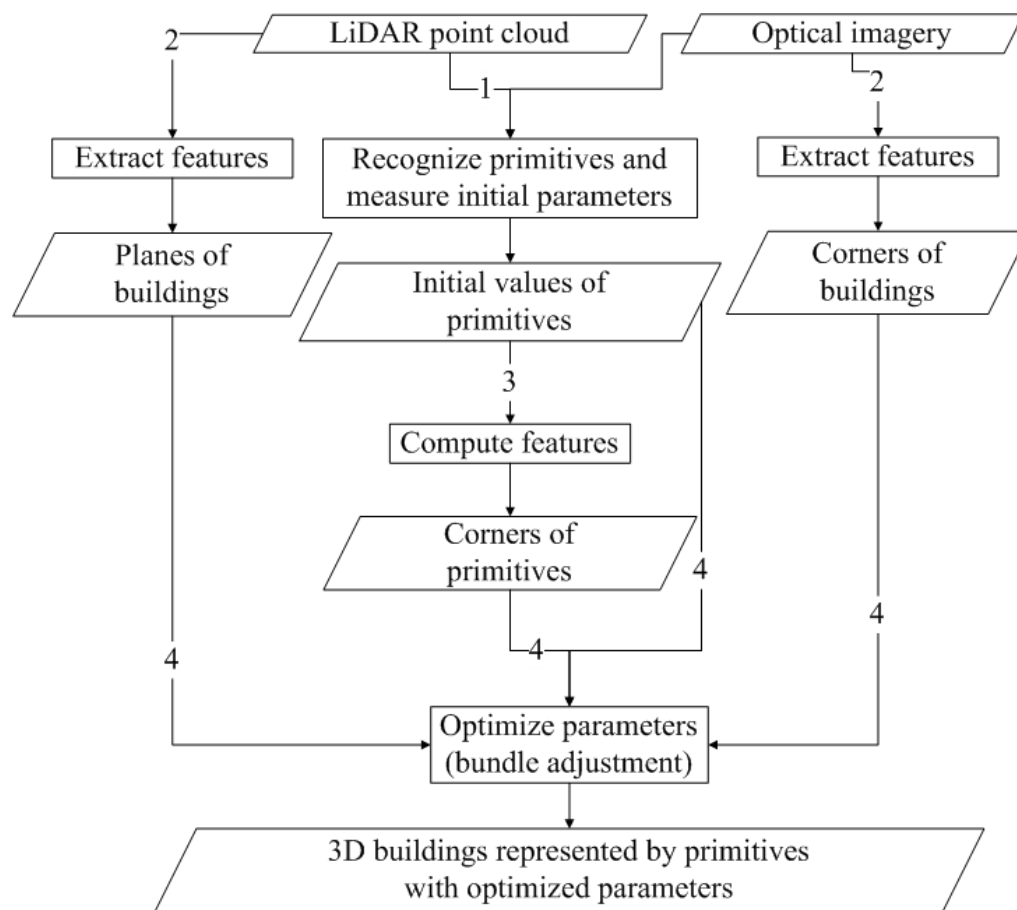


FIGURE 5.9: Flowchart of the reconstruction process using LiDAR data and aerial images [Zhang et al., 2011].

It works as follows:

1- Extraction of primitives and estimation of initial parameters;

With the help of airborne imagery and LiDAR point clouds of the same area, the building is decomposed into several primitives. Then the primitives parameters are measured manually on LiDAR point clouds and airborne imagery, such as length, width, height, and orientation. The parameter values can be used as fixed values (constraints) or initial values in the following optimization procedure.

2- Selection of features primitives on the imagery;

Corners are selected on the airborne imagery, and planes are selected in the LiDAR point clouds. These features will be used as observed values in the following optimization procedure.

3- Optimisation of the values of the primitive parameters by constraints;

Based on the type and parameters of primitives, the 3D coordinates of the features primitives, such as 3D coordinates of the corners, can be calculated. They will be used as computed values in the next optimization procedure.

4- Representation of 3D building models based on optimized primitives;

When a 3D building model has correct shape and is located in the correct place in 3D space, then 3D building can be represented by these primitives with the optimized parameters.

This method has been applied to 26 buildings of the test site. Figure 5.10 shows the results of their 3D reconstruction.

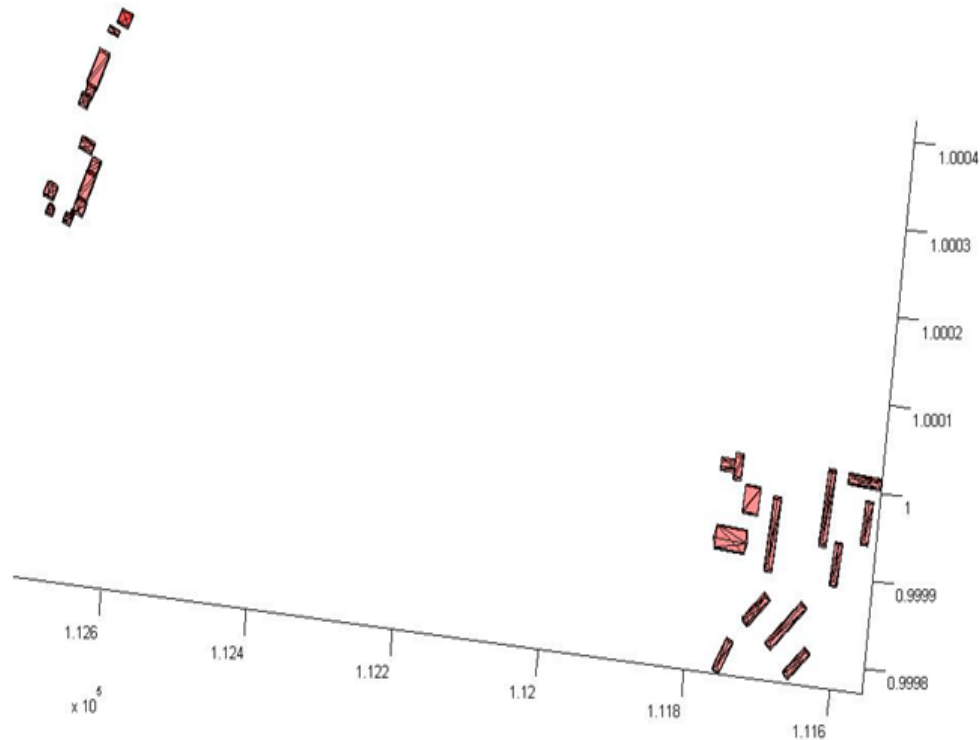


FIGURE 5.10: 3D building reconstruction combination of LiDAR and airborne images.

5.3.4 3D building models reconstructed from LiDAR dataset

In this part, a model-driven building reconstruction method using airborne LiDAR data is presented. This method has been carried out by Yong Xiao from the Chinese Academy of Sciences (China). This semi-automatic reconstruction process comprises 3 steps.

- 1- At first, building points are segmented in order to isolate building roofs (see figure 5.11-a);
- 2- Then, a topological graph is constructed for the roof to recognize shapes of buildings. More details are given in [Verma et al., 2008];
- 3- Once simple roof types are determined, building models are reconstructed with predefined models. Outlines of the buildings are first estimated with the minimum area bounding rectangle while the other key vertices and segments are obtained through the roof-topology graph.

Figure 5.11 shows the result of roof reconstruction in figure 5.11-a and 3D building reconstruction in figure 5.11-b.

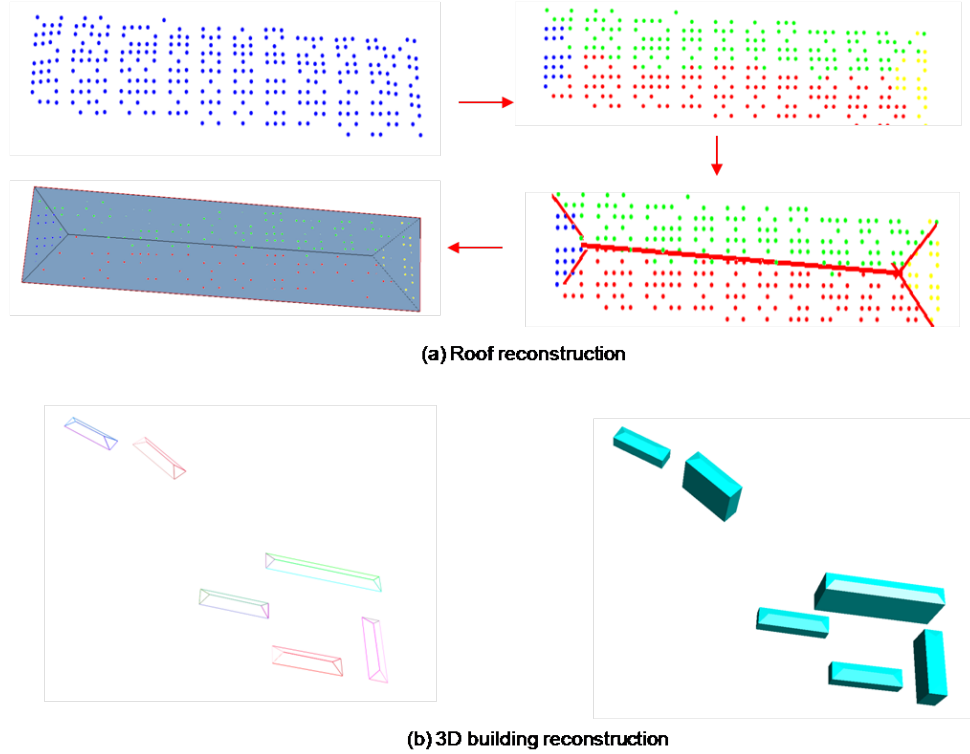


FIGURE 5.11: 3D building reconstruction from LiDAR data; a) Roof reconstruction; b) 3D building reconstruction

The three methods presented in the three previous sections have been used to reconstruct 75 samples of 3D models from aerial images, 26 samples of 3D models from LiDAR and aerial images, and 8 samples of 3D models from LiDAR datasets. In the next part, we assess the 3D reconstructed building models, by applying the proposed multi-dimensional assessment approach.

5.4 Assessment of building models

In this section, results of accuracy assessments are presented after application of the proposed multi-dimensional assessment approach.

5.4.1 1D accuracy assessment

5.4.1.1 Using RMSE computations

The calculation of RMSE for analyzing the precision of the complete 3D building is an interesting solution. RMSE is computed based on the deviations between reference and test models, in X, Y and Z-directions. Deviations are calculated between homologous nodes, as well as between centers of gravity of homologous planes that compose the tested and respectively the reference building. As already mentioned in section 5.3.1, the reference building models are the models reconstructed from UltraCam-X. Table 5.6 and 5.7 present the RMSE results obtained for nodes describing the buildings reconstructed with the three kinds of datasets (exclusively aerial images; exclusively LiDAR data; combination of both). The RMSE obtained for the datasets in both methods (nodes and centers of gravity) are approximately the same. Only the RMSE in X-direction for the models reconstructed from LiDAR datasets is not the same. Tables in appendix A show the RMSE for each building model obtained by considering homologous nodes and centers of gravity of homologous planes.

3D building models based on	RMSE (m)			SD (m)		
	X	Y	Z	X	Y	Z
Airborne images [75 samples]	0.25	0.32	0.51	0.12	0.18	0.25
Combination of airborne images and LiDAR datasets [26 samples]	0.66	0.69	1.18	0.39	0.56	0.24
LiDAR dataset [8 samples]	0.97	1.10	1.13	0.39	0.14	0.10

TABLE 5.6: RMSE results based on homologous nodes.

3D building models based on	RMSE (m)			SD (m)		
	X	Y	Z	X	Y	Z
Airborne images [75 samples]	0.21	0.26	0.50	0.16	0.26	0.43
Combination of airborne images and LiDAR datasets [26 samples]	0.50	0.48	0.94	0.30	0.29	0.26
LiDAR dataset [8 samples]	0.64	0.99	1.00	0.34	0.17	0.09

TABLE 5.7: RMSE results based on gravity centers of homologous planes.

The models reconstructed from aerial images give better results than the other datasets. The models reconstructed from combination of LiDAR and aerial images give high RMSE in Z-direction. Worse results are obtained for models reconstructed with LiDAR data only. If we consider these results and the reconstruction methods presented for creating 3D buildings, we would be tempted to say that the technique used to create the buildings from Zeiss LMK images only is the most effective. However the error budget is not only composed of errors due to the reconstruction algorithm, but also of errors coming from the raw data. For instance, low point clouds density and errors due to the georeferencing of the LIDAR and the imagery data affect also the final results.

5.4.1.2 Using the French legal text published in 2003 (arrêté sur les classes de précision)

Another way to test the reconstructed models consists in applying the French legal text (arrêté sur les classes de précision) published in the Official Journal from October 30, 2003. This legal text gives instructions about accuracy classes applicable to several categories of survey works. In the case of surveying points assessments, we must calculate deviation between the points to check and the reference points (equation 5.1).

$$e = \sqrt{(X_{ref} - X_{test})^2 + (Y_{ref} - Y_{test})^2 + (Z_{ref} - Z_{test})^2} \quad (5.1)$$

Where $(X_{ref}, Y_{ref}, Z_{ref})$ are the coordinates of the reference points and $(X_{test}, Y_{test}, Z_{test})$ are the coordinates of the test points. Then calculate the mean difference is calculated (EmoyPos) in equation 5.2.

$$E_{moypos} = \frac{1}{N} \sum_{i=1}^N e_i \quad (5.2)$$

Where N is the number of points in the sample.

Choice of parameters for the application of the standard model (modèle standard).

To calculate the threshold allowing to validate or not the reconstructed models, one must choose a few parameters:

- An accuracy class (called "classe de précision"). We take here $[xx] = 0.50 \text{ m}$ (according to the characteristic of input data),
- A security coefficient (coefficient de sécurité) C , which corresponds to the minimum ratio of accuracy classes of references and test datasets. Here we take the value $C = 1$ as mentioned in chapter 4. It means that the control points (nodes of the reference models) have been observed with the same precision as the test points (nodes of the test models).
- A factor k , which is equal to 2.11 as given by table.1 of the legal text (Article 5, page. 18547) for an assessment of 3D points (X,Y,Z coordinates).

Calculation of thresholds with the standard model ("modèle standard")

- First threshold

The average difference in position should stay under:

$$0.50 \left(1 + \frac{1}{2 \cdot 1^2}\right) = 0.75 \text{ m}$$

- Second threshold

The second threshold at which the sample is compared corresponds to an upper limit that only a certain number of points N' is allowed to exceed:

$$2.11 * 0.50 \left(1 + \frac{1}{2 \cdot 1^2}\right) = 1.58 \text{ m}$$

- Third threshold

This threshold value is never exceeded and is the same formula as above, increased by a factor of 1.5.

$$1.5 * 2.11 * 0.50 \left(1 + \frac{1}{2 \cdot 1^2}\right) = 2.37 \text{ m}$$

By comparing these thresholds with the 75 buildings reconstructed from airborne imagery datasets (Zeiss LMK), we can find that 48 buildings of these reconstructed

buildings are validated. While the models reconstructed from LiDAR and combination of LiDAR with imagery datasets (UltraCam-X) are not acceptable regarding the required "precision class" (classe de précision). This is due to the quality of the raw data, since both datasets containing imagery data seem to provide better results than the dataset based on LiDAR data exclusively. However, further assessment analysis is necessary. This is done in the next sections.

5.4.2 2D accuracy assessment

As explained in chapter 4, the 2D assessment consists in evaluating surface areas of planes composing the 3D building model. For that, the test planes are compared to reference planes and quality indices are calculated based on their surface areas. These quality indices are applied to all building models reconstructed in our work. The reference surface models are the surfaces of buildings reconstructed from UltraCam-X.

5.4.2.1 Models reconstructed from airborne imagery dataset

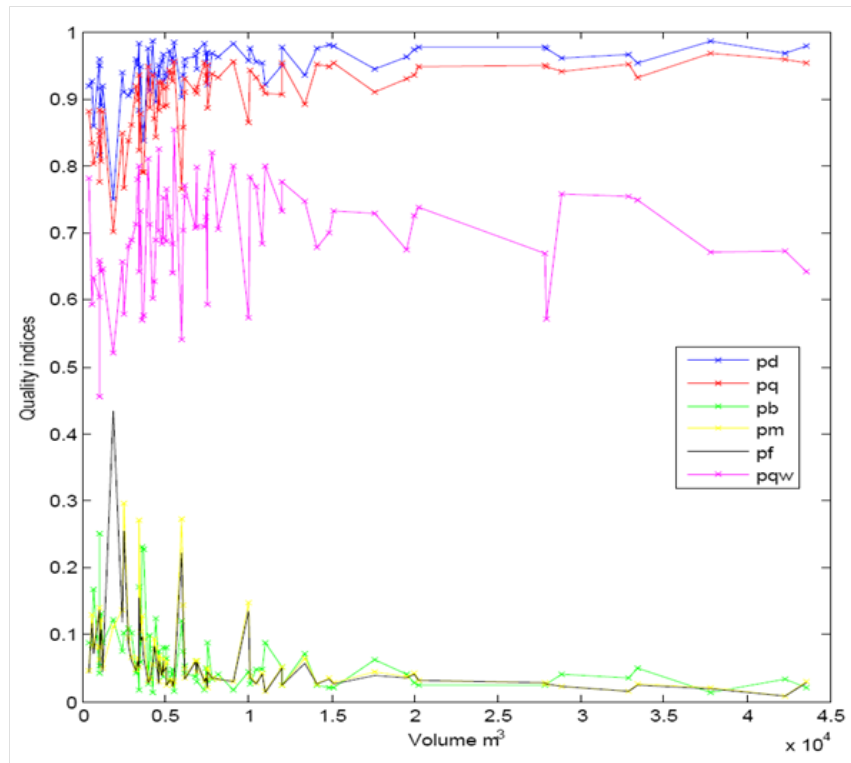
The results of the quality indices calculated for surface samples in building models (75 samples) reconstructed from Zeiss LMK dataset are shown in figure 5.12. The graphs present on the Y-axis the quality indices and on the X-axis the volume of the building. Figure 5.12 to figure 5.14 show that small buildings provide worse quality indices.

Table 5.8 summarizes the statistics of quality indices computed according to chapter 4 and applied to 75 samples of reconstructed building models of airborne imagery datasets. It shows the quality indices in each study case for both raster and vector format. The mean values of ρd and ρq are about 0.9, while $\rho q w$ is higher than 0.6 and the other three indices are close to zero. This means that the general evaluation of the 2D surface of building models extracted from stereopairs are closed from each other. The mean values of quality indices can not be considered alone. Because, in order to evaluate each building, one should check the quality factor values of each building model separately. Moreover, surface quality indices are affected by the building size as shown in figures 5.12 to figure 5.14. In raster

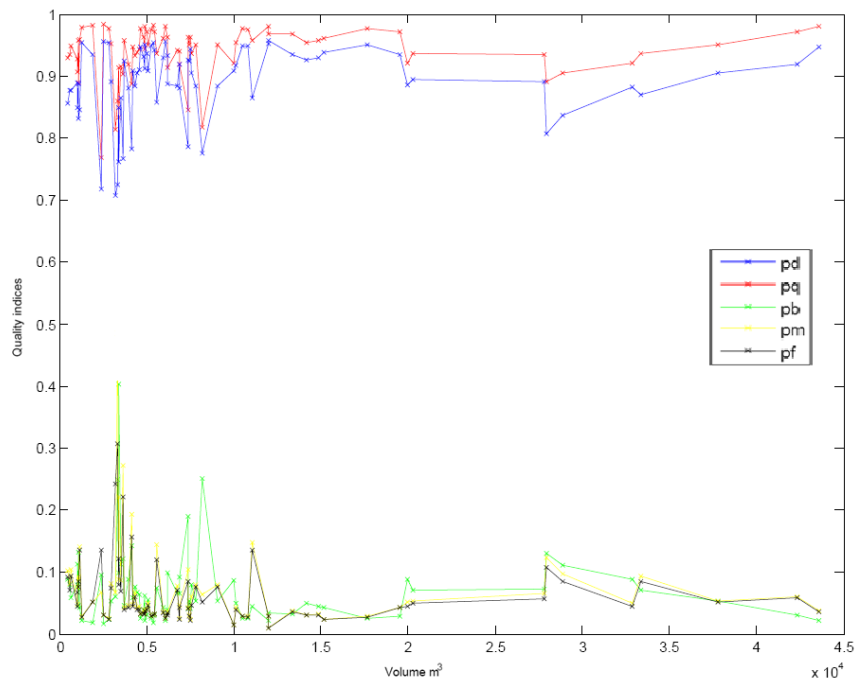
format, the running time of the program depends on the size of the building and the chosen pixel size for rasterizing the polygon describing the face under study.

3D building models based on	Model format	ρd [SD]	ρq [SD]	ρb [SD]	ρm [SD]	ρf [SD]	ρqw [SD]
Airborne images [75 samples]	Vector	0.938 [0.043]	0.891 [0.060]	0.089 [0.132]	0.085 [0.119]	0.062 [0.051]	-
	Raster	0.943 [0.042]	0.899 [0.056]	0.064 [0.050]	0.064 [0.056]	0.061 [0.062]	0.697 [0.078]

TABLE 5.8: Statistics of 2D quality indices obtained for buildings reconstructed from airborne imagery dataset.



(a) Raster format



(b) Vector format

FIGURE 5.12: Quality indices used for 2D assessment and calculated for models obtained from airborne imagery dataset; a) for raster models; b) for vector models.

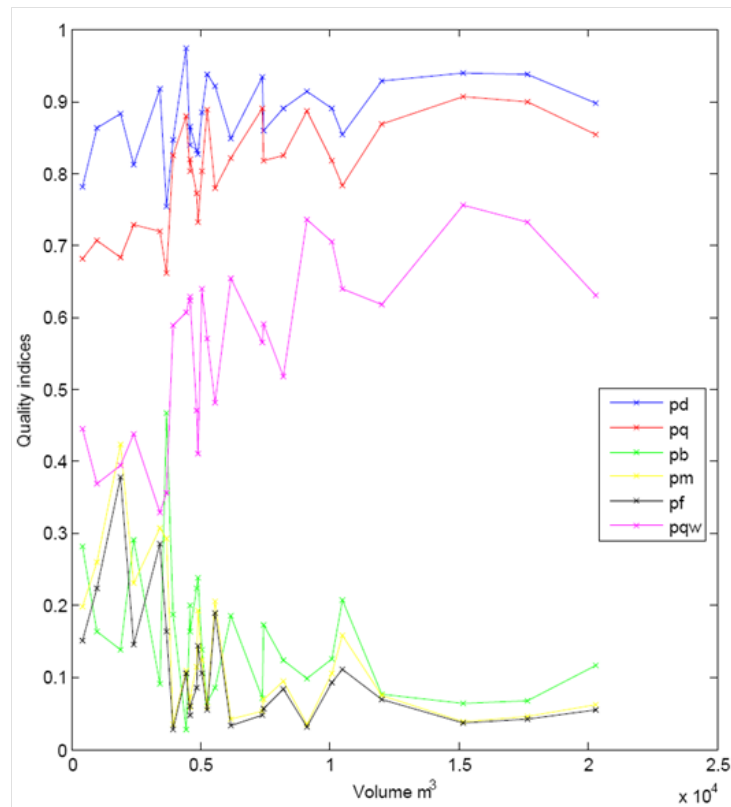
5.4.2.2 Models reconstructed from combination of LiDAR and imagery datasets

Figure 5.13 shows the results of the quality analysis of surface samples reconstructed from combination of LiDAR and imagery (UltraCam-X) datasets.

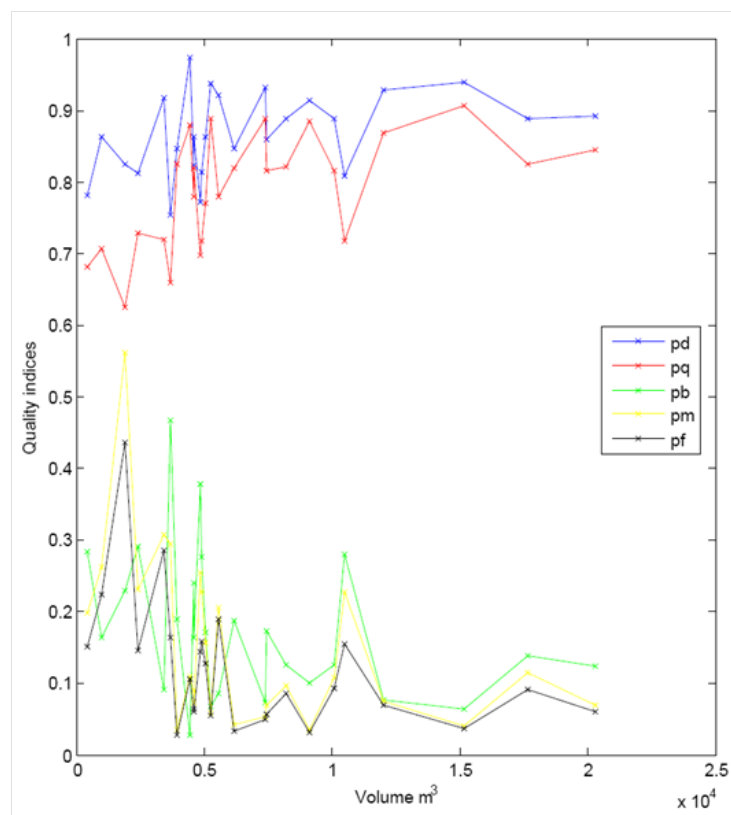
Table 5.9 summarizes the mean values of quality indices in raster and vector format of 26 samples of buildings reconstructed from combination of airborne imagery and LiDAR datasets. The mean values of ρd and ρq are around 0.8. ρqw is higher than 0.5 and the other three indices are higher than 0.1. These results are worse than the results obtained for the assessment of models reconstructed from airborne imagery dataset exclusively. This justifies the high RMSE values obtained in Z direction for that dataset (see table 5.6).

3D building models based on	Model format	ρd [SD]	ρq [SD]	ρb [SD]	ρm [SD]	ρf [SD]	ρqw [SD]
Combination of images and LiDAR datasets [26 samples]	Vector	0.867 [0.057]	0.788 [0.079]	0.177 [0.105]	0.154 [0.121]	0.120 [0.092]	-
	Raster	0.878 [0.053]	0.802 [0.073]	0.157 [0.094]	0.134 [0.102]	0.109 [0.085]	0.558 [0.124]

TABLE 5.9: Statistics of 2D quality indices obtained for buildings reconstructed from combination of imagery and LiDAR datasets.



(a) Raster format



(b) Vector format

FIGURE 5.13: Quality indices used for 2D assessment and calculated for models obtained from combination of LiDAR and imagery datasets; a) for raster models; b) for vector models.

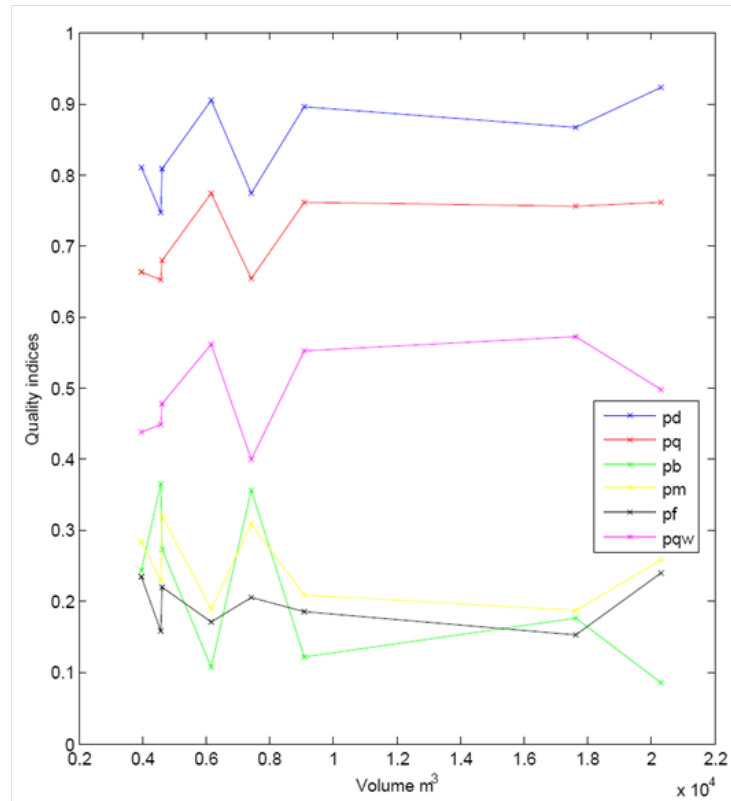
5.4.2.3 Models reconstructed from LiDAR dataset

The results of the quality analysis of surface samples reconstructed from LiDAR dataset are shown in figure 5.14.

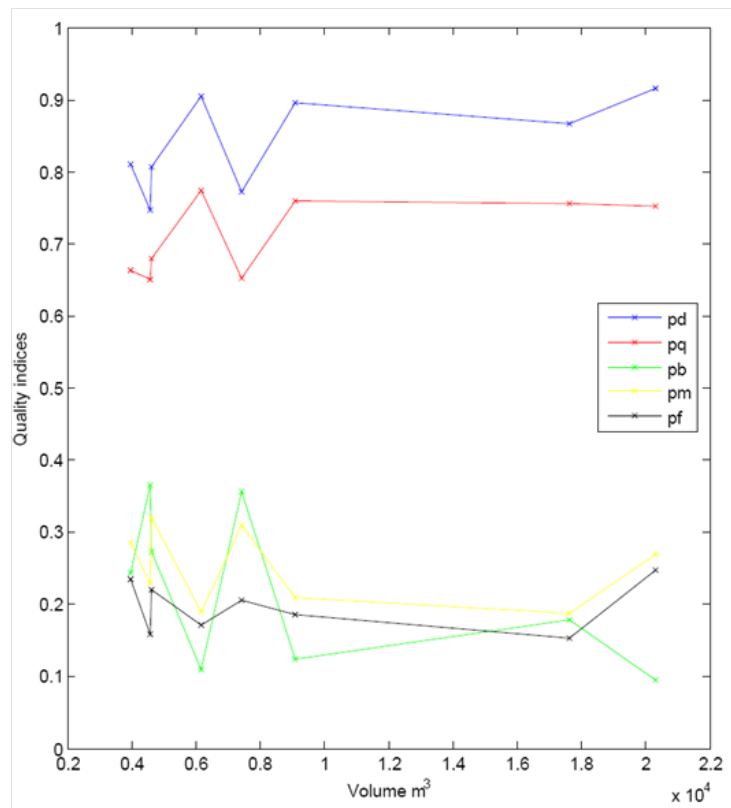
Table 5.10 summarizes the mean values of quality indices of 8 samples of reconstructed building models of LiDAR dataset in raster and vector format. The mean value of ρd is around 0.8 and 0.7 for ρq . $\rho q w$ is higher than 0.5 and the other three indices are around 0.2. These results are worse than the results obtained for the assessment of models reconstructed from airborne imagery dataset exclusively and combination of both airborne imagery and LiDAR datasets. This justifies the high RMSE values obtained in Y and Z directions for that dataset (see Table 5.6). Tables B.3 and B.6 in appendix B show the surface quality indices calculated for every building of the 8 buildings under study, separately.

3D building models based on	Model format	ρd [SD]	ρq [SD]	ρb [SD]	ρm [SD]	ρf [SD]	$\rho q w$ [SD]
LiDAR dataset [8 samples]	Vector	0.840 [0.064]	0.711 [0.054]	0.219 [0.109]	0.250 [0.053]	0.189 [0.035]	-
	Raster	0.841 [0.065]	0.713 [0.055]	0.217 [0.110]	0.249 [0.053]	0.197 [0.034]	0.494 [0.063]

TABLE 5.10: Statistics of 2D quality indices obtained for buildings reconstructed from LiDAR dataset.



(a) Raster format



(b) Vector format

FIGURE 5.14: Quality indices used for 2D assessment and calculated for models obtained from LiDAR dataset; a) for raster models; b) for vector models.

5.4.2.4 Models created from image matching

In this section, the data from RolleiDB44 medium format and UltraCam-X cameras are compared. Digital aerial images from Ultracam-X (4 images) and RolleiDB44 (5 images) of the same sites over Strasbourg City are available. Our approach focuses on characteristic planes extracted from both datasets. The reference dataset has been created from UltraCam-X stereopairs. Ground Control Points are measured by GNSS systems in specific places, in order to distribute them appropriately in the area of interest.

A 3D orientation process includes the determination of the position and attitude of an object. In photogrammetry, the orientations are described as interior and exterior orientations. Interior orientation defines the internal geometry of a camera or sensor as it existed at the time of image capture. Lens distortion deteriorates the positional accuracy of image points located on the image plane. 3D ground coordinates have been generated afterwards by photogrammetric matching algorithms.

As a result of that, the 3D ground coordinates have been calculated at any point in an overlapped area zone of images in the block. LPS software systems is used to compute the DSM composed of cells of 0.2 m in X and Y. Figure 5.15 and 5.16 show the 3D point clouds created from UltraCam-X and RolleiDB44 images. The difference between the two results are due to the change in sensors types and flight parameters.

Design of plane samples

The present section describes the 2D accuracy assessment of 3D photogrammetric data. A segmentation has been performed on the 3D matched point clouds in order to isolate points describing planes. Principal Component Analysis (PCA) is the method used to calculate the parameters of the optimal plane. PCA is a useful statistical technique that reduces a set of data by performing a covariance analysis between factors [Borcard et al., 2011]. PCA is suitable for datasets of multiple dimensions, for example in our case a set of point clouds created from a digital sensor. Figure 5.17 shows how the plane fitting has been realized based on the point clouds. Seven samples are chosen in order to achieve this study. Table 5.11 shows the Mean Distance (MD) in computing medium planes from (UltraCam-X and RolleiDB44) data and number of the used points in order to



FIGURE 5.15: 3D point clouds produced from UltraCam-X image (1,976,578 points).



FIGURE 5.16: 3D point clouds produced from Rollei image (746,475 points).

create plane parameters. The computed distances are lying between 0.09 m and 0.23 m in UltraCam-X samples and between 0.37 m and 0.86 m in Rollei samples. By analysing this table, it is possible to compare planes created from two blocks. Although the plane samples are chosen on the same feature, the MD is higher in Rollei block.

Results of the assessment

The approach developed in this work and detailed in chapter 4 has been applied on these 7 samples in order to evaluate their quality in 2D. In order to achieve

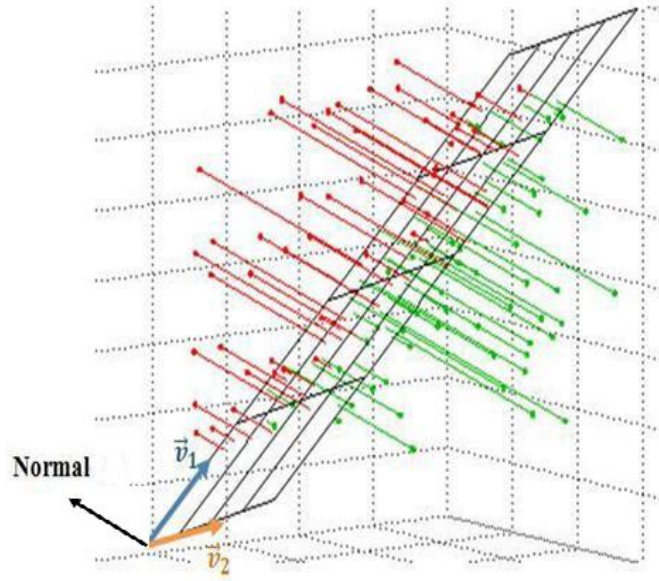


FIGURE 5.17: Fitting plane from 3d dataset
[Mohamed and Grussenmeyer, 2011].

Plane No	Mean Distance calculation (m)	
	For UltraCam-X [Number of points]	For Rollei [Number of points]
1	0.23 [114]	0.56 [117]
2	0.13 [179]	0.45 [78]
3	0.21 [525]	0.48 [142]
4	0.21 [623]	0.64 [402]
5	0.13 [91]	0.86 [124]
6	0.10 [297]	0.37 [191]
7	0.21 [162]	0.75 [134]

TABLE 5.11: Mean Distances calculated for (MD) in computing medium plane

this process, an algorithm has been developed in Matlab for the computing of the quality indices. Table 5.12 presents the results of the comparison. Reference data are the planes created with the UltraCam-X data. The values of two indices (ρd and ρq) are close to 1 and the other three indices are close to zero. This means that the geometry of planes extracted from both datasets is of good quality.

The accuracy of the points clouds obtained through image matching is largely influenced by the geometric configuration (base-to-height ratio B/H). Large B/H ratios entail increased dissimilarity of base and match images. The main reasons are changes in perspective and in illumination. As a consequence, image

Plane	ρd	ρq	ρb	ρm	ρf
1	0.9624	0.7503	0.0390	0.2937	0.2827
2	0.9491	0.8439	0.0536	0.1313	0.1246
3	0.9512	0.9436	0.0513	0.0084	0.0080
4	0.9111	0.8176	0.0976	0.1256	0.1144
5	0.9991	0.9112	0.0009	0.0966	0.0965
6	0.8801	0.8552	0.1363	0.0330	0.0291
7	0.9548	0.8954	0.0474	0.0694	0.0663

TABLE 5.12: 2D quality indices calculated for planes extracted from point clouds.

matching performs worse and the number of successfully matched points is small [Rothermel and Haala, 2011]. The expected height accuracies σ_Z based on the ratio B/H for two sensors is shown in equation 5.3 [Kraus, 1993].

$$\sigma_Z = \frac{Z^2}{c \cdot B} \cdot \sigma_{p_\xi} \quad (5.3)$$

Where c is the focal length of the camera and σ_{p_ξ} is the accuracy of the parallax.

It is assumed that σ_{p_ξ} is given according to the accuracies obtained for each block after bundle adjustment. For UltraCam-X block, σ_{p_ξ} is 2 μm and for RolleiDB44 block is 13 μm . σ_Z for UltraCam-X equal to 0.20 m and for RolleiDB44 equal to 1.28 m.

On the other hand, one can compute the error estimation based on the orthogonal distance between the reference surfaces (UltraCam-X) and tested surfaces (RolleiDB44). Table 5.13 shows the mean distance between planes created from UltraCam-X and RolleiDB44 at the same plane (reference and test). The values of MD between planes are not far from the expected errors in Z deducted from B/H ratio (equation 5.3) and MD was computed for medium planes from two blocks.

Plane No	MD between two planes (m)
1	1.72
2	1.15
3	1.79
4	1.93
5	1.12
6	1.00
7	1.18

TABLE 5.13: Mean distance calculation between two planes.

2D quality indices allow to assess the surface shape that composing the building model by superimposing them to the corresponding surface in the reference. The 3D quality indices can assess building model as one object. The results of quality indices have been applied to photogrammetric and LiDAR datasets will be shown next section.

5.4.3 3D accuracy assessment

The approach developed for assessing reconstructed buildings in 3D is based on the comparison of volumes. The principle has been explained in chapter 4.

5.4.3.1 Models reconstructed from airborne imagery dataset

The results of the quality analysis of surface 3D building models (75 samples) reconstructed exclusively from Zeiss LMK datasets are shown in figure 5.19.

Table 5.14 summarizes the statistics obtained for the indices computed according to chapter 4 and applied to 75 samples of buildings reconstructed from airborne imagery datasets. The 3D quality indices have been calculated for the models reconstructed in vector as well as in raster format. The mean values of $V\rho d$ and $V\rho q$ are around 0.9. $V\rho qw$ is higher than 0.8 and the other three indices are close to zero. This means that the general evaluation of the 3D building models extracted from stereopairs are close to each other as shown in figure 5.18. Figure 5.18 presents 8 of the 75 samples of building models reconstructed in the test site (in yellow colour) as well as the corresponding reference (in red). One can see clearly that both reference and test models are close to each other.

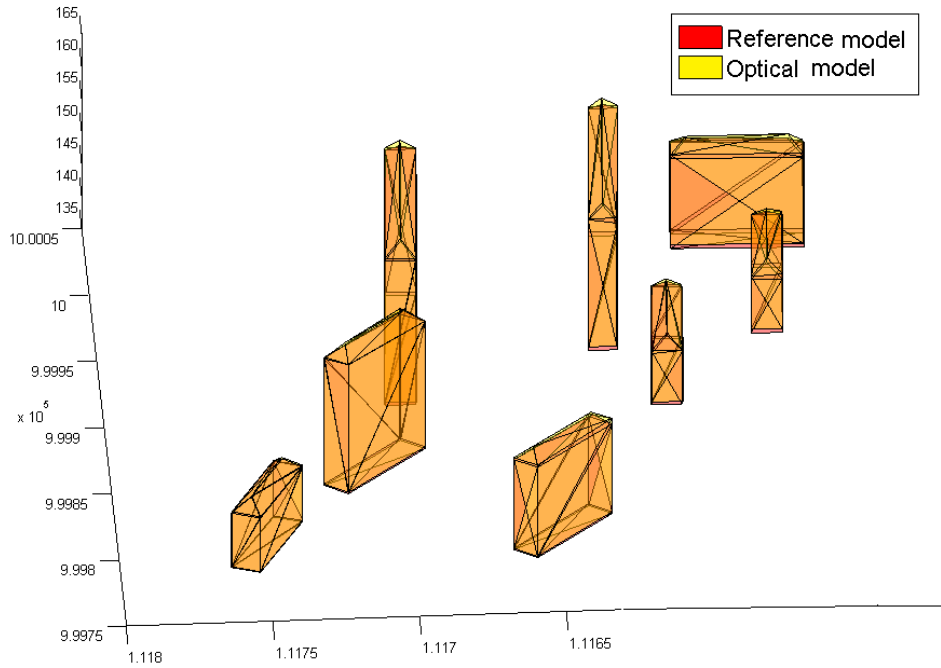
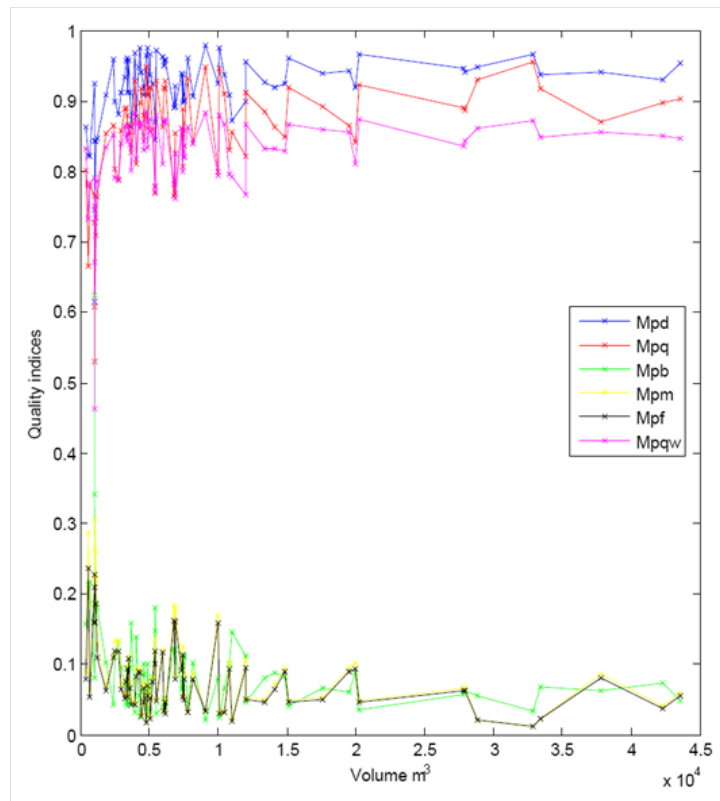


FIGURE 5.18: Reference and test model obtained from aerial images (8 of 75 buildings).

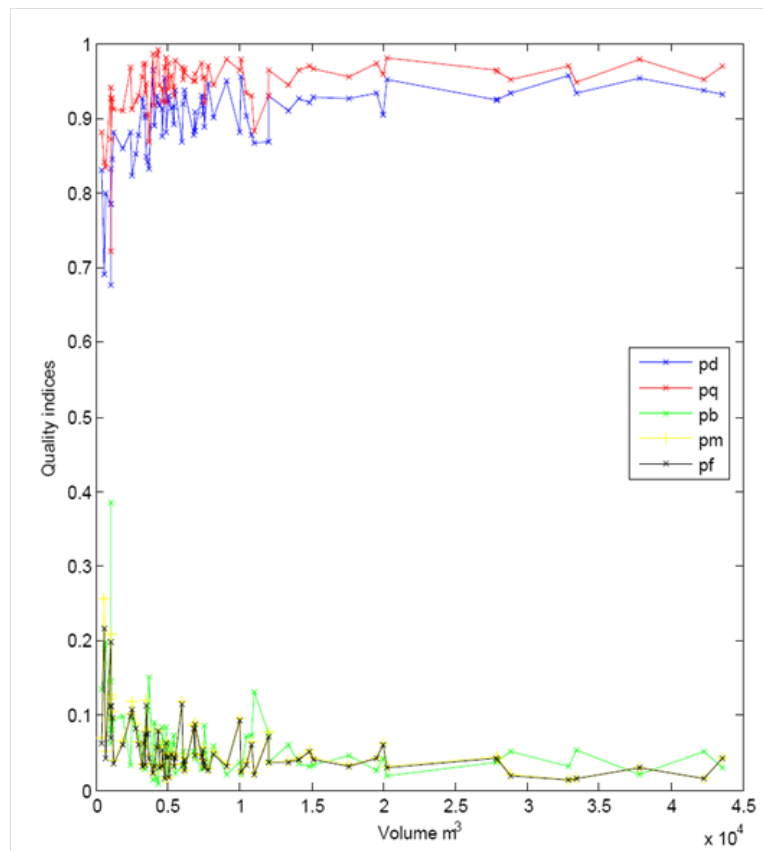
As already mentioned for the 2D assessment, the mean values of volume quality indices can not be considered alone. Because, in order to evaluate each building, one should check the result values of each building model separately. Moreover, volume metrics are affected by the building size as shown in figures 5.19 to 5.23. In raster format, the running time of the function depends on the size of the building model and the chosen voxel size for voxelizing the 3D model. Further analysis of advantages and drawbacks provided by raster and vector formats is made in section 5.5.

3D building models based on	Model format	$V_{\rho d}$ [SD]	$V_{\rho q}$ [SD]	$V_{\rho b}$ [SD]	$V_{\rho m}$ [SD]	$V_{\rho f}$ [SD]	$V_{\rho qw}$ [SD]
Airborne images [75 samples]	Vector	0.943 [0.041]	0.895 [0.054]	0.063 [0.054]	0.058 [0.041]	0.054 [0.036]	-
	Raster	0.917 [0.056]	0.853 [0.077]	0.095 [0.083]	0.088 [0.061]	0.079 [0.049]	0.827 [0.060]

TABLE 5.14: Statistics of 3D quality indices obtained for buildings reconstructed from airborne images.



(a) Raster format



(b) Vector format

FIGURE 5.19: Quality indices used for 3D assessment and calculated for models obtained from airborne images; a) for raster models; b) for vector models.

5.4.3.2 Models reconstructed from combination of LiDAR and airborne imagery datasets

Figure 5.21 shows the results of the quality analysis of 3D building models reconstructed from combination of LiDAR and images (UltraCam-X).

Table 5.15 summarizes the mean values of quality rates in raster and vector format of 26 samples of buildings reconstructed from combination of airborne imagery and LiDAR datasets. In vector format, the mean values of volume quality indices of $V\rho d$ and $V\rho q$ are around 0.8 and the other three indices are around 0.1. In raster format, the mean values of volume quality indices of $V\rho d$ is 0.8 and $V\rho q$ is around 0.7. $V\rho qw$ is higher than 0.7 and the other three indices are higher than 0.1. These results are worse than those obtained for the models reconstructed from airborne imagery datasets. This justifies the high RMSE values obtained in Z direction for that dataset, see table 5.6 and figure 5.20. Figure 5.20 shows 8 of 26 samples of reconstructed buildings (in green) and their reference buildings (in red). One can see that there are shift in Z-direction between reference and test model.

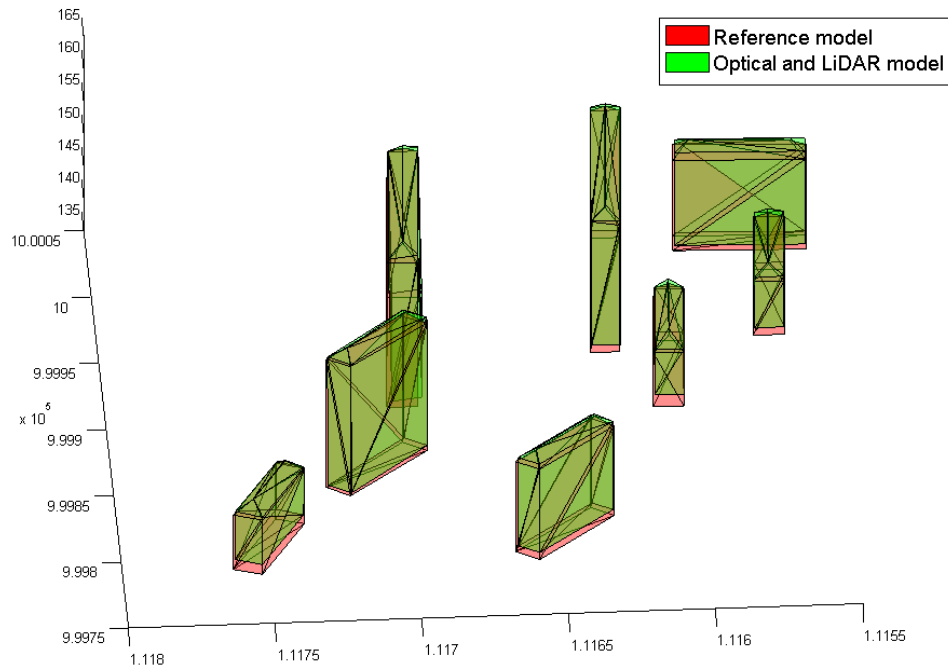
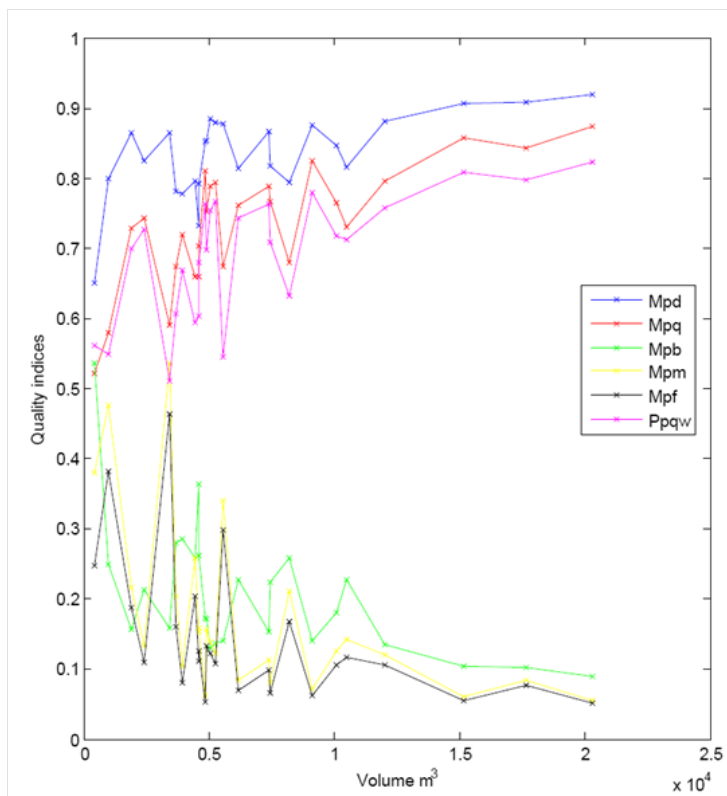


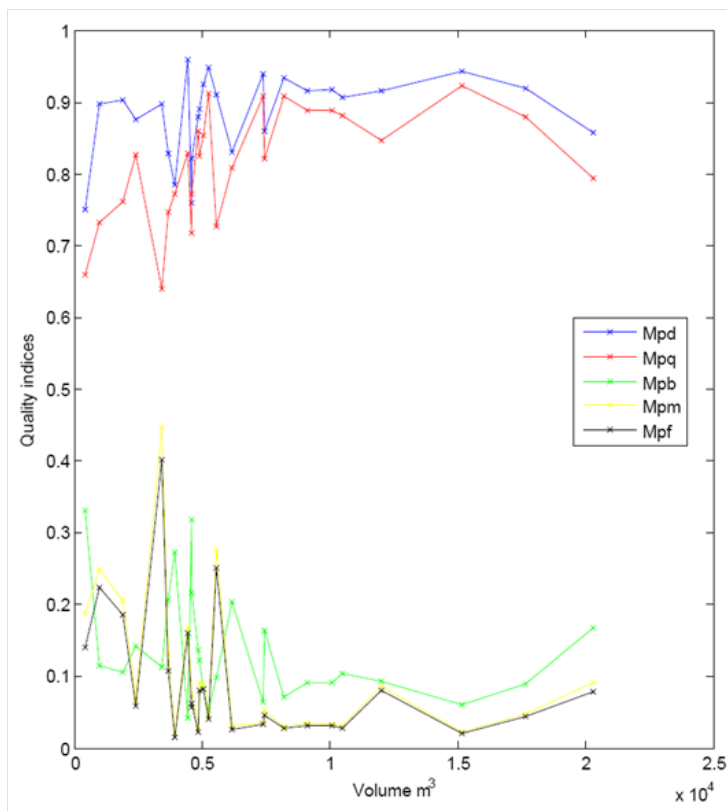
FIGURE 5.20: Models obtained from combination of aerial images and LiDAR datasets (8 of 26 buildings).

3D building models based on	Model format	$V\rho d$ [SD]	$V\rho q$ [SD]	$V\rho b$ [SD]	$V\rho m$ [SD]	$V\rho f$ [SD]	$V\rho qw$ [SD]
Combination of images and LiDAR datasets [26 samples]	Vector	0.875 [0.057]	0.809 [0.082]	0.148 [0.079]	0.102 [0.101]	0.089 [0.089]	-
	Raster	0.846 [0.054]	0.753 [0.079]	0.188 [0.082]	0.155 [0.112]	0.130 [0.094]	0.691 [0.089]

TABLE 5.15: Statistics of 3D quality indices obtained for buildings reconstructed from combination of images and LiDAR datasets.



(a) Raster format



(b) Vector format

FIGURE 5.21: Quality indices used for 3D assessment and calculated for models obtained from combination of LiDAR and images; a) for raster models; b) for vector models.

5.4.3.3 Models reconstructed from LiDAR dataset

The results of the quality analysis of 3D building models reconstructed from LiDAR datasets are shown in the figure 5.23. The graphs present on the Y-axis the quality indices and on the X-axis the volume of the building. Figure 5.19 to figure 5.23 show that small buildings with worse quality indices.

Table 5.16 summarizes the mean values of quality rates in raster and vector format of 8 samples of building models reconstructed from LiDAR datasets. In vector format, the mean values of volume quality indices of $V\rho d$ and $V\rho q$ are around 0.8 and the other three indices are higher than 0.1. In raster format, the mean values of volume quality indices of $V\rho d$ is 0.8 and $V\rho q$ is around 0.6. $V\rho qw$ is around 0.6 and the other three indices are higher than 0.2. These results are worse than those obtained for the models reconstructed from airborne images datasets and combination of both images and LiDAR datasets. This justifies the high RMSE values obtained in Y and Z directions for that dataset, see table 5.6 and figure 5.22. Figure 5.22 shows the results of 8 samples of building reconstruction from LiDAR data in the in cyan colour and reference model in red colour. One can see that there are shift in Y and Z-direction between reference and test model.

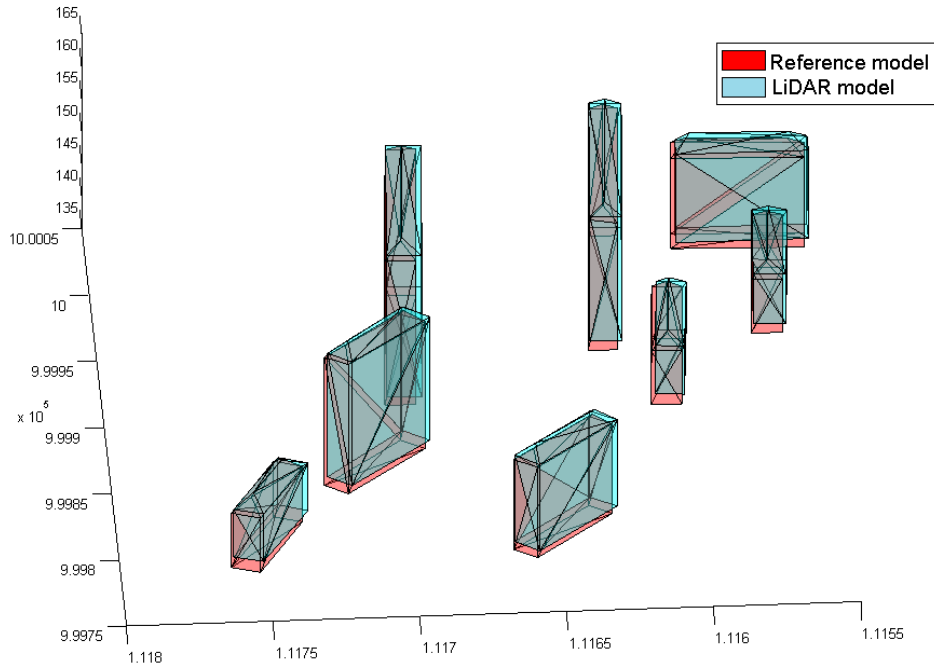


FIGURE 5.22: Models obtained from LiDAR datasets.

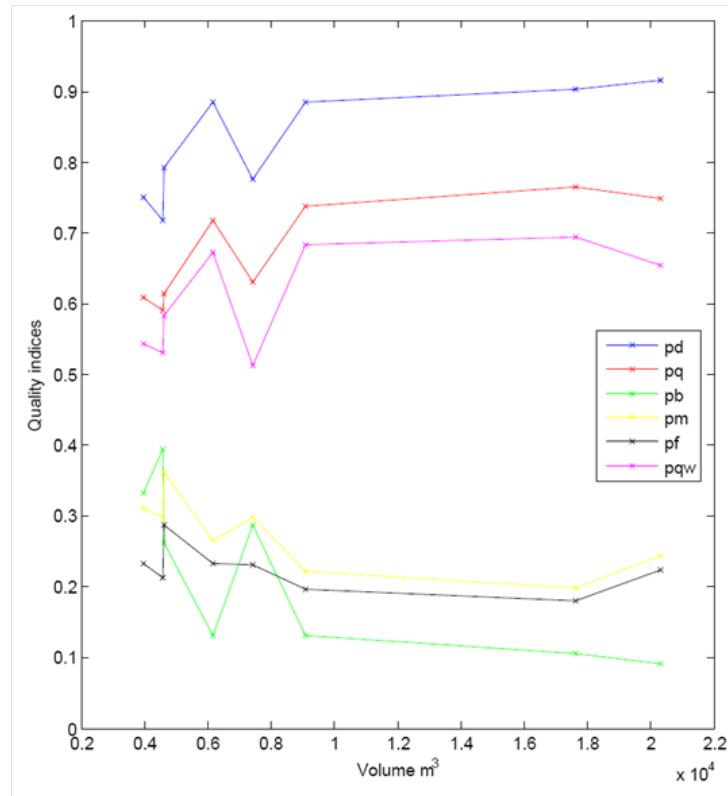
All tests applied on a sample of building reveals that a systematic error affects the Z coordinates of the LiDAR data used here. This vertical shift has already been observed in table 5.6. Moreover it has been observed in a study where combination of airborne laser scanner and terrestrial laser scanner data have been combined [Boulaassal et al., 2011].

The volume calculated for every building is explained and presented in tables A.1, A.2, and A.3 in Appendix A. The volumetric quality indices for each building separately are shown in tables C.1 to C.6 in Appendix C.

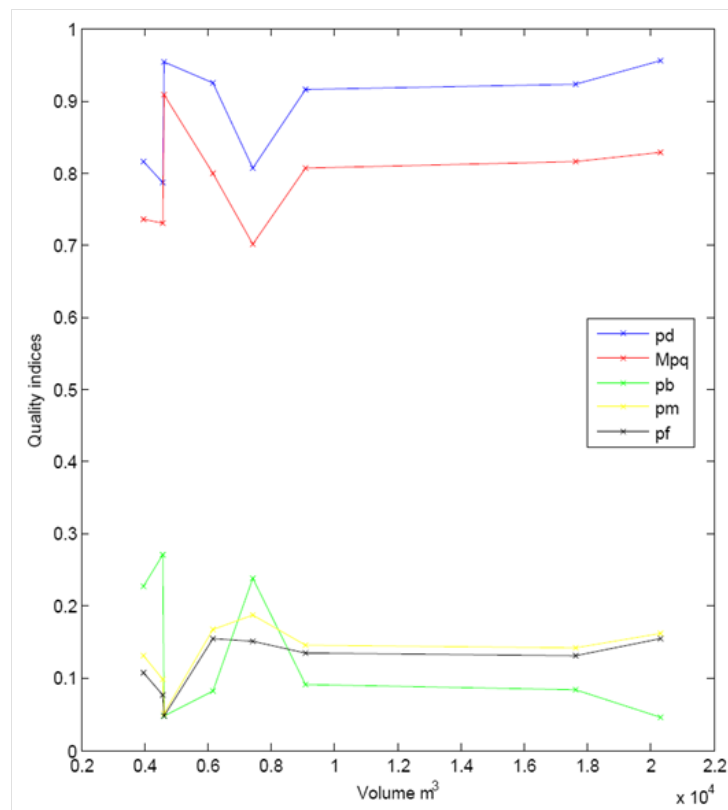
3D building models based on	Model format	$V_{\rho d}$ [SD]	$V_{\rho q}$ [SD]	$V_{\rho b}$ [SD]	$V_{\rho m}$ [SD]	$V_{\rho f}$ [SD]	$V_{\rho qw}$ [SD]
LiDAR dataset [8 samples]	Vector	0.885 [0.070]	0.791 [0.067]	0.136 [0.093]	0.136 [0.043]	0.120 [0.039]	-
	Raster	0.824 [0.082]	0.686 [0.072]	0.225 [0.125]	0.246 [0.040]	0.201 [0.023]	0.609 [0.075]

TABLE 5.16: Statistics of 3D quality indices obtained for buildings reconstructed from LiDAR dataset.

The 2D and 3D quality indices have been used to assess the 75 samples of 3D models from airborne images, 26 samples of 3D models from LiDAR and aerial images, and 8 samples of 3D models from LiDAR datasets. In the next section, we will make a comparison between 2D and 3D assessment.



(a) Raster format



(b) Vector format

FIGURE 5.23: Quality indices used for 3D assessment and calculated for models obtained from LiDAR datasets; a) for raster models; b) for vector models.

5.4.4 Comparison between 2D and 3D assessments

Statistical tests can be used for comparing two standard deviations and to see if they are significantly different. The statistical F-test is applied in order to compare the results of using quality indices in 2D and 3D. The test is applied to the building models reconstructed from airborne images. Since the sample is composed of 75 buildings, the degrees of freedom ($sample\ size - 1 = 74$) and the confidence level = 95 %, we obtain the critical value $F_{crit} = 1.47$. The ratio of variances of samples is tested in this part (between raster and vector format). For that, it can be concluded that there is a significant change between using 2D and 3D for all indices except $V_{\rho m}$ in raster data structure. In vector data structure, there is no significant change between using 2D and 3D for $V_{\rho d}$ and $V_{\rho q}$. For other indices in vector based assessment, there is a significant change between using 2D and 3D assessment. Table 5.17 shows the effect of raster and vector data structure on the quality indices obtained for the 2D assessment and the 3D assessment.

Data structure	significant	unsignificant
Raster	All indices except $V_{\rho m}$	$V_{\rho m}$
Vector	$V_{\rho b}$, $V_{\rho m}$ and $V_{\rho f}$	$V_{\rho d}$ and $V_{\rho q}$

TABLE 5.17: Results of statistical F-test applied between quality indices calculated for the 2D and 3D assessments.

In general, the results of 3D quality assessment are not the same as in 2D assessment. There may be close values in results of some indices. The 3D assessment takes into account the threshold between 2D surfaces, this justifies the differences between 2D and 3D assessments. It is clearly shown on the results of the quality indices obtained for the assessment of the models extracted from LiDAR datasets.

A short discussion about raster and vector models will be given in next section based on the work of 2D and 3D assessment of 3D building models.

5.5 Discussion about raster and vectors models

Vector and raster models are both important in many applications. Spatial data can be stored using either vector or raster data structure. The use of both data structures depends on the techniques used to collect the data. In this part, the two data structures are compared to see the differences between them. Each type of model format has its strengths; therefore, it's interesting to use both. An important difference between these two data structures is noticeable in the visualization of the data. In general, vector data structure produces smaller file sizes than raster image [Polidori, 2011] because a raster data structure needs high capacity for all pixels while vector representation of the same area can be reduced to a list of point coordinates related by primitives (points, lines, and surfaces). In the case of digital terrain models, for example, vector format is particularly efficient when the terrain is homogeneous regarding the relief. This can be extended to urban areas. A 3D model of a city generates bigger files when represented in voxels than in vector shapes. Besides the size issue, to handle vector data is easier than raster data. It is described by fewer items and it is more flexible to be adjusted for different scales. For example, a projection system in mapping application has a good performance in vector models.

Vector data may be converted easily into raster data. In contrast, the conversion from raster to vector data is still difficult to solve without loss of information. The conversion between both data structures is sometimes necessary, as for example in the production of maps [Taie et al., 2011]. The entities "shape" and "position" can be represented more accurately in vector data structure than in raster data structure. Table 5.18 summarizes, though a comparison between raster and vector data structure, the main advantages of each structure, based on several comparison items.

Items	Raster	Vector
Models creation	Fast	Variety from 2D and 3D
Data representation	By pixel (in 2D) or voxel (in 3D)	Represented without generalization
Structure of data	Simple (grid)	Complex (points, lines, surfaces)
Volume of data	Large	small
Representation of linear features	Difficult	Easy
Areas and volumes calculation	Less accurate	High accurate
Analysis of data and processing	Good and usually easy to program	Algorithms or functions are complex
Time processing	High	Less than a second in this research (2D and 3D assessment)

TABLE 5.18: Comparison between raster and vector based on modeling of buildings.

Furthermore, the same statistical F-test can be applied in order to compare the results of raster and vector data structure. The test is applied to the building models reconstructed from airborne images. Since the sample is composed of 75 buildings, the degrees of freedom ($sample\ size - 1 = 74$) and the confidence level = 95 %, we obtain the critical value $F_{crit} = 1.47$. The ratio of sample variances is tested in this part (between raster and vector format). It can be concluded that there is no significant change between using raster and vector for ρd and ρq . For the other quality indices calculated in the 2D assessment, there is a significant change between using raster and vector data structure. The same test is applied in 3D. The parameters of the test are the same as in 2D. Also, the ratio of sample variances will be tested regarding raster and vector formats. For that, it can be concluded that there is a significant change between using raster and vector data structure for all volumetric quality indices. Table 5.19 shows the effect of raster and vector data structure on the result quality indices calculated for the 2D and the 3D assessment.

2D or 3D assessments	significant	unsignificant
2D	$\rho b - \rho m - \rho f$	ρd and ρq
3D	all indices	-

TABLE 5.19: Results of statistical F-test applied between raster and vector data structure.

Chapter 6

Conclusion and perspectives

Aim of this research project was to introduce an approach in order to evaluate 3D building models resulting from the processing of photogrammetric and LiDAR datasets. Currently, the users of 3D models have no tool for evaluating the quality of the models they are working on. Purpose of this work was to analyze existing methods and to provide a solution allowing a thorough examination of the quality of a 3D model. In this study, 3D building models have been created from the processing of aerial images, LiDAR dataset and from the combination of both. The airborne imagery data were Zeiss LMK images, UltraCam-X images and LiDAR point clouds.

For assessing a 3D model, several factors must be taken into account: the data quality, the processing chain quality, and the final 3D building. In this context, various achievements were gained.

Digital aerial cameras can provide highly overlapping airborne imagery. This is asset for automatic image matching especially for surfaces with relatively little texture. The base over height ratio is a factor which impacts also the final accuracy of the building reconstruction. It means that the quality of the 3D building created from stereo-image processing is largely influenced by the geometric configuration of the acquisition (base-to-height ratio) and the image matching step. The matching algorithm developed in LPS software is well known for its high accuracy and reliability. Also, the errors coming from a low point clouds density, or errors due to the georeferencing of the LiDAR are factors which impact the final accuracy of the building reconstruction.

In this thesis, three semi-automatic methods for 3D building reconstruction in vector format have been mentioned and carried out on data covering the same test site. These methods have been selected because they are suggested in the literature and they allow the processing of the photogrammetric data and/or LiDAR data.

In order to guaranty a complete and thorough assessment of individual buildings, we developed a multi-dimensional assessment approach.

Multi-dimensional approach means that the assessment is divided into an assessment performed in the first dimension (1D), second dimension (2D), and third dimension (3D). This approach requires reference buildings, that is to say buildings which are more accurate than the test models. The assessment is based on the comparison of the test model with the corresponding reference model.

1D assessment gives an overall idea about the reliability of the reconstructed model. It is based on the calculation of RMSE (in easting, northing, and height) of differences between corresponding vertices that describe the building. It has been shown that the use of center of gravity of the building faces and roofs avoids a lot of mistakes in the assessment process. The application of the 1D assessment on a large sample of buildings created with multiple datasets and reconstruction processes revealed that a systematic error affects the Z coordinates of the LiDAR data used here. This vertical shift has already been observed in a previous study where the same LiDAR data have been used.

In order to ensure that the deviations observed between the test model and its reference are tolerable, the order of accuracy classes published in the Official Journal in 2003 (arrêté sur les classes de précision) has been applied. It provides a standard model allowing to check if the deviations observed enter in the required precision class. By taking a precision class of $[0.50\text{ m}]$ only 49 of the 75 test models reconstructed from airborne imagery datasets (Zeiss LMK images) and compared to their reference (UltraCam-X) are acceptable. The models created from LiDAR only and from combination of LiDAR with imagery datasets (UltraCam-X) are not accepted. This may be explained by the high shifts in Z-direction coming from LiDAR. This error must be corrected for the whole dataset before reconstructing the building from this dataset.

2D assessment consists in qualifying the superimposition of planar surfaces. It is particularly appropriate for the accuracy assessment of 2D features such as roofs

and facades. A method for 2D quality evaluation has already been suggested in the literature. It is based on the comparison between reference and test planes and provides quality indices. The method is applicable for planes in raster and vector format, as it has been shown in this work. The available photogrammetric and LiDAR datasets have therefore been used for extracting planes. The method is based on estimating the degree of superposition between the surface area of two planes (reference and test). From a computational perspective, the faces of the building are of satisfying quality if the values of ρd , ρq , and ρqw are close to 1, and the values of ρb , ρm , and ρf are close to 0. The main drawback of these quality indices is that they are affected by the size of the surface areas. For a same deviation, a large surface area will provide better quality indices than a small area.

By applying statistical F-test to compare between raster and vector data structure in 2D, the results of quality indices were not the same for ρb , ρm and ρf using raster and vector format with 95% confidence level. While they were the same for ρd and ρq indices.

Therefore, the 2D quality indices give an indication about the degree of similarity of surfaces. They are not sufficient for assessing the geometric position of the elements of the building model and should be supplemented by statistical criteria such as deviations and RMSE.

Two surface areas of building facade (test polygon compared reference polygon) might be superimposing correctly in the frame of the facade, but not in depth, that's why an assessment in the third dimension must also be performed.

For assessing entire 3D building models, quality indices based on volume ratios have been considered. We call them "volumetric quality indices", as counterpart to the 2D quality indices. Although the quality indices suggested in the literature are intended to be used with raster models, this work consider them mainly with vector models. Indeed, vector model buildings are more faithful to reality than raster models. The reason why the vector format is rarely addressed in the literature is given by the complexity of the intersection shape. The 3D assessment consists in comparing a test building to a reference building in 3D. It means that the whole building is considered as one object and not as several planes (as in the 2D assessment) or vertices (as in the 1D assessment). This work introduces an algorithm developed for determining the intersection shape of two vector building models. It leads to the calculation of the intersection volume. A visual check

remains very important in the developed processing chain and more particularly in the step of intersection shape calculation. The 3D assessment also takes into account the direction of errors (shifts in X, Y, and Z or rotations). The developed approach should be improved regarding shape characteristics of the buildings.

By applying statistical F-test to compare between raster and vector data structure in 3D, the results of quality indices were not identical for all indices using raster and vector format with 95% confidence level. By applying statistical F-test to compare between 2D and 3D assessment in vector data structure, the results of quality indices were not identical for all indices except for ρb and ρq with 95% confidence level. The 3D assessment has also been applied on raster building models. The quality indices do not give the same results for all indices except ρm with 95% confidence level.

The multi-dimensional approach developed in this work is suitable for assessing 3D building models (in 1D, 2D, and 3D) reconstructed from photogrammetric and LiDAR datasets. Whatever the processing chain, this approach focuses on the quality of the final product. It has been developed for assessing vector models, as they better reflect the reality than raster models, but it can also be applied on raster models.

The error budget affecting the final 3D building model is not only composed of errors due to the reconstruction algorithm, but also of errors coming from the raw data, like for instance a low point clouds density, errors due to the georeferencing of the considered data, due to the shape of the produced buildings. The developed multi-dimensional assessment approach allows to detect the sources of errors, or at least, to make assumptions about their sources.

Future researches will focus on the extension of this approach to more complex building models, since it has been limited in this work to buildings with flat, slope, gable, hip, and pyramid roofs. The potential of the approach for assessing 3D models of other features like trees, for instance, is also an interesting topic.

Appendix A

Volumes and RMSE of building models

The 3D reference building models have been reconstructed based on the photogrammetric processing of images acquired with UltraCam-X stereopairs. In this part, volumes of reference (*VR*), of test (*VT*), and of intersection (*VI*) building model are shown. These volumes are in raster and vector data structure. These reference models are used in three tests. The first test, table A.1, is applied for 75 of 3D building models reconstruction based on the photogrammetric processing of images acquired with Zeiss-LMK stereopairs. Second test, table A.2, is applied to 26 building models reconstruction based on the combination of both photogrammetric and LiDAR datasets . The third test, A.3, is applied for 8 building models reconstruction based on the LiDAR processing. RMSEs are computed based on the deviations between both models (reference and test) in each test, in X, Y and Z directions. Tables A.4, A.5, and A.6 present the RMSE results from corresponding vertices of each test. Tables A.7, A.8, and A.9 present the RMSE results from gravity centers of homologous planes of each test.

Model ID	Vector data structure			Raster data structure		
	VI (m^3)	VT (m^3)	VR (m^3)	VI (m^3)	VT (m^3)	VR (m^3)
1	4276.444	4610.851	4309.365	4163.674	4520.515	4237.214
2	3078.834	3182.204	3222.063	2986.650	3113.631	3152.934
3	3306.440	3703.864	3496.358	3302.852	3615.412	3407.427
4	4520.418	4741.505	4902.071	4415.306	4656.879	4823.060
5	2762.050	2941.004	2967.645	2619.175	2859.034	2881.049
6	4152.392	4392.801	4217.995	3965.985	4272.408	4113.702
7	4186.011	4313.750	4433.102	4064.504	4178.799	4313.137
8	947.553	1146.843	1006.305	892.377	1093.873	964.368
9	14683.664	15313.493	15179.923	14484.087	15118.141	15008.850
10	3331.064	3590.438	3424.094	3217.397	3530.052	3349.179
11	3205.330	3359.161	3692.371	3132.617	3287.111	3631.680
12	5434.013	5669.180	5559.952	5332.338	5595.264	5486.008
13	11590.245	12029.613	12018.377	11396.992	11872.836	11879.005
14	4806.323	5115.047	4900.544	4697.712	5037.422	4819.586
15	2333.369	2571.906	2409.583	2265.908	2524.253	2361.838
16	2295.352	2568.127	2517.923	2212.389	2506.329	2460.784
17	1740.484	1855.669	1910.986	1697.440	1814.395	1869.939
18	3289.375	3561.789	3637.390	3251.740	3488.481	3559.856
19	4906.431	5132.815	5041.404	4803.516	5059.724	4965.939
20	5766.730	6451.285	5952.467	5684.733	6353.586	5873.841
21	4689.722	4766.653	4844.373	4606.380	4689.374	4775.724
22	402.737	430.920	457.199	378.148	412.182	437.593
23	480.611	604.136	571.230	454.437	584.901	551.407
24	7085.779	7376.255	7431.684	6853.882	7186.612	7252.582
25	4260.782	4506.176	4616.969	4082.071	4336.452	4452.543
26	4311.383	4454.179	4584.849	4117.693	4276.116	4419.531
27	16864.263	17429.262	17642.169	16522.645	17113.045	17356.086
28	19916.806	20534.193	20299.172	19518.426	20236.176	20011.783
29	7755.995	8153.796	8204.808	7423.866	7907.436	7956.486
30	9800.007	10158.199	10497.731	9457.943	9842.882	10158.736
31	8919.581	9211.430	9097.811	8791.357	9065.524	8938.057
32	9887.785	10132.406	10097.651	9654.854	9935.618	9872.397
33	5970.233	6222.817	6173.950	5816.583	6087.078	6032.718
34	3908.737	4000.379	3959.723	3739.594	3866.922	3825.882
35	7171.103	7500.549	7371.508	6840.220	7314.966	7166.232
36	5029.093	5278.854	5252.812	4778.167	5103.522	5070.762
37	5766.582	5972.830	6059.972	5694.561	5876.235	5955.781
38	5955.562	6118.192	6195.963	5808.685	5983.794	6064.245
39	37022.513	38101.990	37786.661	35889.556	37563.035	37234.971
40	19034.619	19853.284	19553.928	18181.103	19548.193	19031.652

Model ID	Vector data structure			Raster data structure		
	VI (m^3)	VT (m^3)	VR (m^3)	VI (m^3)	VT (m^3)	VR (m^3)
41	3774.001	3901.527	4114.781	3582.648	3798.306	3976.826
42	3240.513	3445.602	3334.260	3132.972	3372.651	3248.105
43	4778.802	4864.039	5084.092	4671.301	4752.909	4963.338
44	3194.359	3309.329	3425.470	3106.044	3233.781	3328.182
45	554.113	582.216	664.113	522.450	545.629	621.689
46	7568.001	7776.488	7793.294	7426.705	7637.688	7671.762
47	31666.991	32172.373	33387.216	31247.222	31796.721	33136.781
48	27496.132	28034.074	28887.711	27287.762	27804.632	28684.215
49	31875.992	32302.357	32868.835	31637.146	31932.050	32595.471
50	934.047	1053.849	1069.899	855.319	991.120	1028.718
51	741.368	812.023	1026.811	639.391	753.178	965.988
52	988.704	1109.214	1067.624	900.765	1042.542	1030.572
53	9769.921	9989.591	11063.866	9548.780	9788.144	10831.613
54	10081.651	10736.518	10832.636	9772.799	10504.121	10596.865
55	26829.521	28022.390	27836.545	26392.136	27697.869	27476.217
56	26911.810	28049.474	27971.303	26510.121	27740.673	27655.601
57	9628.137	10554.991	9986.561	9161.095	10353.609	9634.459
58	42338.722	44173.912	43607.948	41847.538	43812.702	43213.185
59	40279.261	40906.448	42321.600	39822.835	40620.537	41959.728
60	7064.492	7466.088	7413.663	6727.297	7256.524	7179.439
61	5042.323	5281.870	5413.442	4799.457	5143.689	5244.075
62	7165.744	7385.436	7505.580	6895.044	7201.507	7313.436
63	5132.599	5300.939	5443.764	4741.402	5114.592	5256.936
64	13672.049	14252.188	14170.994	13201.286	13831.551	13909.968
65	19173.324	20386.840	19977.822	18710.528	20010.623	19716.125
66	6989.490	7273.080	7588.240	6768.900	7066.566	7427.875
67	6530.079	6846.231	6871.494	6307.141	6675.826	6708.307
68	12637.037	13135.530	13390.523	12306.379	12865.887	13176.706
69	1073.821	1185.739	1159.577	969.417	1122.763	1086.133
70	2599.702	2831.145	2815.123	2458.854	2714.508	2705.990
71	1140.658	1186.195	1249.664	1068.570	1118.803	1187.748
72	6452.795	7007.581	6790.963	6184.373	6870.884	6637.158
73	11180.103	12039.204	12015.341	10920.753	11832.282	11834.366
74	6613.393	7210.791	6893.315	6301.229	7040.417	6728.594
75	14397.964	15168.419	14838.722	13956.314	14847.224	14595.251

TABLE A.1: Volumes of buildings reconstructed from UltraCam-X and Zeiss-LMK.

Model ID	Vector data structure			Raster data structure		
	VI (m^3)	VT (m^3)	VR (m^3)	VI (m^3)	VT (m^3)	VR (m^3)
7	3534.070	4122.997	4433.102	3491.618	4229.550	4313.137
8	902.252	1127.301	1006.305	785.961	1111.779	964.368
9	14306.383	14626.482	15179.923	13675.928	14522.229	15008.850
10	3072.418	4448.069	3424.094	2955.528	4414.162	3349.179
11	3056.093	3455.715	3692.371	2861.784	3420.180	3631.680
12	5058.829	6452.939	5559.952	4852.319	6408.423	5486.008
13	10993.629	11955.274	12018.377	10559.552	11702.174	11879.005
14	4365.993	4763.483	4900.544	4103.874	4718.785	4819.586
15	2107.458	2250.742	2409.583	1905.104	2159.417	2310.417
18	1640.824	1979.017	1910.986	1622.295	1946.957	1869.939
20	4658.023	5077.537	5041.404	4415.004	4976.073	4965.939
22	4261.049	4374.572	4844.373	4074.440	4324.356	4775.724
23	343.484	407.859	457.199	300.442	389.362	437.593
24	6382.993	6726.212	7431.684	5973.588	6410.925	7252.582
25	3793.206	4081.798	4616.969	3605.373	4044.402	4452.543
26	3478.432	3742.834	4584.849	3355.272	3740.454	4419.531
27	16205.096	17001.910	17642.169	15961.320	17121.573	17356.086
28	17391.650	18996.168	20299.172	18447.165	19274.062	20011.783
29	7662.695	7893.681	8204.808	6530.850	7697.425	7956.486
30	9512.172	9806.616	10497.731	8560.026	9507.865	10158.736
31	8332.223	8621.330	9097.811	7886.056	8363.718	8938.057
32	9256.716	9570.823	10097.651	8412.907	9427.716	9872.397
33	5125.754	5288.618	6173.950	4979.853	5291.015	6032.718
34	3109.592	3173.794	3959.723	3004.785	3290.418	3825.882
35	6925.619	7173.667	7371.508	6262.303	6963.030	7166.232
36	4981.485	5191.954	5252.812	4571.275	5060.929	5070.762

TABLE A.2: Volumes of buildings reconstructed from UltraCam-X and combination of UltraCam-X with LiDAR.

Model ID	Vector data structure			Raster data structure		
	VI (m^3)	VT (m^3)	VR (m^3)	VI (m^3)	VT (m^3)	VR (m^3)
24	6000.770	7130.548	7431.684	5413.032	6985.175	7252.582
25	3684.300	4630.308	4616.969	3566.187	4613.067	4452.543
26	3603.807	3958.857	4584.849	3150.549	3945.236	4419.531
27	16268.022	18596.357	17642.169	15618.074	18505.760	17356.086
28	19401.712	22548.501	20299.172	18301.716	22490.343	20011.783
29	8336.889	9563.437	9097.811	7904.511	9527.045	8938.057
31	5704.991	6664.102	6173.950	5359.531	6635.002	6032.718
32	3226.103	3652.095	3959.723	2839.531	3629.610	3825.882

TABLE A.3: Volumes of buildings reconstructed from UltraCam-X and LiDAR.

Model ID	RMSE-X (m)	RMSE-Y (m)	RMSE-Z (m)	Total (m)
1	0.52	0.23	0.51	0.77
2	0.24	0.35	0.28	0.51
3	0.13	0.25	0.30	0.41
4	0.54	0.53	0.29	0.81
5	0.18	0.50	0.36	0.64
6	0.17	0.25	0.40	0.51
7	0.23	0.38	0.26	0.51
8	0.43	0.72	0.30	0.89
9	0.19	0.37	0.31	0.52
10	0.20	0.48	0.21	0.56
11	0.48	0.78	0.85	1.25
12	0.11	0.31	0.27	0.43
13	0.30	0.29	0.24	0.48
14	0.17	0.39	0.34	0.54
15	0.32	0.37	0.54	0.72
16	0.19	1.14	0.57	1.29
17	0.30	0.59	0.50	0.83
18	0.30	0.60	0.25	0.72
19	0.21	0.32	0.45	0.60
20	0.56	0.74	0.57	1.09
21	0.18	0.21	0.30	0.41
22	0.27	0.21	0.29	0.45
23	0.19	0.60	0.40	0.75
24	0.08	0.26	0.54	0.60
25	0.34	0.20	0.49	0.63
26	0.22	0.25	0.34	0.47
27	0.40	0.18	0.52	0.68
28	0.24	0.10	0.42	0.49
29	0.19	0.32	0.52	0.64
30	0.30	0.21	0.30	0.47
31	0.16	0.15	0.35	0.41
32	0.18	0.10	0.29	0.36
33	0.27	0.14	0.34	0.46
34	0.22	0.11	0.14	0.28
35	0.34	0.12	0.38	0.53
36	0.29	0.15	0.38	0.50
37	0.41	0.18	0.72	0.85
38	0.43	0.22	0.13	0.50
39	0.12	0.34	0.27	0.45
40	0.23	0.43	0.23	0.54

Model ID	RMSE-X (m)	RMSE-Y (m)	RMSE-Z (m)	Total (m)
41	0.32	0.41	0.23	0.57
42	0.10	0.33	0.43	0.55
43	0.25	0.26	0.40	0.54
44	0.14	0.33	0.42	0.55
45	0.42	0.35	0.42	0.69
46	0.13	0.38	0.20	0.45
47	0.31	0.26	0.49	0.63
48	0.23	0.23	0.43	0.55
49	0.14	0.34	0.18	0.41
50	0.16	0.26	0.52	0.61
51	0.55	0.21	0.44	0.73
52	0.12	0.19	0.41	0.47
53	0.45	0.39	0.96	1.13
54	0.36	0.22	1.11	1.19
55	0.19	0.22	0.98	1.03
56	0.17	0.27	0.94	0.99
57	0.27	0.37	1.04	1.13
58	0.21	0.15	0.90	0.93
59	0.23	0.25	0.79	0.86
60	0.08	0.22	0.80	0.83
61	0.16	0.38	0.78	0.88
62	0.12	0.13	0.74	0.76
63	0.13	0.29	0.71	0.78
64	0.08	0.19	0.65	0.68
65	0.21	0.30	0.77	0.86
66	0.35	0.33	0.47	0.67
67	0.30	0.18	0.55	0.65
68	0.33	0.36	0.58	0.76
69	0.25	0.22	0.72	0.79
70	0.20	0.17	0.62	0.67
71	0.18	0.15	0.44	0.50
72	0.44	0.34	0.85	1.01
73	0.42	0.36	0.98	1.13
74	0.14	0.40	0.99	1.08
75	0.11	0.10	0.80	0.81

TABLE A.4: RMSE computed from corresponding vertices for aerial images.

Model ID	RMSE-X (m)	RMSE-Y (m)	RMSE-Z (m)	Total (m)
7	1.38	2.05	0.87	2.62
8	0.83	0.68	1.49	1.83
9	0.45	0.34	1.02	1.16
10	1.16	1.79	1.10	2.40
11	1.15	0.80	1.85	2.32
12	1.33	1.78	1.14	2.50
13	0.84	0.55	0.91	1.36
14	0.85	0.70	1.73	2.05
15	0.73	0.48	1.09	1.40
18	1.54	2.04	1.06	2.77
20	0.77	0.45	0.83	1.22
22	0.82	0.62	1.03	1.45
23	0.59	0.49	1.40	1.60
24	0.53	0.49	1.23	1.43
25	0.43	0.27	1.19	1.30
26	0.36	0.38	1.21	1.31
27	0.19	0.27	0.98	1.03
28	0.30	0.29	1.07	1.15
29	0.42	0.84	1.29	1.60
30	0.41	0.46	1.03	1.20
31	0.32	0.28	1.17	1.25
32	0.25	0.44	1.20	1.31
33	0.44	0.46	1.09	1.26
34	0.33	0.44	1.15	1.27
35	0.27	0.36	1.28	1.36
36	0.37	0.28	1.28	1.36

TABLE A.5: RMSE computed from corresponding vertices for combination of aerial images and LiDAR datasets.

Model ID	RMSE-X (m)	RMSE-Y (m)	RMSE-Z (m)	Total (m)
24	1.74	1.31	1.21	2.49
25	1.01	1.00	1.19	1.85
26	0.92	1.17	1.20	1.92
27	0.64	0.96	1.05	1.57
28	1.19	1.20	1.04	1.98
29	0.55	1.07	1.06	1.60
31	0.65	0.92	1.00	1.50
32	1.03	1.20	1.25	2.01

TABLE A.6: RMSE computed from corresponding vertices for LiDAR dataset.

Model ID	RMSE-X (m)	RMSE-Y (m)	RMSE-Z (m)	Total (m)
1	0.25	0.15	0.35	0.46
2	0.16	0.13	0.17	0.26
3	0.08	0.19	0.20	0.28
4	0.40	0.53	0.17	0.69
5	0.11	0.37	0.12	0.41
6	0.08	0.13	0.19	0.25
7	0.17	0.32	0.16	0.39
8	0.22	0.69	0.17	0.74
9	0.14	0.35	0.23	0.44
10	0.12	0.43	0.21	0.49
11	0.22	0.68	0.67	0.98
12	0.05	0.20	0.26	0.34
13	0.28	0.24	0.19	0.42
14	0.11	0.32	0.24	0.41
15	0.18	0.35	0.28	0.48
16	0.29	1.30	0.26	1.36
17	0.92	2.10	0.33	2.31
18	0.16	0.54	0.11	0.57
19	0.16	0.30	0.33	0.48
20	0.29	0.61	0.36	0.76
21	0.07	0.15	0.16	0.23
22	0.20	0.17	0.25	0.36
23	0.09	0.58	0.20	0.62
24	0.03	0.19	0.49	0.53
25	0.29	0.10	0.45	0.54
26	0.06	0.11	0.19	0.23
27	0.36	0.13	0.43	0.57
28	0.19	0.05	0.36	0.41
29	0.17	0.24	0.47	0.55
30	0.18	0.09	0.24	0.32
31	0.07	0.06	0.20	0.22
32	0.15	0.05	0.14	0.22
33	0.23	0.08	0.32	0.41
34	0.17	0.04	0.13	0.22
35	0.29	0.05	0.34	0.46
36	0.27	0.15	0.32	0.44
37	0.29	0.09	0.48	0.57
38	0.31	0.11	0.06	0.33
39	0.06	0.33	0.13	0.36
40	0.15	0.37	0.07	0.40

Model ID	RMSE-X (m)	RMSE-Y (m)	RMSE-Z (m)	Total (m)
41	0.13	0.35	0.11	0.39
42	0.04	0.28	0.33	0.43
43	0.11	0.26	0.21	0.35
44	0.06	0.31	0.29	0.43
45	0.23	0.34	0.21	0.46
46	0.07	0.34	0.11	0.37
47	0.24	0.25	0.29	0.46
48	0.18	0.22	0.25	0.38
49	0.07	0.29	0.05	0.30
50	0.16	0.25	0.49	0.57
51	0.89	0.14	0.43	1.00
52	0.11	0.17	0.40	0.44
53	0.20	0.36	0.79	0.89
54	0.33	0.21	1.09	1.16
55	0.17	0.22	0.97	1.01
56	0.17	0.25	0.92	0.96
57	0.17	0.21	0.88	0.92
58	0.19	0.08	0.88	0.90
59	0.11	0.15	0.69	0.71
60	0.03	0.21	0.79	0.81
61	0.12	0.35	0.76	0.85
62	0.08	0.10	0.68	0.69
63	0.04	0.27	0.67	0.72
64	0.04	0.15	0.63	0.65
65	0.14	0.22	0.72	0.77
66	0.30	0.20	0.43	0.56
67	0.23	0.14	0.54	0.60
68	0.23	0.25	0.59	0.68
69	0.08	0.20	0.70	0.74
70	0.14	0.16	0.62	0.66
71	0.11	0.13	0.39	0.42
72	0.21	0.33	0.83	0.91
73	0.26	0.35	0.97	1.06
74	0.10	0.38	0.96	1.04
75	0.04	0.06	0.79	0.79

TABLE A.7: RMSE computed from gravity centers of homologous planes for aerial images.

Model ID	RMSE-X (m)	RMSE-Y (m)	RMSE-Z (m)	Total (m)
7	0.45	0.28	0.44	0.69
8	0.74	0.43	1.37	1.61
9	0.44	0.30	0.92	1.06
10	0.95	0.67	1.01	1.54
11	1.08	0.76	1.43	1.95
12	1.15	1.39	0.89	2.01
13	0.82	0.54	0.91	1.34
14	0.78	0.65	1.21	1.58
15	0.59	0.42	1.00	1.23
18	0.74	1.11	0.72	1.52
20	0.76	0.39	0.76	1.14
22	0.67	0.58	0.90	1.26
23	0.57	0.48	1.31	1.50
24	0.39	0.25	0.86	0.98
25	0.24	0.14	0.83	0.88
26	0.22	0.18	0.87	0.92
27	0.13	0.24	0.66	0.72
28	0.26	0.58	0.77	1.00
29	0.31	0.81	1.27	1.53
30	0.33	0.46	1.00	1.15
31	0.22	0.23	0.56	0.64
32	0.25	0.44	1.05	1.16
33	0.26	0.25	0.71	0.80
34	0.14	0.20	0.66	0.70
35	0.27	0.35	1.21	1.28
36	0.34	0.28	1.14	1.22

TABLE A.8: RMSE computed from gravity centers of homologous planes for combination of airborne imagery and LiDAR datasets.

Model ID	RMSE-X (m)	RMSE-Y (m)	RMSE-Z (m)	Total (m)
24	1.34	1.28	1.16	2.19
25	0.86	0.86	1.09	1.64
26	0.70	1.12	1.07	1.70
27	0.29	0.83	0.94	1.28
28	0.58	1.00	0.93	1.48
29	0.29	0.96	0.94	1.38
31	0.46	0.79	0.91	1.29
32	0.64	1.05	0.98	1.57

TABLE A.9: RMSE computed from gravity centers of homologous planes for LiDAR dataset.

Appendix B

Surface quality indices

In this part, surface quality indices of building models are shown. These quality indices are in raster and vector data structure. The surface quality indices are results of three tests. The first test, table B.1 and table B.4, is applied for 75 3D building models have been reconstructed based on the photogrammetric processing in vector and raster data structure. The second test, table B.2 and B.5, is applied to 26 3D building models have been reconstructed based on the combination of both. Third test, table B.3 and table B.6, is applied for 8 3D building models have been reconstructed based on the LiDAR processing.

Model ID	ρ_d	ρ_q	ρ_b	ρ_m	ρ_f
1	0.929	0.855	0.088	0.102	0.091
2	0.934	0.877	0.079	0.082	0.071
3	0.948	0.877	0.059	0.104	0.093
4	0.927	0.889	0.080	0.048	0.044
5	0.906	0.848	0.112	0.076	0.068
6	0.958	0.887	0.047	0.091	0.084
7	0.889	0.831	0.132	0.088	0.076
8	0.959	0.846	0.043	0.141	0.136
9	0.978	0.953	0.022	0.028	0.027
10	0.981	0.935	0.019	0.052	0.051
11	0.769	0.717	0.095	0.068	0.136
12	0.984	0.955	0.017	0.030	0.030
13	0.976	0.954	0.024	0.025	0.024
14	0.952	0.890	0.053	0.081	0.074
15	0.814	0.708	0.050	0.066	0.242
16	0.860	0.724	0.249	0.485	0.306
17	0.913	0.848	0.098	0.089	0.080
18	0.833	0.761	0.403	0.222	0.121
19	0.915	0.865	0.112	0.087	0.069
20	0.903	0.766	0.121	0.272	0.222
21	0.958	0.924	0.046	0.043	0.039
22	0.919	0.881	0.089	0.047	0.043
23	0.888	0.783	0.142	0.193	0.156
24	0.946	0.908	0.059	0.048	0.044
25	0.933	0.883	0.076	0.068	0.061
26	0.938	0.904	0.068	0.043	0.039
27	0.943	0.910	0.064	0.044	0.040
28	0.977	0.947	0.025	0.033	0.032
29	0.962	0.931	0.040	0.035	0.033
30	0.943	0.912	0.062	0.040	0.037
31	0.980	0.950	0.021	0.033	0.032
32	0.971	0.936	0.031	0.041	0.039
33	0.950	0.909	0.055	0.050	0.046
34	0.975	0.949	0.026	0.029	0.028
35	0.982	0.953	0.019	0.031	0.030
36	0.971	0.942	0.030	0.033	0.032
37	0.936	0.858	0.075	0.144	0.120
38	0.960	0.930	0.043	0.036	0.034
39	0.980	0.956	0.021	0.026	0.026
40	0.963	0.932	0.040	0.036	0.034

Model ID	ρ_d	ρ_q	ρ_b	ρ_m	ρ_f
41	0.913	0.887	0.098	0.035	0.031
42	0.942	0.884	0.066	0.077	0.070
43	0.940	0.918	0.065	0.025	0.024
44	0.918	0.881	0.092	0.047	0.042
45	0.846	0.785	0.189	0.104	0.085
46	0.962	0.926	0.041	0.043	0.041
47	0.950	0.924	0.053	0.031	0.029
48	0.962	0.943	0.041	0.023	0.021
49	0.936	0.905	0.080	0.060	0.046
50	0.950	0.884	0.053	0.080	0.076
51	0.817	0.776	0.251	0.064	0.052
52	0.950	0.884	0.053	0.080	0.076
53	0.920	0.908	0.087	0.015	0.014
54	0.953	0.917	0.049	0.042	0.040
55	0.976	0.949	0.025	0.029	0.028
56	0.974	0.949	0.026	0.028	0.027
57	0.958	0.865	0.045	0.147	0.135
58	0.980	0.952	0.021	0.029	0.029
59	0.968	0.958	0.034	0.010	0.010
60	0.968	0.935	0.033	0.037	0.036
61	0.954	0.926	0.049	0.031	0.030
62	0.958	0.930	0.044	0.032	0.031
63	0.960	0.938	0.042	0.024	0.023
64	0.976	0.950	0.025	0.028	0.027
65	0.972	0.934	0.029	0.043	0.042
66	0.921	0.885	0.088	0.051	0.044
67	0.937	0.895	0.071	0.054	0.049
68	0.935	0.891	0.073	0.065	0.057
69	0.890	0.807	0.131	0.123	0.107
70	0.905	0.836	0.111	0.097	0.085
71	0.920	0.882	0.088	0.050	0.045
72	0.937	0.869	0.071	0.094	0.085
73	0.951	0.905	0.053	0.054	0.051
74	0.971	0.918	0.030	0.061	0.059
75	0.980	0.947	0.021	0.037	0.036

TABLE B.1: 2D quality indices based on vector models reconstructed from airborne imagery.

Model ID	ρ_d	ρ_q	ρ_b	ρ_m	ρ_f
7	0.973	0.880	0.028	0.109	0.107
8	0.863	0.706	0.164	0.262	0.225
9	0.939	0.906	0.065	0.040	0.037
10	0.917	0.720	0.091	0.308	0.286
11	0.754	0.660	0.468	0.295	0.165
12	0.921	0.780	0.086	0.206	0.190
13	0.928	0.868	0.078	0.075	0.069
14	0.814	0.717	0.276	0.227	0.158
15	0.813	0.728	0.291	0.231	0.146
18	0.825	0.625	0.230	0.562	0.436
20	0.863	0.771	0.171	0.157	0.128
22	0.773	0.698	0.379	0.255	0.145
23	0.781	0.681	0.284	0.198	0.151
24	0.859	0.815	0.174	0.069	0.057
25	0.863	0.819	0.165	0.074	0.060
26	0.823	0.780	0.240	0.090	0.064
27	0.888	0.825	0.138	0.116	0.092
28	0.892	0.845	0.124	0.069	0.060
29	0.889	0.821	0.127	0.098	0.086
30	0.809	0.718	0.280	0.228	0.156
31	0.913	0.885	0.100	0.035	0.032
32	0.889	0.815	0.127	0.108	0.094
33	0.847	0.820	0.187	0.042	0.034
34	0.846	0.824	0.189	0.035	0.028
35	0.932	0.888	0.073	0.054	0.050
36	0.937	0.888	0.068	0.059	0.056

TABLE B.2: 2D quality indices based on vector building models reconstructed from integration of airborne imagery and LiDAR datasets.

Model ID	ρ_d	ρ_q	ρ_b	ρ_m	ρ_f
24	0.773	0.653	0.357	0.310	0.206
25	0.807	0.680	0.274	0.321	0.221
26	0.746	0.651	0.366	0.230	0.158
27	0.866	0.755	0.178	0.188	0.154
28	0.915	0.753	0.096	0.270	0.248
29	0.895	0.760	0.124	0.209	0.186
31	0.904	0.774	0.109	0.190	0.172
32	0.810	0.663	0.245	0.285	0.235

TABLE B.3: 2D quality indices based on vector building models reconstructed from LiDAR dataset.

Model ID	ρd	ρq	ρb	ρm	ρf	ρqw
1	0.937	0.870	0.079	0.093	0.083	0.627
2	0.959	0.919	0.043	0.048	0.046	0.712
3	0.948	0.877	0.059	0.104	0.092	0.733
4	0.927	0.889	0.080	0.048	0.044	0.693
5	0.913	0.862	0.103	0.067	0.060	0.689
6	0.987	0.935	0.014	0.056	0.056	0.603
7	0.896	0.843	0.124	0.081	0.069	0.689
8	0.959	0.846	0.043	0.141	0.136	0.604
9	0.979	0.953	0.021	0.028	0.027	0.733
10	0.982	0.935	0.018	0.052	0.051	0.799
11	0.837	0.790	0.228	0.093	0.067	0.577
12	0.984	0.956	0.016	0.030	0.030	0.854
13	0.977	0.954	0.024	0.024	0.024	0.776
14	0.966	0.915	0.037	0.065	0.060	0.753
15	0.939	0.849	0.076	0.136	0.118	0.657
16	0.911	0.768	0.103	0.297	0.255	0.578
17	0.751	0.702	0.123	0.112	0.433	0.520
18	0.859	0.791	0.231	0.127	0.097	0.569
19	0.933	0.891	0.081	0.059	0.051	0.688
20	0.903	0.766	0.121	0.272	0.222	0.540
21	0.958	0.924	0.046	0.043	0.039	0.683
22	0.920	0.882	0.088	0.047	0.043	0.781
23	0.927	0.834	0.084	0.130	0.117	0.594
24	0.955	0.924	0.049	0.038	0.036	0.752
25	0.933	0.884	0.076	0.068	0.061	0.703
26	0.950	0.925	0.054	0.029	0.027	0.825
27	0.944	0.911	0.063	0.044	0.039	0.730
28	0.977	0.948	0.024	0.032	0.031	0.738
29	0.962	0.932	0.040	0.034	0.033	0.706
30	0.955	0.932	0.048	0.028	0.026	0.769
31	0.983	0.955	0.018	0.030	0.030	0.800
32	0.975	0.943	0.027	0.038	0.036	0.783
33	0.950	0.910	0.054	0.049	0.046	0.754
34	0.975	0.949	0.026	0.029	0.028	0.811
35	0.982	0.954	0.018	0.030	0.030	0.709
36	0.972	0.943	0.029	0.032	0.031	0.723
37	0.936	0.858	0.075	0.144	0.120	0.703
38	0.960	0.930	0.042	0.036	0.034	0.771
39	0.987	0.968	0.014	0.020	0.019	0.672
40	0.962	0.930	0.041	0.037	0.035	0.675

Model ID	ρd	ρq	ρb	ρm	ρf	ρqw
41	0.913	0.887	0.098	0.035	0.031	0.712
42	0.950	0.897	0.055	0.066	0.061	0.780
43	0.940	0.918	0.065	0.025	0.024	0.766
44	0.883	0.824	0.171	0.271	0.154	0.643
45	0.860	0.804	0.167	0.083	0.071	0.633
46	0.968	0.937	0.034	0.036	0.035	0.819
47	0.954	0.932	0.049	0.027	0.025	0.750
48	0.961	0.942	0.041	0.023	0.022	0.759
49	0.966	0.952	0.036	0.016	0.016	0.754
50	0.915	0.852	0.095	0.083	0.075	0.658
51	0.817	0.776	0.251	0.063	0.052	0.455
52	0.950	0.884	0.053	0.080	0.075	0.653
53	0.921	0.908	0.087	0.015	0.014	0.800
54	0.954	0.918	0.048	0.042	0.040	0.684
55	0.977	0.950	0.024	0.028	0.028	0.669
56	0.975	0.949	0.026	0.027	0.027	0.571
57	0.958	0.865	0.045	0.147	0.135	0.573
58	0.980	0.953	0.021	0.029	0.028	0.642
59	0.968	0.959	0.033	0.009	0.009	0.673
60	0.969	0.936	0.032	0.037	0.036	0.723
61	0.954	0.927	0.048	0.031	0.029	0.684
62	0.970	0.951	0.031	0.021	0.020	0.593
63	0.961	0.939	0.041	0.024	0.023	0.640
64	0.976	0.952	0.025	0.027	0.026	0.679
65	0.973	0.935	0.028	0.042	0.041	0.725
66	0.922	0.886	0.088	0.050	0.044	0.763
67	0.944	0.908	0.060	0.045	0.042	0.798
68	0.935	0.892	0.072	0.065	0.057	0.748
69	0.890	0.807	0.131	0.123	0.107	0.642
70	0.905	0.837	0.110	0.096	0.085	0.680
71	0.920	0.882	0.088	0.050	0.045	0.645
72	0.964	0.912	0.038	0.060	0.058	0.707
73	0.951	0.906	0.052	0.052	0.050	0.732
74	0.972	0.918	0.029	0.061	0.059	0.710
75	0.981	0.949	0.020	0.035	0.034	0.701

TABLE B.4: 2D quality indices based on raster building models reconstructed from airborne imagery.

Model ID	ρd	ρq	ρb	ρm	ρf	ρqw
7	0.973	0.880	0.028	0.109	0.107	0.607
8	0.863	0.706	0.164	0.261	0.224	0.370
9	0.939	0.907	0.065	0.039	0.037	0.755
10	0.918	0.720	0.091	0.308	0.286	0.330
11	0.754	0.661	0.468	0.294	0.165	0.357
12	0.921	0.780	0.086	0.206	0.189	0.482
13	0.928	0.869	0.077	0.075	0.069	0.618
14	0.827	0.732	0.239	0.193	0.145	0.411
15	0.813	0.728	0.291	0.231	0.146	0.439
18	0.883	0.683	0.139	0.423	0.379	0.395
20	0.885	0.803	0.138	0.125	0.106	0.639
22	0.832	0.772	0.224	0.115	0.086	0.471
23	0.781	0.682	0.283	0.198	0.151	0.446
24	0.860	0.817	0.173	0.069	0.057	0.591
25	0.864	0.820	0.164	0.074	0.060	0.623
26	0.839	0.803	0.200	0.059	0.048	0.629
27	0.937	0.900	0.068	0.047	0.043	0.733
28	0.898	0.854	0.117	0.063	0.055	0.631
29	0.891	0.824	0.125	0.096	0.084	0.518
30	0.854	0.784	0.207	0.158	0.111	0.640
31	0.913	0.886	0.099	0.035	0.032	0.736
32	0.890	0.817	0.126	0.107	0.094	0.705
33	0.848	0.821	0.186	0.042	0.034	0.655
34	0.846	0.824	0.188	0.035	0.028	0.589
35	0.933	0.890	0.072	0.053	0.049	0.565
36	0.937	0.888	0.067	0.059	0.055	0.570

TABLE B.5: 2D quality indices based on raster building models reconstructed from combination of airborne imagery and LiDAR datasets.

Model ID	ρd	ρq	ρb	ρm	ρf	ρqw
24	0.774	0.654	0.357	0.310	0.206	0.401
25	0.808	0.680	0.273	0.321	0.221	0.479
26	0.747	0.652	0.365	0.229	0.158	0.450
27	0.867	0.756	0.177	0.188	0.154	0.573
28	0.922	0.762	0.086	0.259	0.240	0.498
29	0.895	0.761	0.123	0.209	0.186	0.552
31	0.904	0.774	0.108	0.190	0.172	0.561
32	0.810	0.663	0.245	0.284	0.235	0.439

TABLE B.6: 2D quality indices based on raster building models reconstructed from LiDAR dataset.

Appendix C

Volume quality indices

In this part, volume quality indices of building models are shown. These quality indices are in raster and vector data structure. The volume quality indices are results of three tests. The first test, table C.1 and table C.4, is applied for 75 3D building models have been reconstructed based on the photogrammetric processing in vector and raster data structure. The second test, table C.2 and C.5, is applied to 26 3D building models have been reconstructed based on the combination of both. Third test, table C.3 and table C.6, is applied for 8 3D building models have been reconstructed based on the LiDAR processing.

Model ID	V_{pd}	V_{pq}	V_{pb}	V_{pm}	V_{pf}
1	0.992	0.921	0.008	0.078	0.078
2	0.956	0.926	0.047	0.034	0.032
3	0.946	0.849	0.057	0.120	0.114
4	0.922	0.882	0.084	0.049	0.045
5	0.931	0.878	0.074	0.065	0.060
6	0.984	0.931	0.016	0.058	0.057
7	0.944	0.918	0.059	0.031	0.029
8	0.942	0.786	0.062	0.210	0.198
9	0.967	0.929	0.034	0.043	0.041
10	0.973	0.904	0.028	0.078	0.076
11	0.868	0.833	0.152	0.048	0.042
12	0.977	0.938	0.023	0.043	0.042
13	0.964	0.930	0.037	0.038	0.037
14	0.981	0.923	0.020	0.064	0.063
15	0.968	0.881	0.033	0.102	0.099
16	0.912	0.823	0.097	0.119	0.108
17	0.911	0.859	0.098	0.066	0.060
18	0.904	0.841	0.106	0.083	0.075
19	0.973	0.931	0.028	0.046	0.045
20	0.969	0.869	0.032	0.119	0.115
21	0.968	0.953	0.033	0.016	0.016
22	0.881	0.830	0.135	0.070	0.062
23	0.841	0.692	0.189	0.257	0.216
24	0.953	0.918	0.049	0.041	0.039
25	0.923	0.876	0.084	0.058	0.053
26	0.940	0.912	0.063	0.033	0.031
27	0.956	0.926	0.046	0.034	0.032
28	0.981	0.952	0.019	0.031	0.030
29	0.945	0.902	0.058	0.051	0.048
30	0.934	0.903	0.071	0.037	0.034
31	0.980	0.950	0.020	0.033	0.032
32	0.979	0.956	0.021	0.025	0.024
33	0.967	0.929	0.034	0.042	0.041
34	0.987	0.965	0.013	0.023	0.023
35	0.973	0.931	0.028	0.046	0.045
36	0.957	0.914	0.044	0.050	0.048
37	0.952	0.920	0.051	0.036	0.034
38	0.961	0.937	0.040	0.027	0.026
39	0.980	0.953	0.021	0.029	0.029
40	0.973	0.934	0.027	0.043	0.042

Model ID	V_{pd}	V_{pq}	V_{pb}	V_{pm}	V_{pf}
41	0.917	0.890	0.090	0.034	0.031
42	0.972	0.916	0.029	0.063	0.062
43	0.940	0.924	0.064	0.018	0.017
44	0.933	0.902	0.072	0.036	0.034
45	0.834	0.800	0.199	0.051	0.042
46	0.971	0.946	0.030	0.028	0.027
47	0.948	0.934	0.054	0.016	0.015
48	0.952	0.934	0.051	0.020	0.019
49	0.970	0.957	0.031	0.013	0.013
50	0.873	0.785	0.145	0.128	0.112
51	0.722	0.676	0.385	0.095	0.069
52	0.926	0.832	0.080	0.122	0.113
53	0.883	0.866	0.132	0.022	0.020
54	0.931	0.878	0.074	0.065	0.060
55	0.964	0.924	0.038	0.044	0.043
56	0.962	0.925	0.039	0.042	0.041
57	0.964	0.882	0.037	0.096	0.093
58	0.971	0.932	0.030	0.043	0.042
59	0.952	0.938	0.051	0.016	0.015
60	0.953	0.904	0.049	0.057	0.054
61	0.931	0.892	0.074	0.048	0.044
62	0.955	0.928	0.047	0.031	0.029
63	0.943	0.915	0.061	0.033	0.031
64	0.965	0.927	0.036	0.042	0.041
65	0.960	0.905	0.042	0.063	0.061
66	0.921	0.888	0.086	0.041	0.037
67	0.950	0.909	0.052	0.048	0.046
68	0.944	0.910	0.060	0.039	0.037
69	0.926	0.845	0.080	0.104	0.097
70	0.923	0.853	0.083	0.089	0.082
71	0.913	0.881	0.096	0.040	0.036
72	0.950	0.878	0.052	0.086	0.082
73	0.930	0.868	0.075	0.077	0.072
74	0.959	0.883	0.042	0.090	0.087
75	0.970	0.922	0.031	0.054	0.052

TABLE C.1: 3D quality indices based on vector building models reconstructed from airborne imagery.

Model ID	V_{pd}	V_{pq}	V_{pb}	V_{pm}	V_{pf}
7	0.797	0.704	0.254	0.167	0.133
8	0.897	0.733	0.115	0.249	0.224
9	0.942	0.923	0.061	0.022	0.021
10	0.897	0.640	0.114	0.448	0.402
11	0.828	0.747	0.208	0.131	0.108
12	0.910	0.727	0.099	0.276	0.251
13	0.915	0.847	0.093	0.087	0.080
14	0.891	0.824	0.122	0.091	0.081
15	0.875	0.826	0.143	0.068	0.059
18	0.859	0.730	0.165	0.206	0.177
20	0.924	0.853	0.082	0.090	0.083
22	0.880	0.859	0.137	0.027	0.023
23	0.751	0.659	0.331	0.187	0.141
24	0.859	0.821	0.164	0.054	0.046
25	0.822	0.773	0.217	0.076	0.063
26	0.759	0.717	0.318	0.076	0.058
27	0.919	0.879	0.089	0.049	0.045
28	0.857	0.794	0.167	0.092	0.079
29	0.934	0.908	0.071	0.030	0.028
30	0.906	0.881	0.104	0.031	0.028
31	0.916	0.888	0.092	0.035	0.032
32	0.917	0.889	0.091	0.034	0.031
33	0.830	0.809	0.204	0.032	0.026
34	0.785	0.773	0.273	0.021	0.016
35	0.940	0.909	0.064	0.036	0.034
36	0.948	0.912	0.054	0.042	0.040

TABLE C.2: 3D quality indices based on vector building models reconstructed from combination of airborne imagery and LiDAR datasets.

Model ID	V_{pd}	V_{pq}	V_{pb}	V_{pm}	V_{pf}
24	0.746	0.613	0.340	0.290	0.217
25	0.801	0.648	0.249	0.294	0.235
26	0.713	0.604	0.403	0.252	0.180
27	0.900	0.772	0.111	0.185	0.166
28	0.915	0.756	0.093	0.229	0.209
29	0.884	0.748	0.131	0.205	0.182
31	0.888	0.733	0.126	0.238	0.211
32	0.742	0.615	0.347	0.278	0.207

TABLE C.3: 3D quality indices based on vector building models reconstructed from LiDAR datasets.

Model ID	$V_{\rho d}$	$V_{\rho q}$	$V_{\rho b}$	$V_{\rho m}$	$V_{\rho f}$	$V_{\rho qw}$
1	0.976	0.897	0.025	0.091	0.088	0.862
2	0.934	0.888	0.071	0.056	0.052	0.865
3	0.957	0.865	0.045	0.111	0.107	0.864
4	0.908	0.861	0.101	0.060	0.055	0.834
5	0.913	0.858	0.095	0.071	0.064	0.840
6	0.948	0.870	0.055	0.094	0.089	0.869
7	0.942	0.918	0.061	0.028	0.026	0.869
8	0.925	0.765	0.081	0.226	0.209	0.791
9	0.961	0.919	0.041	0.048	0.046	0.866
10	0.961	0.879	0.041	0.097	0.093	0.855
11	0.863	0.827	0.159	0.049	0.043	0.801
12	0.972	0.928	0.029	0.049	0.048	0.879
13	0.956	0.912	0.046	0.051	0.049	0.867
14	0.975	0.911	0.026	0.072	0.070	0.871
15	0.959	0.865	0.042	0.114	0.109	0.853
16	0.899	0.803	0.112	0.133	0.119	0.791
17	0.908	0.854	0.102	0.069	0.063	0.835
18	0.913	0.856	0.095	0.073	0.067	0.837
19	0.967	0.920	0.034	0.053	0.052	0.875
20	0.963	0.863	0.039	0.120	0.116	0.811
21	0.965	0.948	0.037	0.018	0.017	0.885
22	0.864	0.802	0.157	0.090	0.078	0.832
23	0.824	0.666	0.213	0.287	0.237	0.733
24	0.937	0.889	0.067	0.057	0.053	0.854
25	0.908	0.851	0.101	0.074	0.067	0.831
26	0.920	0.880	0.086	0.050	0.046	0.844
27	0.938	0.893	0.066	0.054	0.050	0.859
28	0.966	0.923	0.035	0.048	0.047	0.874
29	0.907	0.840	0.103	0.087	0.079	0.839
30	0.938	0.910	0.066	0.033	0.031	0.866
31	0.980	0.948	0.021	0.034	0.034	0.884
32	0.975	0.946	0.025	0.031	0.030	0.879
33	0.960	0.917	0.041	0.049	0.047	0.871
34	0.969	0.929	0.032	0.044	0.043	0.884
35	0.939	0.861	0.065	0.096	0.091	0.862
36	0.924	0.860	0.082	0.081	0.075	0.852
37	0.951	0.919	0.052	0.036	0.034	0.870
38	0.958	0.929	0.044	0.032	0.030	0.875
39	0.941	0.871	0.062	0.086	0.081	0.856
40	0.943	0.865	0.060	0.096	0.090	0.856

Model ID	$V_{\rho d}$	$V_{\rho q}$	$V_{\rho b}$	$V_{\rho m}$	$V_{\rho f}$	$V_{\rho qw}$
41	0.878	0.811	0.139	0.094	0.083	0.818
42	0.958	0.891	0.044	0.079	0.075	0.849
43	0.938	0.917	0.066	0.024	0.023	0.857
44	0.913	0.867	0.096	0.058	0.053	0.844
45	0.822	0.780	0.217	0.065	0.053	0.783
46	0.961	0.932	0.040	0.032	0.031	0.863
47	0.937	0.917	0.068	0.023	0.022	0.848
48	0.948	0.930	0.055	0.021	0.020	0.861
49	0.967	0.956	0.034	0.012	0.012	0.873
50	0.745	0.607	0.341	0.306	0.228	0.671
51	0.615	0.530	0.625	0.262	0.161	0.462
52	0.844	0.728	0.185	0.188	0.159	0.751
53	0.873	0.856	0.146	0.022	0.019	0.792
54	0.908	0.830	0.101	0.104	0.094	0.797
55	0.946	0.890	0.057	0.067	0.063	0.836
56	0.941	0.886	0.063	0.066	0.062	0.843
57	0.925	0.799	0.081	0.170	0.158	0.795
58	0.954	0.903	0.048	0.059	0.056	0.847
59	0.931	0.898	0.074	0.040	0.037	0.850
60	0.898	0.807	0.113	0.126	0.114	0.799
61	0.871	0.778	0.148	0.137	0.119	0.779
62	0.901	0.836	0.110	0.087	0.078	0.822
63	0.846	0.769	0.181	0.119	0.100	0.771
64	0.919	0.863	0.088	0.071	0.065	0.833
65	0.920	0.841	0.087	0.102	0.094	0.811
66	0.900	0.858	0.111	0.054	0.049	0.819
67	0.922	0.855	0.085	0.085	0.078	0.825
68	0.926	0.885	0.080	0.050	0.047	0.833
69	0.843	0.710	0.187	0.221	0.186	0.734
70	0.882	0.789	0.134	0.134	0.118	0.788
71	0.847	0.764	0.180	0.130	0.110	0.786
72	0.890	0.765	0.123	0.183	0.163	0.782
73	0.900	0.821	0.112	0.106	0.095	0.768
74	0.892	0.769	0.121	0.180	0.160	0.762
75	0.924	0.848	0.083	0.096	0.089	0.829

TABLE C.4: 3D quality indices based on raster building models reconstructed from airborne imagery datasets.

Model ID	$V_{\rho d}$	$V_{\rho q}$	$V_{\rho b}$	$V_{\rho m}$	$V_{\rho f}$	$V_{\rho qw}$
7	0.810	0.691	0.235	0.211	0.171	0.595
8	0.815	0.609	0.227	0.415	0.338	0.549
9	0.911	0.863	0.097	0.062	0.056	0.808
10	0.882	0.615	0.133	0.494	0.436	0.511
11	0.788	0.683	0.269	0.195	0.154	0.607
12	0.884	0.689	0.131	0.321	0.284	0.545
13	0.889	0.811	0.125	0.108	0.096	0.758
14	0.851	0.755	0.174	0.150	0.128	0.698
15	0.840	0.765	0.190	0.117	0.098	0.726
18	0.868	0.739	0.153	0.200	0.174	0.699
20	0.889	0.799	0.125	0.127	0.113	0.754
22	0.853	0.811	0.172	0.061	0.052	0.763
23	0.687	0.571	0.456	0.296	0.203	0.562
24	0.824	0.777	0.214	0.073	0.060	0.709
25	0.810	0.737	0.235	0.122	0.099	0.680
26	0.759	0.698	0.317	0.115	0.087	0.603
27	0.920	0.862	0.087	0.073	0.067	0.798
28	0.922	0.885	0.085	0.045	0.041	0.823
29	0.821	0.716	0.218	0.179	0.147	0.633
30	0.843	0.771	0.187	0.111	0.093	0.713
31	0.882	0.838	0.133	0.061	0.053	0.779
32	0.852	0.773	0.173	0.121	0.103	0.717
33	0.825	0.785	0.211	0.062	0.052	0.743
34	0.785	0.731	0.273	0.095	0.075	0.669
35	0.874	0.796	0.144	0.112	0.098	0.764
36	0.901	0.822	0.109	0.107	0.097	0.767

TABLE C.5: 3D quality indices based on raster building models reconstructed from combination of airborne imagery and LiDAR datasets.

Model ID	$V_{\rho d}$	$V_{\rho q}$	$V_{\rho b}$	$V_{\rho m}$	$V_{\rho f}$	$V_{\rho qw}$
24	0.746	0.613	0.340	0.290	0.217	0.513
25	0.801	0.648	0.249	0.294	0.235	0.583
26	0.713	0.604	0.403	0.252	0.180	0.531
27	0.900	0.772	0.111	0.185	0.166	0.695
28	0.915	0.756	0.093	0.229	0.209	0.654
29	0.884	0.748	0.131	0.205	0.182	0.683
31	0.888	0.733	0.126	0.238	0.211	0.672
32	0.742	0.615	0.347	0.278	0.207	0.543

TABLE C.6: 3D quality indices based on raster building models reconstructed from LiDAR dataset.

Appendix D

Publications

Parts of this study were published in the following papers:

Mohamed, M., Grussenmeyer, P., 2011. Plane-based accuracy assessment in photogrammetry: comparison of Rollei Medium format and Ultracam-X digital cameras. GTC2011 Symposium, "Geomatics in the City", Jeddah, Saudia Arabia, May 11-13, 6 pages.

Zhang, W., Grussenmeyer, P., Yan, G., Mohamed, M., 2011. Primitive-based building reconstruction by integration of Lidar data and optical imagery, International Archives of Photogrammetry, Remote Sensing and Spatial Information Sciences, Calgary, Canada, Vol.38(5/W12), 6 pages.

Zhou, G., Yan, K., Zhang, W., Yan, G., Chen, Y., Grussenmeyer, P., Mohamed, M., 2012. Comparison of 3D buildings reconstructed by different data sources. Geoscience and Remote Sensing Symposium (IGARSS), 2012 IEEE International, pp.6001-6004, 22-27 July 2012 doi: 10.1109/IGARSS.2012.6352240

Landes, T., Grussenmeyer, P., Boulaassal, H., Mohamed, M., 2012. Assessment of threedimensional Models Derived from LIDAR and TLS Data. The XXII ISPRS Congress in Melbourne, Australia 25th August to 1st September 2012, Vol.XXXIX-B2, pp.95-100, 2012.

Mohamed, M., Landes, T., Grussenmeyer, P., Zhang, W., 2013. Multi-dimensional quality assessment of photogrammetric and LiDAR datasets based on a vector approach. International Archives of the Photogrammetry, Remote Sensing and Spatial Information Sciences, Vol. XL- 2/W1, 6 pages. 8th International Symposium on Spatial Data Quality, 30 May - 1 June 2013, Hong Kong.

PLANE-BASED ACCURACY ASSESSMENT IN PHOTOGRAMMETRY: COMPARISON OF ROLLEI MEDIUM FORMAT AND ULTRACAM-X DIGITAL CAMERAS

Mostafa Mohamed and Pierre Grussenmeyer

The Images Sciences, Computer Sciences and Remote Sensing Laboratory (LSIIT)
Photogrammetry and Geomatics Group
INSA Strasbourg
24, Boulevard de la Victoire 67000 Strasbourg, France
mostafa.mohamed | pierre.grussenmeyer@insa-strasbourg.fr

KEY WORDS: : Digital Imagery, Photogrammetry, Orientation, Plane Accuracy, Assessment, Quality

ABSTRACT:

Accuracy assessment of photogrammetry output is one of the most important steps in evaluating imaging sensor data. Without an accuracy assessment, the output or results are of little value. As the performance of data acquisition methods improves, the quality evaluation of building data in 3D city modeling has become an important issue. A simple method to evaluate photogrammetric data is based on the comparison of 3D objects to accurate reference measurements. In this paper we report on the comparison of such data from Rollei medium format and UltraCam-X cameras. Our approach is focused on characteristic planes extracted from both datasets. In a first step, the reference dataset has been created from UltraCam-X stereopairs. Ground Control Points (GCPs) were measured by GNSS systems in the city of Strasbourg. The calculation of the exterior orientation parameters using a photogrammetric bundle adjustment was carried out from those GCPs. 3D ground coordinates have been generated afterwards by photogrammetric matching algorithms. Secondly, the data to be assessed have been created from Rollei medium format images in the same way. For the plane accuracy estimation, samples of planes based on characteristic points have been processed from both cameras. UltraCam-X digital images deliver the reference data. Quality has been assessed by calculating a set of indices of our photogrammetric data. Some of these indices are the detection rate, quality rate, miss factor, false alarm rate, and branch factor. These factors are depending on the relations between the intersection or union areas for the reference and tested data.

1 INTRODUCTION

Originally, the term photogrammetry, according to the American Society for Photogrammetry and Remote Sensing is the art, science and technology of obtaining reliable information about physical objects and the environment through processes of recording. Photogrammetry has dealt for many years with the 3D reconstruction of objects from one or more images. It provides accurate sensor calibration and object modeling using analog or digital images. Several commercial software packages are available for image processing and 3D modeling. There are many applications for photogrammetry such as mapping production, land surveying, extraction of Digital Elevation Model (DTM) and Orthorectification. These applications are not especially new but need accurate data and methods in order to obtain good results. Quality evaluation is important for several reasons. Firstly, it may give important information about deficiencies of an approach and may take place to help in focusing a further research activity. Secondly, quality evaluation is needed in order to compare the results of the different approaches and to convince a user, that an approach can be used in an operational workflow (Schuster and Weidner, 2003).

Much research has been carried out on accuracy assessment for Imagery data. (Grussenmeyer et al., 1994) proposed statistical techniques in order to calculate root mean square errors by point and line based assessment. Also, (Grussenmeyer, 1994) introduced a methodology to assess the photogrammetric data statistically. Recently, empirical tests have been applied by the German Society of Photogrammetry, Remote Sensing and Geoinformation (DGPF) on Digital Airborne Cameras Evaluation (Cramer, 2009 and Cramer, 2010). Evaluation of digital photogrammetric cameras by the generation of Digital Elevation Models (DEM) and the comparisons were carried out from ground truth and airborne Lidar measurements (Haala et al., 2010). All accuracy as-

essment include three fundamental steps (Congalton, 2009):

- Firstly, design the accuracy assessment sample. Sampling design plays a critical role in accuracy assessment;
- Secondly, collecting data for each sample;
- Finally, analyzing the results.

Because high quality reference data are difficult and expensive to obtain, the sampling design issues encountered in accuracy assessment are similar to those traditionally addressed by survey sampling methodology: how to choose sample in a cost-effective and at the same time statistically rigorous manner? Application of basic sampling designs such as simple random, stratified random, systematic and cluster have been summarized in various accuracy assessment papers (Congalton, 2009). Once the reference data are in hand, the next step in accuracy assessment is analysis of these data. The traditional analysis of accuracy assessment begins with detection of errors in the raw data. In this field three approaches for quality evaluation of building models, two of them, namely (McKeown et al., 2000 and Ragia, 2000). Based on their principle ideas, a third approach was developed, taking the good aspects and combining them and introducing alternated quality measurements in (Schuster and Weidner, 2003). While the general emphasis has been to develop methods and tools for automatic, or semi-automatic generation of city models, the concept of quality evaluation has also become very important. No standard solutions are available as yet, although city models are being produced worldwide at a fast rate (Akca et al., 2010).

2 AIM AND OBJECTIVES

Our research into accuracy assessment of 3D data aims at studying the accuracy assessment of photogrammetry outputs. A simple method to evaluate photogrammetric data is based on the comparison of 3D objects to accurate reference measurements.

Our approach is focused on characteristic planes extracted from UltraCam and Rollei camera datasets.

3 THEORY

3.1 Processing of Images

A 3-D orientation process includes the determination of the position and attitude of an object in both coordinate systems. In photogrammetry, the orientations are described as interior and exterior orientations, or as relative and absolute orientations. Interior orientation defines the internal geometry of a camera or sensor as it existed at the time of image capture. Lens distortion deteriorates the positional accuracy of image points located on the image plane. Two types of lens distortion exist: radial and tangential lens distortion. Lens distortion occurs when light rays passing through the lens are bent, thereby changing directions and intersecting the image plane at positions deviant from the norm (ERDAS IMAGINE Version 2011). Exterior orientation defines the position (X_0, Y_0, Z_0) and angular orientation (omega, phi, kappa) of the camera that captured an image. Bundle block adjustment uses the collinearity condition as the basis for formulating the relationship between image space and ground space. For one GCP measured in two overlapping areas, the collinearity equations are.

$$x_{a_1} - x_0 = -f \cdot \frac{m_{11}(X_A - X_{0_1}) + \dots + m_{13}(Z_A - Z_{0_1})}{m_{31}(X_A - X_{0_1}) + \dots + m_{33}(Z_A - Z_{0_1})} \quad (1)$$

$$y_{a_1} - y_0 = -f \cdot \frac{m_{21}(X_A - X_{0_1}) + \dots + m_{23}(Z_A - Z_{0_1})}{m_{31}(X_A - X_{0_1}) + \dots + m_{33}(Z_A - Z_{0_1})} \quad (2)$$

$$x_{a_2} - x_0 = -f \cdot \frac{m'_{11}(X_A - X_{0_2}) + \dots + m'_{13}(Z_A - Z_{0_2})}{m'_{31}(X_A - X_{0_2}) + \dots + m'_{33}(Z_A - Z_{0_2})} \quad (3)$$

$$y_{a_2} - y_0 = -f \cdot \frac{m'_{21}(X_A - X_{0_2}) + \dots + m'_{23}(Z_A - Z_{0_2})}{m'_{31}(X_A - X_{0_2}) + \dots + m'_{33}(Z_A - Z_{0_2})} \quad (4)$$

Where x_a, y_a are image coordinates of point a in images 1 and 2. X, Y, Z are given in the ground coordinate system, m, m' are the parameters of rotation matrix of images 1 and 2, f is a focal length and x_0, y_0 are the image coordinates of principal point.

3.2 Quality Assessment Indices

As mentioned before, the output or results are of little value without an accuracy assessment. The importance of describing the quality of the data enables the contractor to verify measurements and the end users to check the quality of the data with respect to the specifications of the contracts (Schuster and Weidner, 2003). In this section we present some indices that enable the giving of a judgment about the quality of photogrammetric data. As presented in the introduction, there are several approaches for quality evaluation. Here, we can show a summary for these indices in equations 5 to 9 and more details are given in (McKeown et al., 2000; Ragia, 2000; Schuster and Weidner, 2003). Figure 1 shows the relation between the reference surface area (Ar) and the tested surface area (At).

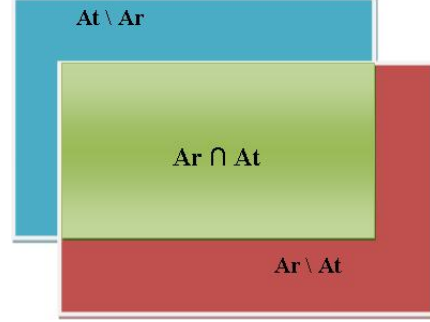


Figure 1: Relationship between reference area (Ar) and tested area (At).

The detection rate (pd) is the ratio between the intersection area between two planes and the reference plane. If the rate is close to 1, then the data will be of good quality.

$$pd = \frac{Ar \cap At}{Ar} \quad pd \in [0 : 1] \quad (5)$$

The branch factor (pb) is the ratio between the area of the reference plane not included in the plane intersection and intersection area between two planes. The factor is always positive and if the factor is close to zero, then the data will be of good quality.

$$pb = \frac{At \setminus Ar}{Ar \cap At} \quad pb \geq 0. \quad (6)$$

The miss factor (pm) is the ratio between the area of the tested plane that is not included in plane intersection and intersection area between two planes. The factor always positive and if the factor is close to zero then the data will be of good quality.

$$pm = \frac{Ar \setminus At}{Ar \cap At} \quad pm \geq 0. \quad (7)$$

The quality rate (pq) is the ratio between the intersection area between two planes and the union of two planes. If the rate is close to 1 is then the data will be of good quality.

$$pq = \frac{Ar \cap At}{Ar \cup At} \quad pq \in [0 : 1] \quad (8)$$

The false alarm rate (pf) is the ratio between the area of the reference plane not included in the plane intersection and the reference plane. The factor is always positive and if the factor is close to zero then the data will be of good quality.

$$pf = \frac{At \setminus Ar}{Ar} \quad pf \geq 0. \quad (9)$$

4 EXPERIMENTAL WORK AND RESULTS

4.1 The Study Site and the Data Used

The study areas of this research are located in the city of Strasbourg, France. Digital aerial images from Ultracam-X (four images) and Rollei (five images) of the same sites were available.

The Leica Photogrammetry Suite (LPS) and KLT software are used for image processing and Matlab is used for computing quality indices. Table.1 shows brief characteristics of the photogrammetric data.

Sensor	Ultracam-X	RolleiDB44
Acquisition date	2007	2004
Focal length (mm)	100.500	80.553
GSD (cm)	16	16
Pixel size (μm)	7.2	9
Flying height (m)	2300	1450
Overlap %	65	60
Base (m)	527	265

Table 1: Brief Characteristics about Photogrammetric Data.

4.2 Acquisition of Images and Image Processing

A block of 4 images was acquired with the UltraCam digital camera, providing an image format of 9420 pixels long track by 14430 pixels cross track. The pixel size of the images is $7.2\mu m$ while in object space it is 16 cm. 9 ground control points were measured with GNNS systems. Also, a set of 5 images in one strip was acquired with the Rollei medium format digital camera, providing an image format of 4080 pixels long track by 4075 pixels cross track. The pixel size of the images is $9\mu m$ while in object space it is 16 cm. 9 ground control points were measured with GNNS systems. Figure 2 shows the distribution of UltraCam-X images surround with large rectangles and Rollei images surround with small rectangles.

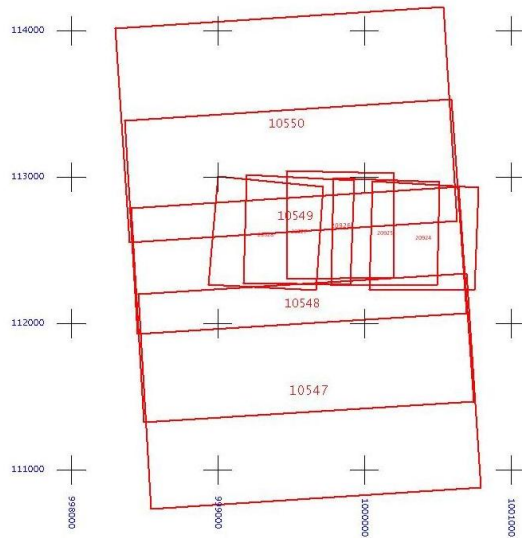


Figure 2: Block of UltraCam-X and Rollei digital images.

The images to be used are digital aerial photographs from the UltraCam and Rollei sensors with unknown imaging orientation parameters. The orientation of the images have to be performed using the Leica Photogrammetry Suite (LPS) and KLT software in order to compute exterior orientation parameters. In our application, the camera information was taken from the calibration sheet given by the camera owner. The exterior orientation approximations were achieved with bundle block adjustment. The

final results of standard deviation for exterior orientation parameters from UltraCam-X and Rollei digital images are presented in Table 2, 3, 4 and 5. The image point standard deviation was 0.3 pixel for the UltraCam and 1.33 pixel for Rollei camera.

Image No	1	2	3	4
σ_{X_0} (m)	0.535	0.533	0.533	0.538
σ_{Y_0} (m)	0.594	0.589	0.591	0.601
σ_{Z_0} (m)	0.339	0.202	0.136	0.22
σ_{OMEGA} (deg)	0.016	0.016	0.016	0.016
σ_{PHI} (deg)	0.014	0.014	0.014	0.014
σ_{KAPPA} (deg)	0.003	0.003	0.003	0.003

Table 2: Accuracy of exterior orientation parameters for UltraCam-X using KLT software package.

Image No	1	2	3	4
σ_{X_0} (m)	0.524	0.521	0.521	0.526
σ_{Y_0} (m)	0.552	0.542	0.544	0.600
σ_{Z_0} (m)	0.314	0.187	0.124	0.200
σ_{OMEGA} (deg)	0.015	0.014	0.014	0.015
σ_{PHI} (deg)	0.017	0.014	0.014	0.014
σ_{KAPPA} (deg)	0.003	0.003	0.003	0.003

Table 3: Accuracy of exterior orientation parameters for UltraCam-X using LPS software package.

Image No	1	2	3	4	5
σ_{X_0} (m)	6.316	3.147	2.383	3.341	5.748
σ_{Y_0} (m)	5.652	5.104	3.866	4.048	4.018
σ_{Z_0} (m)	1.981	0.777	0.554	0.587	0.564
σ_{OMEGA} (deg)	0.222	0.201	0.151	0.158	0.157
σ_{PHI} (deg)	0.251	0.123	0.092	0.130	0.224
σ_{KAPPA} (deg)	0.025	0.016	0.012	0.014	0.023

Table 4: Accuracy of exterior orientation parameters for Rollei using KLT software package.

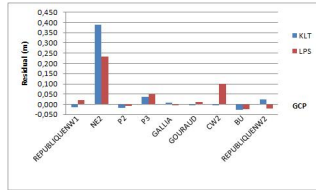
Image No	1	2	3	4	5
σ_{X_0} (m)	5.353	3.608	2.989	3.696	4.835
σ_{Y_0} (m)	6.339	5.962	5.394	5.527	5.925
σ_{Z_0} (m)	1.636	1.087	0.810	0.697	0.765
σ_{OMEGA} (deg)	0.247	0.233	0.211	0.216	0.231
σ_{PHI} (deg)	0.207	0.140	0.115	0.144	0.188
σ_{KAPPA} (deg)	0.027	0.019	0.014	0.017	0.023

Table 5: Accuracy of exterior orientation parameters for Rollei using LPS software package.

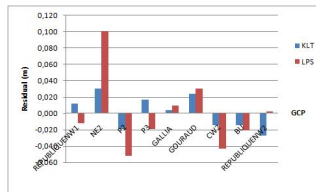
The previous four tables show that for the same block, the accuracy results are approximately the same by using LPS and KLT software package. For UltraCam-X block, the accuracy in X and Y direction are about 0.5 m and between 0.1 to 0.35 m in Z direction. The accuracies of rotation angles are less than 0.017 degree. On other side, for Rollei block, the accuracy in X and Y direction are about 5 m and between 0.5 to 1.9 m in Z direction. The accuracies of rotation angles are less than 0.25 degree.

A bundle solution is computed including the exterior orientation parameters of each image in a block as well as the X, Y, and Z coordinates of the tie points and adjusted GCPs. Block triangulation is the process of defining the mathematical relationship between the images contained within a block, the camera or sensor model, and the ground coordinates. Figure 3 and 4 represent with any pair of columns (KLT and LPS software), the residuals of the nine control points used in this process of X, Y, and Z directions for two blocks. The points identification are in horizontal axis

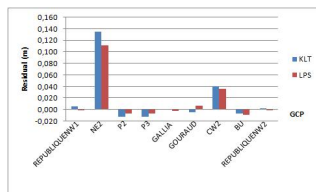
and the residuals in meters are in vertical one. It is also apparent that there is a higher residual in one point of each project in comparison with other points while other points are close together. Of course, these residuals depend on the qualification and precision of the GCPs.



(a) Residuals of GCPs in X-direction

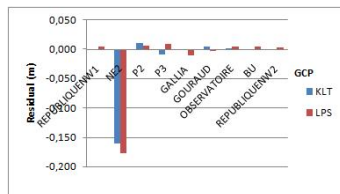


(b) Residuals of GCPs in Y-direction

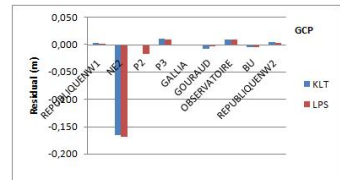


(c) Residuals of GCPs in Z-direction

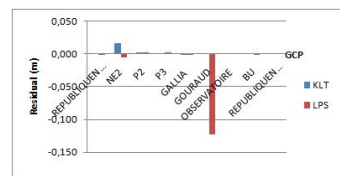
Figure 3: Residuals of GCPs for UltraCam-X block.



(a) Residuals of GCPs in X-direction



(b) Residuals of GCPs in Y-direction



(c) Residuals of GCPs in Z-direction

Figure 4: Residuals of GCPs for Rollei block.

The expected height accuracies σ_Z based on base (B) over height above ground ratio (Z) for two sensors is shown from equation 10 (Kraus and Waldhausl, 1993).

$$\sigma_Z = \frac{Z^2}{c \cdot B} \cdot \sigma_{p\varepsilon} \quad (10)$$

Where c is the focal length of camera and $\sigma_{p\varepsilon}$ is the accuracy of parallax.

By assuming that $\sigma_{p\varepsilon}$ is given according to the accuracies for each block after bundle adjustment. For UltraCam-X block, $\sigma_{p\varepsilon}$ is $2 \mu m$ and for Rollei block is $13 \mu m$. Then σ_Z for UltraCam-X equal to 0.2 m and for Rollei equal to 1.28 m.

After the bundle adjustment, the process of the object surfaces have been carried out. As a result of that, the 3D ground coordinates have been calculated at any point in an overlapped area in the block. Within the test, LPS software systems was used to compute the Digital Surface Model (DSM) with grids 0.2 m cell size in two direction for each block. To evaluate the matching quality while avoiding the influence of interpolation processes 3D point clouds will use in quality and quantity tests. Figure 5 and 6 show the 3D data sets created from UltraCam and Rollei images. The difference between two results are due to the change in sensors types and flight parameters.



Figure 5: 3D data set created from UltraCam-X image.



Figure 6: 3D data set created from Rollei image.

4.3 Design of Plane Samples

The present research describes the plane based accuracy assessment of 3D photogrammetric data. A selection of planes has been defined by segmentation of plane samples from the matched 3D points. Then, Principal Component Analysis (PCA) is the method used to calculate the parameters of the optimal plane. PCA is a useful statistical technique that reduces set of data dimensionality by performing a covariance analysis between factors. It is

suitable for data sets in multiple dimensions, for example in our case a set of data is the point cloud created from a digital sensor. Figure 7 shows how the plane fitting has been done from set of point cloud. Seven samples are chosen in order to achieve this study. Table 6 shows the Mean Distance (MD) in computing medium planes from UltraCam-X and Rollei data and number of points are used in order to create plane parameters. This distances are computed between 0.09 m and 0.23 m in UltraCam samples and between 0.37 m and 0.86 m in Rollei samples. By regarding to this table, we can compare between planes created from two blocks. Although the plane samples are chosen to the same object, the MD is higher in Rollei block even if samples contain the same number of points approximately used in creating plane parameters.

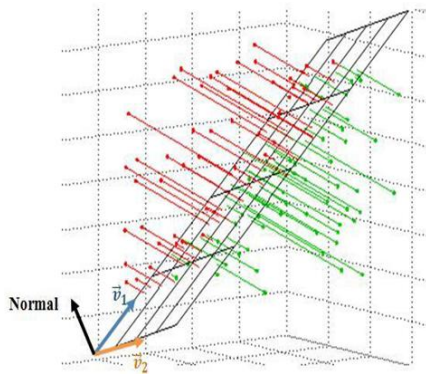


Figure 7: Fitting Plane from 3d data set.

Plane No	MD for UltraCam-X (m) [Number of points]	MD for Rollei (m) [Number of points]
1	0.227 [114]	0.556 [117]
2	0.133 [179]	0.448 [78]
3	0.207 [525]	0.477 [142]
4	0.205 [623]	0.642 [402]
5	0.134 [91]	0.863 [124]
6	0.098 [297]	0.365 [191]
7	0.209 [162]	0.748 [134]

Table 6: Mean Distance (MD) in computing medium plane

4.4 Results of Assessment

The approach for quality evaluation was applied to seven samples of planes which were chosen from UltraCam and Rollei data after images processing. In order to achieve this process, the Matlab toolbox was programmed to compute the quality indices. Table 7 presents results of these quality indices estimated from plane comparisons. The quality indices give an indication about the quality of data. The values of two indices (pd and pq) are close to one and the other three indices are close to zero. This means that the characteristic of planes extracted from both datasets are closed with a good quality.

On the other hand, one can compute the error estimation based on the orthogonal distance between the plane surface of data extracted from UltraCam-X (Ar) and Rollei (At). Table 8 shows the mean distance between plane created from UltraCam and Rollei to the same location. The values of MD between planes are not far from the expected errors in Z deducted from base over height ratio (equation 10) and MD was computed for medium plane from two blocks.

Plane	pd	pq	pb	pm	pf
1	0.9624	0.7503	0.0390	0.2937	0.2827
2	0.9491	0.8439	0.0536	0.1313	0.1246
3	0.9512	0.9436	0.0513	0.0084	0.0080
4	0.9111	0.8176	0.0976	0.1256	0.1144
5	0.9991	0.9112	0.0009	0.0966	0.0965
6	0.8801	0.8552	0.1363	0.0330	0.0291
7	0.9548	0.8954	0.0474	0.0694	0.0663

Table 7: Quality indices estimated from plane samples.

Plane No	MD between two planes (m)
1	1.716
2	1.151
3	1.794
4	1.929
5	1.123
6	0.997
7	1.179

Table 8: Error estimation of surface area.

5 CONCLUSIONS

In this paper we have presented a simple approach towards plane-based accuracy assessment of 3D data in aerial photogrammetry. This approach considers the accuracy of the 3D data based on the comparison between planes created from UltraCam-X and Rollei digital cameras. Very similar results have been obtained from the bundle adjustment of the two blocks using LPS and KLT software packages. In photogrammetry, the base over height ratio is a factor relied on the result elevation accuracy. The indices computed between reference and tested areas are interesting indicators to evaluate the degree of similarity of objects, beside quantitative assessment. Finally, our future researches will concentrate in 3D model accuracy assessment.

REFERENCES

References from Journals

Akca, D., Freeman, M., Sargent, I. and Gruen, A., 2010. Quality assessment of 3d building data. *The Photogrammetric Record* Vol. 25 (132), pp. 339-355.

Grussenmeyer, P., Hottier, P and Abbas, I., 1994. Le contrôle topographique d'une carte ou d'une base de données constituées par voie photogrammétrique. *Journal of the French Association of Topography, XYZ N° 59*, pp. 39-45.

Haala, N., Hastedt, H., Wolf, K., Ressel, C., and Baltrusch, S., 2010. Digital photogrammetric camera evaluation - Generation of digital elevation models. *Photogrammetrie Fernerkundung Geoinformation, Vol.2*, pp. 99-115.

McKeown, D., Bulwinkle, T., Cochran, S., Harvey, W., McGlone, C. and Shufelt, J., 2000. Performance evaluation for automatic feature extraction. *IAPRS International Archives of Photogrammetry and Remote Sensing, Vol.33*, pp. 379-394.

References from Conferences

Cramer, M., 2009. Digital airborne camera performance - The DGPf Test. In: *52nd Photogrammetric Week*, September 7-11, 2009, pp. 51-68. Stuttgart.

Cramer, M., 2010. The DGPF-test on digital airborne camera evaluation - overview and test design. *Photogrammetrie Fernerkundung Geoinformation*, pp. 73-82. Stuttgart.

Ragia, L., 2000. A quality model for spatial objects. In: *ISPRS Congress International Archives of Photogrammetry and Remote Sensing*. Vol. XXXIII, Part B4. pp. 855-862. Amsterdam.

Schuster, H. and Weidner, U., 2003. A new approach towards quantitative quality evaluation of 3D building models. *ISPRS com IV, Workshop (Challenges in Geospatial Analysis, Integration and Visualization II)*, Stuttgart, Germany, pp. 156-163.

References from Book

Congalton, G. and Kass, G., 2009. *Assessing the accuracy of remotely sensed data: Principles and practices*. 2nd, Taylor and Francis Group, 183 pages.

Kraus, K. and Waldhausl, P., 1993. *Photogrammetry: Fundamentals and standard processes*. 4nd, Vol. 1 Ferd. Dummlers, 397 pages.

References from Thesis

Grussenmeyer, P., 1994. Contrôle Géométrique de la Saisie en Photogrammétrie. Phd Thesis, University of Louis Pasteur, Strasbourg - France.

References from Other Literature

ERDAS IMAGINE Version 2011. LPS project manager. ERDAS Inc. pp. 22-29.

PRIMITIVE-BASED BUILDING RECONSTRUCTION BY INTEGRATION OF LIDAR DATA AND OPTICAL IMAGERY

W. Zhang^{a,*}, P. Grussenmeyer^b, G. Yan^a, M. Mohamed^b

^a State Key Laboratory of Remote Sensing Science, School of Geography, Beijing Normal University, 100875 Beijing, China - (wumingz, gjyan)@bnu.edu.cn

^b The Images Sciences, Computer Sciences and Remote Sensing Laboratory, INSA Strasbourg, France, – (pierre.grussenmeyer, mostafa.mohamed)@insa-strasbourg.fr

Commission III, WG III/4

KEY WORDS: Building Reconstruction, LiDAR, Optical Imagery, Primitive-based, Bundle Adjustment

ABSTRACT:

Airborne LiDAR data and optical imagery are two datasets used for 3D building reconstruction. In this paper, the complementarities of these two datasets are utilized to perform a primitive-based 3D building reconstruction. The proposed method comprises following steps: (1) recognize primitives from LiDAR point cloud and roughly measure primitives' parameters as initial values, and (2) select primitives' features on the imagery, and (3) optimize primitives' parameters by the constraints of LiDAR point cloud and imagery, and (4) represent 3D building model by these optimized primitives. Compared with other model-based or CSG-based methods, the proposed method is simpler. It only uses the most straightforward features, i.e. planes of LiDAR point cloud and points of optical imagery. The experimental result shows this primitive-based method can accurately reconstruct 3D building model. And it can tightly integrate LiDAR point cloud and optical imagery, that is to say, all primitives' parameters are optimized with all constraints in one step.

1. INTRODUCTION

3D reconstruction of buildings is an important approach to obtain the 3D structure information of buildings, and has been widely used in the applications of telecommunication, urban planning, environmental simulation, cartography, tourism, and mobile navigation systems. It has been the major topic of photogrammetry, remote sensing, computer vision, pattern recognition, surveying and mapping. Traditionally, photogrammetry is the primary approach for deriving geospatial information through the use of multiple optical images. Optical imagery has sharp and clear edges, so the 3D information derived from photogrammetric measurements consists of accurate metric and rich descriptive object information (Mikhail et al., 2001). But it is hard to obtain dense 3D points on the building's surface because of the matching problem at the homogeneous or occluded places. Also because of matching problem, it is hard to generate 3D building model automatically by photogrammetry (Schenk and Csatho, 2002).

Since it was introduced in the 1980s, as a promising method, Light Detection And Ranging (LiDAR) technology is used in the applications of acquiring digital elevation data. Because LiDAR technology is fully automated for generating digital elevation data, many researchers have paid attention to the technology and its applications (Ackermann, 1999; Arefi, 2009; Habib et al., 2004; Mayer et al., 2008; Rottensteiner and Briese, 2002; Zhang and Li, 2006). Although LiDAR point cloud has dense 3D points, these points are irregularly spaced, and don't have accurate information regarding breaklines such

as building boundaries. Thus, the reconstructed 3D building's model is not very accurate (the accuracy depends on the points density), not only the shape but also the position of the building. Obviously, to generate a more accurate 3D building model using LiDAR point cloud, the help of other datasets with accurate boundaries is necessary.

Both ground plan and optical imagery satisfy this requirement. Compared with ground plan, optical imagery has the advantages of easy availability and up-to-date state. A variety of research has been conducted using LiDAR point cloud and optical imagery, whatever data-driven or model-driven approaches (Habib, 2009; Kim, 2008; Tarsha-Kurdi et al., 2007b; Wang, 2008). The existing methods have some drawbacks. Firstly, most of these methods use edges as the features to connect LiDAR point cloud and optical imagery, the data processing procedure is complex due to the edge detection, filtering, combination and other operations. Secondly, the LiDAR point cloud and optical imagery are often processed respectively, and then the results are combined simply.

In this paper, using airborne LiDAR data and optical imagery, a primitive-based 3D building reconstruction method is proposed to overcome the problems mentioned above. Two datasets are tightly integrated, and the accurate 3D building model can be acquired by the straightforward and simple features. The organization of this paper is as follows. In section 2, the proposed primitive-based method is described in detail, including motivation, workflow, and explanation of some crucial steps. Section 3 is the result of the preliminary

* Corresponding author.

experiment and some discussions. Finally, we draw the conclusion and identify the work of near future.

2. METHODOLOGY

2.1 Selection of Reconstruction Method and Features

In this section, two crucial points will be explained, i.e., the selection of method and features for building 3D reconstruction.

There are two reasons for the selection of primitive-based method to reconstruct 3D building model.

Firstly, LiDAR point cloud has dense 3D points, but these points are irregularly spaced, and don't have accurate information regarding breaklines such as building boundaries. On the contrary, optical imagery has sharp and clear edges, but it is hard to obtain dense 3D points on the building's surface. In order to reconstruct 3D building model by integration of LiDAR point cloud and optical imagery, the selected object must have clear edges and dense surface points at the same time. Obviously, primitives, for example, box, gable-roof and hip-roof can satisfy this requirement. Suitable primitives will "glue" LiDAR point cloud and optical imagery.

Secondly, from the point view of computation, primitive-based representation of 3D building model has less parameters. For example, to represent a box, 3 parameters (width, length and height) are used to represent the shape; together with 3 parameters for position and 3 parameters for orientation, totally 9 parameters are enough to determine the shape and locate the box in 3D space. So the solution can be calculated easily and robustly.

For the selection of features, it is crucial because it affects the complexity of the process and the accuracy of the reconstructed 3D building model. As we have seen, LiDAR point cloud and optical imagery have different characteristics, so different features will be selected for these two datasets. The features should be as straightforward and simple as possible, so that they can be easily located and accurately measured. Plane is the feature that we selected for LiDAR point cloud, and corner is the feature that we selected for optical imagery. Using these straightforward and simple features, the computational procedure is simplified, and the result can be obtained precisely and robustly.

Because of above reasons, we select primitive-based method to reconstruct 3D building model, and plane feature for LiDAR point cloud and corner feature for optical imagery. In this paper, only two kinds of primitives are studied, i.e., box and hip-roof.

2.2 Workflow

Fig. 1 shows the workflow of this primitive-based 3D building reconstruction method. The numbers denote the order of processing.

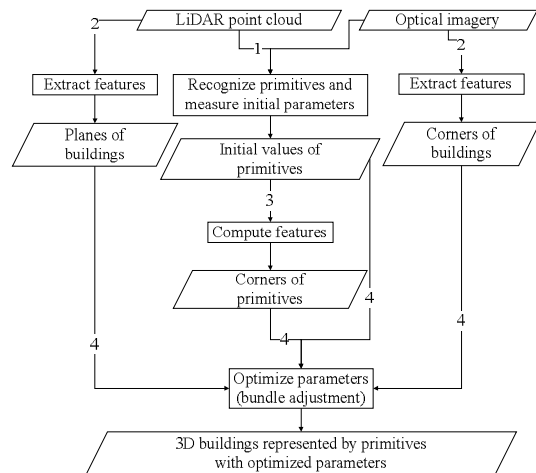


Figure 1. Flowchart of the proposed method

- 1. Recognize primitives and measure initial parameters.** With the help of optical imagery and LiDAR point cloud, the building is decomposed into several primitives. Then the primitive's parameters are measured roughly on LiDAR point cloud and optical imagery, such as length, width, height, orientation and translation of the primitive. These measurements can be used as fixed values (constraints) or initial values in the following bundle adjustment procedure.
- 2. Extract features.** Corners are detected/selected on the optical imagery, and planes are detected/selected in the LiDAR point cloud. These features will be used as observed values/observations in the following bundle adjustment procedure.
- 3. Compute features.** Based on the type and parameters of primitives, the 3D coordinates of the primitives' features, such as corners, can be calculated. They will be used as model/computed values in the following bundle adjustment procedure.
- 4. Optimize parameters (bundle adjustment).** Using Collinearity Equation and 3D Plane Equation as mathematical models, a cost function can be established. The inputs of this cost function are observed values, model values, and initial values above. When the bundle adjustment procedure is finished, the optimized/refined primitives' parameters will be outputted.

Finally, 3D building can be represented by these primitives with the optimized parameters.

In the following paragraphs, the detail of each step will be depicted. A building consisting of several hip-roof primitives is used as an example to facilitate the understanding. Fig. 2 is the LiDAR point cloud of this building, and Fig. 3 is the corresponding optical image. They are a part of an experimental data of Strasbourg, France. This experiment was carried out in September, 2004. In this experiment, LiDAR sensor is Optech ALTM 1225, flight height is 1440m, and point density is 1.3 points/m²; camera sensor is Voxel UltraCamX, flight height is 2330m, and GSD (Ground Sample Distance) is 15cm.

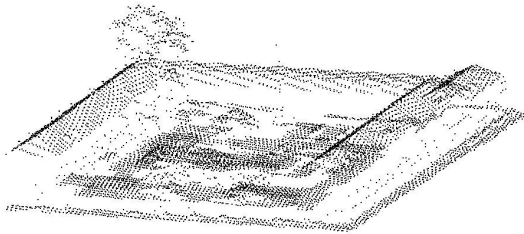


Figure 2. LiDAR point cloud

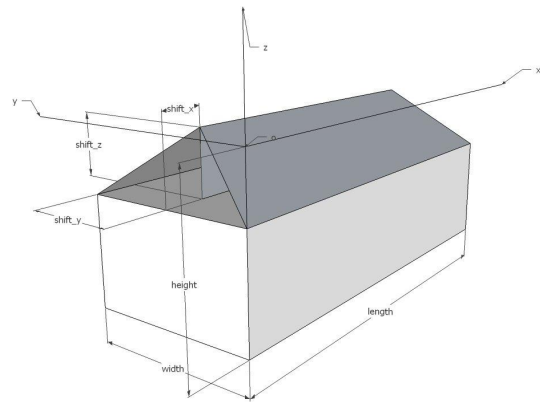


Figure 4. Hip-roof primitive



Figure 3. Optical image

2.3 Recognize Primitives and Measure Initial Parameters

2.3.1 Hip-roof Primitive: The primitive mainly used in this example is hip-roof primitive, which is shown in Fig. 4. The coordinates framework and the parameters are labelled. It can be seen that 6 parameters are used to define the shape of this hip-roof primitive. Further more, another 6 parameters define how a primitive is placed in 3D space, 3 for position and 3 for orientation.

2.3.2 Recognize Primitives: In order to carry out the primitive-based 3D building reconstruction, a building must be decomposed into several primitives. It is hard to perform this task all by computers. At current stage, the recognition of primitives is done in interactive mode. The decomposition is not unique, it depends on the operator. After analyzing both LiDAR point cloud (see Fig. 2) and optical image (see Fig. 3), this building can be decomposed into 5 hip-roof and 1 box primitives.

2.3.3 Measure Initial Parameters: When the way of decomposition is determined, the parameters of each primitive should be measured. Height parameters can only be derived from LiDAR point cloud. Plane parameters, such as length, width and primary orientation of the building can be obtained from LiDAR point cloud or optical imagery. The parameters related with relative displacement and rotation to the adjacent primitive should also be determined.

As mentioned earlier, the measured parameters will be used as initial values and will be optimized in the following bundle adjustment procedure. It doesn't need to measure these parameters accurately. So the process can be simplified and the efficiency will be high.

2.4 Extract Features

Corners are detected/selected on the optical imagery. All visible vertexes are measured; the pixel coordinates of x and y directions are recorded. Every vertex has a unique ID; the bigger numbers in Fig. 3 are these IDs. The pixel coordinates of these corners will be used as the observed values of Collinearity Equation and contribute to the cost function.

Planes are detected/selected in the LiDAR point cloud. In Fig. 3, these planes are labelled with smaller numbers. Every plane has a unique ID, and the plane equation is calculated using all 3D points that form this plane. These 3D plane equations will be used as constraints and contribute to the cost function.

2.5 Compute Features

Based on the type and parameters of primitives, the 3D coordinates of the primitives' features, such as corners, can be calculated. For example, in Fig. 4, the bottom four corners'

coordinates are (0,0,-height), (length,0,-height), (length,width,-height) and (0,width,-height). They will be used as model/computed values in the following bundle adjustment procedure. Certainly, before these model values are substituted into equations, the coordinates must be transformed from the primitive's local coordinates system to the global coordinates system. This can be done by 3D rigid body transformation using a serial of translation and rotation parameters of primitives.

2.6 Optimize Parameters (Bundle Adjustment)

On the basis of previous preparation works, all primitives' parameters can be optimized by a bundle adjustment procedure. To achieve this goal, an important thing is to construct a simple and effective cost function.

Our idea is straightforward and simple. When a 3D building model has correct shape and is located in the correct place in 3D space, two conditions will be satisfied. Firstly, the back-projections of primitive's vertexes (computed features) on the optical image should perfectly superpose on the measured corners (extracted features). Secondly, the primitive's vertexes should be exactly on the planes which are formed by LiDAR point cloud.

Two mathematical models, i.e., Collinearity Equation and 3D Plane Equation are used to represent these two conditions respectively. And the cost function is established based on these two mathematical models. The inputs of this cost function are observed values, model values, and initial values above. The cost function can be optimized by bundle adjustment technique. When the bundle adjustment procedure is finished, the optimized/refined primitives' parameters will be outputted.

So far, 3D building can be represented by these primitives with the optimized parameters. The experimental result will be shown and some discussions will be made in the next section.

3. EXPERIMENTAL RESULT AND DISCUSSION

3.1 Experimental Result

Fig. 5 shows the reconstructed 3D building model of the example data. The wireframes of the model are overlaid on the original LiDAR point cloud. It can be seen that they are fitted very well.

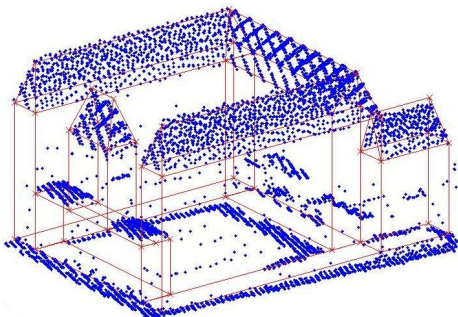


Figure 5. Reconstructed 3D building model

Because there are no surveyed data of this building, we use another way to verify the effectiveness of the proposed primitive-based 3D building reconstruction method. As shown in Fig. 6, the wireframes of both initial model and optimized model are back projected to the optical image, which is used to reconstruct this building. They are represented by yellow lines and white lines. The region circled in Fig. 6 is zoomed and shown in Fig. 7. Obviously, the initial polygons diverge from the real building's edges. While, the optimized polygons fit the real building's edges very well.

As shown in Fig. 3, there are totally 27 vertexes. The distances of the vertexes in the initial model and the optimized model compared to the imagery are computed. The result is shown in Tab. 1. It can be seen, the mean value and standard deviation are improved in both x and y directions after optimization procedure.

		mean value/pixel	standard deviation/pixel
Initial model	x	-23.74	17.29
	y	-10.00	15.12
Optimized model	x	-0.04	1.65
	y	0.17	1.90

Table 1. Statistics of distances of vertexes

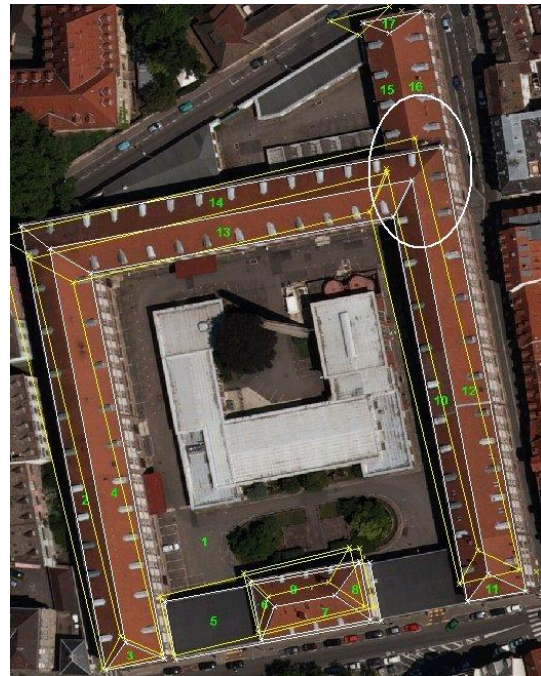


Figure 6. Wireframes of initial model and optimized model

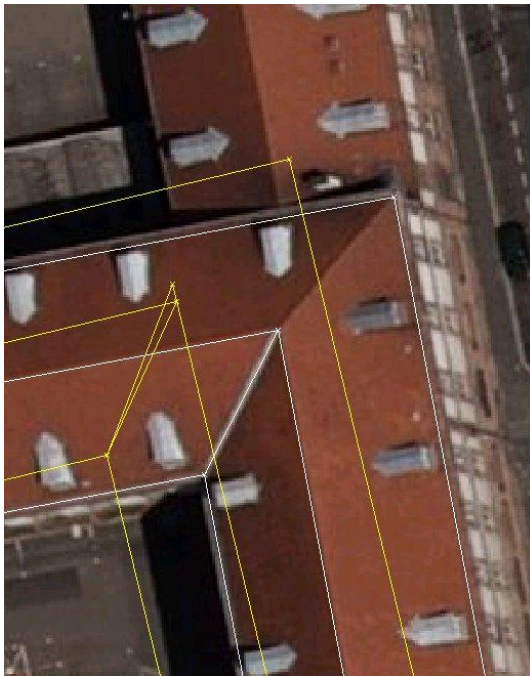


Figure 7. Zoom view of circled region of Fig. 6

In this experiment, only one image (Fig. 6) is used. In order to reinforce the effectiveness of proposed method, the optimized model is also back projected to another image (Fig. 8), which covers this building but is not used during the reconstruction procedure. The optimized polygons fit the real building's edges very well too.



Figure 8. Wireframes of optimized model on the image which doesn't involve in optimization procedure

3.2 Discussion

From this preliminary experiment, it can be seen that the proposed method can utilize the complementarity of imagery and LiDAR point cloud, and a model is established as soon as the cost function is solved. This is only the first step, perhaps the reconstructed model is not very accurate, because:

1. The 3D parameters and 2D features were measured roughly by manual work.
2. The actual building doesn't exactly coincide with the used simple model.
3. At present, only one image is used during optimization procedure.

Besides, there exist some deficient places.

1. The accuracy of the reconstructed model is only verified semi-quantificationally.
2. Only two simple primitives are used, i.e., box and hip-roof.
3. There are many manual works. For example, extraction of 2D corner features and 3D plane features, selection of primitives and measurement of the initial parameters of these primitives.
4. Not all images covering the studied building are used during the data processing procedure.
5. Only the data of one separated building was studied and processed.

To make the proposed method more automated and to apply this method to a wide urban area, there are some places needing improvement in subsequent research.

1. To represent more complex buildings, more primitives such as cylinder and sphere will be considered, and boolean operations of primitives will be used.
2. To improve the accuracy and the efficiency, instead of current manual work, either specific human-interactive software (Brenner, 1999) or some automatic algorithms will be developed, for example, extracting features from LiDAR point cloud and optical imagery (Tarsha-Kurdi et al., 2007a), recognizing types of primitives and obtaining the initial parameters of primitives.
3. To apply to a wide urban area where a lot of buildings in it, some in-depth topics will be studied, i.e., building detection, extraction and segmentation from LiDAR point cloud and optical imagery (Hu, 2003; Tarsha-Kurdi et al., 2006).

4. CONCLUSIONS AND FUTURE WORK

Airborne LiDAR data and optical imagery are two datasets used for 3D building reconstruction. In this paper, the complementarities of these two datasets are utilized to perform a primitive-based 3D building reconstruction. The preliminary experimental result demonstrates the feasibility of the proposed 3D building reconstruction method.

The proposed primitive-based method is a kind of model-based method, so it has the following merits as other model-based methods.

1. For buildings with regular shapes, it can increase efficiency than point-by-point measurement.
2. The operator only needs to select primitives and approximately measure parameters as initial values, while the labor-consuming precise measurement is carried out by computer.
3. The inner constraints guarantees the geometric nature unchanged after reconstructing.
4. It is possible to reconstruct the whole building even if a part of it is occluded.

Beyond that, the proposed primitive-based method in this paper is simpler, because it only uses the most straightforward features, i.e. planes of LiDAR point cloud and points of optical imagery. Further more, it can tightly integrate LiDAR point cloud and optical imagery, that is to say, all primitives' parameters are optimized with all constraints in one step.

The following researches will be carried out in the near future.

1. All images covering the reconstructed building will be used to improve the accuracy and integrality of the reconstructed 3D model.
2. The corner features will be extracted more precisely from the optical imagery, so that they can be used to improve and validate the accuracy of reconstructed 3D model.
3. The result will be validated quantitatively or by in-situ data.

Acknowledgements

This work is supported by National Natural Science Foundation of China Grant No. 40801131 and the National High-Tech Research and Development Plan of China Grant No. 2010AA122202. This work is also supported by the Special Foundation for Free Exploration of State Key Laboratory of Remote Sensing Science of China. Thanks to two anonymous reviewers for their helpful comments and suggestions.

References

Ackermann, F., 1999. Airborne laser scanning—present status and future expectations. *ISPRS Journal of Photogrammetry and Remote Sensing*, 54: 64–67.

Arefi, H., 2009. From LIDAR Point Clouds to 3D Building Models. PhD thesis, Bundeswehr University Munich.

Brenner, C., 1999. Interactive Modelling Tools for 3D Building Reconstruction. In: *Photogrammetric Week '99*. Wichmann, Stuttgart, pp. 23-34.

Habib A., 2009. "Integration of Photogrammetric and LIDAR Data for Accurate Reconstruction and Visualization of Urban Environments". *Proceedings of FIG COM3 Workshop on Spatial Information for Sustainable Management of Urban Areas*, Mainz, Germany.

Habib, A.F., Ghanma, M.S., Morgan, M.F., Mitishita, E.A., 2004. Integration of laser and photogrammetric data for calibration purposes. *International Archives of XXth ISPRS Congress, commission I*, Istanbul, Turkey, pp. 170-176.

Hu, Y., 2003. Automated extraction of digital terrain models, roads and buildings using airborne LiDAR data, (PhD Thesis), Department of Geomatics Engineering, The University of Calgary, Calgary, Alberta, Canada.

Kim, C., 2008. Object-based Integration of Photogrammetric and LiDAR Data for Accurate Reconstruction and Visualization of Building Models, (PhD Thesis), Department of Geomatics Engineering, The University of Calgary, Calgary, Alberta, Canada.

Mayer H., Hinz, S., Stilla, U., 2008. Automated extraction of roads, buildings and vegetation. Chapter in Li, Z., Chen, J., & Baltsavias, E., (Eds), 2008. *Advances in Photogrammetry, Remote Sensing and Spatial Information Sciences: 2008. ISPRS Congress Book, ISPRS Book Series*, Volume 7 (527p.), © 2008 Taylor & Francis Group, London, ISBN 978-0-415-47805-2, p. 213-226.

Mikhail, E.M., Bethel, J.S., McGlone, J.C., 2001. *Introduction to Modern Photogrammetry*, John Wiley & Sons, Inc., New York, 479 p.

Rottensteiner, F., and Ch. Briese, 2002. A new method for building extraction in urban areas from high-resolution LiDAR data, *International Archives of Photogrammetry and Remote Sensing*, 34(3A): 295-301.

Schenk, T., and B. Csatho, 2002. Fusion of LIDAR data and aerial imagery for a more complete surface description. In: *IAPRSIS* 32(3A): 310.

Tarsha-Kurdi, F., Landes, T., Grussenmeyer, P., 2007a. Hough-Transform and Extended RANSAC Algorithms for Automatic Detection of 3D Building Roof Planes from Lidar Data. *International Archives of Photogrammetry, Remote Sensing and Spatial Information Systems*. Vol. XXXVI, Part 3 / W52, 2007, pp. 407-412.

Tarsha-Kurdi, F., Landes, T., Grussenmeyer, P., Koehl, M., 2007b. Model-driven and data-driven approaches using LIDAR data : analysis and comparison, *International Archives of Photogrammetry, Remote Sensing and Spatial Information Systems* Vol. XXXVI Part3 W49A / ISSN 1682-1750, pp. 87-92.

Tarsha-Kurdi, F., Landes, T., Grussenmeyer, P., Smigiel, E., 2006. New approach for automatic detection of buildings in airborne laser scanner data using first echo only, *International Archives of Photogrammetry and Remote Sensing and Spatial Information Sciences*, ISSN: 1682-1750, Vol. XXXVI, Part 3, pp. 25-30.

Wang, S., 2008. Floating model for building reconstruction from topographic maps and lidar data. *XXI Congress of the International Society for Photogrammetry and Remote Sensing (ISPRS 2008)*. Vol. XXXVII. Part B3b:681-686.

Zhang W., Li Q., 2006. A preliminary simulation to study the potential of integration of LIDAR and imagery, *Proceedings of the SPIE*, Volume 6366, pp.63660W-10.

COMPARISON OF 3D BUILDINGS RECONSTRUCTED BY DIFFERENT DATA SOURCES

K. Yan ^a, W. Zhang ^{a,*}, Y. Chen ^a, G. Zhou ^b, P. Grussenmeyer ^c, M. Mohamed ^c

^a Beijing Normal University, 100875 Beijing, China - wumingz@bnu.edu.cn

^b Guilin University of Technology, 541004 Guilin, Guangxi, China - zgq@glite.edu.cn

^c University of Strasbourg, INSA Strasbourg, France, – (pierre.grussenmeyer, mostafa.mohamed)@insa-strasbourg.fr

KEY WORDS: 3D Building Reconstruction, LiDAR, Optical Imagery, Primitive-based

ABSTRACT:

1. INTRODUCTION

Airborne LiDAR data and optical imagery are two data sources used for 3D building reconstruction. The researchers have developed a variety of modelling method using these two kinds of data. According to different data sources, these methods can be divided into three categories: photography measuring using digital images only; building reconstruction using LiDAR points only; building reconstruction by integration of LiDAR data and optical imagery. These methods are different in precision, complexity, efficiency and so on. So a qualitative comparison for the three modeling methods is needed. In this paper, we firstly reconstructed the buildings in the test site using the above three kinds of data sources. And then, we compared the results quantitatively. We adopted the primitive-based building reconstruction method to reconstruct the buildings using the two types of data (W. Zhang, 2011).

The organization of this paper is as follows. In section 2, the building reconstruction methods are described in detail, and the methods used to compare the results are also introduced in this section. Section 3 is the result of the comparison and some discussions. Finally, we draw the conclusion.

2. METHODOLOGY

2.1 Introduction to data sources

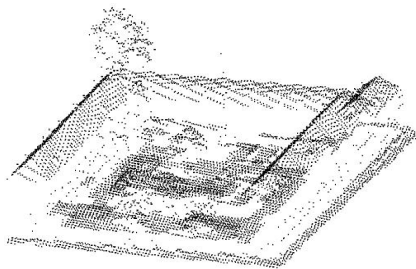


Fig. 1. LiDAR point cloud

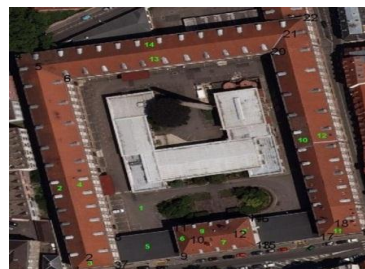


Fig. 2. Optical image

Fig. 1 is the LiDAR point cloud of this building, and Fig. 2 is the corresponding optical image. They are a part of an experimental data of Strasbourg, France. This experiment was carried out in September, 2004. In this experiment, LiDAR sensor is Optech ALTM 1225, flight height is 1440m, and point density is 1.3

* Corresponding author.

points/m²; camera sensor is Voxel UltraCamX, flight height is 2330m, and GSD (Ground Sample Distance) is 15cm.

2.2 Methods of modelling

2.2.1 Image-based modelling

The development of photography measurement technology provides us a wide range and non-contact location measuring method. In this paper, three aerial photographs of the test area are available and their internal and external orientation elements are known. We respectively used two and three photos to intersect the building corners' coordinates. The pixel coordinates of the corners were measured manually and the measurement accuracy was on sub-pixel level.

2.2.2 Point-cloud-based modelling

Light Detection and Ranging (LiDAR) technology is used in the applications of acquiring digital elevation data. To improve the accuracy of the building outline and location, people often intersect the planes to get a line or a point. The steps include extraction of the points which are part of the same plane, and then fitted to obtain the plane equation. Then line equations or point coordinates will be calculated by solving the equations. LiDAR points used in this paper covered the roofs and there were only a few points on the side walls. For corners of the buildings, if three or more planes were available, we used multiple planes to intersect the points; if no enough available planes, we firstly fitted lines using the points at the edges and then intersected points using these lines.

2.2.3 Primitive-based modelling

LiDAR point cloud has dense 3D points, but these points are irregularly spaced, and don't have accurate information regarding breaklines such as building boundaries. On the contrary, optical imagery has sharp and clear edges, but it is hard to obtain dense 3D points on the building's surface. The two data sources have obvious complementary and some scholars are working on the joint reconstruction using both of the two data sources. W. Zhang, who used primitive-based method to achieve the joint between the two data sources, initially proved to be effective and accurate. In this paper, this method was used to reconstruct.

2.3 Methods of comparison

2.3.1 Comparison between each other

Using the three modelling methods, we obtained three models of the test area. These models can be regarded as constituted by 20 corner points. In order to analyse the results of the models, we made pairwise comparisons between these three sets of point coordinates. Firstly, we did subtraction between the point coordinates respectively to obtain the errors. Then we calculated the mean and variance of these errors. These two parameters can reflect the modelling accuracy.

2.3.2 Comparison between pixels

According to principles of photogrammetry, the pixel coordinates can be obtained by the back-projection using the points from each model. These three sets of pixel coordinates should be the same and should match those measured on the images manually. In fact there were differences between these pixel coordinates.

It was assumed that the pixel coordinates measured manually were more accurate and could be regarded as a standard. Firstly, we did subtraction between the pixel coordinates of back-projection and the pixel

coordinates measured manually. The errors could be attained by this subtraction. Then the mean and variance of these errors were calculated.

3. RESULT AND DISCUSSION

3.1 Result of comparison between each other

Table1 depicts the mean value and standard deviation of the differences between each two models. It shows the differences between point-cloud-based modelling and others are larger. It also can be seen that the differences of Z are larger and less intent than that of X or Y. This can be explained by previous studies that the horizontal accuracy of photography measurement is significantly higher than the elevation accuracy.

	LiDAR only & Both image and LiDAR		Image only & LiDAR only		Image only & Both image and LiDAR	
	Mean value (mile)	std	Mean value (mile)	std	Mean value (mile)	std
X	0.4551	0.4737	0.4528	0.4895	0.1144	0.0752
Y	0.4585	0.3829	0.3622	0.3845	0.1667	0.1231
Z	0.6310	0.3296	0.7636	0.5315	0.6304	0.5049

Table1 Mean value and standard deviation of the differences between each two models

3.2 Result of comparison between pixels

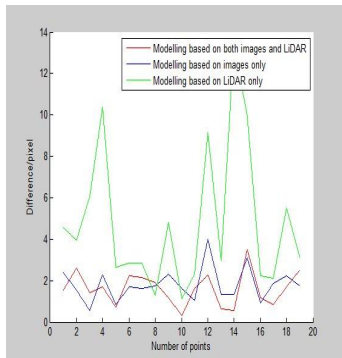


Fig. 3. Differences of pixels



Fig. 4. Back-projection of the three models



Fig. 5. Zoom view of circled region of Fig. 4

Fig. 3 is the plot of result of comparison between pixels. It depicts the differences of image-based modelling and primitive-based modelling are less than 4 pixels, while the differences of point-cloud-based modelling can reach 13 pixels.

		mean value/pixel	standard deviation/pixel
Image only	x	1.2203	0.8602
	y	1.1981	0.4805
LiDAR only	x	2.4175	2.6590
	y	3.6713	3.0033
Both image and LiDAR	x	0.8989	0.6576
	y	1.1789	0.8131

Table2 Mean value and standard deviation of the differences between pixels

As shown in Fig. 4, the wireframes of the three models are back projected to the optical image, which is used to reconstruct this building. The accuracy of each model can be seen in Fig .5 more clearly (green lines stand for point-cloud-based modelling; blue lines stand for image-based modelling; red lines stand for primitive-based modelling). Table2 can show the same result by using mean value and standard deviation.

Compared with other two models, the mean value and standard deviation of primitive-based modelling are improved in both x and y directions. It also can be seen that the green wireframes are shrivelled compared with the true profiles of buildings. This is caused by the missing of LiDAR points on the edges. These errors depend on point density of LiDAR.

4. CONCLUSIONS AND FUTURE WORK

In this paper, we reconstructed the buildings based on three kinds of data sources and compared the results quantitatively. The results of this comparison show: (1) Modelling by integration of point cloud and optical imagery is superior to point-cloud-based modelling in the accuracy (2) For image-based modelling, the horizontal accuracy is higher than the elevation one (3) The accuracy of point-cloud-based modelling is different from point to point and the models are shrivelled compared with the true profiles of buildings. (4) Primitive-based modelling is a desirable method to combine the advantages of the two types of data.

To a certain extent, the methods of comparison used in this paper can express the accuracy of modelling. But this is only the first step, there are some places needing improvement in subsequent research:

1. To select the most advanced methods of modelling to compare.
2. To represent more complex buildings, and to involve more points for comparison.
3. To obtain more accurate coordinates to serve as the reference.

References

- W. Zhang, P. Grussenmeyer, G. Yan, M. Mohamed, "Primitive-based building reconstruction by integration of Lidar data and optical imagery," ISPRS Laser scanning Workshop, Calgary, 2011.
- Arefi, H., 2009. From LIDAR Point Clouds to 3D Building Models. PhD thesis, Bundeswehr University Munich.
- Mikhail, E.M., Bethel, J.S., McGlone, J.C., 2001. *Introduction to Modern Photogrammetry*, John Wiley & Sons, Inc., New York, 479 p.
- Rottensteiner, F., and Ch. Briese, 2002. A new method for building extraction in urban areas from high-resolution LiDAR data, *International Archives of Photogrammetry and Remote Sensing*, 34(3A): 295-301.
- Ackermann, F., 1999. Airborne laser scanning—present status and future expectations. *ISPRS Journal of Photogrammetry and Remote Sensing*, 54: 64–67.
- Wang, S., 2008. Floating model for building reconstruction from topographic maps and lidar data. *XXI Congress of the International Society for Photogrammetry and Remote Sensing (ISPRS 2008)*. Vol. XXXVII. Part B3b:681-686.
- Zhang W., Li Q., 2006. A preliminary simulation to study the potential of integration of LIDAR and imagery, *Proceedings of the SPIE*, Volume 6366, pp.63660W-10.

ASSESSMENT OF THREE-DIMENSIONAL MODELS DERIVED FROM LIDAR AND TLS DATA

T. Landes, P. Grussenmeyer, H. Boulaassal, M. Mohamed

The Image Sciences, Computer Sciences and Remote Sensing Laboratory LSIIT-TRIO UMR 7005,
INSA Strasbourg, France
tania.landes@insa-strasbourg.fr

Commission II, WG4

KEY WORDS: accuracy, precision, assessment, three-dimensional, quality, TLS, LIDAR

ABSTRACT:

This paper suggests the use of specific methods for assessing the geometry of 3D building models, by considering models extracted automatically from terrestrial laser scanning (TLS) data and aerial laser scanning (ALS) data. Well known quality factors have been applied for assessing roofs and façades separately. A projection into 2D makes sense in this case, because currently, 3D models or point clouds of façades are often projected into 2D for generating 2D façade maps, as required in the building trades. For assessing roofs in 3D, error maps have been suggested especially for analysing the spatial distribution of plane adjustment errors which might affect the final reconstructed 3D model. For assessing 3D building vector models as one object, first experiments based on volumetric quality factors are presented. This approach is based on ratios inspired from quality factors that have already proven themselves in the literature for comparing surface areas. The volumes considered here are computed on vector models (faceted solids) and not voxels. Further investigations are necessary on the one hand, for testing the sensitivity of these factors. On the other hand, the approach must be completed by criteria allowing the detection of shape differences, independently of the building volume.

1. INTRODUCTION

Whether airborne or terrestrial, laser scanners have the great potential to enable with high speed the acquisition of 3D data especially in urban areas. If data acquisition seems easy, the subsequent processing steps (filtering, segmentation, reconstruction) are more or less complex. Development of fully automatic algorithms providing reliable 3D building models remains an important challenge, due to the complexity of urban scenes (Akca *et al.*, 2008). Nowadays, no process is able to provide with laser data a 3D city model or even a 3D building in a complete automatic way. Achieving a result is a first important step, but it should be completed by quality assessments. Result assessments for 3D building models are mostly approached in a qualitative visual way. For surveyors, quantitative assessments are essential. Nevertheless, calculating uncertainties in a 3D model is not a trivial task. Unfortunately, 3D is not yet generalized to the building trades. Many surveyors working with laser scanners are forced to degrade the data into 2D drawings, because the contractors are used to work with 2D maps. Therefore 2D assessment approaches must be considered. For assessing 3D models, statistical criteria and error maps have been used. Finally, for assessing the entire 3D building, quality factors based on volume calculations are suggested.

2. RELATED WORKS

While the general emphasis has been to develop methods and tools for automatic or semi-automatic generation of city models, the concept of quality evaluation has also become very important. Assessment is generally considered at the end of a work and frequently limited to a visual check. A few papers address the topic of quality assessment of 3D building models produced with aerial imagery or LIDAR data (McGlone and Shufelt, 1994; Ragia, 2000; Rutzinger *et al.*, 2009, Akca *et al.*,

2008, Schuster and Weidner, 2003, etc.). Although city models are being produced worldwide at a very fast rate, there is a certain lack of standardization regarding the evaluation techniques (Akca *et al.*, 2010; Rutzinger *et al.*, 2009). The rigor of an assessment method is often depending on the ground truth available or on the contractor's specifications. Visual inspection is the minimum required.

The topic of assessment of models produced with TLS data is also a current issue. The quality of the data provided by this increasingly used technology has been analyzed in several papers (Baltasvias, 1999; Reshetuk, 2006; Lichti, 2010) in order to assess the a priori accuracy of points composing a point cloud.

Approaches leading to 3D models by ALS or TLS generally imply several processing steps, which might contribute to the final error budget. However, when public authorities order the modeling of a city or individual buildings, they are limited to the evaluation of the submitted models. For this reason, only the uncertainties occurring in the reconstruction step will be considered in this paper. More details about the assessment of intermediate results like segmentation results obtained with terrestrial or aerial laser scanner data can be found in (Landes *et al.*, 2012, Tarsha-Kurdi, 2008).

The purpose of this work is to propose solutions for the geometric assessment of 3D vector models obtained by processing of ALS and TLS data. Several methods are investigated. 2D quality factors and errors metrics like RMSE are produced, as suggested in Rutzinger *et al.* (2009) or Schuster and Weidner (2003). Also less common indicators, like error maps or volumetric quality factors are suggested. These assessment approaches will be illustrated on 3D building façades obtained from TLS data, and on 3D building roofs obtained from LIDAR data acquired in Strasbourg, France.

Every accuracy assessment study includes three fundamental steps (Congalton, 2009): firstly, design the accuracy assessment sample; secondly, collecting data for each sample, and finally, analyzing the results.

It is useful to remind the distinction between accuracy and precision, because both concepts are sometimes mixed up in the literature. Accuracy calculations suppose that a reference model (ground truth) is gained through an independent and more precise surveying technique than the laser scanning technique. Precision describes the way the points are distributed around the most probable value of the observation or result. Thus for gaining a reference model for precision calculations, it is appropriate to work on the same data, but to use a more precise method for the model creation (generally manual).

3. ASSESSMENT OF RECONSTRUCTED 3D BUILDING MODELS

An interesting study towards quantitative quality evaluation of building models has been achieved in Schuster and Weidner (2003). They refer to approaches developed in (McKeown *et al.* 2000) and (Ragia, 2000) generally for 2D pixel based analysis. Also Song and Haitcoat (2005) suggest the use of surface area based indicators. These indicators are originally coming from remote sensing classification assessments (confusion matrix). But they can also be applied on vector polygons, which surface area will be compared to surface areas of reference polygons. Since point clouds acquired on façades are still too often “degraded” into 2D maps, these factors have been selected for helping to assess 2D building façade models. Also for the assessment of roof models extracted from LIDAR data, these factors provide interesting results.

3.1 Assessment of façade and roof models in 2D

The roofs and façades are produced through as 3D vector data. As mentioned above, several quality factors expressed as ratios have been selected in the literature and calculated on the basis of surface areas of vector polygons. Table 1 reminds their expression where SR means the surface area of the reference vector polygon and ST the surface area of the polygon to be tested.

Quality factor	Explanation
$\rho d = \frac{SR \cap ST}{SR}$ $\rho d \in [0; 1]$	Detection rate: it is the ratio between the intersection area between two planes and the reference plane. $\rho d = 1$ means that the calculated polygon is perfectly superposed to the reference polygon.
$\rho q = \frac{SR \cap ST}{SR \cup ST}$ $\rho q \in [0; 1]$	Quality rate: it is the ratio between the intersection area between two planes and the union of two planes. $\rho q = 1$ means that both polygons are perfectly superposed.
$\rho b = \frac{ST \setminus SR}{SR \cap ST}$ $\rho b \geq 0$	Branch factor: it is the ratio of the part of the reference polygon which is not included in the polygon under study and the intersection of the two polygons.
$\rho m = \frac{SR \setminus ST}{SR \cap ST}$ $\rho m \geq 0$	Miss factor: Ratio of the part of the polygon being evaluated which is not included in a reference polygon and the intersection of the two polygons.
$\rho f = \frac{ST \setminus SR}{SR}$ $\rho f \geq 0$	False alarm rate: it is the ratio of the part of the reference polygon which is not included in the polygon under study compared to the area of the reference polygon.

Table 1. Quality factors used to evaluate surface areas of polygons in vector models

The main difficulty consists into defining an adequate reference model. Satisfying results are reached when the value of ρd and ρq is close to 1, and the three others are close to 0.

3.1.1 Roofs assessment: A complete processing chain leading to 3D building models based exclusively on LIDAR data has been developed in (Tarsha-Kurdi *et al.*, 2008). One algorithm of this chain deals with the reconstruction of roofs and provides automatically 3D vector models of roofs. The reference model chosen for assessment is a stereorestituted vector map of roofs. Roofs are composed of planes, edges and nodes. The point cloud used presents a low point density (1.3 points/m²), and covers the center of Strasbourg where 16 buildings with different levels of complexity have been chosen (Figure 2). The accuracy analysis of these samples based on the quality factors provides mean values higher than 0.83 for ρd and ρq , and lower than 0.13 for ρb , ρm , ρf (Tarsha-Kurdi *et al.*, 2008). These good values confirm the efficiency of the algorithm. Obviously, the point cloud characteristics (density, accuracy, noise), and the complexity of the roof impact the final result.

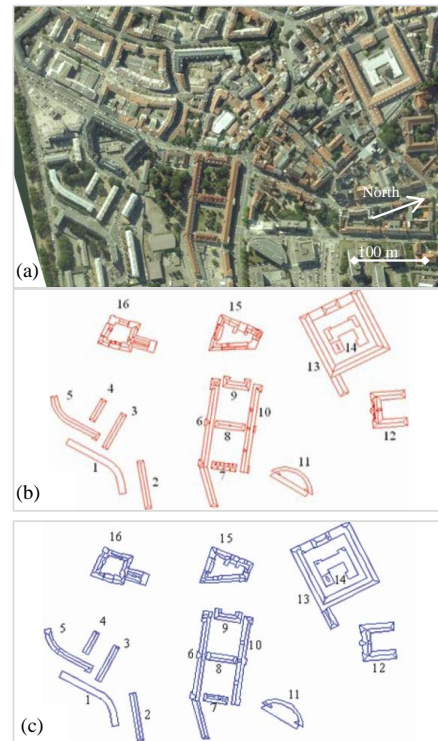


Figure 2. (a) Aerial image of a test site in Strasbourg; (b) vector model of building roofs obtained (b) by photogrammetric stereorestitution (reference) and (c) by automated approach (Tarsha-Kurdi *et al.*, 2008).

Two types of errors may cause bad rates for the quality factors. If small objects on the roof (antennas, chimneys, windows) cannot be modeled due to the low point density, they affect the roof plane equation. They appear in the global error budget like systematic errors. Since the reference roof models have been produced with independent photogrammetric data, also errors stemming from geocoding uncertainties might distort the plane

equations of the roofs and therefore their contours in the 2D plane.

When LIDAR is not able to capture points on building façades, a reconstruction of the buildings by combination of TLS and ALS data is required (Boulaassal *et al.*, 2011). At this stage the assessment must be continued on façades.

3.1.2 Façades assessment: The building façades reconstruction based on TLS data can be assessed by comparing a survey map with the vector model projected on a plane. A complete processing chain leading to 3D geometric façade models has been developed in (Boulaassal *et al.*, 2009) and assessed in (Landes *et al.*, 2012). For illustration purpose, an old building in the center of Strasbourg has been scanned by TLS (Leica C10) with 1 point every cm after registration of three point clouds (Figure 3). It has been chosen for its architecture and because a 3D elevation map produced by stereorestitution was available (Figure 4).

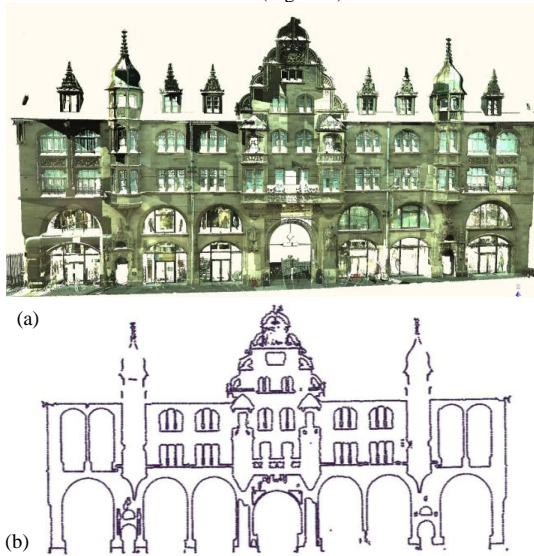


Figure 3. Scanned façade of a complex architectural building (a) and extracted contours (b)

After segmentation in planes, the contour points of the main façade plane have been extracted (Figure 3b) and adjusted in order to produce a vector model of the façade. A few polygons from the restituted model have been chosen for the contours evaluation (Figure 4).

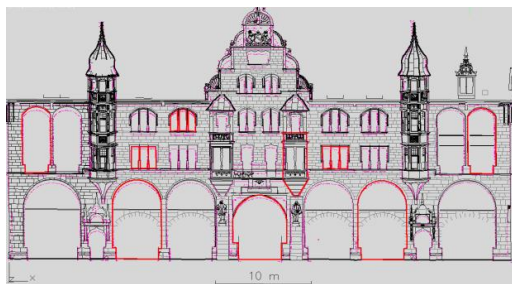


Figure 4. Restituted map (in black) with assessment contours (in red). Extracted contour points appear in magenta.

Sample No.	ST (m ²)	SR (m ²)	SR / ST	ρd	ρq	ρb	ρm	ρf
1	19,36	18,31	17,96	0,93	0,89	0,07	0,01	0,01
2	1,75	1,72	1,66	0,95	0,90	0,05	0,03	0,03
3	5,81	5,65	5,51	0,95	0,92	0,05	0,02	0,02
4	38,26	37,55	37,62	0,98	0,97	0,02	0,00	0,00
5	18,62	17,94	18,12	0,97	0,95	0,03	0,01	0,01
mean				0,96	0,93	0,05	0,02	0,02

Table 5. Quality factors calculated for 5 polygons extracted in the façade.

Then the quality factors ρd , ρq , ρb , ρm , and ρf have been calculated for 5 windows, of various sizes, and showing visually the highest differences with the reference (Table 5). The quality factors are very satisfying and confirm the quality of the produced 2D vector map. However, they do not quantify the geometric accuracy of the reconstructed façade elements.

To complete the assessment, errors metrics like the calculation of deviations and RMSE are relevant. Here, the 3D deviations between the 5 reference contours and the calculated contours reach 6 to 20 cm depending on the window, i.e. 12 cm in average. The RMS error of all the Euclidian distances in 3D reaches 14 cm, which could be better given the technology involved. A visual inspection enables to understand these results. Given that the calculated contours are based on the point cloud, they cannot describe the parts of the façade which are hidden when scanned from a terrestrial point of view (see the shadows at the bottom of windows in Figure 6). Therefore, a visual assessment is essential for justifying the sometimes low geometric accuracy.

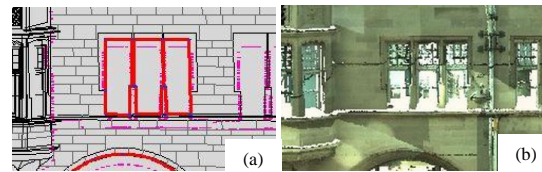


Figure 6. Impact of shadows on the reconstruction of the façade. (a) Reference vector model in red and extracted contour points in magenta before vectorization; (b) colored TLS point cloud.

As a summary, for 2D analyses, the quality factors are useful for roughing out the detection quality, although they imply the definition of thresholds. However, they are not sufficient for assessing the geometric position of the vectors and must be supplemented by statistical criteria like deviations and RMSE.

3.2 Assessment of 3D models

This section considers the assessment of 3D models of roofs and finally of the entire building.

3D roofs assessment: Rottensteiner (2003) suggests the analysis of Root Mean Square Errors (RMSE) for analyzing the precision of the complete 3D building. RMSE are interesting to analyze, especially when plane adjustments are carried out, as it is the case for roofs. However, RMSE describe only the dispersion of points around an average value but not their spatial distribution, which is assumed to be Gaussian. For this reason, a method is proposed for completing the assessment of the 3D roof vector model previously converted into raster format. It is based on the calculation of the distance between each point of the cloud and the mean plane to which it is assigned.

An image called ‘error map’ is produced for every plane entering into the model. A pixel value of zero means that the model coincides with the point cloud. Several buildings acquired with high density (7 points/m²) by ALS over an industrial area have been modeled. Subsequently errors maps have been calculated. Figure 7 presents an example of a building of simple geometry. As deduced from in the error map, more than 90 % of the points are located in +/- 0.25 m around the adjusted roof plane. Since a large amount of pixels is close to zero, it can be affirmed that the results are precise but not necessarily accurate since the reference model is derived from the same data as the those used for reconstruction.

The building roof shown in Figure 8 is of complex architecture and has been extracted from ALS data with lower density (1.3 point/m²). Since the small roof details cannot be detected in that case, they enter in the plane calculation like points describing actually the roof. This influences inevitably the building error map, in which only 60% of points are located in the interval +/- 30cm around the plane. Consequently, the roof plane equations are unrealistic and the 3D building model contains visual distortions. Therefore, the error map is helpful for improving the calculation of the roof plane models and consequently the 3D building model. More details can be found in (Tarsha-Kurdi, 2008).

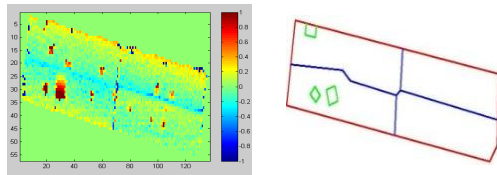


Figure 7. Color coded error map (left) for a 2D roof model (right) of a simple building (Hermann site)

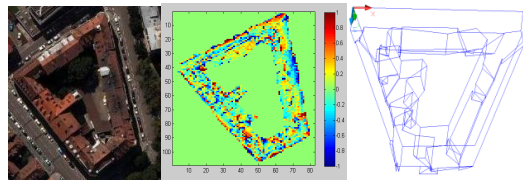


Figure 8. Automatic building modeling of a complex building (Strasbourg site). From left to right: aerial image, error map, complete (distorted) 3D building model.

The same principle can be applied for assessing the accuracy (instead of the precision) of the roof plane extraction. This means having a reliable reference, which is validated as exact (ground truth). In this case, a difference image between label images could be carried out and pixel-based performance metrics can be adopted (Rutzinger *et al.*, 2009).

3.2.2 Entire 3D building assessment: Considering a building as one object, volume comparisons seem to be rather appropriate than surface areas comparisons. Volume comparisons between reference building and modeled building cannot be considered alone, because volume metrics are affected by the building size. Thus, in presence of a majority of small buildings, object-based performance metrics like the volume metric may lead to high error rates (McKeown, 2000; Rutzinger *et al.*, 2009). A new approach aiming to evaluate 3D

buildings is experimented here. The quality factors used in section 3.1 and also applied in (Mohamed and Grussenmeyer, 2011) for plane-based accuracy assessment in photogrammetry, have been extended to the assessment of 3D volumes. It suggests a volume based comparison between a 3D building vector model and an accurate 3D reference model (Figure 9). The volumes are not computed on voxels but on solids obtained by meshing the vector models. The “volumetric” quality factors used for the assessment express the relationships between the volume of the modeled building and the volume of its reference. They take into account the volume of their intersection as well as the volume of their union. Figure 9a illustrates the volume of the reference model (*VR*), volume of the tested model (*VT*) and the volume of intersection (*VI*). Table 10 details the volumetric quality factors. Satisfying results are reached when the value of *Vpd* and *Vpq* are close to 1, and the three others are close to 0.

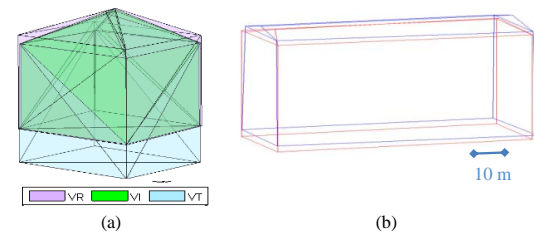


Figure 9. (a) Relationship between reference model (*VR*) and tested model (*VT*), with $VI = VR \cap VT$; (b) superimposition of the reference model (in red) and the extracted model for the building No. 2 (in blue).

For this first experiment, a 3D building model has been extracted by processing of low density LIDAR data (1.3 point/m²). The 3D reference building model has been created based on the photogrammetric processing of images acquired with UltraCam-X stereopairs. The pixel size on the ground is about 16 cm. An accuracy of about 16 cm in X, Y and 25 cm in Z can be estimated for a point digitized in the stereopairs. It is satisfactory, considering that the accuracy of the LIDAR point clouds used here is lower (around 30 to 40 cm in X, Y, Z). Building No. 2 in Figure 2 has been chosen and compared to its reference. The building is about 10m large, 82 long and 22 high. Figure 9b presents the tested model in blue and the reference model in red.

The resulting volumes and quality factors for the building under study are presented in Table 11. The values obtained for the quality factors show that *Vpd* and *Vpq* are higher than 0.8 and the other three factors are close to zero. This means that the 3D building models extracted from both LIDAR and from stereopairs are closed from each other. Since the photogrammetric model is more accurate, the model provided by LIDAR data processing is therefore validated.

This example is interesting, because it shows the interest to undertake an analysis of the entire model in 3D. By applying the assessment on surface areas (see section 3.1) for each side of the building, the results would obviously be much better (values higher than 0.93 for *pd* for example) because projected in 2D, the planes overlap very well. Thus, a 2D analysis alone would overestimate the quality of the model.

Quality factor	Explanation
$V\rho d = \frac{VR \cap VT}{VR}$ $V\rho d \in [0; 1]$	Volumetric detection rate: it is the ratio between the volume of intersection of the two buildings and the volume of the reference building. $V\rho d$ close to 1 means that the calculated model is perfectly superposed to the reference building.
$V\rho q = \frac{VR \cap VT}{VR \cup VT}$ $V\rho q \in [0; 1]$	Volumetric quality rate: it is the ratio between the parts which are common to both volumes and the union of the two volumes.
$V\rho b = \frac{VT \setminus VR}{VR \cap VT}$ $V\rho b \geq 0$	Volumetric branch factor: it is the ratio of the part of the reference building volume which is not included in the building volume under study and the intersection of the two volumes.
$V\rho m = \frac{VR \setminus VT}{VR \cap VT}$ $V\rho m \geq 0$	Volumetric miss factor: it is the ratio of the part of the volume being evaluated which is not included in the reference volume and the intersection of the two volumes.
$V\rho f = \frac{VT \setminus VR}{VR}$ $V\rho f \geq 0$	Volumetric false alarm rate: it is the ratio of the part of the reference volume which is not included in the volume under study compared to the volume of the reference polygon.

Table 10. Volumetric quality factors for assessing 3D building vector models

Building No.2	Volume (m ³)				
	VT	VR	VI = VR ∩ VT		
	20063,31	20299,17	18368,79		
	Volumetric quality factors				
	$V\rho d$	$V\rho q$	$V\rho b$	$V\rho m$	$V\rho f$
	0,905	0,835	0,105	0,092	0,083

Table 11. Volumes of tested and reference buildings and volumetric quality factors for a building.

This volume based approach has the advantage to be easy to apply, and to be data and process independent; it requires only reference datasets. A drawback is the necessity for the user to set a threshold for describing the level of concordance between models. As mentioned in (McKeown, 2000), the metrics should not be tunable via thresholds, because they introduce a subjective element into evaluation.

Moreover, the quality factors might be favorable although the building shape is not validated. Figure 9b clearly shows that a vertical shift affects the model to be tested. Any shift or rotation between the reference and the tested model will affect the intersection volume between the models. But the same shift for a small or for a big building will not provide the same factors. The sensitivity of the approach regarding the effect of the building size, building shape, building shifts, rotations must be analyzed.

However, it becomes clear that the calculation of volume ratios for assessing the quality of 3D building modeling is not sufficient.

For taking into account the shifts, a RMSE is computed based on the deviations between both models, in X, Y and Z directions. Deviations are not calculated between homologous nodes, but between centers of gravity of homologous planes that compose the tested and respectively the reference building. This choice has been made, because it is not trivial –for our knowledge– to automatically find corresponding vertices to compute the RMSE between the vertices of two vector

buildings in 3D. Table 12 presents the RMSE results obtained for the building under study. The value of RMSE in X-direction is about 0.4 m while the RMSE in Y-direction is 0.5 m and 1 m for Z-direction.

Building ID	RMSE(m) on plane gravity centers		
	RMSE_X	RMSE_Y	RMSE_Z
No. 2	0,41	0,51	1,09

Table 12. RMSE values obtained for the planes of the building No. 2

The error budget affecting the final product is not only composed of errors due to the reconstruction algorithm, but also of errors coming from a low point cloud density, errors due to the georeferencing of the LIDAR and the aerial data, due to the shape of the produced buildings, etc. Several tests applied on a large sample of building reveals that a systematic error affects the Z coordinates of the LIDAR data used here. This vertical shift has already been observed in a study where LIDAR data have been combined to TLS data (Boulaassal *et al.*, 2011). Once detected, this error must be corrected for the whole dataset before starting again the assessment.

At this stage, further investigations regarding the completeness of the assessment approach as a combination of quality factors and statistical criteria are necessary. As underlined in (Rutzinger *et al.*, 2009), there is no single optimum evaluation technique and the combination of several evaluation methods is advised. Regarding the setting of thresholds for the volumetric quality factors and the RMSE values, a standard model inspired from a national order helping the contractors checking the quality of subcontracted work is under study.

4. CONCLUSION

Currently, no standard has been defined to assess 3D models and which automatically assess whether a 3D model is acceptable or not. This paper presents the assessment of 3D vector models of façades, roofs and complete buildings, using several approaches. Of course, visual inspection cannot be avoided. For assessing façades or roofs outlines in 2D, quality factors already suggested in the literature have been applied. For assessing 3D vectors, statistical criteria like RMSE are somewhat restrictive and that's why they have been supplemented by error maps. For assessing entire 3D building models, quality factors based on volume ratios have been considered and completed by RMSE considerations. This approach must be further investigated regarding shape characteristics of the buildings.

Our future researches will also focus on the study of a standard assessment model, helping the end user to make a judgment on the level of accuracy provided by the building models with respect to their requirements. Finally, the main difficulty of assessment approaches is to create sufficient high quality reference data at low cost.

5. REFERENCES

Akca, D., Freeman, M., Sargent, I. and Gruen, A., 2010. Quality assessment of 3d building data. *Photogrammetric Record* Vol. 25 (132), pp. 339-355.

- Baltsavias, E. P. 1999. Airborne laser scanning: basic relations and formulas. *ISPRS Journal of Photogrammetry and Remote Sensing*, 54(2-3): 199–214.
- Boulaassal, H., Landes, T., Grussenmeyer, P., 2009. Automatic extraction of planar clusters and their contours on building façades recorded by terrestrial laser scanner. In *Special issue of the International Journal of Architectural Computing IJAC*, Issue 07, Vol. 01, p. 1-20.
- Boulaassal, H., Landes, T., Grussenmeyer, P., 2011. Reconstruction of 3D Vector Models of Buildings by Combination of ALS, TLS and VLS Data. *4th 3D-ARCH International Conference on 3D Virtual Reconstruction and Visualization of Complex Architectures*, Trento (Italy), 2-5 March 2011, 6 pages.
- Landes, T., Boulaassal, H., Grussenmeyer, P., 2012. Quality assessment of geometric façade models reconstructed from TLS Data. *The Photogrammetric Record*, DOI: 10.1111/j.1477-9730.2012.00674.x, 18 pages.
- Lichti, D. D., 2010. Terrestrial laser scanner self-calibration: correlation sources and their mitigation. *ISPRS Journal of Photogrammetry and Remote Sensing*, 65(1): 93–102.
- McGlone, J. C. and Shufelt, J. A., 1994. Projective and object space geometry for monocular building extraction. *IEEE Computer Society Conference on Computer Vision and Pattern Recognition*. 54–61.
- McKeown, D., Bulwinkle, T., Cochran, S., Harvey, W., McGlone, C. and Shufelt, J., 2000. Performance evaluation for automatic feature extraction. *IAPRS International Archives of Photogrammetry and Remote Sensing*, Vol.33, pp. 379-394.
- Mohamed, M., Grussenmeyer, P., 2011. Plane-based accuracy assessment in photogrammetry: comparison of Rollei Medium format and Ultracam-X digital cameras. *GTC2011 Symposium, Geomatics in the City*, Jeddah, Saudi Arabia, May 11-13, 6 pages.
- Ragia, L., 2000. A quality model for spatial objects. *International Archives of Photogrammetry and Remote Sensing*, 33(B4): 855–862.
- Reshetyuk, Y., 2006. Investigation and calibration of pulsed time-of-flight terrestrial laser scanners. Licentiate thesis in Technology, *Royal Institute of Technology (KTH)*, Stockholm, Sweden. 152 pages.
- Rottensteiner, F., 2003. Automatic generation of high-quality building models from LIDAR data. *IEEE Computer Graphics & Applications*, 23 (6), 42-51.
- Rutzinger, M., Rottensteiner, F., Pfeifer, N., 2009. A comparison of evaluation techniques for building extraction from airborne laser scanning. *IEEE Journal of selected topics in applied earth observations and remote sensing*, Vol. 2, No.1.
- Schuster, H. F. and Weidner, U., 2003. A new approach towards quantitative quality evaluation of 3D building models. *ISPRS Commission IV Joint Workshop on Challenges in Geospatial Analysis, Integration and Visualization II*, Stuttgart, Germany. 8 pages.
- Song, W. and Haithcoat, T.-L., 2005. Development of comprehensive accuracy assessment indexes for building footprint extraction, *IEEE Trans. Geosc. Remote Sensing*, vol. 43, no. , pp. 401-404.
- Tarsha-Kurdi, F., Landes, T., Grussenmeyer, P., 2008. Extended RANSAC algorithm for automatic detection of building roof planes from LIDAR data. *The Photogrammetric Journal of Finland*. Vol. 21, n°1, 2008, pp.97-109.
- Tarsha-Kurdi, F., 2008. Extraction et reconstruction de bâtiments en 3D à partir de relevés LIDAR aéroportés. PhD Thesis of the Strasbourg University, supervised by INSA Strasbourg.

6. ACKNOWLEDGEMENTS

Authors want to thank Fayez Tarsha-Kurdi, who made his PhD at the INSA Strasbourg until 2008. Some datasets of his work have been used in this paper.

MULTI-DIMENSIONAL QUALITY ASSESSMENT OF PHOTOGRAMMETRIC AND LIDAR DATASETS BASED ON A VECTOR APPROACH

M. Mohamed^a, T. Landes^a, P. Grussenmeyer^a, W. Zhang^b

^aINSA Strasbourg, ICube Laboratory UMR 7357, Photogrammetry and Geomatics Group
Strasbourg, France- (mostafa.mohamed, tania.landes, pierre.grussenmeyer@insa-strasbourg.fr)

^bState Key Laboratory of Remote Sensing Science, Beijing Key Laboratory of Environmental Remote Sensing and
Digital City, School of Geography, Beijing Normal University, 100875 Beijing, China - (wumingz@bnu.edu.cn)

KEY WORDS: Optical imagery, LiDAR, 3D building modeling, Quality assessment, RMSE, Surface indices, Volume indices.

ABSTRACT:

The production of 3D city models requires the reconstruction of individual 3D building models. As the performance of data acquisition methods improves, the quality evaluation of building models in 3D has become an important issue. The main objective of the presented work is to introduce a multi-dimensional approach for assessing the quality of 3D building vector models. This approach performs assessments in 1D, 2D and 3D by comparing calculated building models to their reference. For 1D assessment, homologous points in two buildings to be compared are analyzed. For 2D assessment, homologous planes enter in the evaluation process. Quality of the planes under study is assessed by calculating a set of indices in vector format. For 3D assessment, building models are considered as one object. Quality of the buildings is assessed by calculation of vector volumetric quality factors. These factors require the not trivial calculation of vector intersection volumes which calculation is presented in the paper. Intersection volume is defined by superimposing the building model to be tested with the reference one. The multi-dimensional vector assessment approach has been applied to evaluate the building models produced with three different reconstruction processes created from different types of datasets. The datasets are obtained by photogrammetry (UltraCam-X and Zeiss LMK cameras), by LiDAR, and also by integration of photogrammetric and LiDAR datasets. The 1D, 2D or 3D assessment approach allows highlighting the source of deviations in the tested buildings. The error budget affecting the final product is not only composed of errors due to the reconstruction algorithm. Also errors due to the quality of the raw data, the processing of LiDAR data, of aerial data and the shape of the produced buildings should be considered.

1 INTRODUCTION

Photogrammetric and LiDAR data are used since many years for the 3D reconstruction of objects such as buildings. These applications need accurate data and methods in order to produce good results. Quality assessment is critical for 3D data production and is important for several reasons. Firstly, it may give important information about deficiencies of an approach and may take place to help in focusing a further research activity. Secondly, accuracy evaluation is needed in order to compare the results of the different approaches and to convince a user (Schuster and Weidner, 2003). Several methods were presented in order to evaluate photogrammetric and LiDAR datasets. Calculation of Root Mean Square Errors (RMSE) for analyzing the precision of the complete 3D building is an interesting process. It shows the shifts between reference and test models in X, Y and Z directions. (Grussenmeyer et al., 1994) proposed statistical techniques in order to calculate RMSE by point and line based assessment. Several approaches using quality factors for quality evaluation of building models were introduced ((McKeown et al., 2000), (Rajia, 2000)). Based on these, a further approach was developed, which introduced alternative quality measurements (Schuster and Weidner, 2003).

All accuracy assessments processes include three fundamental steps (Congalton and Kass, 2009). Firstly, the accuracy assessment sample should be designed. The sampling design issues are similar to those traditionally addressed by survey sampling methodology: how to choose sample in a cost-effective and at the same time statistically rigorous manner? Application of basic sampling designs such as simple random, stratified random, systematic and cluster have been summarized in (Congalton and Kass, 2009). Secondly, data must be collected for each sample; and finally, results must be analyzed. Because high quality reference data are difficult and expensive to obtain, reference

model may be considered as error-free, more accurate than the test model, or with the same accuracy as the test model (Meidow and Schuster, 2005). Once the reference data are available, the assessment process can start.

Related works were done by the Photogrammetry and Geomatics Group at INSA-Strasbourg. In the context of assessing the quality of planes detection in a 3D building reconstruction process based on LIDAR data, several solutions have been suggested (Tarsha-Kurdi et al., 2008). For evaluating the quality of geometric facade models reconstructed from TLS data, (Landes et al., 2012a) suggested the use of quality factors and RMSE calculations. Also, the evaluation of characteristic planes extracted from digital airborne sensors have been published in (Mohamed and Grussenmeyer, 2011). A new approach has been proposed for assessing 3D building models based on vector volumetric quality factors (Landes et al., 2012b). The main objective of the presented work is to introduce a multi-dimensional approach for evaluating the quality of 3D building models reconstruction. The approach used in this research is vector based.

2 ASSESSMENT OF 3D BUILDING MODELS

2.1 1D assessment

Point accuracy assessment allows to evaluate fully 3D geometry datasets by comparing points to points (Rottensteiner and Briese, 2002). Calculations are performed to compare two different 3D building models. This is done by computing RMSE based on the deviations between both models (reference and test), in X, Y and Z directions. Deviations are not calculated between homologous nodes, but between centers of gravity of homologous planes that compose the tested and respectively the reference building.

2.2 2D assessment

Our method to evaluate 2D data is based on the comparison of 3D planes of two building models (reference and test) by calculating a set of indices. This approach uses well known quantities, as mentioned in (McKeown et al., 2000), (McGlone and Shufelt, 1994), (Ragia, 2000), (Schuster and Weidner, 2003) and (Landes et al., 2012b). These indices are namely the detection rate (ρd), the branch factor (ρb), the quality rate (ρq), miss factor (ρm), and false alarm rate (ρf) as summarized in Table 1. The principle idea of these indices is based on the relation between the reference surface area (A_r) and the tested surface area (A_t) as shown in Figure 1(a).

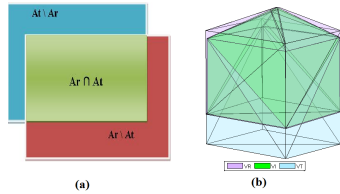


Figure 1: Relationship between reference and tested models in 2D (a) and 3D (b).

Quality factor	Explanation
$\rho d = \frac{A_r \cap A_t}{A_r}$ $\rho d \in [0 : 1]$	Detection rate: it is the ratio between the intersection area between two planes and the reference plane. $\rho d = 1$ means that the calculated polygon is perfectly superposed
$\rho q = \frac{A_r \cap A_t}{A_r \cup A_t}$ $\rho q \in [0 : 1]$	Quality rate: it is the ratio between the intersection area between two planes and the union of two planes. $\rho q = 1$ means that both polygons are perfectly superposed.
$\rho b = \frac{A_t \setminus A_r}{A_r \cap A_t}$ $\rho b \geq 0$	Branch factor: it is the ratio of the part of the reference polygon which is not included in the polygon under study and the intersection of the two polygons.
$\rho m = \frac{A_r \setminus A_t}{A_r \cap A_t}$ $\rho m \geq 0$	Miss factor: Ratio of the part of the polygon being evaluated which is not included in a reference polygon and the intersection of the two polygons.
$\rho f = \frac{A_t \setminus A_r}{A_r}$ $\rho f \geq 0$	False alarm rate: it is the ratio of the part of reference polygon which is not included in the polygon under study compared to the area of the reference polygon.

Table 1: Quality indices based on surface areas ratios.

2.3 3D assessment

Considering a building as one object to be evaluated, volume comparisons are rather appropriate than surface areas comparisons. Therefore, the quality of buildings is assessed by the calculation of volumetric quality factors. The quality factors in 3D are deduced from the 2D quality factors and depend on ratios of volumes. These factors take into account the volume of the intersection as well as the union volume of two vector buildings. A first experiment has been introduced in (Landes et al., 2012b). The principle idea of these indices is based on the relation between the reference volume (V_r) and the tested volume (V_t) as shown in Figure 1(b).

Equations in Table 2 detail the volumetric quality factors. Satisfying results are reached when the value of $V \rho d$ and $V \rho q$ is close to 1, and the three others are close to 0.

Quality factor	Explanation
$V \rho d = \frac{V_r \cap V_t}{V_r}$ $V \rho d \in [0 : 1]$	Volumetric detection rate: it is the ratio between the volume of intersection of the two buildings and the volume of the reference building.
$V \rho q = \frac{V_r \cap V_t}{V_r \cup V_t}$ $V \rho q \in [0 : 1]$	Volumetric quality rate: it is the ratio between the parts which are common to both volumes and the union of two volumes.
$V \rho b = \frac{V_t \setminus V_r}{V_r \cap V_t}$ $V \rho b \geq 0$	Volumetric branch factor: it is the ratio of the part of reference building volume which is not included in the building volume under study and the intersection of two volumes.
$V \rho m = \frac{V_r \setminus V_t}{V_r \cap V_t}$ $V \rho m \geq 0$	Volumetric miss factor: it is the ratio of the part of the volume being evaluated which is not included in reference volume and the intersection of two volumes.
$V \rho f = \frac{V_t \setminus V_r}{V_r}$ $V \rho f \geq 0$	Volumetric false alarm rate: it is the ratio of the part of reference volume which is not included in volume under study compared to the volume of reference polygon.

Table 2: Quality indices based on volume ratios.

3 GEOMETRIC COMPUTATIONS

The operation of determining the union and intersection of areas (or volumes) when two models must be compared is a topic of geometric computation. This section describes the algorithms leading to calculate union and intersection of areas/volumes which come into consideration when a model to be assessed is compared to a reference model. First of all the areas and volumes of the models under study must be calculated.

3.1 Surface area computation

For the area computation in vector form, we use the formula based on Green's theorem (O'Rourke, J, 1998) and given in Equation (1).

$$A = \frac{1}{2} |\sum_{k=1}^n X_k Y_{k+1} - X_{k+1} Y_k| \quad (1)$$

Where n is the number of vertices, $X_{n+1} = X_1$ and $Y_{n+1} = Y_1$. X and Y are the coordinates of vertices points of the polygon numbered in ascending order.

3.2 Intersection area computation

The operation of determining the intersection area of two vector polygons is performed in two steps: the detection of the points located inside the polygons and the detection of lines intersections.

Step1: classification of the points located inside the polygons

As shown in Figure 2(a), points 3 and 5 are "inside points". In Figure 2(b), all points of the red polygon are classified as inside points. Matlab built-in function uses a simple and commonly used technique for point-in-polygon detection, and works as follows. Assuming the polygon is defined by n points in an array P , this algorithm computes the summation of angles between the query point and every pair of points defining each edge of the polygon (i.e. the angle is formed by the $P[n]$ point, query point, and $P[n+1]$). If this summation computes to 2π (or near 2π within some tolerance), then the point is inside the polygon. If

the summation computes to zero (or near zero) then the point is outside the polygon.

Step2: detection of points at the intersection between lines

For example, in Figure 2(a), the point of intersection between line (2, 3) and line (5, 6) is a "point of intersection" to consider, as well as the intersection point of lines (4, 3) and (5, 8). However, the intersection between lines (4, 3) and (6, 7) is not an intersection point to consider. That's why it must be checked if the intersection point lies on the edges of both polygons. This check is done by computing the distance between the intersection point and the two points of the line. If the maximum of the two distances is shorter than the edge length, the point of intersection belongs to the edge. Then the resulting intersection shape can be calculated based on the coordinates of its vertices (see Equation (1)).

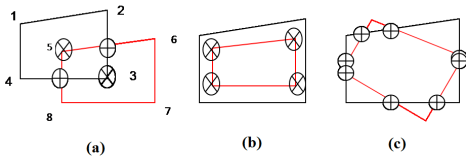


Figure 2: Intersection area calculation for vector polygons in 2D.

3.3 Volume calculation

In order to compute the volume of 3D objects, one has to solve two tasks; firstly determine the convex hull of the given boundary, then, calculate the volume of the resulting 3D polyhedron. Convex hull is the boundary of a closed convex surface generated by applying Delaunay triangulation on the corner points. In three dimensions, the convex hull corresponds to a closed polyhedron. Convex hull calculation is a hard process in computational geometry (Barber et al., 1996). A large class of algorithms that compute the exact volume of a convex object is based on triangulation methods (Büeler et al., 1997). The result of convex hull calculation for a gable roof building is shown in Figure 3(a). The convex hull of a set of points in two or three dimensions is given by Matlab built-in function (*convhulln* in 2D or *convhulln* in 3D) as presented in Equation (2). These functions use meshed objects for storing and displaying polyhedra. The faces of such polyhedra are triangles.

$$[K \quad V] = \text{convhulln}(x, y, z); \quad (2)$$

In 3D, the boundary of the convex hull, K, is represented by a triangulated 3D object. It is a set of triangular facets in face-vertex format that is indexed with respect to the point array. Each row of the matrix K represents a triangle. The volume, V, bounded by the 3D convex hull can optionally be returned by *convhulln*.

In a first step, the meshed model is computed. It is defined by the input points. The sum of the volumes composing the meshed model equals to the volume of the convex object.

3.4 Intersection volume calculation

The calculation of volume of intersection between two 3D models in vector format is more accurate than in raster format, but also much more complicated. We propose an algorithm allowing to simplify this process. Our method consists of extracting the vertices of 3D intersection volumes. The flowchart in Figure 4 shows the process of intersection volume calculation.

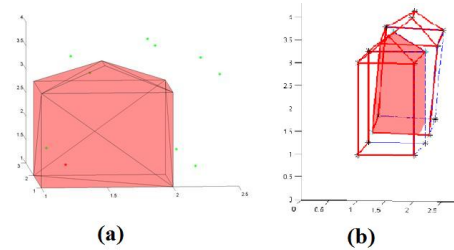


Figure 3: Calculation of convex hull(a) and intersection volume (b).

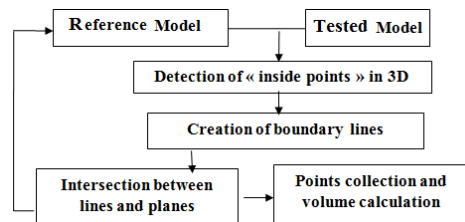


Figure 4: Flowchart of the method of intersection volume calculation.

The following steps are performed:

Step 1: detection of inside points

Extraction of the first group of points is defined by searching about vertices of the reference points located inside the model to assess. This can be done by applying the function "*convhulln*" to the points of the model to assess. The points that are inside the reference model are located on the positive side of the plane normals of all of the faces. The result of this process is shown in Figure 3(a) where inside points are in red and outside points in green color.

Step 2: creation of boundary lines and their intersection with planes

The second group of points describing the intersection shape can be determined by calculating the intersection of the lines composing the reference model with all planes that are composing the model to assess. This process can be achieved firstly by separating the edge lines of each plane of the reference model. Then, the duplicated lines are cancelled in order to avoid repeating the same process. After that, the intersections of all lines with all planes of the model to assess are calculated. In order to check if the resulting point is located on the edge line (and not on the extension of the edge line) and simultaneously belongs to the face of model to assess, two tests should be made. Firstly, we test if the point is placed on the edge line by distance computation as shown in section 3.2. A second test is achieved by looking for the "points inside a polygon" in 2D (in the frame of the intersected plane), as explained in section 3.2.

Step 3: repetition of steps 1 and 2

Steps 1 and 2 are repeated by replacing the reference model by the model to assess for the process leading to edge line creation. Then the intersection between lines of the model to assess with all the planes of reference model is performed. Finally, as a result of these steps, the coordinates of vertices of the intersection shape are determined and the volume of this shape can be calculated. Figure 3(b) shows the intersection shape (filled with red color) obtained by the intersection of a reference model and a test model.

4 3D BUILDINGS RECONSTRUCTION

In this paper, three methods for 3D buildings reconstruction are presented.

4.1 Test site and datasets

The study area is located in the city of Strasbourg, France. Digital aerial images from UltraCam-X (4 images) and frame Zeiss LMK (6 images) of the same area were available. Table 3 shows characteristics of the photogrammetric data. Moreover, LiDAR data of the same area has been captured in 2004 (Table 4).

Sensor	Ultracam-X	Zeiss LMK
Acquisition date	2007	1998
Focal length (mm)	100.500	211.03
Ground Sampling Distance (cm)	16	24
Pixel size (μm)	7.2	30
Image format (pixels)	9420 by 14430	7680 by 7680
Flying height (m)	2300	1700
Overlap %	65	70
Base (m)	527	556

Table 3: Characteristics of photogrammetric datasets.

LiDAR system	TopScan / Optech ALTM 1225
Acquisition date	2004
Flying height (m)	1440
Density of points	1.3 points/ m^2

Table 4: Characteristics of the LiDAR datasets.

14 ground control points were measured by GNSS. The digital aerial photographs have unknown imaging orientation parameters. Using bundle block adjustment, the exterior orientation parameters of the images have been calculated by KLT software. In our application, the camera information was taken from the calibration sheet given by the camera owner.

3D reference buildings models have been created based on the photogrammetric processing of images acquired with UltraCam-X stereo-pairs. After relative and absolute orientation of the images, an accuracy of about 16 cm in X, Y and 25 cm in Z can be estimated for a point digitized in the stereo-pairs. It is satisfactory, considering that the accuracy of the LiDAR point clouds used here is lower (around 30 to 40 cm in X, Y, Z). So, it has been decided that the 3D buildings from UltraCam-X stereo-pairs will be used as references for assessing the 3D buildings reconstructed a) from Zeiss LMK stereo-pairs (75 buildings), b) from LiDAR data (8 buildings), and c) from integration of LiDAR and UltraCam-X stereo-pairs (26 buildings). For illustration purposes, only 8 buildings are shown in Figure 7. The reconstructed buildings in the test site have three types of roofs: flat, hip and gable roofs.

4.2 3D models from aerial images

The geometry of objects (roofs, walls, and footprints) are extracted from multiple images. The flowchart of the semi-automatic approach is depicted in Figure 5. The first step of building reconstruction is roof digitizing. Then, the projection of these points onto the ground is done in order to obtain footprints and thus to create the walls. Finally, planes of faces and footprints are created.

The reconstruction approach is based on the assumption that: (a) every solid object can be described by a decomposition of its boundaries; (b) the walls are vertical and reach either the ground

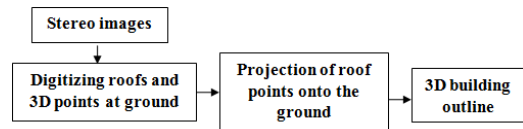


Figure 5: Flowchart of 3D building modeling from aerial images.

or another surface of the constructed model. The wall faces can be constructed using the outlines of the roofs (no facade details). Therefore it is not necessary to digitize the footprints of the buildings. In this work, we restrict our study to simple polyhedral models. Figure 7(b) presents 8 of the 75 samples of building models reconstructed in the test site (in yellow colour) as well as the corresponding reference (in red).

4.3 3D models from LiDAR and aerial images

The semi-automatic method proposed by (Zhang et al., 2011) is based on the complementarities of airborne LiDAR and optical imagery (UltraCam-X). It consists of 4 steps (Figure 6).

Firstly, the building is decomposed into several primitives. The primitives parameters are measured manually on LiDAR and aerial imagery, such as length, width, height, orientation and translation of the primitive. These measurements can be used as constraints or initial values in the following optimization procedure. Secondly, features primitives are selected on the imagery. Corners are detected on the optical imagery, and planes are selected in the LiDAR point cloud. These features are used as observations in the following optimization procedure. Thirdly, the algorithm optimizes primitives parameters by the constraints of LiDAR point cloud and imagery. Based on the type and parameters of primitives, the 3D coordinates of the features primitives, such as corners, can be calculated. These 3D coordinates will be used as computed values in the next iteration. Finally, 3D building models are produced.

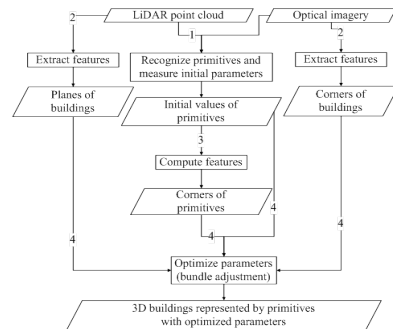


Figure 6: Flowchart of the reconstruction process using LiDAR data and aerial images (Zhang et al., 2011).

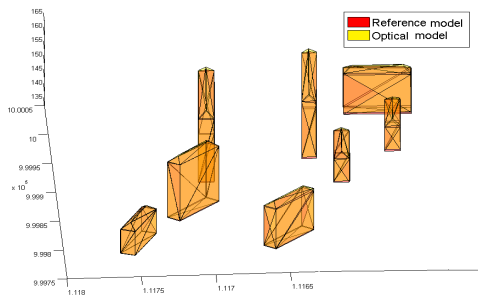
This method has been applied to 26 building models of the test site. Figure 7(c) shows 8 of 26 samples of reconstructed buildings (in green) and their reference buildings (in red).

4.4 3D models from LiDAR datasets

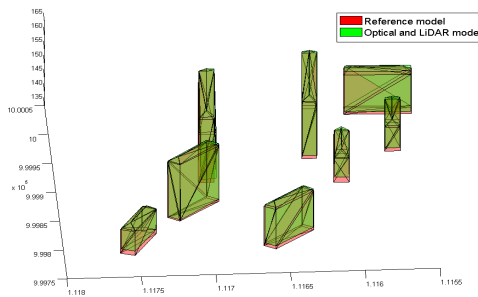
In this part, a model-driven building reconstruction method using airborne LiDAR data is presented. This method has been carried out by Yong Xiao from the Chinese Academy of Sciences (China). This semi-automatic reconstruction process comprises 3 steps.



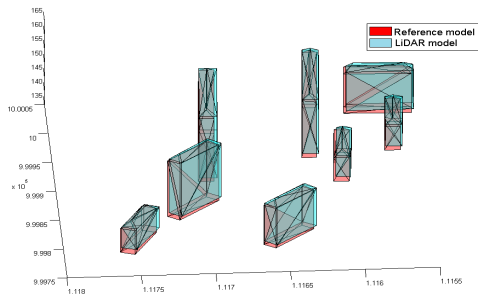
(a) Part of the models under study



(b) Models obtained from aerial images (8 of 75 buildings).



(c) Models obtained from aerial images and LiDAR datasets (8 of 26).



(d) Models obtained from LiDAR datasets.

Figure 7: Reference and tested building models.

At first, the point cloud covering the building is segmented to isolate building roofs. Then, a topological graph is constructed

to recognize the shape of the buildings. Finally, once simple roof types are determined, building models are reconstructed with predefined models. Outlines of the buildings are first estimated with the minimum area bounding rectangle while the other key vertices and segments are obtained through the roof-topology graph. More details are given in (Verma et al., 2008). Figure 7(d) shows the results. The buildings reconstructed from LiDAR datasets are in cyan colour and their reference in red.

5 ASSESSMENT RESULTS

In this section, we assess the 3D vector building models reconstructed previously, by applying the multi-dimensional assessment approach suggested in section 2.

5.1 1D assessment

The reference building models are the models reconstructed from UltraCam-X (see section 4.2). Deviations are calculated between centers of gravity of homologous planes that compose the tested and respectively the reference building. Table 5 presents the RMSE results obtained. The models reconstructed from aerial images give better results than the other methods. The models reconstructed from integration of LiDAR and aerial images give high RMSE in Z-direction. Worse results are obtained for models reconstructed with LiDAR data only. The error budget is not only composed of errors due to the reconstruction algorithm, but also of errors coming from the raw data. For instance, low point cloud density and errors due to the georeferencing of the LiDAR and the optical data affect the final results.

Reconstruction from	RMSE (m)		
	X	Y	Z
Aerial images [75 buildings]	0.21	0.26	0.50
Integration of aerial images and LiDAR datasets [26 buildings]	0.50	0.48	0.94
LiDAR dataset only [8 buildings]	0.64	0.99	1.00

Table 5: RMSE calculated on gravity centers of homologous planes.

5.2 2D assessment

The statistics of the 2D quality indices calculated for assessing the faces of the building models are summarized in Table 6. For models created from aerial images, the mean values of ρ_d and ρ_q are about 0.9 and the other three indices are close to 0. The worse values obtained for the other models are explained by the high RMSE in Y and/or Z-directions (Table 5). This means that the 3D surface of building models extracted from stereo-pairs are close from each other. Also, the models reconstructed from LiDAR or integration of LiDAR and aerial images are less accurate than the models reconstructed from aerial images alone. However, the mean values of quality indices can not be considered alone. In order to evaluate the building reconstruction quality in detail and to analyze the values of the 2D quality factors, one should check the quality indices for each building separately. Moreover, surface metrics are affected by the building size. Small buildings generally lead to bad results regarding the 2D quality indices.

Reconstruction from	ρ_d	ρ_q	ρ_b	ρ_m	ρ_f
Aerial images	0.938	0.891	0.089	0.085	0.062
Images & LiDAR	0.867	0.788	0.177	0.154	0.120
LiDAR only	0.840	0.711	0.219	0.250	0.189

Table 6: 2D quality indices.

5.3 3D assessment

The results of the quality analysis based on volumetric quality factors are shown in Table 7. The mean values of V_{pd} and V_{pq} are about 0.9, while the other three indices are close to 0 for 75 models of aerial images. The mean values of volume quality indices, V_{pd} and V_{pq} are about 0.8. The other three indices are about 0.1 for 8 models created from LiDAR datasets and 26 models of integration of optical and LiDAR datasets. This means that the models reconstructed from aerial images are more accurate than the other models.

Reconstruction from	V_{pd}	V_{pq}	V_{pb}	V_{pm}	V_{pf}
Aerial images	0.943	0.895	0.063	0.058	0.054
Images & LiDAR	0.875	0.809	0.148	0.102	0.089
LiDAR only	0.885	0.791	0.136	0.136	0.120

Table 7: 3D quality indices.

The 3D assessment provides more information than the 2D assessment, because it takes into account the shift which might exist in the third dimension between the two 2D surfaces. This occurs for the quality indices obtained for the models reconstructed from the LiDAR dataset. All tests applied on the building models reveal that a systematic error affects the Z coordinates of the LiDAR data used here. This vertical shift has already been observed in a study where ALS and TLS data were combined (Boulaassal et al., 2011).

6 CONCLUSIONS AND FUTURE WORK

In this paper, three semi-automatic methods for 3D building reconstruction in vector format have been mentioned and carried out on the same test site. The quality evaluation of these models has been achieved by applying the proposed multi-dimensional quality assessment approach. This approach considers the accuracy of the 3D building models based on the comparison of points in 1D, of surfaces in 2D, and of volumes in 3D. 1D assessment gives an overall idea about the reliability of the reconstructed models. 2D assessment checks the superimposition of faces, despite its dependency on the size of the polygons to be compared. 3D assessment compares the buildings in 3D through the comparison of their volumes intersection. It is appropriate for detecting the direction of errors (shifts in X, Y, and Z or rotations). This multi-dimensional approach is suitable for 3D building vector models created from aerial images and/or LiDAR datasets. Future researches will focus on the extension of this approach to more complex building models. In this context, it will be focused on the benefits of using raster assessment approaches.

REFERENCES

Barber, C., Dobkin, D. and Huhdanpaa, H., 1996. The Quickhull algorithm for convex hulls. *ACM Transactions on Mathematical Software*. pp. 469-483.

Boulaassal, H., Landes, T. and Grussenmeyer, P., 2011. Reconstruction of 3D vector models of buildings by combination of ALS, TLS and VLS data. 4th 3D-ARCH International Conference on 3D Virtual Reconstruction and Visualization of Complex Architectures. Trento (Italy), 2-5 March 2011, 6 pages.

Büeler, B., Enge, A. and Fukuda, K., 1997. Exact volume computation for polytopes: A practical study. *Polytopes - Combinatorics and Computation*. 18 pages.

Congalton, G. and Kass, G., 2009. *Assessing the Accuracy of Remotely Sensed Data: Principles and Practices*. Taylor and Francis Group LLC. 2nd Ed. 183 pages.

Grussenmeyer, P., Hottier, P. and Abbas, I., 1994. Le contrôle topographique d'une carte ou d'une base de données constituées par voie photogrammétrique. *Journal of the French Association of Topography, XYZ*. No. 59, pp. 39-45.

Landes, T., Boulaassal, H. and Grussenmeyer, P., 2012a. Quality assessment of geometric facade models reconstructed from TLS data. *The Photogrammetric Record*. Vol. 27, Issue 138, pp. 137-154.

Landes, T., Grussenmeyer, P., Boulaassal, H. and Mohamed, M., 2012b. Assessment of three-dimensional models derived from LiDAR and TLS data. *International Archives of the Photogrammetry, Remote Sensing and Spatial Information Sciences*. Vol. XXXIX-B2, Commission II, WG4, pp. 95-100.

McGlone, J. and Shufelt, J., 1994. Projective and object space geometry for monocular building extraction. In: *Proceedings Computer Vision and Pattern Recognition CVPR '94, IEEE Computer Society, Seattle, WA, USA*. pp. 54-61.

McKeown, D., Bulwinkle, T., Cochran, S., Harvey, W., McGlone, C. and Shufelt, J., 2000. Performance evaluation for automatic feature extraction. *IAPRS International Archives of Photogrammetry and Remote Sensing*. Vol. XXXIII, Part B2. Amsterdam 2000. pp. 379 - 394.

Meidow, J. and Schuster, H., 2005. Voxel-based quality evaluation of photogrammetric building acquisitions. In: *ISPRS Workshop on Object Extraction for 3D City Models, Road Databases and Traffic Monitoring (CMRT05)*, Vol. XXXXVI, Part 3/W24. pp. 117-124.

Mohamed, M. and Grussenmeyer, P., 2011. Plane-based accuracy assessment in photogrammetry: comparison of Rollei medium format and UltraCam-X digital cameras. In: *GTC2011 Symposium, Geomatics in the City, Jeddah, Saudi Arabia*. 6 pages.

O'Rourke, J., 1998. *Computational geometry in C*. Cambridge University Press, second edition. 392 pages.

Ragia, L., 2000. A quality model for spatial objects. In: *ISPRS Congress, Part B4*, Vol. Vol. XXXIII, Amsterdam. pp. 855-862.

Rottensteiner, F. and Briese, C., 2002. A new method for building extraction in urban areas from high-resolution LIDAR data. *IAPRSIS*. pp.295 - 301.

Schuster, H. and Weidner, U., 2003. A New Approach Towards Quantitative Quality Evaluation of 3D Building Models. In: *ISPRS com IV, Workshop Challenges in Geospatial Analysis, Integration and Visualization II*, Stuttgart, Germany. pp. 156-163.

Tarsha-Kurdi, F., Landes, T. and Grussenmeyer, P., 2008. Extended RANSAC algorithm for automatic detection of building roof planes from Lidar data. *The Photogrammetric Journal of Finland*. Vol. 21 No.1, pp.97-109.

Verma, V., Kumar, R. and Hsu, S., 2008. 3D building detection and modeling from aerial Lidar data. In: *IEEE Computer Society Conference on Computer Vision and Pattern Recognition*. 8 pages.

Zhang, W., Grussenmeyer, P., Yan, G. and Mohamed, M., 2011. Primitive-based building reconstruction by integration of LiDAR data and optical imagery. *International Archives of Photogrammetry, Remote Sensing and Spatial Information Sciences*, Calgary, Canada. Vol. 38(5/W12), 6 pages (on CD-ROM).

Appendix E

Definition of Points, lines, and planes in space

E.1 Points in space

Point P is described in the 3D space by 3 real numbers, indicating the positions of the perpendicular projections from the point to three fixed, perpendicular, graduated lines, called the axes. If the coordinates are denoted X, Y , and Z in that order, the axes are called the x-axis, etc., and $P = (X, Y, Z)$. Often the X-axis is imagined to be horizontal and pointing roughly toward the viewer (out of the page), the Y-axis also horizontal and pointing more or less to the right, and the Z-axis vertical, pointing up. The system is called right-handed if it can be rotated so the three axes are in this position. The point $X = 0, Y = 0, Z = 0$ is the origin, where the three axes intersect. Point P as shown in figure E.1, it has the coordinates (X, Y, Z) .

E.2 Lines in space

Line is a series of points that extended in two opposite directions without end. A line segment is a part of a line that is bounded by two distinct end points and contains every point on the line between its end points. In coordinate geometry, lines in a Cartesian plane can be described algebraically by linear equations and linear functions. In three dimensions, a line is described by a parametric representation (see equation E.1):

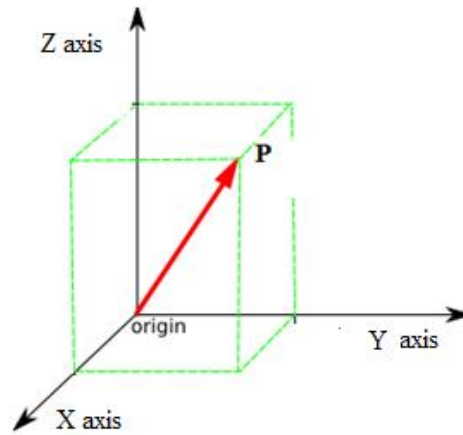


FIGURE E.1: Point P in space.

$$X = x_0 + at \quad Y = y_0 + bt \quad Z = z_0 + ct. \quad (\text{E.1})$$

Where $X, Y,$ and Z are all functions of the independent variable t . $x_0, y_0,$ and z_0 are the initial values of each respective variable or (x_0, y_0, z_0) is any point on the line. $a, b,$ and c are related to the slope of the line, such that the vector (a, b, c) is parallel to the line.

Take a line BP in the 3D space as shown in figure E.2. This line connects B and P and defines the direction B to P.

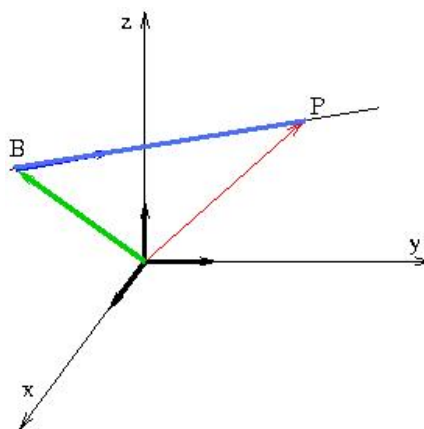


FIGURE E.2: Line in space from point B to point P.

E.3 Planes in space

A plane has a length, a width, but no height (two-dimensional), and extends infinitely on all sides. Planes are thought of as flat surfaces without thickness (figure E.3). A plane is made up of an infinite amount of lines. Coordinate of planes are two-dimensional graphs that use ordered pairs to define the position of points. In three dimensions, a plane is described by a parametric equation E.2

$$Ax + By + Cz + D = 0 \quad (\text{E.2})$$

Where A, B, C, D are plane parameters. D represents the minimum distance from the plane to the origin.

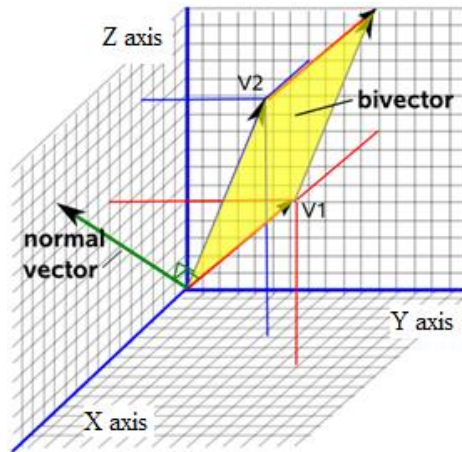


FIGURE E.3: Plane in 3D.

E.4 Plane fitting

This section recall some concepts about fitting a plane through some data in three dimensions (X, Y, Z) Figure E.4 shows the process of plane fitting. Principal Components Analysis (PCA) can be used to fit a linear regression that minimizes the perpendicular distances from the data to the fitted model.

There are three steps to consider in the process of plane fitting; a) input 3D points that are needed to be fitted; b) calculate plane parameters containing this data (basis and normal vector for the plane); c) project this 3D data to the plane.

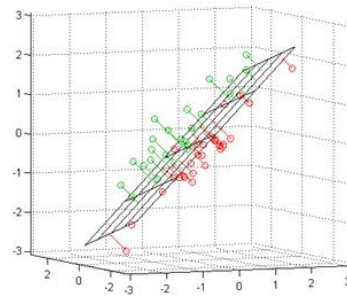


FIGURE E.4: Projection of points on the fitted plane.

The first two coordinates of the principal component scores give the projection of each point onto the plane, in the coordinate system of the plane. To get the coordinates of the fitted points in terms of the original coordinate system, each PC coefficient vector must be multiplied by the corresponding score. The residuals are the distances between the points and the fitted plane.

Appendix F

Arrêté du 30 octobre 2003

Cet arrêté a été publié au journal officiel du 30 octobre 2003
(<http://www.legifrance.gouv.fr/>).

Arrêté du 27 octobre 2003 autorisant au titre de l'année 2003 l'ouverture d'un concours réservé pour l'accès d'agents non titulaires appartenant ou ayant appartenu au ministère de l'économie, des finances et de l'industrie dans le corps des traducteurs

NOR : ECOP0300854A

Par arrêté du ministre de l'économie, des finances et de l'industrie, du ministre de la fonction publique, de la réforme de l'Etat et de l'aménagement du territoire et du ministre délégué au budget et à la réforme budgétaire en date du 27 octobre 2003, est autorisée au titre de l'année 2003 l'ouverture d'un concours réservé pour l'accès d'agents non titulaires appartenant ou ayant appartenu au ministère de l'économie, des finances et de l'industrie dans le corps des traducteurs.

Le nombre de postes offerts à ce recrutement est fixé à 1.

La date limite de retrait des dossiers d'inscription est fixée au 17 novembre 2003, avant 18 heures au bureau des concours ou par courrier (le cachet de la poste faisant foi) avant minuit, délai de rigueur.

La date limite de dépôt des dossiers d'inscription est fixée au 21 novembre 2003, délai de rigueur, avant 18 heures au bureau des concours ou par courrier avant minuit (le cachet de la poste faisant foi), et à l'exclusion de tout autre mode de transmission (l'envoi interne par télécopie notamment ne pourra être accepté). Tout dossier posté ou déposé hors délai ne pourra être pris en considération.

Les candidats doivent fournir, en vue de l'épreuve orale, un *curriculum vitae* de deux pages maximum. Ce *curriculum vitae* devra être retourné avec le dossier d'inscription au plus tard le 21 novembre 2003.

Nota. - Tous renseignements peuvent être obtenus auprès du ministère de l'économie, des finances et de l'industrie (direction du personnel, de la modernisation et de l'administration, sous-direction des ressources humaines, bureau 4 C, concours, télécopie 768), 120, rue de Bercy, 75572 Paris Cedex 12 (téléphone : 01-53-18-75-02).

Internet : <http://www.minefi.fr>, rubrique « infos pratiques », menu déroulant « accès thématique : métiers concours ».

Intranet Alizé : rubrique « la vie de l'agent », sous-rubrique « métiers-concours ».

**MINISTÈRE DE L'ÉQUIPEMENT, DES TRANSPORTS,
DU LOGEMENT, DU TOURISME ET DE LA MER**

Arrêté du 16 septembre 2003 portant sur les classes de précision applicables aux catégories de travaux topographiques réalisés par l'Etat, les collectivités locales et leurs établissements publics ou exécutés pour leur compte

NOR : EQUIP0300864A

Le ministre de l'équipement, des transports, du logement, du tourisme et de la mer,

Vu le décret n° 92-706 du 21 juillet 1992 modifiant le décret n° 85-790 du 26 juillet 1985 relatif au rôle et à la composition du Conseil national de l'information géographique ;

Vu la loi n° 95-115 du 4 février 1995 d'orientation pour l'aménagement et le développement du territoire, modifiée par la loi n° 99-533 du 25 juin 1999 d'orientation pour l'aménagement et le développement durable du territoire, notamment son article 89 ;

Vu le décret n° 2000-1276 du 26 décembre 2000 portant application de l'article 89 de la loi n° 95-115 du 4 février 1995 modifiée d'orientation pour l'aménagement et le développement du territoire relatif aux conditions d'exécution et de publication des levés de plans entrepris par les services publics ;

Vu l'arrêté du 20 mai 1948 fixant les conditions d'exécution et de publication des levés de plans entrepris par les services publics ;

Vu l'arrêté du 21 janvier 1980 fixant les tolérances applicables aux levés à grande échelle entrepris par les services publics ;

Vu l'avis du Conseil national de l'information géographique dans sa séance du 13 novembre 2002.

Arrête :

Art. 1^{er}. - Tous les travaux topographiques réalisés par l'Etat, les collectivités locales et leurs établissements publics ou exécutés pour leur compte doivent être spécifiés et évalués selon les modalités définies dans le présent arrêté, à l'exception des levés hydrographiques.

I. - Spécifications et classes de précision

Art. 2. - Les écarts déterminés lors des contrôles des levés topographiques permettent de vérifier le respect de la classe de précision de ceux-ci. Lors de levés d'objets géographiques, les mesures d'écarts s'appliquent sur des points caractéristiques des objets levés, bien identifiés et ne présentant aucun caractère d'ambiguïté. Ces points sont comparés aux points correspondants du terrain nominal. La précision d'un levé d'objets géographiques peut être spécifiée soit par un gabarit d'erreurs spécifique, soit par un modèle standard.

Art. 3. - La position des points est définie par 1, 2 ou 3 coordonnées, et parmi celles-ci on ne comptabilise ensemble que celles qui suivent un même modèle statistique, selon la nature des levés (un levé altimétrique concerne une coordonnée, un levé planimétrique, deux, un levé tridimensionnel isotrope, trois, mais un levé tridimensionnel dont le modèle statistique planimétrique est différent du modèle statistique altimétrique fera l'objet de traitements séparés

pour les deux coordonnées planimétriques et pour la coordonnée altimétrique). L'écart en position E_{pos} pour un point donné, par rapport à sa position issue d'un contrôle, est défini par la distance euclidienne, c'est-à-dire la racine carrée de la somme des carrés des écarts sur chacune des coordonnées soumise à la même classe de précision.

Une mesure n'est considérée comme mesure de contrôle que lorsque sont mis en œuvre des procédés fournissant une précision meilleure que celle de la classe de précision recherchée, avec un coefficient de sécurité C au moins égal à 2. C est le rapport entre la classe de précision des points à contrôler et celle des déterminations de contrôle, classe de précision qui est elle-même évaluée selon les règles de l'art. La taille et la composition de l'échantillon d'objets géographiques de contrôle sont précisées par contrat.

Art. 4. - Un gabarit d'erreurs est déterminé par une courbe, un histogramme ou une table de valeurs, précisant pour chaque catégorie d'objets géographiques, et pour chaque classe de valeurs d'écarts, le nombre toléré d'écarts dépassant le seuil correspondant.

Pour chaque catégorie d'objets géographiques, on spécifiera le pourcentage d'écarts pouvant dépasser un premier seuil donné, puis le pourcentage de ceux pouvant dépasser un second seuil donné, etc., et ceci pour autant de seuils que souhaité. On pourra en particulier, si besoin est, spécifier un seuil qu'aucun écart ne devra dépasser. La taille et la composition du gabarit d'erreurs sont précisées par contrat.

Art. 5. - Pour tout échantillon comportant N objets géographiques, on calcule l'écart moyen en position $E_{moy, pos}$. Celui-ci est défini par la moyenne arithmétique des écarts en position E_{pos} relevés sur les points des objets géographiques. On dit que la population dont est issu l'échantillon comportant N objets est de classe de précision $[xx]$ cm lorsque simultanément les trois conditions a , b , et c , sont remplies :

a) L'écart moyen en position $E_{moy, pos}$ de l'échantillon est inférieur à

$$[xx] \times \left(1 + \frac{1}{2 \times C^2} \right) \text{ cm}$$

(C étant le coefficient de sécurité des mesures de contrôle),

b) Le nombre N' d'écarts dépassant le premier seuil

$$T = k \times [xx] \times \left(1 + \frac{1}{2 \times C^2} \right)$$

n'excède pas l'entier immédiatement supérieur à

$$0,01 \times N + 0,232 \times \sqrt{N}$$

(où k prend les valeurs indiquées dans la table 1 en fonction du nombre n de coordonnées caractérisant la position des objets géographiques et suivant la même loi statistique).

Table 1 : valeurs du coefficient k en fonction du nombre n de coordonnées caractérisant la position des objets géographiques considérés et suivant la même loi statistique.

<i>n</i>	1	2	3
<i>k</i>	3,23	2,42	2,11

Lorsque $N < 5$, aucun écart supérieur à T n'est admis (cf. table 2).

Table 2 : exemples de nombre N' maximaux d'écarts dépassant le premier seuil T acceptés pour un échantillon de N éléments.

<i>N</i>	De 1 à 4	De 5 à 13	De 14 à 44	De 45 à 85	De 86 à 132	De 133 à 184	De 185 à 240	De 241 à 298	De 299 à 359	De 360 à 422	De 423 à 487
N'	0	1	2	3	4	5	6	7	8	9	10

c) Aucun écart en position dans l'échantillon n'excède le second seuil

$$T = 1,5 \times k \times [xx] \times \left(1 + \frac{1}{2 \times C^2} \right)$$

II. - Catégories de travaux topographiques

Art. 6. - Les points de canevas sont déterminés par 1, 2 ou 3 coordonnées.

Les écarts observés sur les canevas sont issus de trois origines : les erreurs internes, les erreurs de rattachement et les erreurs propres du réseau légal de référence. Ces erreurs peuvent parfois être individualisées, en particulier lorsque les mesures présentent une surabondance suffisante. On désigne par surabondance d'un canevas le taux formé par le rapport du nombre de mesures indépendantes observées sur un canevas au nombre minimal de mesures permettant de déterminer celui-ci. Les classes de précision totale et de précision interne d'un canevas sont définies à partir des trois types d'erreurs suivantes :

a) L'erreur interne s'analyse à partir de l'écart entre les coordonnées obtenues pour chaque point par les mesures de contrôle et celles que l'on obtient par calcul dans un système indépendant en appliquant une translation (et pour 2 ou 3 coordonnées, une rotation), la plus favorable possible, sur l'ensemble des coordonnées fournies pour ces points. Les éventuels points d'appui inclus dans le canevas figurent avec leurs coordonnées déterminées dans le système indépendant.

b) L'erreur propre au réseau légal de référence est spécifiée par son gestionnaire, avec éventuellement plusieurs niveaux possibles en fonction des éléments du réseau effectivement utilisés lors du rattachement. Si la discordance relevée entre les points du réseau légal de référence est plus importante que la précision spécifiée par le gestionnaire, alors la précision est remplacée dans toutes les évaluations ultérieures par la discordance de rattachement effectivement constatée.

c) L'erreur de rattachement s'analyse, lorsque cela est possible, à partir des écarts sur les mesures permettant le lien entre le réseau légal de référence et le canevas lui-même. Un rattachement ne peut être considéré comme effectué que si le canevas considéré est rattaché à suffisamment de points du réseau légal de référence pour mettre en évidence d'éventuelles discordances dans ce réseau. En outre, la précision fournie pour le rattachement doit être cohérente avec celle des éléments du réseau légal de référence effectivement utilisés pour celui-ci. Cette erreur de rattachement ne peut pas toujours être individualisée, ce qui est en particulier le cas lorsque les mesures du canevas offrent peu de surabondance.

6.1. Classe de précision totale

La classe de précision définie précédemment s'applique aux écarts entre les coordonnées fournies pour chaque point et celles que l'on obtient pour des mesures de contrôle. L'erreur totale résulte de la composition des erreurs internes, des erreurs de rattachement, et de l'erreur propre au réseau légal de référence. Donc l'erreur totale ne peut être inférieure à l'une de ces trois sources d'erreurs, et en particulier à l'erreur propre du réseau légal de référence, telle qu'elle est spécifiée ou telle qu'elle résulte des discordances relevées lors du rattachement.

6.2. Classe de précision interne

La classe de précision définie précédemment s'applique à l'écart entre les coordonnées obtenues pour chaque point par les mesures de contrôle et celles que l'on obtient par calcul dans un système indépendant en appliquant une translation (et pour 2 ou 3 coordonnées, une rotation), les plus favorables possible, sur l'ensemble des coordonnées fournies pour ces points. Les éventuels points d'appui inclus dans le canevas figurent avec leurs coordonnées déterminées dans le système indépendant.

6.3. Critères possibles

Les classes de précision des canevas doivent être spécifiées selon tout ou partie de 4 critères possibles : classe de précision planimétrique totale, classe de précision planimétrique interne, classe de précision altimétrique totale et classe de précision altimétrique interne, en suivant les définitions des points 6.1 et 6.2 ci-dessus.

Art. 7. - Les classes de précision de levés d'objets géographiques sont relatives aux canevas qui leur servent de référence, et s'analysent selon 2 critères indépendants : classe de précision planimétrique par rapport au canevas, classe de précision altimétrique par rapport au canevas, selon les critères de l'article 2. Des classes de précision différentes peuvent être spécifiées pour des types d'objets géographiques différents dans un même levé.

7.1. Objets géographiques ponctuels

Si les spécifications l'indiquent, certains objets géographiques peuvent être considérés comme ponctuels. Ils sont alors déterminés par les coordonnées planimétriques et au besoin altimétriques de leur point de référence. La classe de précision s'applique à l'écart entre les coordonnées obtenues pour chaque point par une mesure de contrôle et les coordonnées fournies pour ces points ; les éventuels points d'appui et de canevas inclus dans le levé étant exclus des points testés.

7.2. Les objets géographiques linéaires, surfaciques et volumiques

Si les spécifications l'indiquent, ces objets sont définis uniquement à partir de lignes et de points, et certains de ces points peuvent ne pas être identifiables. Une surface est définie par un périmètre, un volume est défini par ses arêtes.

Les classes de précision sur les points identifiables sont spécifiées comme celles des objets géographiques ponctuels.

On dénomme points non identifiables ceux qui servent à la détermination d'un objet géographique linéaire, et dont la position le long de cet objet n'est pas précisément identifiée.

Sauf spécification contraire figurant au cahier de charges, les classes de précision sur les lignes joignant des points non identifiables s'appliquent à l'écart entre le terrain nominal et les segments de droites joignant ces points. Cet écart est mesuré par la plus petite distance entre le point de contrôle et la ligne levée, chaque point de contrôle étant choisi le plus près possible de l'un des points levés.

7.3. Spécifications de contenu

Les objets géographiques faisant l'objet du levé sont rangés par classes en fonction des spécifications de contenu qui précisent aussi les critères de sélection retenus, conformément au terrain nominal. Les spécifications s'appliquent indépendamment aux objets mal classés et aux objets oubliés ou surnuméraires, en spécifiant les gabarits d'erreurs correspondants décrits à l'article 4.

7.4. Représentation altimétrique du terrain

La représentation altimétrique du terrain utilise des points du terrain nominal définis par des coordonnées altimétriques et planimétriques. Ces points sont reliés par des arêtes destinées à structurer un modèle de surface (maillage régulier, triangulation, courbe de niveau, etc.). Les classes de précision s'appliquent à l'écart entre le terrain nominal et la surface levée. Les points de contrôle sont pris à la verticale des points du modèle de surface.

Le terrain nominal introduit un certain niveau de simplifications et de lissage de la réalité en fonction du pas d'échantillonnage ou de l'espacement des courbes de niveau. Les écarts entre le terrain nominal et le terrain réel doivent rester inférieurs à la classe de précision spécifiée.

Les réseaux des lignes de thalweg, de crêtes et de rupture de pente sont considérés comme des objets géographiques linéaires et

font l'objet de spécifications propres. Leurs classes de précision planimétrique et altimétrique suivent les spécifications des objets géographiques linéaires, surfaciques et volumiques.

Art. 8. – Les spécifications de précision applicables aux images rectifiées et aux documents cartographiques scannés et remis en géométrie s'analysent selon 5 paramètres ci-après ; un au moins parmi les deux premiers étant obligatoire et les trois derniers étant facultatifs :

8.1. Classe de précision interne

La classe de précision définie précédemment s'applique à l'écart entre les coordonnées obtenues par les mesures de contrôle, pour des détails bien identifiés, calculées dans un système indépendant, et celles que l'on obtient par calcul en appliquant une rotation et une translation, les plus favorables possible, sur l'ensemble des coordonnées de ces points obtenues dans l'image ou le document, également dans un système indépendant. Le système de coordonnées planes de contrôle sera caractérisé par le même système de représentation plane que celui des coordonnées des points évalués. La classe de précision ne peut être meilleure que la taille du pixel utilisé.

8.2. Classe de précision totale

La classe de précision définie précédemment s'applique à l'écart entre les coordonnées obtenues par les mesures de contrôle, pour des détails bien identifiés, et celles des coordonnées de ces points obtenues dans l'image ou le document. Le système de coordonnées planes de contrôle sera caractérisé par le même système de représentation plane que celui des coordonnées des points évalués. La classe de précision ne peut être meilleure que la taille du pixel utilisé.

8.3. Redressement des objets géographiques du sur-sol

La spécification doit préciser si les erreurs internes décrites à l'article 6.1 s'appliquent uniquement aux objets géographiques au sol ou également aux objets du sur-sol.

8.4. Qualité radiométrique du mosaïquage

S'il y a effectivement eu un mosaïquage, la classe de précision sera exprimée par la différence de valeur radiométrique par canal tolérée sur les raccords entre images ne correspondant pas à un linéament, divisée par la radiométrie maximale de l'image et exprimée sous forme de pourcentage.

8.5. Qualité géométrique du mosaïquage

La classe de précision s'applique, conformément aux éléments définis précédemment et s'il y a effectivement eu un mosaïquage, aux distances entre les points en bordure d'une des images assemblées au sein du document final et les mêmes points tels qu'ils seraient représentés dans l'image voisine si elle était prolongée jusque-là, les points étant caractérisés par des coordonnées sous forme de pixels. Ces distances sont mesurées sur des points n'offrant aucune ambiguïté d'identification sur les deux images voisines concourant au document final.

Art. 9. – Le présent arrêté sera publié au *Journal officiel* de la République française.

Fait à Paris, le 16 septembre 2003.

GILLES DE ROBIEN

Arrêté du 9 octobre 2003 relatif aux modalités d'application pour les personnels travaillant en horaires de bureau à la direction générale de l'aviation civile, à l'inspection générale de l'aviation civile et de la météorologie, au bureau d'enquêtes et analyses pour la sécurité de l'aviation civile et à l'École nationale de l'aviation civile du décret n° 2002-634 du 29 avril 2002 portant création du compte épargne-temps dans la fonction publique de l'Etat

NOR : EQUA0301464A

Le ministre de l'économie, des finances et de l'industrie, le ministre de l'équipement, des transports, du logement, du tourisme et de la mer et le ministre de la fonction publique, de la réforme de l'Etat et de l'aménagement du territoire,

Vu la loi n° 83-634 du 13 juillet 1983 modifiée portant droits et obligations des fonctionnaires, ensemble la loi n° 84-16 du 11 janvier 1984 modifiée portant dispositions statutaires relatives à la fonction publique de l'Etat ;

Vu le décret n° 84-972 du 26 octobre 1984 relatif aux congés annuels des fonctionnaires de l'Etat ;

Vu le décret n° 86-83 du 17 janvier 1986 relatif aux dispositions générales applicables aux agents non titulaires de l'Etat, pris pour l'application de l'article 7 de la loi n° 84-16 du 11 janvier 1984 portant dispositions statutaires relatives à la fonction publique de l'Etat ;

Vu le décret n° 2000-815 du 25 août 2000 relatif à l'aménagement et à la réduction du temps de travail dans la fonction publique de l'Etat ;

Vu le décret n° 2002-634 du 29 avril 2002 portant création du compte épargne-temps dans la fonction publique de l'Etat ;

Vu l'arrêté du 12 septembre 2001 pris en application du décret n° 2000-815 du 25 août 2000 relatif à l'aménagement et à la réduction du temps de travail à la direction générale de l'aviation civile, à l'inspection générale de l'aviation civile et de la météorologie, au bureau enquêtes-accidents et à l'École nationale de l'aviation civile, notamment son titre I° ;

Vu l'arrêté du 12 septembre 2001 relatif à l'aménagement et à la réduction du temps de travail des services travaillant en horaires de bureau à la direction générale de l'aviation civile, à l'inspection générale de l'aviation civile et de la météorologie, au bureau enquêtes-accidents et à l'École nationale de l'aviation civile ;

Vu l'avis du comité technique paritaire de la direction générale de l'aviation civile en date du 12 décembre 2002 ;

Vu le comité technique paritaire de l'École nationale de l'aviation civile du 24 juin 2003,

Arrêtent :

Art. 1°. – Le présent arrêté est applicable, sous réserve des dispositions de l'article 2 du décret du 29 avril 2002 susvisé, aux agents titulaires et non titulaires travaillant en horaires de bureau, au sens de l'arrêté du 12 septembre 2001 relatif à l'aménagement et à la réduction du temps de travail des services travaillant en horaires de bureau à la direction générale de l'aviation civile, à l'inspection générale de l'aviation civile et de la météorologie, au bureau enquêtes-accidents et à l'École nationale de l'aviation civile susvisé, à la direction générale de l'aviation civile, à l'inspection générale de l'aviation civile et de la météorologie, au bureau d'enquêtes et d'analyses pour la sécurité de l'aviation civile et à l'École nationale de l'aviation civile.

Art. 2. – Le compte épargne-temps est ouvert sur demande expresse de l'agent transmise au service gestionnaire de ses congés annuels à l'aide d'un formulaire, renseigné et signé par l'intéressé. La demande d'ouverture du compte épargne-temps n'est pas motivée. Elle peut être formulée à tout moment.

Art. 3. – La demande d'alimentation du compte épargne-temps est formulée une fois par année civile, à l'initiative de l'agent, dans la deuxième quinzaine de décembre de l'année en cours.

Le service gestionnaire de l'agent qui a ouvert un compte épargne-temps informe expressément ce dernier, au plus tard le 15 janvier suivant l'année en cours, des droits épargnés et consommés et de la date d'expiration du délai prévu à l'article 6 du décret susvisé.

Art. 4. – L'accord ou le refus de l'utilisation partielle ou totale des droits épargnés fait l'objet d'une décision expresse du chef de service de l'agent.

Art. 5. – L'utilisation partielle ou totale des droits épargnés peut précéder ou être consécutive à l'un des congés mentionnés à l'article 34 de la loi du 11 janvier 1984 susvisée.

Art. 6. – La rémunération servie à l'agent qui bénéficie d'un congé issu d'un compte épargne-temps est celle qui lui est servie à la date où il dépose sa demande de congé.

Art. 7. – L'agent qui souhaite utiliser son compte épargne-temps en fait la demande à son chef de service. Cette demande est formulée :

- dix semaines au moins avant cette date lorsque le congé est d'une durée inférieure à six mois ;
- trois mois au moins avant cette date lorsque la durée du congé excède six mois.

Art. 8. – L'agent est informé de son droit à utiliser les congés accumulés à la date de clôture du compte, préalablement à cette date et sous un délai au moins égal à la somme de ces congés plus un mois.

Art. 9. – Par dérogation aux dispositions de l'article 3 du présent arrêté, sont validées les demandes d'ouverture et d'alimentation d'un compte épargne-temps au titre de l'année 2002 datées au plus tard d'un mois après la publication du présent arrêté. Cette disposition ne peut avoir pour effet de permettre la prise de jours de réduction du temps de travail acquis au titre de l'année 2002 au-delà du 31 décembre de cette année.

Bibliography

- [Abd-Elrahman et al., 2001] Abd-Elrahman, A., Pearlstine, L., Dewitt, B., and Smith, S. (2001). Small-format digital aerial imagery and navigation sensors using area-based matching techniques. *Photogrammetric Engineering and Remote Sensing*. vol. 67(7), pp. 825-831.
- [Akca et al., 2010] Akca, D., Freeman, M., Sargent, I., and Gruen, A. (2010). Quality assessment of 3D building data. *The Photogrammetric Record*. vol. 25(132), pp. 339-355.
- [Al-Bayari et al., 2002] Al-Bayari, O., Al-Hanbali, N., Barbarella, M., and Nashwan, A. (2002). Quality assessment of DTM and orthophoto generated by airborne laser scanning system using automated digital photogrammetry. *International Archives of the Photogrammetry, Remote Sensing and Spatial Information Sciences*. vol. XXXIV(3B), pp. 7-12.
- [Amat et al., 2010] Amat, N., Setan, H., and Majid, Z. (2010). Integration of aerial and close-range photogrammetric methods for 3D city modeling generation. *Geoinformation Science Journal*. vol. 10(1), pp. 49-60.
- [Baltsavias, 1999] Baltsavias, E. (1999). A comparison between photogrammetry and laser scanning. *ISPRS Journal of Photogrammetry and Remote Sensing*. vol. 54, pp. 83-94.
- [Barber et al., 1996] Barber, C., Dobkin, D., and Huhdanpaa, H. (1996). The Quickhull algorithm for convex hulls. *ACM Transactions on Mathematical Software*. vol. 22, pp. 469-483.
- [Borcard et al., 2011] Borcard, D., Gillet, F., and Legendre, P. (2011). *Numerical ecology with R*. Springer Science. 319 pages.
- [Boulaassal et al., 2011] Boulaassal, H., Landes, T., and Grussenmeyer, P. (2011). Reconstruction of 3D vector models of buildings by combination of ALS, TLS and VLS data. *4th 3D-ARCH International Conference on 3D Virtual Reconstruction and Visualization of Complex Architectures*. Trento (Italy), 2-5 March 2011, 6 pages.

- [Büeler et al., 2000] Büeler, B., Enge, A., and Fukuda, K. (2000). Exact volume computation for polytopes : A practical study. *Polytopes - Combinatorics and Computation*. vol. 29, pp. 131-154.
- [Casella et al., 2008] Casella, V., Franzini, M., Kocaman, S., and Gruen, A. (2008). Geometric accuracy assessment of ADS40 imagery under various network configurations. *The International Archives of the Photogrammetry, Remote Sensing and Spatial Information Sciences*. Vol. XXXVII(B1), pp. 627- 632.
- [Chong et al., 2000] Chong, M. M., Gay, K. R., Tan, H. N., and Liu, J. (2000). *Geometric knowledge-based systems framework for structural image analysis and post processing*. Elsevier Inc. Part of Knowledge-based systems techniques and applications, vol. 2, pp. 379-408.
- [Congalton, 2005] Congalton, G. (2005). Thematic and positional accuracy assessment of digital remotely sensed data. In *2005 Proceedings of the Seventh Annual Forest Inventory and Analysis Symposium*. pp. 149-154.
- [Congalton and Kass, 2009] Congalton, G. and Kass, G. (2009). *Assessing the accuracy of remotely sensed data: principles and practices*. Taylor and Francis Group LLC, 2nd edition. 183 pages.
- [Cooper and Cross, 1988] Cooper, M. A. R. and Cross, P. A. (1988). Statistical concepts and their application in photogrammetry and surveying. *The Photogrammetric Record*. vol. 12(71), pp. 637-663.
- [Cramer, 2001] Cramer, M. (2001). On the use of direct georeferencing in airborne photogrammetry. In *International Symposium on Mobile Mapping Technology, January 2001, Cairo*. digital publication on CD, 13 pages.
- [Cramer, 2009] Cramer, M. (2009). Digital airborne camera performance - the DGPF test. In *52nd Photogrammetric Week*. pp. 51-68, Stuttgart September 7-11, 2009.
- [Cramer, 2010] Cramer, M. (2010). The DGPF-test on digital airborne camera evaluation - overview and test design. *Photogrammetrie Fernerkundung Geoinformation (PFG)*. vol. 2, pp. 73-82.
- [Cramer, 2011] Cramer, M. (2011). Geometry perfect radiometry unknown? *53rd Photogrammetric Week*. pp. 65-77, in Stuttgart from 5 to 9 September.

- [Eisenbeiss, 2011] Eisenbeiss, H. (2011). The potential of unmanned aerial vehicles for mapping. *53rd Photogrammetric Week, in Stuttgart from 5 to 9 September*. pp. 135- 145.
- [ERDAS Inc., 2011] ERDAS Inc. (Version 2011). *LPS automatic terrain extraction*. ERDAS IMAGINE. Manual, 163 pages.
- [Fruh and Zakhor, 2003] Fruh, C. and Zakhor, A. (2003). Constructing 3D city models by merging aerial and ground views. *IEEE Computer Graphics and Applications*. vol. 23(6), pp. 52-61.
- [Ghilani and Wolf, 2006] Ghilani, C. and Wolf, P. (2006). *Adjustment computation: spatial data analysis*. John Wiley and Sons, fourth edition. 611 pages.
- [Goodchild and Hunter, 1997] Goodchild, M. and Hunter, G. (1997). A simple positional accuracy measure for linear features. *International Journal of Geographical Information Science*. vol. 11(3), pp. 299- 306.
- [Grenzdörffer, 2008] Grenzdörffer, G. (2008). Medium format digital cameras - A EUROSDR project. *The International Archives of the Photogrammetry, Remote Sensing and Spatial Information Sciences*. vol. XXXVII(B1), pp. 1043-1049.
- [Gruber et al., 2008] Gruber, M., Ponticelli, M., Bernögger, S., and Leberl, F. (2008). UltraCamX, the large format digital aerial camera system by Vexcel Imaging / Microsoft. *The International Archives of the Photogrammetry, Remote Sensing and Spatial Information Sciences*. vol. XXXVII(B1), pp. 665-670.
- [Gruber et al., 2011] Gruber, M., Ponticelli, M., and Wiechert, A. (2011). Ultra-Cam, a brand for continuous developments. *53rd Photogrammetric Week*. pp. 103- 109, in Stuttgart from 5 to 9 September.
- [Grussenmeyer et al., 1994] Grussenmeyer, P., Hottier, P., and Abbas, I. (1994). Le contrôle topographique d'une carte ou d'une base de données constituées par voie photogrammétrique. *Journal de l'Association Française de Topographie (XYZ)*. N° 59, pp. 39-45.
- [Haala and Brenner, 1999] Haala, N. and Brenner, C. (1999). Extraction of building and trees in urban environments. *ISPRS Journal of Photogrammetry and Remote Sensing*. vol. 54, pp. 130-137.
- [Haala and Hahn, 1995] Haala, N. and Hahn, M. (1995). *Data fusion for the detection and reconstruction of buildings*. In *Automatic Extraction of Man-Made Objects from Aerial and Space Images*. Birkhäuser Basel. pp. 211-220.

- [Haala and Kada, 2010] Haala, N. and Kada, M. (2010). An update on automatic 3D building reconstruction. *ISPRS Journal of Photogrammetry and Remote Sensing*. vol. 65, pp. 570-580.
- [Hammoudi and Dornaika, 2011] Hammoudi, K. and Dornaika, F. (2011). A featureless approach to 3D polyhedral building modeling from aerial images. *sensors Journal*. vol. 11, pp. 246-277.
- [Heipke, 1996] Heipke, C. (1996). Automation of interior, relative, and absolute orientation. *International Archives of Photogrammetry and Remote Sensing*. vol. 31(B3), pp. 297-311.
- [Henn et al., 2013] Henn, A., Gröger, G., Stroh, V., and Plümer, L. (2013). Model driven reconstruction of roofs from sparse LIDAR point clouds. *ISPRS Journal of Photogrammetry and Remote Sensing*. vol. 76, pp. 17-29.
- [Henricsson, 1997] Henricsson, O. (1997). The role of color attributes and similarity grouping in 3D building reconstruction. *Computer Vision and Image Understanding*. vol. 72(2), pp. 163-184.
- [Heuvelink, 1998] Heuvelink, G. (1998). *Error propagation in environmental modelling with GIS*. Taylor & Francis, first edition. 150 pages.
- [Heuvelink, 2007] Heuvelink, G. (2007). Error-aware GIS at work: Real-world applications of the data uncertainty engine. *The International Archives of the Photogrammetry, Remote Sensing and Spatial Information Sciences*. vol. 34, 6 pages.
- [Hinks et al., 2013] Hinks, T., Carr, H., Truong-Hong, L., Laefer, D., and ASCE, M. (2013). Point cloud data conversion into solid models via point-based voxelization. *Journal of Surveying Engineering*. vol. 139, pp. 72-83.
- [Hirschmüller, 2011] Hirschmüller, H. (2011). Semi-global matching motivation, developments and applications. In *53. Photogrammetric Week*. 5.-9. September 2011, Stuttgart, Germany, 10 pages.
- [Huaan, 2010] Huaan, F. (2010). *Theory of errors and least squares adjustment*. Stockholm, 10 th edition. Royal Institute of Technology (KTH) Division of Geodesy and Geoinformatics. 266 pages.
- [Jacobsen et al., 2010] Jacobsen, K., Cramer, M., Landstadter, R., Ressel, C., and Spreckels, V. (2010). DGPF-Project: Evaluation of digital photogrammetric

- camera systems - geometric performance. *Overview on the last findings from the DGPF project evaluation teams - special issue PFG*. 14 pages.
- [Jamet et al., 1995] Jamet, O., Dissard, O., and Airault, S. (1995). Building extraction from stereopairs of aerial images : accuracy and productivity constraint of a topographic production line. In *Automatic extraction of man-made objects from aerial and space images, Basel, Switzerland*. 8 pages.
- [Karabork et al., 2004] Karabork, H., Yildiz, F., and Coskun, E. (2004). Object recognition for interior orientation in digital photogrammetry. *International Archives of Photogrammetry and Remote Sensing and Spatial Information Science*. vol. 35(3), pp. 811-814.
- [Kasser, 2003] Kasser, M. (2003). The new legal text about the precision of the surveys for public administration in France. *FIG Working Week 2003*. Paris, France, April 13-17, 2003, 14 pages.
- [Kheiri, 2006] Kheiri, M. (2006). Digital aerial cameras. *International Archives of the Photogrammetry, Remote Sensing and Spatial Information Science*. vol. XXXVI(6), pp. 229-234.
- [Kocaman et al., 2007] Kocaman, S., Gruen, A., Casella, V., and Franzini, M. (2007). Accuracy assessment of ADS40 imagery over the Pavia testsite. In *Proceedings of Asian Conference on Remote Sensing*, Kuala Lumpur, Malaysia. pp. 989-994.
- [Konecny, 2003] Konecny, G. (2003). *Geoinformation: remote sensing, photogrammetry and geographic information systems*. Taylor & Francis. 266 pages.
- [Konecny, 2008] Konecny, G. (2008). Economic considerations for photogrammetric mapping. *International Archives of the Photogrammetry, Remote Sensing and Spatial Information Sciences*. vol. XXXVII(6a), pp. 207 - 211.
- [Kraus, 1993] Kraus, K. (1993). *Photogrammetry: fundamental and standard processes*. Dummlers, 4th edition. vol. 1, 397 pages.
- [Lafarge et al., 2006] Lafarge, F., Descombes, X., and Zerubia, J. (2006). An automatic 3D city model: A Bayesian approach using satellite images. *Proceedings of IEEE International Conference on Acoustics, Speech and Signal Processing, Toulouse, France*. vol. 2, 4 pages.

- [Landes et al., 2012a] Landes, T., Boulaassal, H., and Grussenmeyer, P. (2012a). Quality assessment of geometric facade models reconstructed from TLS Data. *The Photogrammetric Record*. vol. 27(138), pp. 137- 154.
- [Landes et al., 2012b] Landes, T., Grussenmeyer, P., Boulaassal, H., and Mohamed, M. (2012b). Assessment of three-dimensional models derived from LiDAR and TLS data. In *International Archives of the Photogrammetry, Remote Sensing and Spatial Information Sciences*. vol. XXXIX(B2), pp. 95-100, Melbourne, Australia.
- [Leberl et al., 2012] Leberl, F., Gruber, M., Ponticelli, M., and Wiechert, A. (2012). The UltraCam story. *International Archives of the Photogrammetry, Remote Sensing and Spatial Information Sciences*. vol. XXXIX(B1), pp. 39-44, XXII ISPRS Congress, 25 August to 01 September 2012, Melbourne, Australia.
- [Leberl et al., 2002] Leberl, F., Perko, R., Gruber, M., and Ponticelli, M. (2002). Novel concepts for aerial digital cameras. In *Integrated Remote Sensing at the Global, Regional and Local Scale*, Colorado USA. ISPRS. vol. 34(1), 6 pages.
- [Lemmens, 2004] Lemmens, M. (2004). Product survey on airborne laserscanners. *GIM International*. vol. 5, pp. 45-47.
- [Lemmens, 2008] Lemmens, M. (2008). Digital aerial cameras. *GIM International*. Product survey, 3 pages.
- [Lesparre and Gorte, 2012] Lesparre, J. and Gorte, B. (2012). Simplified 3D city models from LiDAR. *International Archives of the Photogrammetry, Remote Sensing and Spatial Information Sciences*. vol. XXXIX(B2), pp. 1-4, XXII ISPRS Congress, 25 August to 1st September 2012, Melbourne, Australia.
- [LI and WU, 2008] LI, Y. and WU, H. (2008). Adaptive building edge detection by combining LiDAR data and aerial images. *The International Archives of the Photogrammetry, Remote Sensing and Spatial Information Sciences*. vol. 37(B1), pp. 197-202.
- [Li et al., 2013] Li, Y., Wu, H., An, R., Xu, H., He, Q., and Xu, J. (2013). An improved building boundary extraction algorithm based on fusion of optical-imagery and LiDAR data. *Optik International Journal for Light and Electron Optics*. vol. XXX, 6 Pages, 2013 Elsevier GmbH journal homepage: www.elsevier.de/ijleo.

- [Li et al., 2008] Li, Z., Chen, J., and Baltsavias, E. (2008). *Advances in Photogrammetry, Remote Sensing and Spatial Information Sciences*. ISPRS Congress Books. 527 pages.
- [Loopez and Spain, 2007] Loopez, F. and Spain (2007). Analysis of some positional accuracy assessment methodologies. *Journal of Surveying Engineering*. vol. 134(2), pp. 45-54.
- [Maas and Vosselman, 1999] Maas, H. and Vosselman, G. (1999). Two algorithms for extracting building models from raw laser altimetry data. *ISPRS Journal of Photogrammetry and Remote Sensing*. vol. 54, pp. 153-163.
- [McGlone, 2004] McGlone, C. (2004). *Manual of photogrammetry, American Society of Photogrammetry and Remote Sensing*. amazon. 1151 pages, fifth edition.
- [McGlone and Shufelt, 1994] McGlone, J. and Shufelt, J. (1994). Projective and object space geometry for monocular building extraction. In *Proceedings Computer Vision and Pattern Recognition CVPR94*. IEEE Computer Society. pp. 54-61.
- [Mcintosh and Krupnik, 2002] McIntosh, K. and Krupnik, A. (2002). Integration of laser-derived DSMs and matched image edges for generating an accurate surface model. *ISPRS Journal of photogrammetry and remote sensing*. vol. 56, pp. 167-176.
- [McKeown et al., 2000] McKeown, D., Bulwinkle, T., Cochran, S., Harvey, W., McGlone, C., and Shufelt, J. (2000). Performance evaluation for automatic feature extraction. *IAPRS International Archives of Photogrammetry and Remote Sensing*. vol. 33(B2), pp. 379 - 394.
- [Meidow and Schuster, 2005] Meidow, J. and Schuster, H. (2005). Voxel-based quality evaluation of photogrammetric building acquisitions. *ISPRS Workshop on Object Extraction for 3D City Models, Road Databases and Traffic Monitoring (CMRT05)*. vol. XXXXVI(3), pp. 117-124.
- [Mohamed and Grussenmeyer, 2011] Mohamed, M. and Grussenmeyer, P. (2011). Plane-based accuracy assessment in photogrammetry: comparison of Rolleiflex Medium format and Ultracam-X digital cameras. In *GTC2011 Symposium, Geomatics in the City*, Jeddah, Saudia Arabia. 6 pages.
- [Mohamed et al., 2013] Mohamed, M., Grussenmeyer, P., Landes, T., and Zhang, W. (2013). Multi-dimensional quality assessment of photogrammetric and LiDAR datasets based on a vector approach. *International Archives of the*

- Photogrammetry, Remote Sensing and Spatial Information Sciences.* vol. XL(2/W1), pp. 93-98, 8th International Symposium on Spatial Data Quality, 30 May - 1 June 2013, Hong Kong.
- [Neumann, 2011] Neumann, K. (2011). The Z/I DMC II "Imaging Revolution". *53rd Photogrammetric Week.* pp. 97-101, in Stuttgart from 5 to 9 September.
- [Nonin, 2003] Nonin, P. (2003). Automatic extraction of digital surface models from airborne digital cameras. In *Optical 3-D Measurement Techniques.* vol. I(I), pp.106-113, Zurich, Switzerland, September 22-25.
- [O'Rourke, J, 1998] O'Rourke, J (1998). *Computational geometry in C.* Cambridge University Press, second edition. 392 pages.
- [Ortner et al., 2007] Ortner, M., Descombes, X., and Zerubia, J. (2007). Building outline extraction from digital elevation models using marked point processes. *International Journal of Computer Vision.* vol. 72(2), pp. 107-132.
- [Petrie and Walker, 2007] Petrie, G. and Walker, A. (2007). Airborne digital imaging technology: A new overview. *Photogrammetric Record.* vol.22(119), pp. 203-225.
- [Podobnikar, 2009] Podobnikar, T. (2009). Methods for visual quality assessment of a digital terrain model. *Survey And Perspectives Integrating Environment and Society.* vol. 1(2), pp. 1-10, <http://sapiens.revues.org/index738.html>.
- [Polidori, 1997] Polidori, L. (1997). *Cartographie radar.* Gordon and Breach Science. ISBN : 90-5699-051-9, 302 pages.
- [Polidori, 2011] Polidori, L. (2011). New trends in remote sensing and geoprocessing: technological developments and benefits for society. In *GTC2011 Symposium, Geomatics in the City.* Jeddah, Saudia Arabia, 6 pages.
- [Prandi et al., 2008] Prandi, F., Achille, C., Brumana, R., Fassi, S., and Fregonese, L. (2008). LiDAR and pictometry images integrated use for 3D model generation. *The International Archives of the Photogrammetry, Remote Sensing and Spatial Information Sciences.* vol. XXXVII(B2), pp. 763-769.
- [Ragia, 2000] Ragia, L. (2000). A quality model for spatial objects. In *ISPRS Congress, Amsterdam.* Vol. XXXIII(4), pp. 855-862.
- [Reulke et al., 2000] Reulke, R., Franke, K., Pomierski, T., Schnermark, M., Tornow, C., and Wiest, L. (2000). Target related multispectral and true colour

- optimization of the colour channels of the LH Systems ADS40. *International Archives of Photogrammetry and Remote Sensing*. vol. 33(B1), pp. 244-250.
- [Rizaldy and Firdaus, 2012] Rizaldy, A. and Firdaus, W. (2012). Direct georeferencing: a new standard in photogrammetry for high accuracy mapping. *ISPRS - International Archives of the Photogrammetry, Remote Sensing and Spatial Information Sciences*. vol. XXXIX(B1), pp. 5-9, XXII ISPRS Congress, 25 August to 01 September 2012, Melbourne, Australia.
- [Roeser et al., 2000] Roeser, H., Eckardt, A., von Schnermark, M., Sandau, R., and Fricker, P. (2000). New potential and applications of ADS. *International Archives of Photogrammetry and Remote Sensing*. vol. XXXIII(B1), pp. 251-257.
- [Rothermel and Haala, 2011] Rothermel, M. and Haala, N. (2011). Potential of dense matching for the generation of high quality Digital Elevation Models. *International Archives of the Photogrammetry, Remote Sensing and Spatial Information Sciences*. vol.XXXVIII(4/W19), pp. 271-276, ISPRS Hannover 2011 Workshop, 14-17 June 2011, Hannover, Germany.
- [Ruther et al., 2002] Ruther, H., Hagai, M., and Mitalo, E. (2002). Application of snakes and dynamic programming optimisation technique in modeling of buildings in informal settlement areas. *ISPRS Journal of Photogrammetry and Remote Sensing Remote Sensing*. vol. 56, pp. 269-282.
- [Rutzinger et al., 2009] Rutzinger, M., Rottensteiner, F., and Pfeifer, N. (2009). A comparison of evaluation techniques for building extraction from airborne laser scanning. *IEEE Journal of selected topics in applied earth observations and remote sensing*. vol. 2(1), pp. 11-20.
- [Sandau, 2009] Sandau, R. (2009). *Airborne Camera : Introduction and Technology*. Wichmann Verlag, first edition. ISBN: 978-1-4020-8877-3, 215 pages.
- [Schenk, 2005] Schenk, T. (2005). *Introduction to photogrammetry*. Department of Civil and Environmental Engineering and Geodetic Engineering, The Ohio State University. 95 pages.
- [Schuster and Weidner, 2003] Schuster, H. and Weidner, U. (2003). A new approach towards quantitative quality evaluation of 3D building models. In *ISPRS Com IV, Workshop Challenges in Geospatial Analysis, Integration and Visualization II*, Stuttgart, Germany. pp. 156-163.

- [Shi and Liu, 2000] Shi, W. and Liu, W. (2000). A stochastic process-based model for the positional error of line segments in GIS. *International Journal of Geographical Information Science*. vol. 14(1), pp. 51-66, <http://dx.doi.org/10.1080/136588100240958>.
- [Siriba, 2009] Siriba, D. (2009). Positional accuracy assessment of a cadastral dataset based on the knowledge of the process steps used. In *12th AGILE International Conference on Geographic Information Science*, Hannover, Germany. Leibniz University. 9 pages.
- [Taie et al., 2011] Taie, S., ElDeeb, H., and Atiya, D. (2011). A new model for automatic raster to vector conversion. *International Journal of Engineering and Technology*. vol. 3(3), pp. 182-190.
- [Tarsha-Kurdi et al., 2007] Tarsha-Kurdi, F., Landes, T., and Grussenmeyer, P. (2007). Joint combination of point cloud and DSM for 3D building reconstruction using airborne laser scanner data. *Proceedings of IEEE Urban Remote Sensing Joint Event, Paris, France*. pp. 1-7.
- [Tarsha-Kurdi et al., 2008] Tarsha-Kurdi, F., Landes, T., and Grussenmeyer, P. (2008). Extended RANSAC algorithm for automatic detection of building roof planes from Lidar data. *The Photogrammetric Journal of Finland*. vol. 21(1), pp. 97-109.
- [Tveite and Langaas, 1999] Tveite, H. and Langaas, S. (1999). An accuracy assessment method for geographical line data sets based on buffering. *International Journal of Geographical Information Science*. vol. 13(1), pp. 27- 47.
- [Verma et al., 2008] Verma, V., Kumar, R., and Hsu, S. (2008). 3d building detection and modeling from aerial LiDAR data. In *IEEE Computer Society Conference on Computer Vision and Pattern Recognition*. 8 pages.
- [Wagner, 2011a] Wagner, R. (2011a). Leica ADS80 and Leica XPro: a total solution for photogrammetric mapping. *53rd Photogrammetric Week*. pp. 79-87, in Stuttgart from 5 to 9 September.
- [Wagner, 2011b] Wagner, R. (2011b). The Leica RCD30 medium format camera: imaging revolution. *53rd Photogrammetric Week*. pp. 89- 95, in Stuttgart from 5 to 9 September.
- [Wang et al., 2008] Wang, M., Bai, H., and Hu, F. (2008). Automatic texture acquisition for 3D model using oblique aerial images. *Proceedings of IEEE*

- International Conference on Intelligent Networks and Intelligent Systems.* pp. 495 - 498, Wuhan, China.
- [Wang, 1998] Wang, Z. (1998). Extracting building information from LiDAR data. *ISPRS Commission III Symposium on Object Recognition and Scene Classification from Multi-Spectral and Multi-Sensor Pixels.* 6 pages.
- [Weidner, 2008] Weidner, U. (2008). Contribution to the assessment of segmentation quality for remote sensing application. *The International Archives of the Photogrammetry, Remote Sensing and Spatial Information Sciences.* vol. XXXVII(B7), pp. 479-484.
- [Wolf and Dewitt, 2000] Wolf, P. and Dewitt, B. (2000). *Elements of photogrammetry with application in GIS.* McGraw, 3rd edition. 624 pages.
- [Zeng et al., 2013] Zeng, C., Wang, J., and Lehrbass, B. (2013). An evaluation system for building footprint extraction from remotely sensed data . *IEEE Journal of Selected Topics in Applied Earth Observations and Remote Sensing publication information.* vol. 6(3), pp. 1640 - 1652.
- [Zhan et al., 2005] Zhan, Q., Molenaar, M., Tempfli, K., and Shi, W. (2005). Quality assessment for geo-spatial objects derived from remotely sensed data. *International Journal of Remote Sensing.* vol. 26(14), pp. 2953-2974.
- [Zhang et al., 2012] Zhang, W., Chen, y., Yan, K., Yan, G., and Zhou, G. (2012). Primitive-based 3D building reconstruction method tested by reference airborne data. *International Archives of the Photogrammetry, Remote Sensing and Spatial Information Sciences.* vol. XXXIX(B3), pp. 373-378, XXII ISPRS Congress, 25 August - 01 September 2012, Melbourne, Australia.
- [Zhang et al., 2011] Zhang, W., Grussenmeyer, P., Yan, G., and Mohamed, M. (2011). Primitive-based building reconstruction by integration of LiDAR data and optical imagery. *International Archives of Photogrammetry, Remote Sensing and Spatial Information Sciences.* vol. 38(5/W12), pp. 6 pages, Calgary, Canada.
- [Zhou et al., 2012] Zhou, G., Yan, K., Zhang, W., Yan, G., Chen, Y., Grussenmeyer, P., and Mohamed, M. (2012). Comparison of 3D buildings reconstructed by different data sources. *Geoscience and Remote Sensing Symposium (IGARSS), 2012 IEEE International.* pp. 6001-6004, 22-27 July 2012 doi: 10.1109/IGARSS.2012.6352240.



UNIVERSITE DE STRASBOURG

RESUME EN FRANÇAIS DE LA THESE DE DOCTORAT

Evaluation de la qualité des modèles 3D de bâtiments
en photogrammétrie numérique aérienne

Discipline : Génie civil
Spécialité : Photogrammétrie

Présentée par : Mostafa MOHAMED

Unité de Recherche : Laboratoire ICube UMR 7357
Équipe TRIO à l'INSA Strasbourg

Directeur de Thèse : Pierre GRUSSENMEYER, Professeur des Universités

École Doctorale 269 : Mathématiques, Sciences de l'Information et de l'Ingénieur

Evaluation de la qualité des modèles 3D de bâtiments en photogrammétrie numérique aérienne

Mostafa MOHAMED

Résumé des travaux en français

1. Introduction

Les systèmes de photogrammétrie numérique et de balayage laser aéroportés, étroitement liées aux évolutions technologiques, sont essentiels pour l'acquisition et l'extraction de l'information géographique en 3D. Les méthodes et les outils de génération automatique ou semi-automatique de modèles 3D urbains se développent rapidement, mais l'évaluation de la qualité de ces modèles et des données spatiales sur lesquelles ils s'appuient n'est que rarement abordée. Les travaux relatifs à l'évaluation des données/produits photogrammétriques ou lasergrammétriques se cantonnent souvent à une évaluation visuelle des résultats voire à un simple calcul d'écarts, une évaluation complète en 3D n'étant pas triviale. Cette thèse s'intéresse plus particulièrement à la qualité des modèles 3D de bâtiments restitués ou extraits à partir d'images aériennes ou de nuages de points. Un bâtiment peut être décrit soit par un ensemble de points caractérisant les extrémités des lignes directrices, soit par des lignes, par des surfaces ou encore par des volumes.

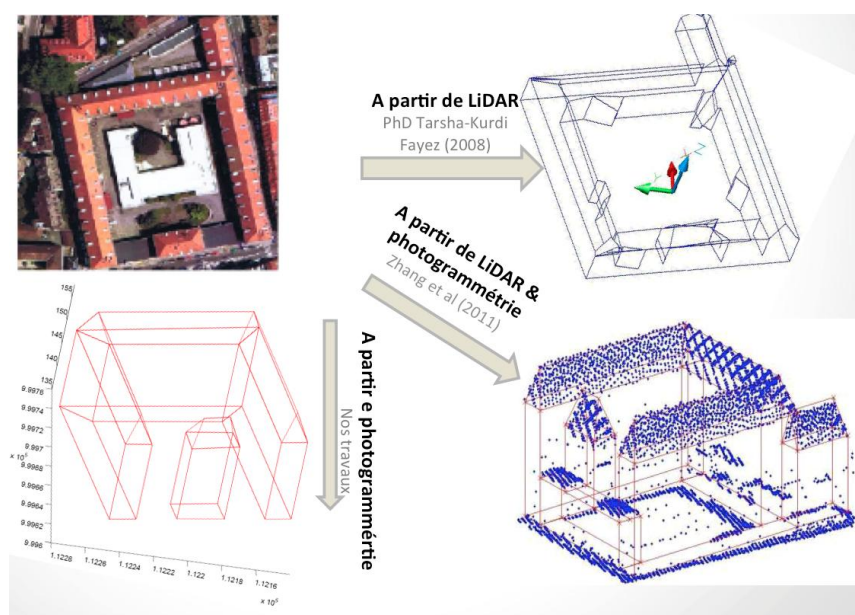


Figure 1. Acquisition des données et modélisation

Notre objectif est de proposer une approche multidimensionnelle standard pour évaluer la qualité des modèles 3D de bâtiments en 1D, 2D et 3D. Elle suppose toutefois de disposer, pour chaque modèle de bâtiment à évaluer, de son modèle de référence, considéré comme étant a priori plus précis.

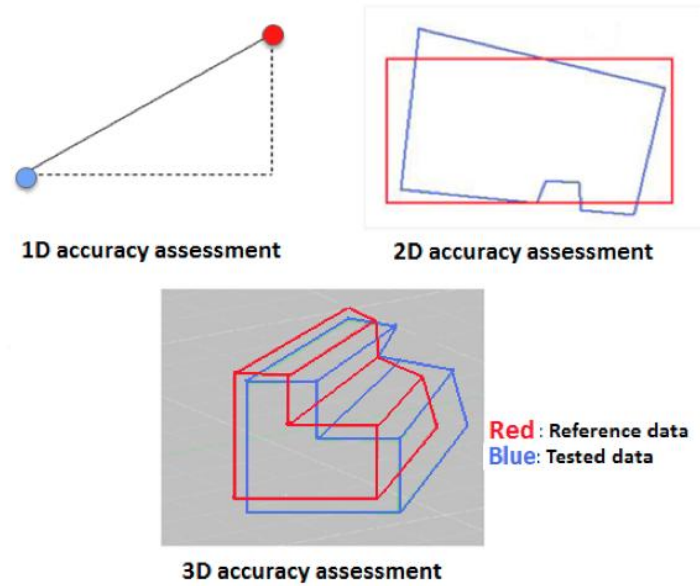


Figure 2. Evaluation de modèles 3D de bâtiments (modèle de référence et modèle testé)

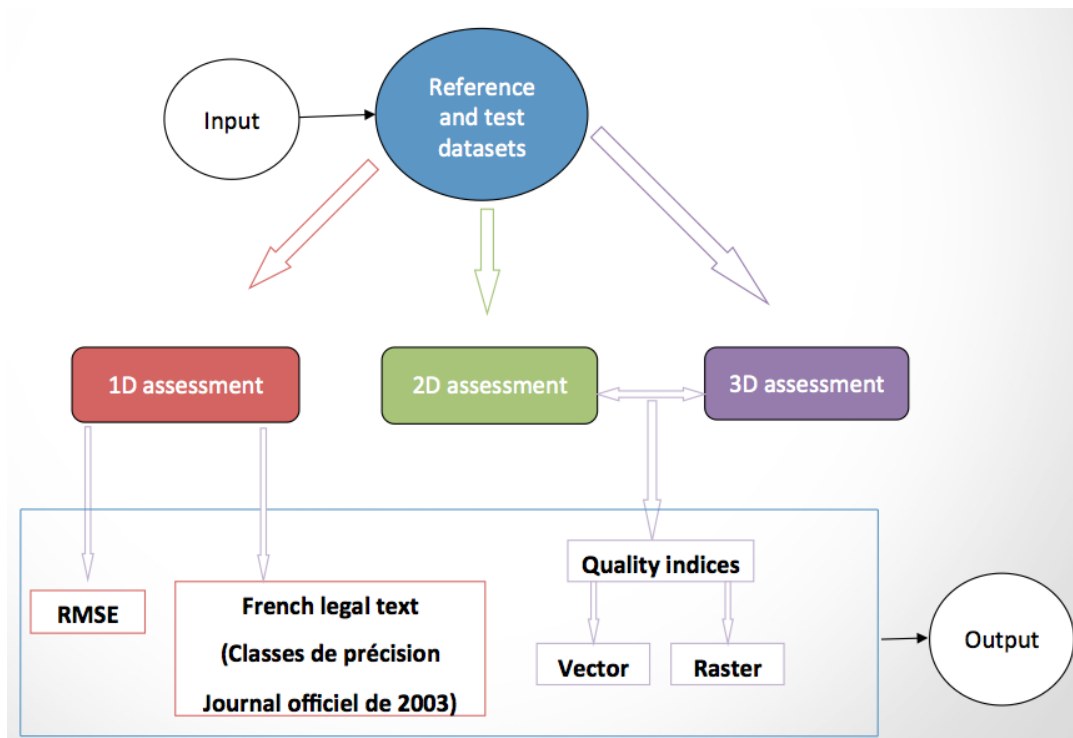


Figure 3. Approche multi-dimensionnelle pour l'évaluation de la qualité développée dans la thèse

L'approche que nous proposons se penche sur le calcul d'indices de qualité fréquemment rencontrés dans la littérature. Ces indices rejoignent ceux rencontrés dans l'évaluation des classifications (erreurs d'omission, de commission) et passent par la discrétisation de l'espace en pixels (2D) ou en voxels (3D) pour mesurer le degré de superposition d'objets 2D ou 3D. L'originalité de notre approche réside dans le fait que les modèles employés en entrée ne se limitent pas au mode raster, mais s'étendent au mode vecteur. Il semble évident que les modèles définis en mode vecteur s'avèrent plus fidèles à la réalité qu'en mode raster. En revanche, la confrontation de deux modèles vectoriels est plus délicate, notamment lorsqu'il s'agit de calculer le volume correspondant à l'intersection des deux. Les expérimentations menées dans cette étude se concentrent sur l'évaluation de la qualité des modèles 3D de bâtiments à Strasbourg, créés à partir de relevés photogrammétriques, lasergrammétriques ou de l'intégration simultanée de ces deux sources de données.

2. Evaluation 1D

L'évaluation 1D de la géométrie du modèle 3D consiste à comparer le bâtiment à tester au bâtiment de référence, en s'appuyant sur le calcul des écarts entre points homologues. Les points considérés caractérisent la forme du bâtiment (coins de bâtiment, faitières...). Deux solutions sont présentées pour l'évaluation 1D. La première se base sur l'analyse de l'erreur moyenne quadratique en X, Y et Z calculée à partir des écarts entre les deux modèles (référence et test). Ils sont ensuite confrontés à une tolérance fixée par l'utilisateur ou le cahier des charges. La deuxième solution s'appuie sur les instructions parues au Journal Officiel du 30 octobre 2003 et exigeant le respect de classes de précisions. On entend par écarts, aussi bien ceux calculés entre les nœuds homologues que ceux calculés entre les centres de gravité des plans homologues composant le bâtiment.

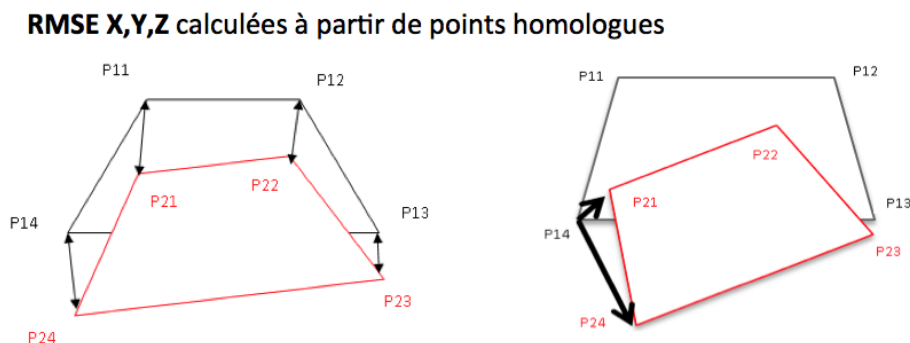


Figure 4a

RMSE X,Y,Z calculées à partir des écarts entre les centres de gravités des plans homologues

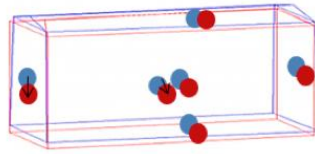


Figure 4b

$$X_c = \left(\frac{x_1 + x_2 + x_3 + \dots + x_N}{N} \right)$$

$$RMSE_X = \sqrt{\frac{1}{N} \sum (X_{ref} - X_{test})^2}$$

$$Y_c = \left(\frac{y_1 + y_2 + y_3 + \dots + y_N}{N} \right)$$

$$RMSE_Y = \sqrt{\frac{1}{N} \sum (Y_{ref} - Y_{test})^2}$$

$$Z_c = \left(\frac{z_1 + z_2 + z_3 + \dots + z_N}{N} \right)$$

$$RMSE_Z = \sqrt{\frac{1}{N} \sum (Z_{ref} - Z_{test})^2}$$

X_c, Y_c, Z_c coordinates of centroid.

x_i, y_i, z_i coordinates of vertices.

N number of points.

$X_{ref}, Y_{ref}, Z_{ref}$ coordinates of reference points. X_{test}

Y_{test}, Z_{test} coordinates of test points.

N number of points.

Figure 4a et 4b. Calculs des Erreurs Moyennes Quadratiques (RMSE) pour l'évaluation 1D

Cette méthode est simple et intuitive, mais présente des limites. Si les calculs d'écarts sont automatisables, il réside toutefois la difficulté, dans un jeu de données particulièrement bruité, de garantir l'exacte correspondance entre les points du modèle 3D et ceux de sa référence. La proximité des points n'est pas un critère suffisant pour les appairer, en particulier si les deux ensembles de points sont mal géoréférencés. Dans la pratique, le calcul du centre de gravité soulève moins d'ambiguïtés, car quelle que soit la distribution des points, il n'y a qu'un seul centre de gravité par face. Nous privilégierons donc, pour l'évaluation à 1D, la prise en compte de l'erreur moyenne quadratique sur les distances entre le centre de gravité de chaque plan composant le bâtiment testé et celui de son plan homologue dans le bâtiment de référence.

3. Evaluation 2D

L'évaluation 2D de la géométrie du modèle 3D est basée sur la comparaison des plans des deux modèles de bâtiments (référence et test) et passe par le calcul d'un ensemble d'indices de qualité. Ces indices font intervenir des opérations booléennes telles que l'union et l'intersection de surfaces de plans homologues.

ST: Surface to Test



SR: Surface of Reference

Figure 5. Superposition des surfaces de référence et de test

Indice de qualité (ρq)

(Schuster and Weidner, 2003, Weidner, 2008)

$$\rho q = \frac{ST \cap SR}{ST \cup SR} = 1 - \frac{(ST \setminus SR) \cup (SR \setminus ST)}{ST \cup SR}$$

$$\rho q = 1 - \frac{(ST \setminus SR) \cup (SR \setminus ST)}{ST \cap SR + (ST \setminus SR) \cup (SR \setminus ST)}$$

Indice de qualité pondéré ($\rho q w$)

$$\rho q w = 1 - \frac{A}{ST \cap SR + A}$$

$$A = \sum_{(x \in ST \setminus SR)} w(d(x, SR)) + \sum_{(x \in SR \setminus ST)} w(d(x, ST))$$

$$d(x, S) = \inf\{p(x, s) : s \in S\}$$

$$w(d(x, S)) = \frac{1}{\Delta d} d(x, S)$$

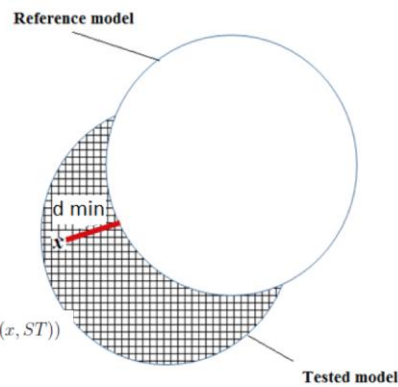


Figure 6. Indices de qualité pour l'évaluation 2D

<i>Detection rate :</i>	$\rho d = \frac{ST \cap SR}{SR}$	$\rho d \in [0; 1]$
<i>Quality rate:</i>	$\rho q = \frac{ST \cap SR}{ST \cup SR}$	$\rho q \in [0; 1]$
<i>Branch factor:</i>	$\rho b = \frac{ST \setminus SR}{ST \cap SR}$	$\rho b \geq 0$
<i>Miss factor:</i>	$\rho m = \frac{SR \setminus ST}{ST \cap SR}$	$\rho m \geq 0$
<i>False alarm rate:</i>	$\rho f = \frac{ST \setminus SR}{SR}$	$\rho f \geq 0$
<i>Quality weight rate:</i>	$\rho q w = \frac{A}{ SR \cap ST + A}$	$\rho q w \in [0; 1]$
$A = \sum_{x \in (SR \cup ST)} (w(d(x, SR)) + w(d(x, ST)))$ $d(x, S) = \inf\{p(x, a) : a \in S\}$ $w(d(x, SR)) = \frac{1}{\Delta d} d(x, S)$		

Résultats satisfaisants si :

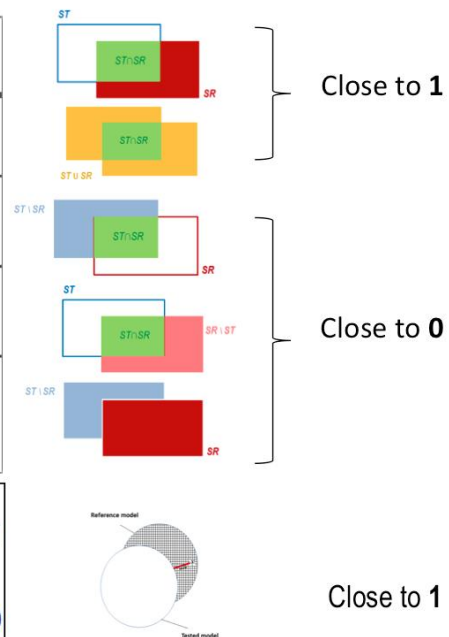


Figure 7. Interprétation des indices de qualité pour l'évaluation 2D

En mode raster, le calcul de la surface d'un plan 3D s'opère en trois étapes : a) le plan moyen est calculé à partir des points 3D du nuage le décrivant, b) la surface 2D est générée en mode raster en projetant les sommets du polygone sur le plan décrit précédemment, c) les pixels se trouvant à l'intérieur du polygone 2D sont identifiés puis comptabilisés pour arriver au calcul de la superficie totale. Le calcul de la surface d'intersection entre le polygone testé et son homologue de référence s'effectue à partir des pixels communs aux deux surfaces. En mode vecteur, le calcul de la surface d'un plan s'appuie sur le théorème de Green, faisant intervenir les coordonnées des sommets du polygone en 2D.

Mode Vecteur

Calcul des surfaces

Formule basée sur le théorème de Green (O'Rourke, 1998)

$$A = \frac{1}{2} \left| \sum_{k=1}^n x_k y_{k+1} - x_{k+1} y_k \right|$$

Où n est le nombre de sommets
 $x_{n+1} = x_1$ and $y_{n+1} = y_1$

Intersection des surfaces: étude de cas

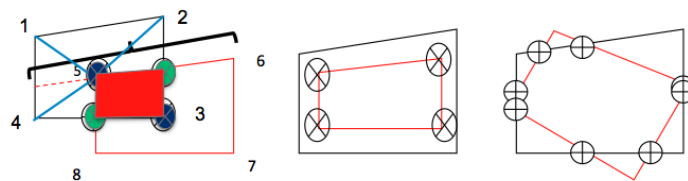


Figure 8. Calculs des surfaces pour l'évaluation 2D

L'opération consistant à déterminer la zone d'intersection de deux polygones s'effectue quant à elle en deux étapes : a) la détection des points situés à l'intérieur des polygones, suivi de b) la détection des points d'intersection entre lignes. Pour ces derniers, il faudra s'assurer qu'ils se trouvent sur le contour des deux polygones et non pas sur l'extension de lignes formant contour. La surface de la zone d'intersection peut ensuite être calculée à partir des coordonnées 2D des sommets.

4. Evaluation 3D

Pour l'évaluation 3D, chaque modèle 3D de bâtiment est considéré comme un objet à part entière.

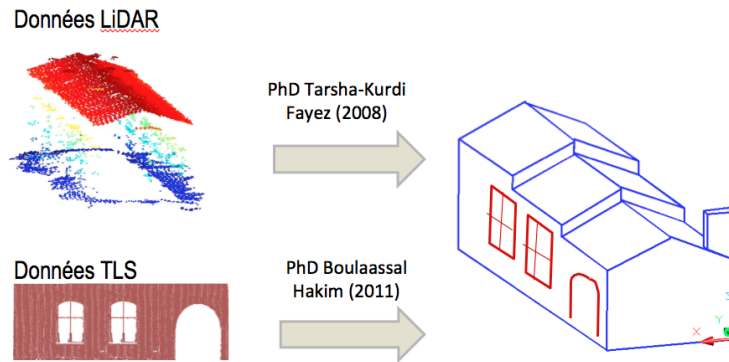


Figure 9. Mode d'obtention de modèles 3D à partir de données LiDAR aéroportée et terrestre

Les indices de qualité, déduits de ceux définis en 2D, se rapportent dans ce cas au degré de superposition du volume testé et du volume de référence. Ils prennent en compte le volume de l'intersection ainsi que le volume de l'union de deux bâtiments. En mode raster, La méthode utilisée pour calculer le volume d'un objet consiste à additionner le nombre de voxels qui composent le modèle 3D.

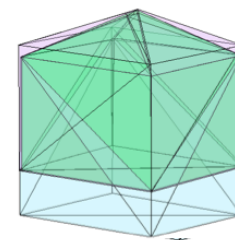
Les facteurs de qualité se rapportent aux volumes et remplacent les indices surfaciques

Volumetric detection rate : $V_{pd} = \frac{VR \cap VT}{VR}$; $v_{pd} \in [0:1]$
Volumetric quality rate: $V_{\rho q} = \frac{VR \cap VT}{VR \cup VT}$; $v_{\rho q} \in [0:1]$
Volumetric Branch factor: $V_{\rho b} = \frac{VT \setminus VR}{VR \cap VT}$; $v_{\rho b} \geq 0$
Volumetric Miss factor : $V_{\rho m} = \frac{VR \setminus VT}{VR \cap VT}$; $v_{\rho m} \geq 0$
Volumetric false alarm rate : $V_{\rho f} = \frac{VT \setminus VR}{VR}$; $v_{\rho f} \geq 0$

Résultats satisfaisants si :

Proche de 1

Proche de 0



Proche de 1



Volumetric weighted quality rate:
$V_{\rho qw} = 1 - \frac{V}{ VR \cap VT + V} \quad V_{\rho qw} \in [0:1].$
$V = \sum_{(y \in VT \setminus VR)} w(d(y, VR)) + \sum_{(y \in VR \setminus VT)} w(d(y, VT))$
$d(y, VT) = \inf\{\rho(y, vt) : vt \in VT\}$
$w(d(y, VT)) = \frac{1}{\Delta d} d(y, VT)$

Figure 10. Interprétation des indices de qualité pour l'évaluation 3D

Le volume de l'intersection se calcule aisément en comptabilisant les voxels communs aux deux modèles comparés. En mode vecteur, ces calculs sont moins triviaux. On détermine tout d'abord l'enveloppe convexe formée par les sommets des modèles pour calculer le volume de chaque bâtiment. L'état de l'art confirme les difficultés liées à la détermination

du volume d'intersection des deux modèles 3D en mode vecteur. L'algorithme que nous proposons repose sur l'extraction des sommets du polyèdre 3D d'intersection. Comme pour le calcul menant à la surface d'intersection de deux polygones, il est nécessaire de distinguer deux groupes de points : a) les points situés à l'intérieur des volumes des bâtiments, en l'occurrence les sommets du volume de référence se trouvant à l'intérieur du modèle testé ; b) les points situés à l'intersection des lignes (arêtes) composant le modèle de référence avec tous les plans du modèle testé. Dans l'itération suivante, cette détection de points est effectuée en permutant modèle de référence et modèle à tester. Au final seront détectés aussi bien les sommets de bâtiments situés à l'intérieur d'un volume que les points d'intersection entre plans et arêtes. L'ensemble de ces points caractérise le polyèdre 3D d'intersection dont il ne reste qu'à calculer le volume. A ce stade, les éléments indispensables à la détermination des indices de qualité en 3D sont réunis.

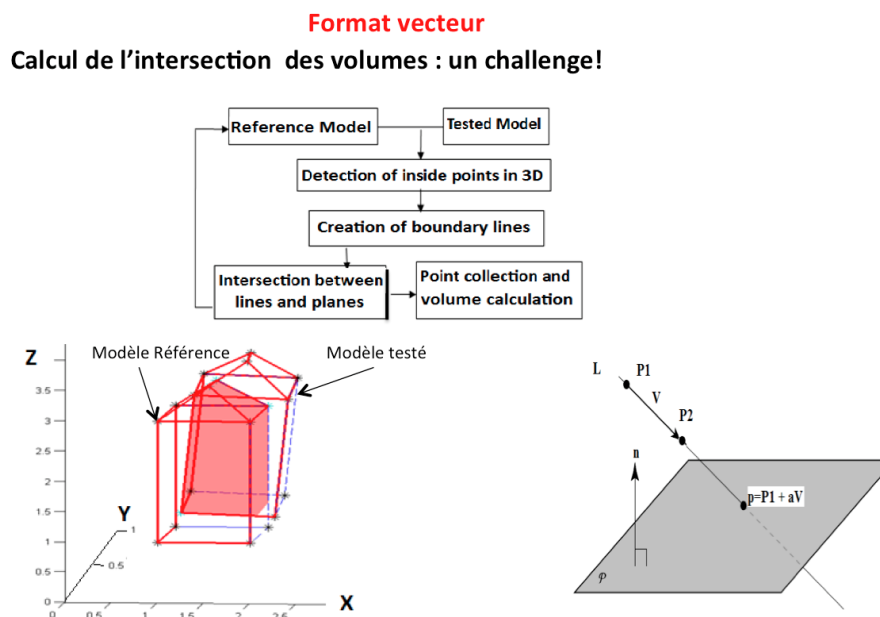


Figure 11. Calculs des volumes pour l'évaluation 3D

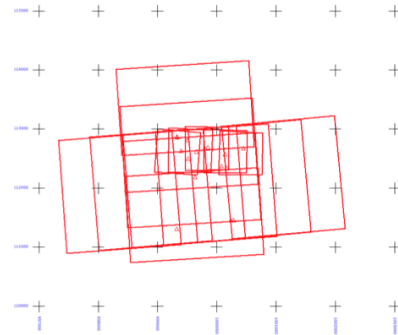
5. Résultats

La zone d'étude qui a permis d'expérimenter notre approche est située sur le territoire de la ville de Strasbourg. Nous disposons sur cette zone d'images aériennes numériques à haute résolution spatiale acquises par des caméras de type UltraCam-X (Vexcel), Rollei (moyen format) et par une chambre de prise de vue métrique Zeiss LMK. Des données LiDAR à un seul écho couvrent le même secteur géographique. Ces données n'ont pas été acquises la

même année, mais permettent toutefois d’être combinées, étant donné que nos objets d’étude sont des bâtiments 3D présents dans tous les jeux de données.

Caractéristiques des données photogrammétriques

Capteurs	UltraCam-X (4 images)	RolleiDB44 (5 images)	Zeiss LMK (6 images)
Acquisition date	2007	2004	1998
Focal length (mm)	100.500	80.553	211.030
GSD (cm)	16	16	24
Flying height (m)	2300	1450	1700
Overlap %	65	60	70
Base (m)	527	265	556
Pixel size (µm)	7.2	9	30.0



Photos UltraCam-X (grand format, bande Nord-Sud), RolleiDB44 (moyen format, bande Ouest-Est), et photos Zeiss LMK (grand format, bande Ouest-Est).

Caractéristiques des données LiDAR

LiDAR system	TopScan / Optech ALTM 1225
Acquisition date	2004
Flying height (m)	1440
Density of points	1.3 points/m ²

Figure 12. Description des données testées dans le cadre de la thèse

Les modèles 3D des bâtiments de référence ont été reconstruits par voie photogrammétrique à partir des images UltraCam-X géoréférencées préalablement à l’aide de 14 points d’appui mesurés avec un système GNSS. Les modèles à évaluer ont été reconstruits en considérant trois approches semi-automatiques de reconstruction de bâtiments en 3D : l’une s’appuyant exclusivement sur des images aériennes, l’autre exclusivement sur des données LiDAR et la troisième sur la combinaison des deux (figure 1).

Modèles 3D de bâtiments restitués à partir de photos aériennes

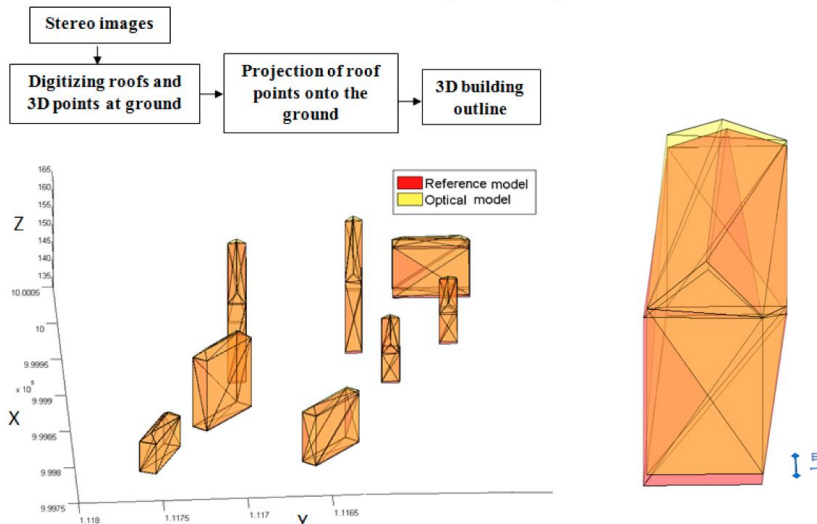


Figure 13. Etapes de restitution des bâtiments par voie photogrammétrique

Nous disposons actuellement de 75 échantillons de modèles 3D obtenus à partir des images aériennes, 26 échantillons de modèles 3D issus à la fois des données LiDAR et des images aériennes, et 8 échantillons de modèles 3D issus des données LiDAR seules.

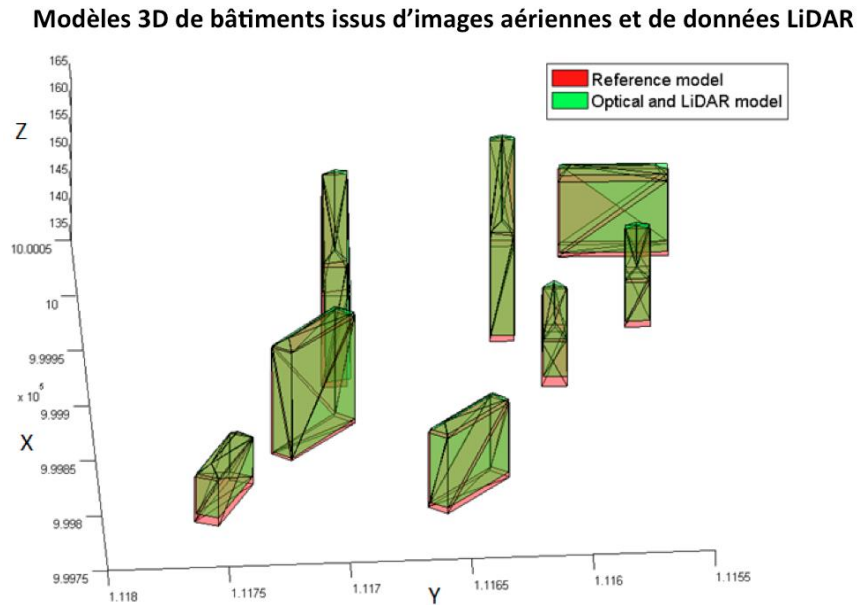


Figure 14. Exemples de modèles 3D obtenus par photogrammétrie et LiDAR comparés à une référence

L'approche d'évaluation multidimensionnelle décrite précédemment, aussi bien pour des modèles vectoriels que rasters, a été appliquée à cet important échantillon de modèles 3D de bâtiments. Nous constatons que les modèles reconstruits à partir des images aériennes fournissent de meilleurs résultats, aussi bien d'un point de vue qualitatif que quantitatif, que ceux reconstruits à partir des nuages de points issus du LiDAR. Un écart altimétrique significatif entre les modèles issus des données LiDAR et ceux issus des images a été mis en évidence.

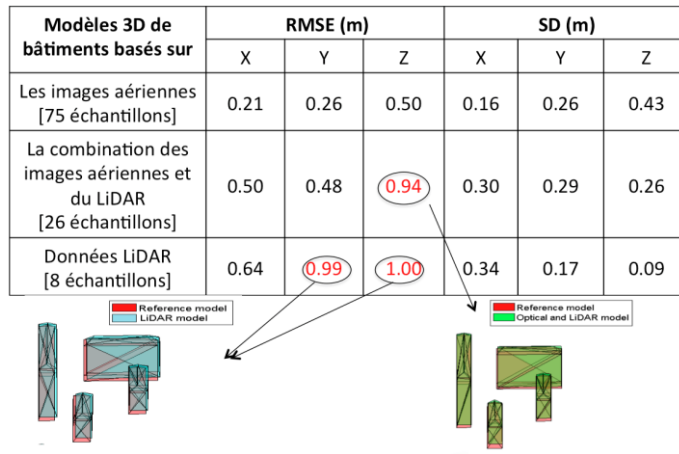
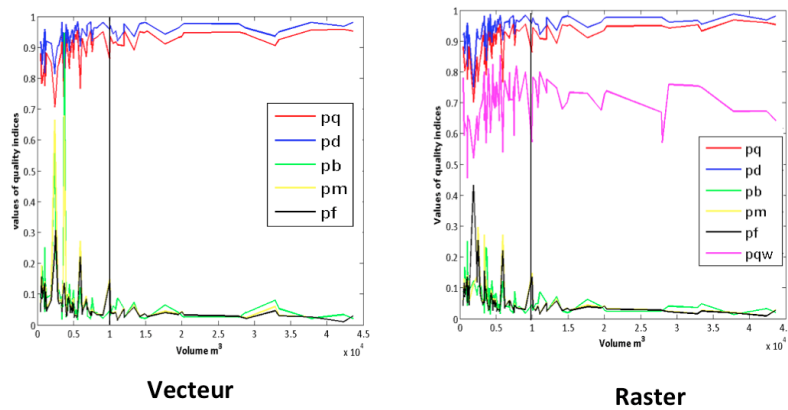


Figure 15. Valeurs moyennes des erreurs moyennes quadratiques obtenues à partir des centres de gravité des plans homologues (évaluation 1D)



Bons résultats car les indices de qualité ρ_d , ρ_q , ρ_{qw} sont proches de 1 et les autres indices proches de 0

Figure 16. Exemples de résultats d'évaluation 2D pour des modèles issus de photogrammétrie aérienne

Modèles 3D de bâtiments à partir de	Structure des données	ρ_d [SD]	ρ_q [SD]	ρ_b [SD]	ρ_m [SD]	ρ_f [SD]	ρ_{qw} [SD]
Photos aériennes [75 exemples]	Vecteur	0.938 [0.043]	0.891 [0.060]	0.089 [0.132]	0.085 [0.119]	0.062 [0.051]	-
	Raster	0.943 [0.042]	0.899 [0.056]	0.064 [0.050]	0.064 [0.056]	0.061 [0.062]	0.697 [0.078]
Combinaison d'images et de données LiDAR [26 exemples]	Vecteur	0.867 [0.057]	0.788 [0.079]	0.177 [0.105]	0.154 [0.121]	0.120 [0.092]	-
	Raster	0.878 [0.053]	0.802 [0.073]	0.157 [0.094]	0.134 [0.102]	0.109 [0.085]	0.558 [0.124]
Données LiDAR dataset [8 exemples]	Vecteur	0.840 [0.064]	0.711 [0.054]	0.219 [0.109]	0.250 [0.053]	0.198 [0.035]	-
	Raster	0.841 [0.065]	0.713 [0.055]	0.217 [0.110]	0.249 [0.053]	0.197 [0.034]	0.494 [0.063]

Figure 17. Résultats de l'évaluation 2D. En vert, les résultats satisfaisants pour les modèles issus d'images aériennes. En rouge, les mauvais résultats pour les modèles issus des données LiDAR.

Modèles 3D de bâtiments à partir de	Structure des données	V _{pd} [SD]	V _{pq} [SD]	V _{pb} [SD]	V _{pm} [SD]	V _{pf} [SD]	V _{pqw} [SD]
Photos aériennes [75 exemples]	Vecteur	0.943	0.895	0.063	0.058	0.054	-
		[0.041]	[0.054]	[0.054]	[0.041]	[0.036]	
	Raster	0.917	0.853	0.095	0.088	0.079	0.827
		[0.056]	[0.077]	[0.083]	[0.061]	[0.049]	[0.060]
Combinaison d'images et de données LiDAR [26 exemples]	Vecteur	0.875	0.809	0.148	0.102	0.089	-
		[0.057]	[0.082]	[0.079]	[0.101]	[0.089]	
	Raster	0.846	0.753	0.188	0.155	0.130	0.691
		[0.054]	[0.079]	[0.082]	[0.112]	[0.094]	[0.089]
Données LiDAR [8 exemples]	Vecteur	0.885	0.791	0.136	0.136	0.120	-
		[0.070]	[0.067]	[0.093]	[0.043]	[0.039]	
	Raster	0.824	0.686	0.225	0.246	0.201	0.609
		[0.082]	[0.072]	[0.125]	[0.040]	[0.023]	[0.075]

Figure 18. Résultats de l'évaluation 3D. En vert, les résultats satisfaisants pour les modèles issus d'images aériennes. En rouge, les mauvais résultats pour les modèles issus des données LiDAR.

Les statistiques sur les indices de qualité 2D et 3D calculés montrent que les modèles 3D de bâtiments extraits à partir des couples d'images stéréoscopiques sont cohérents. Les modèles reconstruits à partir du LiDAR ou de l'intégration du LiDAR et des images aériennes sont moins exacts. Cette imprécision est à rapporter essentiellement à la qualité des données brutes transmises. Cependant, les valeurs des indices de qualité ne peuvent être considérées uniquement sous forme moyennée. Afin d'évaluer la qualité de la reconstruction du bâtiment en détail et d'analyser les défauts liés à sa géométrie, il faut interpréter les indices de qualité pour chaque bâtiment séparément. Par ailleurs, les valeurs des indices sont également affectées par la taille du bâtiment. Ainsi, les indices de qualité calculés pour des petits bâtiments conduisent généralement à de moins bons résultats.

Critères	Raster	Vecteur
Création des modèles	Rapide	Variable entre 2D et 3D
Représentation des données	par pixel (2D) ou voxel (3D)	Représenté sans généralisation
Structure des données	Simple	Complexe
Volume des données	Important	Faible
Représentation des éléments linéaires	Difficile	Facile
Calcul des surfaces et des volumes	Peu précis	Plus précis
Analyse des données et calculs	Simple et facile à programmer	Les algorithmes et les fonctions sont complexes
Temps de calcul	Elevé	Moins d'une seconde pour les évaluations 2D et 3D de cette thèse

Figure 19. Comparaison des critères relatifs à la modélisation des bâtiments en modes vecteur et raster

6. Conclusion

Cette thèse a abouti à l'élaboration d'une approche d'évaluation multidimensionnelle de bâtiments en 3D reconstruits à partir de trois méthodes semi-automatiques. L'approche a été validée pour des modèles vectoriels et rasters. Notre approche considère l'exactitude des modèles 3D de bâtiments calculée sur la base de comparaisons de points en 1D, de surfaces en 2D, et de volumes en 3D. L'évaluation 1D donne une idée globale de la fiabilité des modèles reconstruits en fournissant une mesure métrique de proximité des centres de gravité. L'évaluation 2D qualifie le degré de superposition des faces, en dépit de sa sensibilité à la taille des polygones. Une évaluation 2D satisfaisante ne valide toutefois pas encore le modèle reconstruit, puisque deux plans parfaitement superposés dans le système d'axes parallèle au plan sont susceptibles d'être décalés en profondeur. Ce défaut est révélé dans l'étape de l'évaluation 3D. L'évaluation 3D analyse les bâtiments en tant qu'objets à part entière en estimant le degré de superposition des volumes à tester et des volumes de référence. L'approche proposée dans cette thèse est adaptée et opérationnelle pour des modèles vectoriels et rasters de bâtiments 3D simplifiés. Les futures recherches porteront sur l'extension de cette approche à la construction de modèles 3D plus complexes de bâtiments.

Les contributions de cette thèse ont fait l'objet de cinq communications dans des congrès internationaux:

Mohamed, M., Grussenmeyer, P., 2011. Plane-based accuracy assessment in photogrammetry: comparison of Rollei Medium format and Ultracam-X digital cameras. *GTC2011 Symposium, "Geomatics in the City"*, Jeddah, Saudi Arabia, May 11-13, 6 pages.

Zhang, W., Grussenmeyer, P., Yan, G., **Mohamed, M.**, 2011. Primitive-based building reconstruction by integration of Lidar data and optical imagery, *International Archives of Photogrammetry, Remote Sensing and Spatial Information Sciences*, Calgary, Canada, Vol. 38(5/W12), 6 pages.

Zhou, G., Yan, K., Zhang, W., Yan, G., Chen, Y., Grussenmeyer, P., **Mohamed, M.**, 2012. Comparison of 3D buildings reconstructed by different data sources. Geoscience and Remote Sensing Symposium (IGARSS), 2012 *IEEE International*, pp.6001-6004, 22-27 July 2012 doi: 10.1109/IGARSS.2012.6352240

Landes, T., Grussenmeyer, P., Boulaassal, H., **Mohamed, M.**, 2012. Assessment of three-dimensional Models Derived from LIDAR and TLS Data. *The XXII ISPRS Congress in Melbourne, Australia 25th August to 1st September 2012*, Vol.XXXIX-B2, pp.95-100, 2012.

Mohamed, M., Landes, T., Grussenmeyer, P., Zhang, W., 2013. Multi-dimensional quality assessment of photogrammetric and LiDAR datasets based on a vector approach. *International Archives of the Photogrammetry, Remote Sensing and Spatial Information Sciences*, Vol. XL-2/W1, 6 pages. 8th International Symposium on Spatial Data Quality, 30 May - 1 June 2013, Hong Kong.